SOLUTION-PROCESSED ORGANIC/HYBRID SEMICONDUCTORS AND USE OF LOW MELTING ALLOYS AS ELECTRODES

A Thesis Submitted in The partial Fulfillment of the
Requirements for the Degree of

Doctor of Philosophy

By

Prashant Kumar

Chemistry and Physics of Materials unit

Jawaharlal Nehru Centre for Advanced Scientific Research

Bangalore - 560 064

Karnataka, INDIA

February 2017

DECLARATION

I hereby declare that the matter embodied in this thesis is the result of the work carried out by me under the supervision of Prof. K. S. Narayan, at Molecular Electronics Laboratory, in Chemistry and Physics of Materials Unit, Jawaharlal Nehru Centre for Advanced Scientific Research, Bangalore, India. It has not been submitted for the Award of any degree or diploma or associateship of any other university or institute.

In keeping with the general practice in reporting a scientific observation, due acknowledgment has been made whenever the work described is based on the findings of other investigators.

(Prashant Kumar)

Candidate

JAWAHARLAL NEHRU CENTRE FOR ADVANCED SCIENTIFIC RESEARCH
Jakkur, Bangalore 560064, India

K. S. NARAYAN
Professor
Dean (Research and Development)
PHONE: +91 80 2208 2822/2548
E-mail: narayan@jncasr.ac.in
Fax: 91 80 22082766

February 16th, 2017

CERTIFICATE

I hereby certify that the matter embodied in the thesis entitled "*Solution-Processed Organic/Hybrid Semiconductors and Use of Low Melting Alloys as Electrodes*" has been carried out by Mr. Prashant Kumar at the Molecular Electronics Laboratory, Chemistry and Physics of Materials Unit, Jawaharlal Nehru Centre for Advanced Scientific Research, Bangalore, India, under my supervision and it has not been submitted elsewhere for the award of any degree or diploma.

Prof. K. S. Narayan

(Research Supervisor)

Dedicated to

My Parents and Teachers

Acknowledgement

An immeasurable amount of help cannot be acknowledged in limited words.

I express my sincere gratitude to my research supervisor, Prof. K. S. Narayan, for providing a wonderful and encouraging environment to learn and explore with utmost freedom. It is under his guidance that I learned to pursue science in the right attitude and mindfulness. At Molecular Electronics Laboratory, I learned to not give up, unless it should be. At the same time, I cannot thank enough to his family for providing the moments of being felt at home.

I will always be motivated by the example that Prof. C.N.R Rao has been. His energy and enthusiasm to pursue science along with the inspiring words will always be a source of encouragement.

I am especially grateful to the coordinators of integrated Ph.D. program, Prof. Balasubramanian Sundaram and Prof. Tapas K. Maji for teaching and motivating me into the scientific research.

I thank the chairman of Chemistry and Physics of Materials Unit (Prof. G.U.Kulkarni, Prof. Balasubramanian Sundaram, and Prof. Chandrabhas Narayana) for their constant help and support.

I am forever indebted to my teachers, Prof. Swapan K. Pati, Prof. Balasubramanian Sundaram, Prof. Aloknath Chakrabarti, Prof. Tapas K. Maji, Prof. K. S. Narayan, Prof. N.S.Vidyadhiraja, Prof. Rajesh Ganapathi, Prof. Shobhana Narasimhan, Shobha Madam, Prof. Chandrabhas Narayana, Prof. Ranjan Datta, Prof. A Sundaresan, Prof. S. M. Shivaprasad, Prof. G.U.Kulkarni, Prof. Umesh V.

Waghmare, Prof. M. Eswaramoorthy, Prof. H. Ila and other faculty members for all the teaching and interactive sessions.

I thank Prof. Suchi Guha at the University of Missouri, the USA for the wonderful collaboration and numerous helpful discussions.

I am thankful to my collaborators Prof. Chandrabhas Narayana and Shantanu Aggarwal at JNCASR, Prof. Vijayakumar C. Nair and Mr. Chinnadurai Muthu at NIIST Trivandrum, Prof. S. K. Asha and Dr. Rekha Narayanan at NCL Pune, Prof. A. K. Raychaudhuri, Dr. Rabaya Basori and Dr. Kaustuv Das at S. N. Bose national center for basic sciences, Kolkata, Prof. Anil Kumar at IIT Mumbai for providing with the opportunity to work on a range of interesting problems.

I express my sincere thanks to Prof. Sir Richard Friend, Dr. Aditya Sadhanala, Dr. Shahab Ahmad his wife Mrs. Uzma Akthar, Ms. Baodan Zhao, Ms. Darshana Joshi, Dr. Nishit Srivastava, Dr. Satyaprasad Senanayak and other friends at Cambridge for all the help and support and their wonderful hospitality during my stay.

I am thankful Prof. Subi George and his lab members for helping with various synthesis and measurements. I also thank Prof. Reji Philip and his lab members, especially Dr. Shafi at Raman Research Institute, for helping with the optical measurements.

I sincerely thank Jawaharlal Nehru Centre for Advanced Scientific Research for providing with the fellowship during the entire length of integrated Ph.D. program.

I am thankful to the staff at JNC administrative office, academic section, computer lab, dining hall, purchase section, CPMU office, security and workshop. I especially thank hostel wardens, office and mess staffs for making the stay in hostel comfortable and cheerful.

I acknowledge the Science and Engineering Research Board and Indo-UK, APEX-II project, Department of Science and Technology, Govt. of India for providing the travel funding for my UK and Italy visit. These visits were immensely useful for exploring science and interacting with people from around the globe.

My seniors and lab members have been of immense help, it is their experimental mastery, that I could see the world ahead. They have been teachers and friends, providing immeasurable help and advice in almost every aspect. I take this opportunity to thank my past and present colleagues who have been instrumental in shaping my research experience, Dr. Manohar Rao, Dr. Monojit Bag, Dr. Sabyasachi Mukhopadhyay, Dr. Balraju, Dr. Srinidhi Ramchandra, Dr. Kishor V. C., Dr. Poonam Sharama, Dr. Vini Gautham, Dr. Satyaprasad P. Senanayak, Dr. Ravichandran S., Dr. Suman Banerjee, Dr. Rahul Sharma, Dr. Mansa, Dr. Arun Dhumal Rao, Vijay Venugopalan, Dr. Nishit Srivastava, Ashar, Swathi, Raaghesh, Rishav, Vikas, Nisha, Apoorva, Deepak, Ganesh, Anaranya, Sumukh, and Sukanya. Big thank you to all of them.

I am also indebted to all my friends in and out of JNC, Dr. Soumik Siddhanta, Abhay Tiwari, Dr. Sandeep Lahiri, Dr. Poojashri Mishra, Sunil, Deelip, Chandan, Satish, Rajnish, Vivek, my integrated PhD batch mates (Dr. Dibyajyoti, Dr. Anindita, Darshana and Ajamala) for all the memorable and supportive moments.

I am blessed to have several inspiring teachers throughout my school and graduation; I especially thank Prof. Sood and Prof. Malik, at Banaras Hindu University, for encouraging me to pursue research.

I am also blessed to have the never-ending love, support, and encouragement of my nani, parents, uncles and aunts, my brothers and sisters. Without them, this journey would not have been possible.

The list has no limit, but to conclude, I pay my utmost respect to the ancient wisdom, knowledge, and teaching, for without them the life would have been a mere matter.

February 16th, 2017

JNCASR, Bangalore Prashant Kumar

List of Publications

In this thesis:

1. **Prashant Kumar**, Shantanu Aggarwal, Chandrabhas Narayana, K. S. Narayan, “Eutectic Metal Alloys for large area solution processed electrodes”, (manuscript submitted).

2. **Prashant Kumar**, K. Shadi, S Guha and K. S. Narayan, “Hybrid n-GaN and polymer interfaces: model systems for tunable photodiodes”, Organic Electronics, 14, 11, 2818-2825 (2013).

3. **Prashant Kumar**, Baodan Zhao, Richard H. Friend, Aditya Sadhanala, and K. S. Narayan, “Kinetic Control of Perovskite Thin Film Morphology and Application in Printable Light Emitting Diodes”, ACS Energy letters, 2, 1,81-87, (2016).

4. **Prashant Kumar**, Chinnadurai Muthu, Vijayakumar C Nair, and K. S. Narayan, “Quantum Confinement Effects in Organic Lead Tribromide Perovskite Nanoparticles”, J. Phys. Chem. C, 120, 32, 18333-18339, (2016).

5. **Prashant Kumar**, Ganesh N, K. S. Narayan, “Electrospun perovskite quantum dot/PMMA fibers as luminescent emitters”, (manuscript under preparation).

Synopsis

Printable semiconductors are a part of the new generation of electronic devices which can be flexible and lightweight. Organic-inorganic hybrids offer a natural improvement over solution processable organic semiconductors. These systems consist of organic and inorganic components offering a combination of enhanced performance and processability. Organic-inorganic hybrid perovskite (OIP) have recently demonstrated a range of superior electronic and optical properties. This thesis focuses on studies of a set of specific organic and hybrid semiconductors and interfaces.

The first part of the work probes into the use of meltable alloys for vacuum free cathode and interconnects applications. Meltable alloys are a suitable alternative for metal dispersion and carbon based inks. This study is directed towards understanding the adhesion, optical and electrical properties of indium based alloys. These alloys are ternary-quaternary eutectic systems, forming conformal contact with a polymer layer and the workfunction is comparable to that of aluminum. Optical and electrical studies indicate charge-transfer interaction at the alloy/organic semiconductor interface. Efficient devices have been realized using printing techniques. These studies suggest the role of indium in controlling the properties of the alloy.

The second part of the work consists of hybrid interfaces and materials. Chapter 3 discusses the bilayer hybrid interface consisting of large band gap inorganic and small gap organic layer. Such systems can be difficult to realize with ease, in pure inorganic heterojunction where surface states can be detrimental. High band gap n-doped gallium nitride (n-GaN) and low gap organic layers can form a type I or type II hybrid junction. The n-GaN surface polarization modifies the energy level of the polymer layer near the interface, which manifests in to a symbatic and antibatic spectral response (I_{ph})

depending on the direction of illumination. Its energy diagram is arrived based on the spectral response.

In next part of the work, the formation of thin film structure of organic-inorganic hybrid perovskite ($CH_3NH_3PbBr_3$) system and their correlation with emission has been studied. Organic small molecule additives have been used for controlling the morphology and crystallization kinetics of OIP. Maze like the growth of fibrous network composed of sub-micron OIP grains was observed upon additive assisted antisolvent treatment. Simultaneously a significant increase in photoluminescence and an accompanied decrease in disorder were observed. Modified OIP thin films were used in the printable light emitting diode which showed luminescence up to 50 Cd/m^2.

In the next chapter, the study focuses on perovskite nanocrystals (NC) which show high fluorescence quantum yield. The OIP's property to rapidly react with moisture has been overcome by the formation of capped NCs. The increase in optical band gap and exciton binding energy is associated with the onset of confinement effects, which get amplified in NCs of sizes smaller than 6 nm. Variation in emission properties of NCs are observed compared to that of bulk and can be associated with confinement effects. Single pixel emitter-detector device combination has been studied in bilayer structure using NC and organic acceptor layers.

The OIP quantum dots embedded in fibrous dielectric matrix show enhanced environmental stability. Such structures are known to show narrowing of emission. Large tunability in emission wavelength, exciton-phonon coupling and lifetime have been seen as a function of particle size. The emission peak shift shows a dependence on the bulk OIP band gap.

Contents

List of Figures

Abbreviations and Symbols

OSC	**Organic solar cells**
OIP	**Organic-Inorganic Hybrid perovskite**
PV	**Photovoltaics**
PET	**Polyethylene terephthalate**
PMMA	**Poly(methyl methacrylate)**
PS	**Polystyrene**
$MAPbBr_3$	**Methylammonium lead bromide**
$MAPbI_3$	**Methylammonium lead iodide**
QDs	**Quantum dots**
LED	**Light emitting diode**
D-A/ CT	**Donor-acceptor/ charge transfer**
HOMO	**Highest occupied molecular orbital**
LUMO	**Lowest unoccupied molecular orbital**
CB/VB	**Conduction band/valence band**
PLQY	**Photoluminescence quantum yield**
0D/1D/3D	**Zero-dimensional/One-dimensional /Three-dimensional**
SMC/A-SMC/S-SMC	**Sub-micron crystal/additive assisted sub-micron crystal/solvent assisted sub-micron crystal**
n-GaN	**N doped Gallium nitride**
AFM	**Atomic force microscopy**

J-V/C-V/QE	**Current density vs. voltage/ Capacitance vs. voltage/ Quantum efficiency**
BHJ	**Bulk Heterojunction**
FWHM	**Full width at half maxima**
W_F	**Work function**
V_{OC}/J_{SC}/FF/PCE	**Open-circuit voltage/short circuit current density/fill factor/power conversion efficiency**
EQE	**External quantum efficiency**
SERS	**Surface enhanced Raman scattering**
I_{ph}	**Photocurrent**
α	**Absorption coefficient**
EL	**Electroluminescence**
PL	**Photoluminescence**
MCP	**Micro-crystal pinning**
XRD	**X-ray diffraction**
SCLC	**Space charge limited current**
E_g	**Band -gap**
E_B	**Exciton binding energy**
µFET	**Field effect mobility**

Chapter 1: Introduction

1.1: Overview of printable electronics

The advent of solution processed, polymer semiconductors have paved the way for a large area, roll to roll processing of electronic devices. Solution-processed, organic active layer based semiconducting components like organic solar cells (OSC) [1-7], light emitting diode (LED) [8-10] and transistors [11-14] have been extensively studied for over last two decades. Flexible electronic devices like detectors, display, memories and circuits form an integral part of the new generation of smart technology. Some of the key features of printed electronic devices include low-cost manufacturing, low material consumption and light weight which make this technology energy efficient [15-18]. Availability of a large catalog of solution-processed semiconductors with tunable band gap allows for application specific material selection.

Besides semiconductors, conductors and buffer layers play an important role in device operation [19]. The solution processed active inks and metal inks lie at the core of the printed electronics, which can be cast into thin films using numerous available printing techniques [20-23]. The printable inks can be classified into various categories based on their physical and chemical nature. Active ink materials include organic polymer semiconductors [24-27], organic-inorganic hybrid perovskite (OIP) [28-30] and inorganic/hybrid quantum dots (QDs) [31, 32] have been successfully used in efficient electronic devices. One of the key advantages of solution processed semiconductor based ink lies in the ability to tune its absorption and emission properties [33, 34]. These allow for materials to be designed for specific applications such as tunable band detector [35] and narrow width emitter [36], which are particularly important for optical communications [37, 38]. Note that the printed electronics is benefited by the already available knowledge on various application-specific printing processes. This chapter presents the necessary background required to describe the main observations and results of subsequent chapters in this thesis. Since the field is vast, only the relevant topics have been selected for discussion.

1.2: Solution processed semiconducting inks

Solution processed semiconductors can easily fit in the role of printing inks while also being electronically active. Semiconducting ink has been grouped into three major categories namely (i) organic, (ii) organic-inorganic hybrid and (iii) QDs, The classification is based on their physical and chemical composition. Though the primary components of each class of semiconductor varies significantly, some of the features, common across different class of materials include, (i) facile dissolution/dispersion in a variety of polar and non-polar solvents, (ii) range of materials with access to tunable band gap, (iii) optimum interface formation for homogeneous films and suitable electronic interface.

1.2.1: Organic semiconducting inks

The organic semiconductors are π-conjugated organic molecules which can be either a small molecule or a chain of repeated monomers (polymers). The carbon atoms, in an organic semiconductor, are mostly sp^2 hybridized and the π bond is formed by the overlap of half-filled *2p* orbital between the adjacent carbon atoms. An example of an organic semiconductor is shown in Figure 1.1a. The delocalization of π electron cloud across the polymer chain is essential for the electronic transport [39]. The band gap of an organic semiconductor is defined as the energy gap (~ 1-3 eV) between the highest occupied molecular orbital (HOMO) and lowest unoccupied molecular orbital (LUMO) [40, 41]. The band gap, in organic semiconductors, originates from the dimerization of delocalized π electron cloud, the π-π^* transition is the lowest possible transition and defines the absorption edge [42]. The tunability of energy gap is achieved by varying the π conjugated chromophores in the molecular structure. With this understanding, it is possible to design semiconductors with molecular components as side groups and hetero-aromaticity to give a wide selection with tunable properties.

The optical and electronic properties of organic semiconductors are very different from their inorganic counterpart. The difference arises from the ease of polarizability in the organics due to their low bond strength [43, 44]. The absorption coefficient of a typical organic semiconductor (~ 10^5 cm^{-1}) is 1-2 orders of magnitude higher than that of the inorganic semiconductor; consequently, the active layer thickness required is much lower (~ 100-200 nm) in organic semiconductor devices [45]. The charge transport species in organic semiconductors are polarons, which are quasi-particles where charge carriers are coupled with electronic and structural distortions [46, 47]. In organic semiconductors, the low mobility of charge carriers arises from the localization effect. This results in an activated behavior, where mobility increases with an increase in temperature [48].

1.2.1 I: Excitonic Character

On absorbing a photon, a quasi-particle of coulombically bound electron-hole pair is formed (excitons), which has a Frenkel character in the organic semiconductors [49], the exciton binding energy (E_B) in organic semiconductors (~ 0.1 - 0.2 eV) is much higher than the room temperature thermal energy (kT ~ 25 meV at T = 300K) [50]. Low dielectric constant (~ 2.5-3) and ease of polarizability of organic materials results in a large E_B [43, 51]. In order to efficiently separate the excitons into free carriers, carefully tailored heterostructure interfaces are required. The energetic offset between the phases is a necessary driving force for dissociating the excitons [52]. This is achieved, in general, by using a bulk heterojunction (BHJ) morphology consisting of donor (D) (hole transporting) and acceptor (A) (electron transporting) type organic semiconductors [53]. A schematic of BHJ morphology in a thin film diode structure is shown in Figure 1.1b. The free charges created at D-A interface, following dissociation of excitons, are transported to respective electrodes via D and A domains [52]. Most designs of PVs based on organic semiconductors use this architecture to improve the light to charge conversion efficiency [54], table 1.1 lists the properties for a range of organic materials. The D-A phase separation is strongly dependent on thin film deposition techniques, materials, and solvents used for fabricating BHJ architecture [55]. Understanding the mechanics of D-A phase separation in printed devices is a key step towards improving their performance.

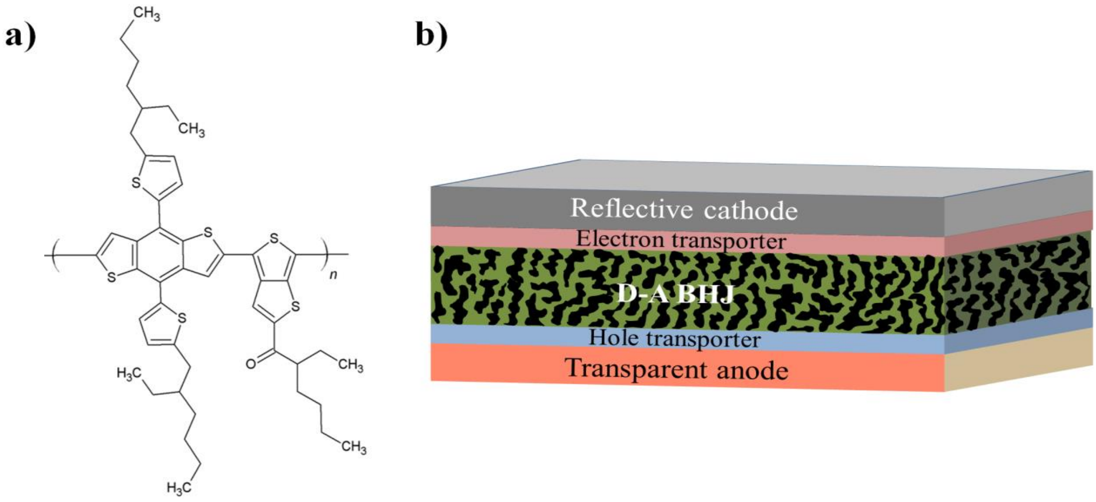

Figure 1.1: *a) Molecular structure of a typical organic semiconductor (PBDTTT-C-T), b) Schematic representation of the BHJ D-A phase separation in organic photodetectors.*

Table 1.1: Properties of organic semiconductors used in this thesis.

Semiconductor	**Band gap (eV)**	**LUMO (eV)**	**HOMO (eV)**	**Mobility (hole) (cm^2/Vs)**
Donor				
P3HT	1.9	-3.0	-4.9	~ 10^{-4} [56]
PBTTT-C14	2.0	-3.46	-5.46	~ 0.2-0.6 (μFET) [57]
PBDTTT-C-T[58]	1.68	-3.6	-5.28	~ 10^{-3}
Acceptor				**electron**
N2200	1.45	-3.95	-5.40	~ 0.45 - 0.8 (μFET) [59]
PCBM-C70	2.0	-3.9	-5.9	~ 10^{-3} [60]
TPBi[61]	4.0	-2.7	-6.7	---
PTCDA[62]	2.2	-4.6	-6.8	---

Large E_B in the organic materials also results in higher fluorescence quantum yield (PLQY), which is evident from their utility as dyes for a variety of applications. Dyes with very high PLQY (~ 90-100 %) finds applications as lasing materials [63]. The organic dyes are also used as efficient down converters for lighting and solar concentrators [64].

1.2.2: Organic-inorganic hybrid perovskite (OIP) inks

Conjugated organic semiconductors have been extensively studied for over four decades, whereas, OIPs in their current form are a new class of materials for PV applications, where the mechanics are relatively less understood. Perovskites are compounds with the ABX_3 molecular structure, where the A is a monovalent cation, B is a divalent cation and X is a monovalent anion [65]. Perovskites are inorganic compounds in general, however, by replacing any of the A, B or X with an organic molecule an organic-inorganic hybrid can be formed. The perovskite structure which is specifically useful in printed electronics applications constitutes of organic monovalent cations at A site [66]. The organic cation like methylammonium ion ($CH_3NH_3^+$) or formamidinium ion ($CH(NH_2)_2^+$) have an ionic radius (~ 2.6 Å) suitable for this role [67]. The heavy metal ions like Pb^{2+} and Sn^{2+} are used as divalent cation for B site and the halogens (I^-, Br^-, Cl^-) are used as monovalent anions. A typical hybrid perovskite structure can be written as $CH_3NH_3PbI_3$, where the PbI_6 forms the corner-sharing octahedral structure and the $CH_3NH_3^+$ ion occupies the octahedral site, which has a coordination number of 12 (Figure 1.2) [68]. Like their inorganic counterparts, the OIPs exist in cubic phase at higher temperatures. However, the phase change from cubic to tetragonal and orthorhombic with a decrease in temperature (the phase transition temperature varies with composition) [69].

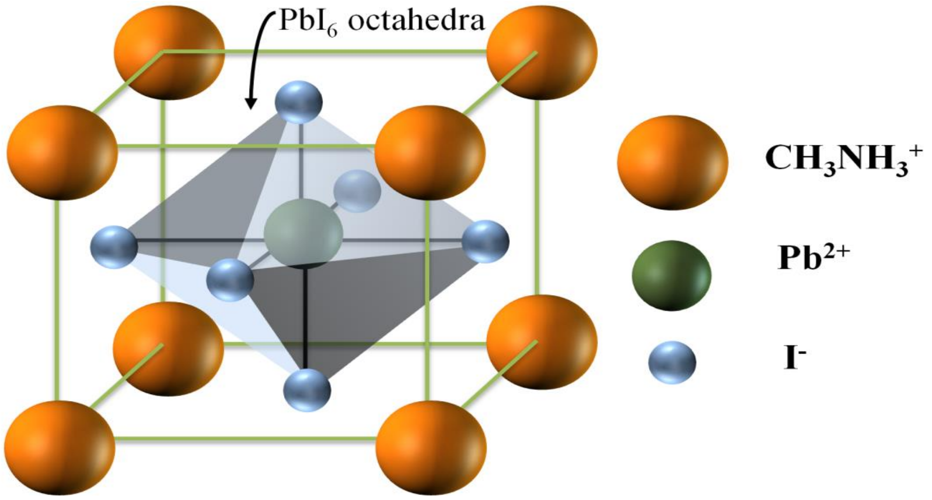

Figure 1.2: *Schematic representation of organic-inorganic hybrid perovskite unit cell.*

Though being known for a long time, recent interest in hybrid OIP is motivated by their superior performance as extremely low-cost photovoltaic materials [70-72]. The absorption coefficient ($\alpha(E)$) for OIPs is comparable to that of organic semiconductors (~ 10^5 cm^{-1}) [73, 74], requiring thin layers (~ 300 nm) for efficiently harvesting a major fraction of the incident solar radiation. The low band gap of $CH_3NH_3PbI_3$ (~ 1.6 eV) enables absorption of nearly all of visible and near infrared solar spectrum. This allows for achieving the Shockley-Queisser limit for a single junction cell [75]. Superior absorption in these materials is also supported by easy dissociation of excitons (E_B ~ 12-16 meV) under room temperature thermal energy (~ 25 meV) and efficient charge transport [69] [76]. Large carrier diffusion length (~ μm for polycrystalline films) [77-79] and very low trap densities at the surface and in bulk reduces recombination losses [80]. The charge carrier mobilities for polycrystalline films (~ 10^1 cm^2/Vs) are similar to that of inorganic semiconductors [81, 82].

The hybrid OIPs show properties, superior to that of pure organic semiconductors; nevertheless, they can be easily solution processed and have low formation energy [83]. The band gap in OIP is formed between the unoccupied p orbital of Pb (conduction band (CB)) and X (valance band (VB)). Though organic cation plays an important role in stabilizing the OIP structure, it has a very small influence on the valence and conduction band levels [84]. The band gap of OIP can be tuned easily by varying the B (Pb^{2+} and Sn^{2+}) and X (I^-, Br^-, Cl^-) site ions, which gives an energy range from 1.3 - 2.6 eV [85-87], table 1.2 lists the band gap of different Pb-based OIPs. The possibility to solution process and easily tune the band gap makes the OIP a versatile material for various printed electronics applications like PVs, LEDs, Transistors and LASER (Light Amplification by Stimulated Emission of Radiation) [29, 30, 33, 88]. The morphology of the thin film plays a key role indevice characteristics, large grains sizes are preferred for PV application, while small grains are essential for improving the luminescence and LED output [29, 89]. Solvent engineering has been shown to be useful in finely controlling the morphology of OIP films, where many interesting morphologies can be achieved [90]. In this thesis, organic small molecule mediated solvent engineering technique has been utilized as an effective route for realizing the unique morphologies in thin films of OIP.

Table 1.2: Properties of Pb-based OIP perovskites.

OIP	**Bang gap (eV)**
$MAPbI_3$	~1.56
$MAPbI_{3-x}Br_x$	1.55 - 2.3
$MAPbBr_3$	~ 2.33
$MAPbBr_{3-x}Cl_x$	2.3 - 2.7
$MAPbCl_3$	~ 2.7

1.2.3: Inorganic/Hybrid quantum dots based inks

The energy gap and stability of inorganic and hybrid semiconductors can be further tuned by lowering the dimensionality. The QDs are quasi-zero-dimensional, nanometer (~ 2-10 nm diameters) sized particles of classical semiconductors, where the electronic properties show large dependence on the particle diameter [91]. The QDs of inorganic semiconductors have been proven to be useful in controlling the energy gap by introducing the geometrical confinement [92]. Some of the interesting features include high PL yield, greater band gap tunability, improved color purity and processability from different solutions, such features are difficult to achieve in bulk inorganic semiconductors [93]. There are numerous ways for creating QDs, simplest being the reaction flask chemistry [94, 95]. The surfaces of QDs are generally passivated by organic surfactant ligands which restrict aggregation [94]. The hybrid QDs of OIP are formed by using a combination of long (octyl ammonium) and short (methylammonium) chain organic cation (Figure 1.3) [96, 97]. Long chain cations act as surface termination groups, which restricts further crystallization and defines the size of QDs.

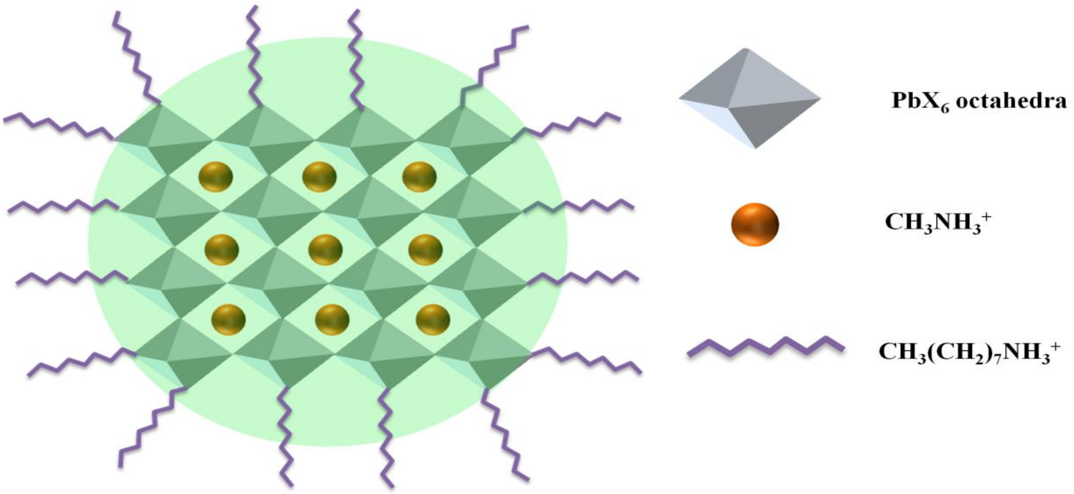

Figure 1.3: *Schematic representation of hybrid OIP QDs.*

The band gap of QDs as a function of particle diameter can be estimated by using the effective mass approximation,

$$E_{g,QD} = E_{g,bulk} + \frac{\hbar^2\pi^2}{2\mu r^2} - 1.786\frac{e^2}{4\pi\varepsilon r} \tag{1.1}$$

where μ is the effective mass of carriers, r is the particle radius and e is the electronic charge. The second term represents the confinement induced attraction energy and the third term represents Columbic interaction energy between the electron-hole pair. The exciton Bohr radius (r_B) is given as, $r_B = \frac{\varepsilon h^2}{\mu\pi e^2}$. When, $r_B \geq$ r, the quantum nature dominates and its signatures can be seen as a large blue shift in *α(E)* and PL(E) spectra.

The QDs of OIP show many remarkable properties which advance the usefulness of OIPs. One of the most notable properties of hybrid QDs is their enhanced moisture tolerance compared to the bulk [97, 98]. Simultaneously, the PL quantum yield and lifetime improves [99, 100]. Unlike the bulk OIPs, the QDs can be easily suspended in a variety of non-polar solvents, which allows for depositing very thin layers on any surface [97, 101]. In general, confinement of charge pairs can result in the excitonic nature of QDs, while the respective bulk semiconductor may not be excitonic [102]. The charge transport properties of QDs are different from that of the bulk; the capping layers can severely restrict the electron transport by acting as a barrier. Modifications to the QD design by choosing right organic ligands can improve the charge transport property, making them useful for device applications [103]. Large PLQY and tunable band gap observed in OIP QDs are also advantageous for optical down conversion in lighting and display application, solar concentrators and emission tuned lasing. Due to their superior emission and greater dispersibility in various solutions, QDs can serve as a potential alternative for organic and hybrid semiconducting inks. In this thesis, electronic properties of OIP QDs have been studied in detail in the subsequent chapters (5 and 6), new routes for in-situ fabrication of QDs encapsulated in the dielectric matrix has also been explored.

1.3: Printable conductive inks

Apart from the semiconducting active layer, the second most important part, of an electronics device, is the metal contacts/electrodes and interconnects. They serve the purpose of injecting and transporting charges between the semiconducting devices. Different formulations have been proposed for these applications, which include carbon-based inks, high conductivity metal particle paste, and metal alloys. Some of the important features desirable for conductive inks are (i) suitable work function (W_F), (ii) low resistivity (~ 10 mΩ sq) and (iii) good adhesion to various substrates.

1.3.1: Carbon based inks

Conductive carbon inks used in printed electronics technology can be broadly classified into two categories, (i) conducting polymers like Poly(3,4-

ethylenedioxythiophene):poly(styrene sulfonate) (PEDOT: PSS) and polyaniline dispersed in an aqueous medium, used as conducting inks [104-106] and (ii) dispersions based on a mixture of polymer binding agent and conductive carbon pigments (graphite, carbon black, carbon nanotube) in a suitable solvent [107-109].

1.3.1 I: Conducting polymer-based inks

Conducting polymer-based inks, like PEDOT: PSS and polyaniline have found applications in various electronic devices due to their unique properties. Some of the interesting features of PEDOT:PSS include homogeneous coverage with low surface roughness (< 5 nm) when fabricated using different printing processes, high optical transmission in the visible EM spectrum (~ 90% at 2.5 eV), good photo and thermal stability in air and wide range of electrical conductivity (10^{-2} to 10^{3} S cm^{-1}) [110].

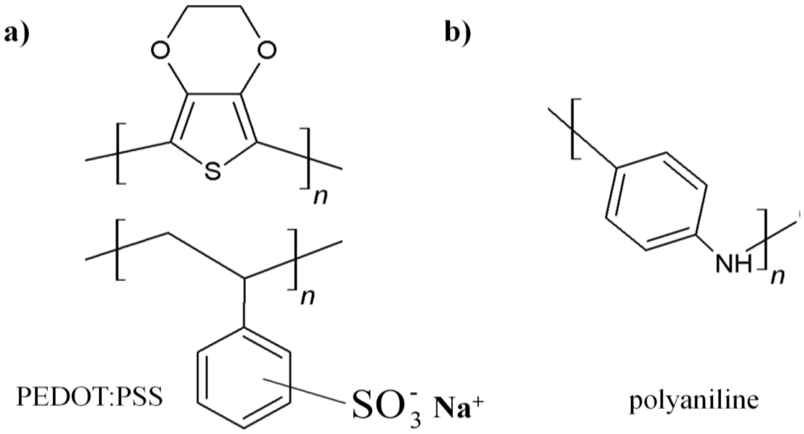

Figure 1.4: *Chemical structure of PEDOT: PSS.*

The PEDOT: PSS consists of conjugated PEDOT which is positively charged and is stabilized by negatively charged surfactant, PSS, dispersed in an aqueous medium (the chemical structure is shown in Figure 1.4a). The conductivity of the PEDOT: PSS film can be tuned by varying the PEDOT to PSS ratio and using different polymer and ionic additives [110-112]. In thin film PVs and LEDs, the low conductivity

PEDOT: PSS is also used as a buffer layer for selective hole transport due to its high work function (~ 5.1 eV) [110]. Charge transport in PEDOT: PSS films occur through hole polaron along the conjugated PEDOT chain, this results in large anisotropy in conductivity along lateral and transverse directions [113]. These inks are suitable for a variety of applications like displays and antistatic coatings.

1.3.1 II: Carbon pigment based inks

Inks based on carbon pigment suspended in the organic binder have a large variety depending on the type of carbon pigment and the binder/solvent used. Some of the common variants include powdered graphite [114], carbon black (soot) [115] and graphene/carbon nanotubes [116] which can be suspended in dielectric binder matrix like Poly(methyl methacrylate) (PMMA). Micron-sized pigments are finely and evenly dispersed in a polymer matrix, which allows for a uniform coating. After the solvent has dried, the pigments are left embedded evenly in the polymer film, allowing the electrical conductivity across the film. In order to achieve low electrical resistance, the conductive particles must be in contact with each other or the separation should be less than ~ 10 nm. The resistance decreases with an increase in pigment loading, and above a critical concentration (percolation threshold) the resistance drops significantly [117]. The pigment loading is decided by the amount of pigment that can be evenly dispersed in the polymer. Some of the important features of carbon pigment based inks include (i) availability of different printing methods, (ii) high mechanical, Thermal and chemical stability, (iii) good adhesion with different plastic substrates. The resistance value ~ 10 Ω/sq can be achieved for 25 μm thick coatings. Carbon pigment based inks can be cheaper than metal particle-based inks. However, a better W_F and contact uniformity is desirable for an electrode.

1.3.2: Metal powder based inks

The micron-sized metal powders can be formed into inks, very similar to that of carbon pigment based inks. Powders of high conductivity metals like silver, copper, and aluminum (particle size ~ 1-5 μm) is used as conductive pigments mixed in different polymer binders. The electrical conductivity of these inks is higher than that of carbon pigment based inks, mainly due to the higher specific conductance of metals. Charge transport in these inks is also controlled by the percolation (Figure 1.5), which requires a critical concentration of metal powder in a polymer matrix. By varying the polymer binder, different formulations suitable for specific applications can be created.

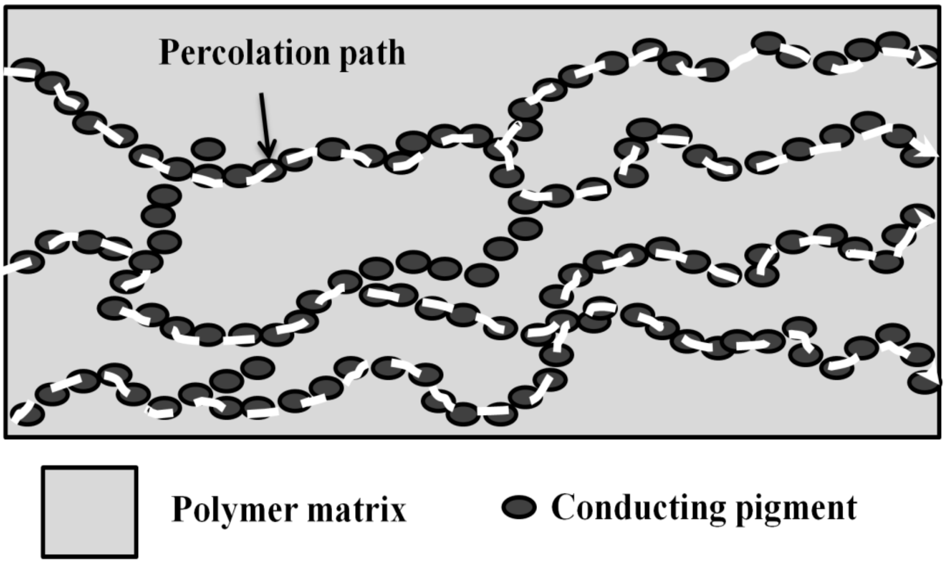

Figure 1.5: *Schematic representation of percolation pathways through the network of conducting pigments.*

Low resistances values ~ 10 mΩ/sq are easily attainable, which makes these inks ideal for printable electrode and interconnects. However, the cost associated with atomizing high melting point, noble metals makes these inks expensive.

1.3.3: Liquid metal alloys as inks

Eutectic alloys can be an alternative to traditional inks; they have been used for long in the electronics industry. However, their use as a printable metal electrode has not been realized due to the high melting point which is not compatible with flexible plastic substrates. Fusible alloys of solder metals (tin, lead, bismuth, indium and gallium) can have melting point lower than ~ 100 ^{0}C, which makes them suitable for printing applications. Metal alloys with indium can form soft, conformal contact with the underneath layer [118, 119]. Their usefulness as an efficient cathode has already been demonstrated for thin film OPVs. The work function, for indium-based alloys, is close to that of Al, which makes the fusible alloys a suitable metallic ink for the cathode and interconnects application [64, 90]. The bulk electrical and thermal conductivity of these alloys are much lower than that of the noble metals. However, they are comparable to that of metal powder based inks. Due to their low melting point, fusible alloys can locally melt and self-heal the cracks upon thermal treatment.

Metal surfaces are also known to host surface plasmons which can amplify local electric field in presence of nanostructures [120]. These structures are especially useful for light harvesting applications; the net amount of light absorbed in PVs can be increased by incorporating plasmonic mediums into the device structure. Metal gratings and periodic metallic structures of silver, gold, and Al have been successfully used to improve the efficiency of inorganic and organic PVs alike [121-124]. Metals like Indium, used in low-temperature fusible alloys, also show plasmonic activity [125], which can impart light harvesting properties to printable metal alloys. This thesis (chapter 2), explores the optical and electronic properties of low-temperature metal alloy inks for printable electrode and interconnects application.

1.4: Transferring inks onto surfaces

The process of printing various inks over different substrates has been well understood for decades. However, the physical characteristics of thin films required for printed electronics application are very different from that of standard graphic printing. One of the important steps is to create an ink formulation of semiconducting materials which is compatible with different printing processes.

1.4.1: Properties of printing inks

The physical properties of the solutions of different semiconducting materials may vary significantly based on the type of solvent used, solubility, and physical state in the solution. These properties play a major role in controlling the deposition process, film uniformity and drying. The process of transferring the active inks to a printing substrate is controlled by the viscosity and surface tension of the ink. The viscosity of an ink defines its capacity to transfer the pressure onto the substrate while the surface tension at the ink-substrate interface is responsible for homogeneous distribution of ink across the surface.

The liquid ink can be categorized into Newtonian or non-Newtonian fluids based on the change in their viscosity with applied shear force. For Newtonian fluids, like water, the viscosity remains constant at a particular temperature. However, the majority of printing inks show non-Newtonian behavior, where the viscosity either increases (shear-thickening) or decreases (shear-thinning) with an increase in shearing force. Polymer solutions and solid particles in liquid mediums are examples of shear-thinning liquids. The viscosity (η) of a non-Newtonian liquid, as a function of shear rate ($\acute{\gamma}$) can be written as,

$$\eta = \eta_{ref}\left(\frac{\dot{\gamma}}{\dot{\gamma}_{ref}}\right)^{\alpha} \qquad (1.3)$$

Where η_{ref} is a nominal viscosity measured at a defined shear rate $\dot{\gamma}_{ref}$. The exponent α is 0 for Newtonian liquids, α > 0 for shear-thickening and -1 < α < 0 for shear-thinning liquids [126].

The surface tension of the ink controls the amount of mechanical stress a liquid interface exerts onto the substrate; determining the wettability of the substrate by the ink. The surface tension is a force per unit surface area on the curved liquid surface. This is directed towards the liquid volume for convex surface (cohesive nature) and away from the liquid volume for concave surface (adhesive nature) [126]. The optimum range of surface tension and viscosity suitable for different printing techniques varies significantly, as shown in Figure 1.6.

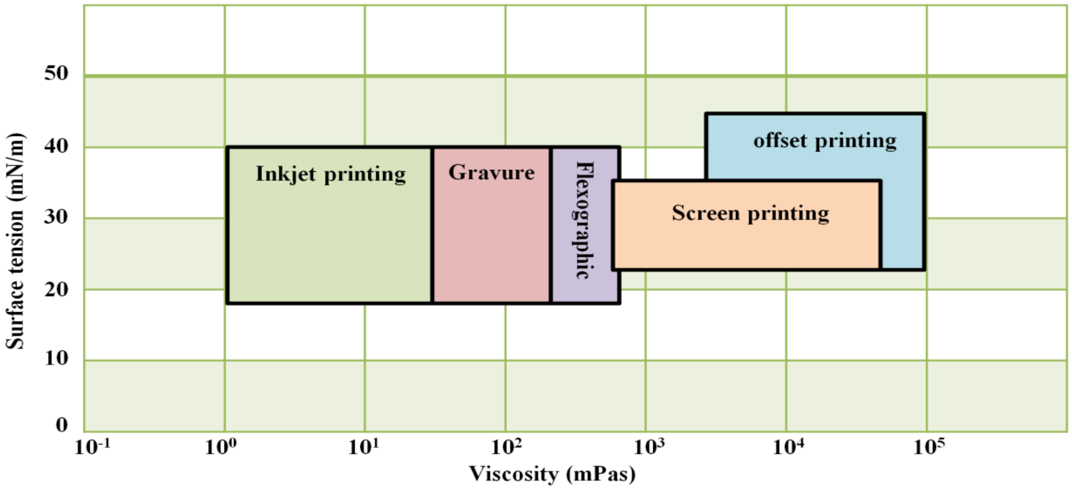

Figure 1.6: *Surface tension and viscosity range for inks used in common printing techniques. Figure adapted with permission from [126].*

The inks, which do not lie in the range indicated for a specific technique, can still be processed successfully. However, the ratio of ink transferred and printing resolution can be very different.

1.4.2: Surface wettability

Wetting of the printed surface is one of the most important requirements for the printing. By definition, wetting is the ability of an ink to evenly spread on a solid surface by creating a thermodynamically favorable condition [126]. Wettability of any ink on a substrate is controlled by the surface tension of the liquid (σ_L), the surface energy of solid (σ_s) and the angle between the surface and tangent at the free liquid-gas interface ($\theta \equiv$ contact angle). The relation between the quantities is given by Young's equation:

$$\sigma_{LG} cos\theta = \sigma_{SG} - \sigma_{SL} \tag{1.4}$$

where σ_{LG} is surface tension at liquid-gas interface and σ_{SG} and σ_{SL} are substrate surface energy towards gas and liquid phase of the ink [126]. Then the wetting of any substrate surface can be characterized by the wetting parameter (S),

$$S = \sigma_{SL} - \sigma_{SG} - \sigma_{LG} \tag{1.5}$$

and, the energy of adhesion ($W_{adh}(LS)$), which is defined as attractive interaction energy per unit area, between the ink and the substrate is given as,

$$w_{adh}(LS) = \sigma_{SG} + \sigma_{LG} - \sigma_{SL} \overset{\text{def}}{=} \sigma_{LG}(1 - \cos\theta) \tag{1.6}$$

In printing, a perfect wetting (S > 0) is characterized by even distribution of deposited ink, onto the surface. A large $\sigma_{LG} >> -S > 0$, represents small contact angle and a large adhesion energy [126]. Under dynamic processes like printing, the properties of the thin layer of ink deposited on the surface of the substrate can be explained in the lubrication limit [126]. The redistribution of printed ink form can be described using a simplified Stokes equation (Landau-Levich equation) under the assumption that the ink thickness is much smaller than the feature size of the print. The contributing factors to the equation are surface tension at liquid-gas interface, volume related pressure and lateral drag [126].

In drop based printing techniques, the film thickness consists of an average height h_0 and a very small surface modulation $h_1(x, y, t)$ (where $|h_1| << h_0$) arising from hydrodynamic instability. With time the surface is leveled by the surface tension and the speed of leveling is controlled by the viscous friction of the lateral flow. The leveling is exponential in time and the relaxation time $\propto$ (modulation wavelength)^4. Hence, small modulations (~ μm) may decay fast (~ ms) while the larger modulation will require longer time [126].

1.4.2 I: Drying of printed inks

Printing inks are pigments dissolved in a liquid medium, the surface tension of the ink can change with the concentration of the pigment (ϕ). Upon drying the thickness (h) of the film decreases and the ϕ increases accordingly: $\frac{\Delta\phi}{\phi} = -\frac{\Delta h}{h}$, consequently, the surface tension will change with decrease in the ink film thickness.

$$\phi \frac{\partial\sigma}{\partial\phi} \approx -h \frac{\partial\sigma}{\partial h} \tag{1.7}$$

Drying liquid film gives rise to lateral fluid transport which is driven by the gradient of capillary forces. Using Landau-Levich equation, a relaxation time scale can be derived which varies as a square of perturbation wavelength. The liquid flow can either result in relaxation of the perturbation or formation of spontaneous patterns depending on the sign of $\sigma_\phi = \frac{\partial\sigma}{\partial\phi}$. Sign of σ_ϕ is dependent on the solvent and the pigments used. Spontaneous dewetting of the surface can occur if the σ_ϕ is negative, even if perfect wetting was achieved initially [126].

1.4.3: Printing process

Independent of the layer being printed, certain steps are common which is necessary to ensure a pin-hole free, a uniform surface coating of the active layer. The processes can be subdivided into five steps which are listed below [126],

i. Conditioning of printing ink and pretreatment of printing surface is required to ensure a maximum wetting. This step is essential for achieving the uniformity of printed film.
ii. Ink acquisition, predosing and dosing of printing forms or press to allow for an equal distribution of printing ink over the entire printable surface.
iii. Transfer of dosed ink from printing form to the substrate using mechanical pressure, hydrodynamic shear, chemical and thermodynamic force. A forced wetting is ensured for a short moment to allow adhesion.
iv. Relaxation of the printing ink surface to even out any surface perturbations which can result in undesirable wavy patterns.
v. The final step in the printing process is the drying of printed inks. This process may involve the use of temperature or electromagnetic radiation to achieve fast curing of printed inks.

1.4.4: Printing and coating techniques

Various techniques have been utilized for depositing thin films of semiconducting materials for printed electronics applications. These techniques can be broadly classified into two major categories: (i) printing, where well-defined structures are printed from the printing form, (ii) coating, where thin films are deposited in regular strips without any pattern. Printing can be further divided into conventional and digital printing based on the use of printing plate. A conventional printing technique uses physical plates where the printed and non-printed regions have different physical characteristics. These can be summarized into 4 different classes, as described below [126],

i. Printing forms are raised above non-printed forms, like in flexographic printing.
ii. Printing forms are below the non-printing forms, like in gravure printing.
iii. Printing and non-printing regions are in the same plane but have different wettability for the ink, like in offset printing.
iv. Printing and non-printing regions are in the same plane but they have a different permeability for the ink, like in screen printing.

The schematic of different printing processes is shown in Figure 1.7. Flexographic, gravure and screen printing are an example of conventional printing technique, while the inkjet printing represents digital printing process. In the digital printing process, there is no physical plate and the digital information is either printed directly or transferred using a temporary printing form. Inkjet printing transfers the image directly to the substrate using a nozzle, the ink volume to be deposited is controlled by a piezo or thermal element. A transient printing form is used as an intermediate step in electrophotography [126].

Conventional printing techniques allow for the rapid fabrication process, which reduces fabrication time and production cost. However, the film quality required for printed electronics (continuous active layer without pinhole) is much higher than that for conventional graphic printing (pixilated deposition). Active ink differs significantly from graphic inks in their viscosity and surface tension; this requires tuning of the printing parameters which can provide homogeneous films with the suitable electrical property.

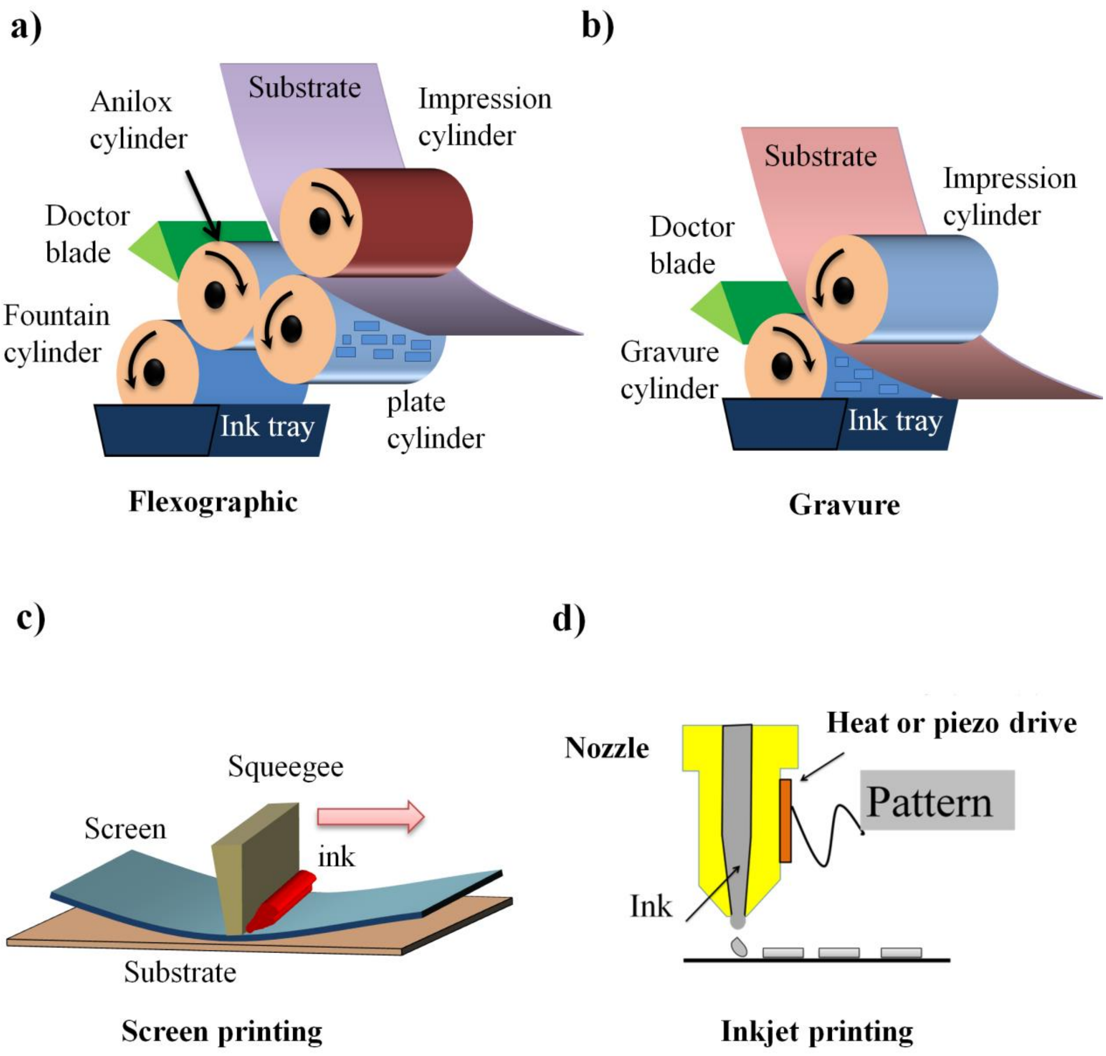

Figure 1.7: *Schematic representation of a) Flexographic, b) Gravure, c) Screen printing and d) Inkjet printing process.*

Unlike the printing process, where an irregular pattern can be deposited on the substrate, the coating techniques are used to deposit a uniform layer of ink without any patterns. Some of the conventionally used techniques include spin coating, spray coating, slot-die coating and knife edge coating (Figure 1.8).

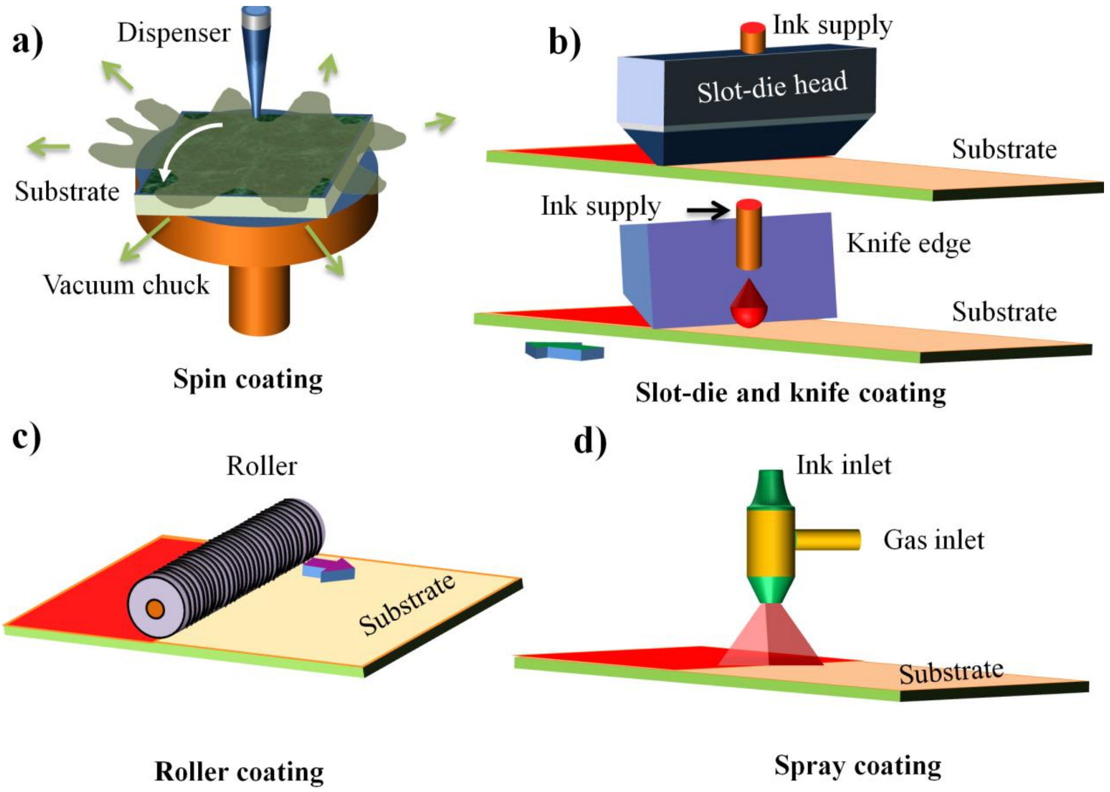

Figure 1.8: *Schematic representation of different coating techniques, a) spin coating, b) slot die and knife coating, c) roller coating, d) spray coating.*

Compared to the printing techniques, the coating techniques provide a more uniform and continuous layer. In printed electronic devices the coating techniques have been preferred for depositing semiconducting layers while the printing techniques are more suited for depositing patterned electrode layers.

1.5: Solution processed electronic devices

The end goal of printed electronics is to realize efficient, flexible, thin film devices which are low cost and require less material. Various device architectures based on solution processed semiconductor layers have been well reported in the literature. Some of the typical printed electronic devices include thin film PVs, photodetectors, LEDs and transistors.

1.5.1: Photovoltaics

Thin film PVs are being extensively studied for their application in low-cost energy harvesting. In a single p-n junction PV, the upper limit of light to charge conversion efficiency was proposed by William Shockley and Hans J. Queisser in 1961 using the second law of thermodynamics [127].

1.5.1 I: Shockley Queisser (SQ) limit of efficiency

The efficiency limit of single p-n junction PV was estimated to be ~ 30% under 1 sun (100 mW/cm^2) illumination. The limit of maximum efficiency results from multiple factors including,

1 **Radiative losses**: In a PV, upon absorption of a photon, electron-hole pairs are created. Assuming minimum non-radiative losses, the radiative recombination becomes the dominant loss mechanism. The radiative recombination is also a function of the voltage across the cell. At any given voltage, the total current is given as a difference between photogenerated current and carriers lost due to radiative recombination.

$$I_{tot} = I_L - I_0 \left[exp\left(-\frac{qV}{k_B T}\right) - 1\right] \tag{1.8}$$

Where I_L is photogenerated current, I_0 is a radiative loss at zero bias, V is the voltage applied across the PV and T is the cell temperature.

2 **Spectrum mismatch:** The process of creating a charge-pair upon photoexcitation requires transferring one electron from VB to CB of the semiconductor. The minimum energy required for this process is equal to the band gap of the material. Photons, which are below the band gap, will not contribute towards charge-pair creation while photons much higher in energy will lose excess energy, as heat, to the lattice. This mismatch in the solar spectrum and the band gap of the material is a major factor in limiting the

maximum efficiency (48% in silicon (Si)). The best band gap for absorbing sunlight is ~ 1.1 eV which is also the band gap value of Si.

3 **Impedance matching:** The maximum amount of power drawn from a PV, at a given illumination level, depends on the external load attached. The impedance matching factor (m) is defined as the ratio of power extracted to the maximum power available (also known as fill factor). The optimum value of m depends on the J-V curve and approaches unity at high illumination intensity.

Combining all the losses in a PV the net efficiency can be written as,

$$\eta = t_s u\left(\frac{V_g}{V_s}\right) v\left(f, \frac{V_c}{V_s}, \frac{V_g}{V_s}\right) m\left(v\frac{V_g/V_s}{V_c/V_s} \right) \tag{1.9}$$

Where, t_s represent a fraction of above bandgap photons absorbed, u, v and m represent ultimate efficiency factor, the ratio of the band gap voltage to open circuit voltage and impedance matching factor respectively. V_g, V_s, V_c represents band gap voltage, voltage equivalent of the temperature of the sun (6000K) and voltage equivalent of the temperature of the cell respectively. Factors like finite mobility and non-radiative recombination contribute towards additional losses. The theory was further modified by C. Henry to include (i) graphical analysis method, (ii) single and multi-junction cells, (iii) terrestrial solar spectrum (AM 1.5) instead of a black body radiation, (iv) effect of concentrated solar light and (v) a discussion on efficiency of ideal solar cell being lower than the limit [128].

1.5.1 II: overcoming the SQ limit

The basic SQ limit of efficiency in a single junction PV can be surpassed using various techniques like use of (i) multi-junction cell (tandem cell) [129], (ii) light concentrators [130, 131], (iii) multiple exciton generation [132] (iv) upconversion of below band gap photons [133] (v) down conversion of above bandgap photons [134]

(vi) singlet exciton fission [135]. Use of light concentrators is an effective way to improve the amount of light absorbed as it can be employed on any existing PV structure.

Surface plasmons in metallic nanostructures present an effective way for locally trapping the incident light. Plasmons are electron oscillations, induced by the excitation light, they have been studied extensively for their role in enhancing the local electric field, resulting in a large increase in Raman scattering signals [136-138]. Similar mechanisms are also useful in PVs for increasing the efficiency by improving the absorption. Two basic mechanisms proposed for light enhancement using plasmonic medium are,(i) light scattering and (ii) near field concentration of light [139]. Metal nanoparticle with diameter well below the wavelength of light can be considered as point dipole, the absorption and scattering is given as [140],

$$C_{scat} = \frac{1}{6\pi}\left(\frac{2\pi}{\lambda}\right)^4 |\alpha|^2\,, C_{abs} = \frac{2\pi}{\lambda} Im|\alpha| \tag{1.10}$$

Where

$$\alpha = 3V\left[\frac{\varepsilon_p/\varepsilon_m - 1}{\varepsilon_p/\varepsilon_m + 2}\right] \tag{1.11}$$

Is the polarizability of the metal nanoparticle, V is the volume, ε_p is the dielectric function of the metal particle and ε_m is the dielectric function of embedded medium. At plasmon resonance ($\varepsilon_p = -2\varepsilon_m$) polarizability becomes large and the scattering cross-section can be larger than geometrical cross-section. Metal nanoparticles and metallic gratings incorporated in Si and BHJ PV structure [141-143] have been shown to be useful in improving the performance of thin film PVs. The metal films coated at the back end of the PV is also shown to be useful in harvesting light by exciting surface plasmons at the metal/semiconductor interface [144].

1.5.1 III: Bulk heterojunction solar cell

The device structure of different generations of PV is strongly influenced by the E_B of the semiconductor. In the case of inorganic semiconductors, where the room temperature thermal energy is sufficient to split the excitons into free charge carriers, bilayer architecture of n and the p-type layer is efficient for light harvesting. However, in the case of organic semiconductors, large E_B requires an additional driving force for splitting excitons into free polarons [145]. This is achieved by creating a nanoscale D-A interface which allows energetic dissociation of excitons. The exciton diffusion length, in the organic semiconductors, is in tens of nm, this places the upper limit on the size of pure D(A) domains in BHJ [146, 147]. The BHJ architecture is the most widely used architecture in organic thin film PVs.

The characteristic photo response of a PV cell is shown in Figure 1.9. Under zero bias or small forward bias, lower than the open circuit voltage (V_{OC}), the device operates in photovoltaic mode. In this mode the diode delivers power to the external circuit, working as a battery.

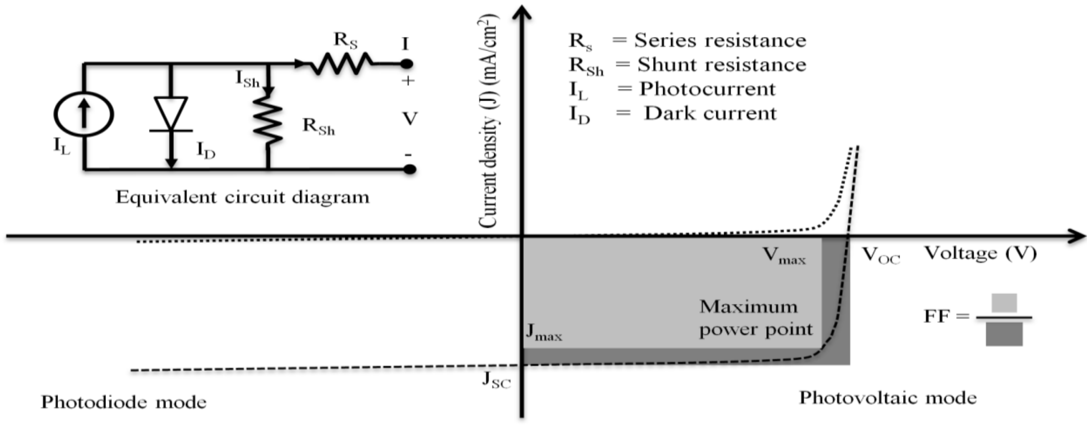

Figure 1.9: *Schematic representation of the J-V characteristics of the photodiode. The inset shows the equivalent circuit model for a typical photodiode.*

The inset of Figure 1.9 shows the equivalent circuit model for a typical solar cell. The performance of a solar cell is characterized by four quantities, V_{OC}, short circuit current density (J_{Sc}), fill factor (FF) and power conversion efficiency (PCE).

$$FF = \frac{V_{max}J_{max}}{V_{OC}J_{SC}}\ , PCE = \frac{J_{max}V_{max}}{P_{in}} \qquad (1.12)$$

The PCE of a photovoltaic cell is defined by the fraction of input optical power (P_{in}) delivered as electrical power at the output. The Standard reference for measuring this parameter is AM 1.5G illumination (1 Sun = 100 mW/cm^2).

1.5.2: Photodetectors

A photodetector is a PV operating in reverse bias, which ensures maximum charge extraction thereby improving the sensitivity. The response time of a photodetector is reduced in photoconductive mode due to the increased depletion width. In the operational intensity range of photodetector, the photocurrent should be a linear function of excitation density. One of the important parameters for characterizing a photodiode is the spectral responsivity ($R(E) = J_{ph}(E)/W_{in}(E)$) where E is photon energy. In an efficient photodiode, the $R(E)$ should be high in the spectral region of interest. Organic photodetectors are composed of solution processed blend of organic D-A molecules; general schematic for such a device structure is shown in Figure 1.10a. The response time of organic materials is slower compared to traditional inorganic semiconductors due to low charge carrier mobility. Hybrids of organic and inorganic semiconductors can offer significant improvements over the pure organic photodetectors while still preserving the ease of manufacturing and tunability of operation range.

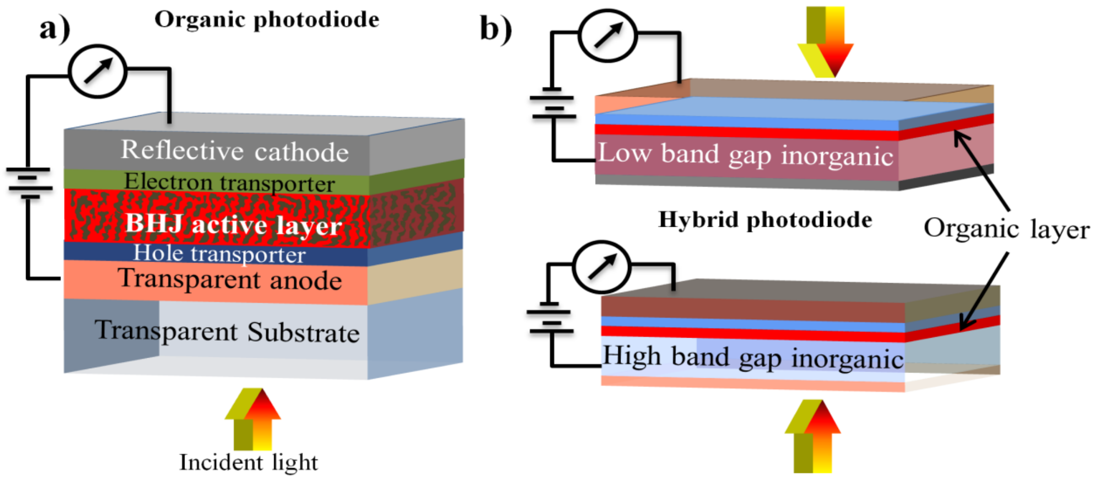

Figure 1.10: *Schematic representation of a) organic photodiode and b) hybrid photodiode.*

Different combinations of inorganic semiconductors (silicon, gallium nitride, zinc oxide) and organic conducting and semiconducting polymers have been shown to work efficiently as photodiodes [148-151]. A general schematic of the hybrid photodetector is shown in Figure 1.10b. The hybrid photodiodes can benefit from the properties of both the semiconductor families, some of the advantages of hybrid system over conventional system are listed below,

i. The widely available p-type donor polymers are a good match for inherently n-type inorganic semiconductors.

ii. The requirement for an epitaxially matched interface is relaxed when forming a heterojunction of two different semiconductors.

iii. Hybrid photodetectors can have large tunability in spectral response by making use of a variety of donor polymer, where the band gap can be easily controlled.

iv. Inorganic semiconductors can act as substrate as well as a protective window from ultraviolet light when a large band gap semiconductor like gallium nitride is used.

v. Organic-inorganic hybrids are model systems for studying heterojunction with different energy alignment, such energy level alignment is difficult to achieve in conventional systems.

This thesis emphasizes the role of energy level alignment and hybrid interfaces in controlling the charge transport in hybrid photodetectors, using model systems comprising high bandgap inorganic and low gap organic semiconductors.

1.5.2: Light emitting diodes

The LEDs operation is opposite of a photodiode, where the light is generated at the expense of externally supplied electrical power. Conventional inorganic LEDs are made using stacked multilayer structure where the emissive layer is sandwiched between a highly doped p and the n-type semiconductor layer. Solution processed LEDs have layered construction, identical to that of inorganic LEDs; however, the light is out coupled through the substrate (Figure 1.11).

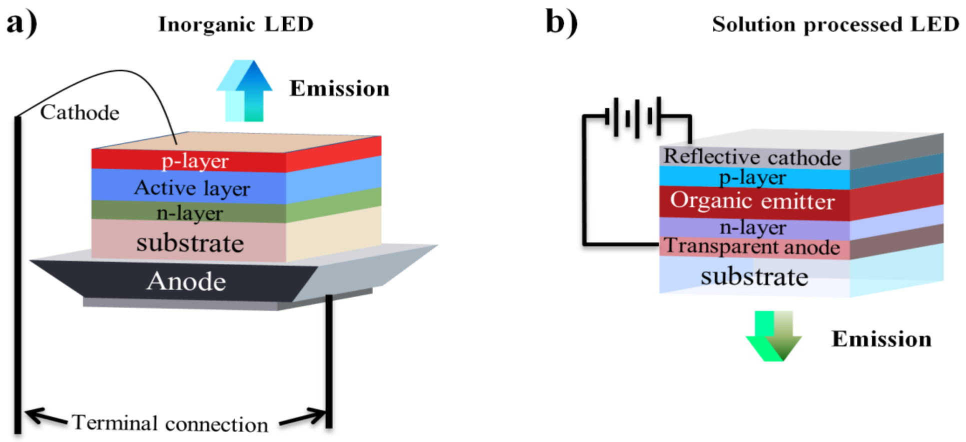

Figure 1.11: *a) Layered structure of a conventional inorganic LED and b) solution-processed thin film LED structure.*

The emissive layer, in any given LED structure, is sandwiched between electron (ETL) and hole (HTL) transport layer. These layers allow for efficient injection of charges from the respective electrodes. The electron mobility in ETL and hole mobility in HTL should remain comparable to ensure that the recombination centers are located in the emissive layer. The electron and holes, injected into the emissive layer, combine to form excitons. The spins of the injected carriers are randomly distributed; this results in the formation of both singlet and triplet excitons. Due to the quantum statistics of singlet and triplet states, there is a 75% probability of forming triplet state, while only 25% for singlet state [152]. The transition from triplet excited state to ground state is forbidden by the selection rules. This process limits the upper efficiency of LEDs to 25%. However, in the organic molecules and in the case of OIP the spin-orbit coupling is significant, which allows for single to triplet inter-system crossing and increases the limit for maximum efficiency [153-155].

Printable LEDs fabricated using organic and hybrid OIP emitter layers offer many advantages over their inorganic counterpart. Due to their ability to form uniform thin films, large area emission can be more easily realized in printed LEDs as compared to inorganic LEDs were emission centers are small crystal. The easy tunability of band gap in solution-processed semiconductors allows a continuously tunable emission range. The OIP emitters have high color purity compared to other solution-processed semiconductors which are desirable for display applications. This thesis explores OIP based new printable LED structures using low melting eutectic alloys (chapter 4).

1.6: Thesis outline

This thesis focuses on studying different device architectures comprising solution-processed semiconductors and meltable alloy electrodes and explores the underlying optical and electronic properties for maximizing their applicability. The mechanism underlying the superior performance of low temperature (> 50 ^{0}C) meltable alloy cathodes has been emphasized in chapter 2. The performance parameters of meltable alloys have been compared with thermally evaporated Al cathode. The hybrid interface between metal and polymer film has been probed using atomic force microscopy, post mechanical stress, and shearing, which suggests strong adhesion upon the inclusion of indium in the alloy. Surface enhanced Raman studies have been used to study the increase in optical activity of alloys surfaces upon addition of indium, a comparison is also shown with widely used metal layers. Photocurrent measurements as a function of excitation energy and active layer thickness support the results observed in surface enhanced Raman studies. Impedance measurements show the high quality of alloy electrodes fabricated in ambient conditions, which is comparable to thermally evaporated Al electrode. These observations suggest that indium (a primary constituent) plays a crucial role in enhancing the adhesion properties of alloy electrodes, which is critical for realizing optical activity and electrical compatibility with organic semiconductors. Alloy work function, being lower than that of Al, is useful in minimizing the degradation due to oxidation and improving the device stability. Consistent performance enhancement has been demonstrated for OPVs with alloy cathodes compared to that with Al. Utilization of the alloy is extended for other systems and is described in other chapters.

Chapter 3 deals with an example of the hybrid device composed of organic and inorganic layers. The Hybrid structure comprising n-doped gallium nitride (n-GaN) and D(A) polymers has been used to study charge transport in non-conventional systems. The J-V and excitation energy dependence of photocurrent suggests a large modification in photo response compared to standard photodiodes. The spontaneous polarization present at the n-GaN surface strongly influences the charge transport and photo-response of hybrid photodetectors. Electric field and white light bias have been used as external perturbation for tuning the energy level of the hybrid interface.

Active layers based on hybrid crystal structure using perovskite (OIP) have been discussed in chapter 4. Large scale morphology restructuring of hybrid OIP semiconductor film has been demonstrated using solvent engineering technique. Rapid crystallization of OIP structure results in the reduction of the average grain size. The macroscopic morphology shows a large dependence on the small molecule additives used in the kinetic control of the growth of OIP thin films. Morphologically modified films show a decrease in disorder and significant improvements in PLQY and lifetime, which is useful for numerous applications like electroluminescent emitters. Printable LED structure has been fabricated using low melting alloys.

The nanocrystals (NCs) of OIP demonstrate improved stability compared to their bulk counterparts. The emission characteristics of OIP NCs have been studied in chapter 5. Hybrid OIP NCs demonstrate absorption and emission properties comparable to that of bulk; however, the solution processability is greatly improved. Added effects of a reduction in average crystallite size are visible as an increase in energy gap, large E_B and high PLQY. NCs show larger exciton-lattice interaction compared to that of bulk, suggesting dominant exciton localization effects. The NCs/acceptor polymer hybrid show the difference in photo-response of acceptor polymer, compared to the diodes made using bulk perovskite, while the EL properties remain unaltered.

Fabrication of luminescent OIP QDs embedded in a 1D fibrillar network using electrospinning of PMMA/OIP precursor mixture is demonstrated in chapter 6. The QDs are formed in-situ during the spinning of fibers, resulting in an alignment of OIP grains within the fiber growth direction. Optical absorption and emission studies of OIP

QDs embedded PMMA fibers show a large blue shift in the optical band gap. The QDs embedded fibers show high PLQY, comparable to conventionally prepared OIP QDs. Localized emission maps suggest a large-scale spatial and spectral uniformity for a given fiber, which indicates a uniform distribution of QDs across the fiber. The cylindrical structure of PMMA fibers and the ellipsoidal geometry of OIP grains are advantageous for realizing effects like wave guiding of local emission, a 3D cavity for lasing and propagation of whispering gallery modes. Temperature dependence of PL indicates size dependent exciton-lattice coupling, which is similar to conventional QDs. Excitation intensity dependence suggests an excitonic nature of emission in QDs of larger diameter, the emission nature changes to donor-acceptor type for smaller QDs which is an indicative of stronger confinement. Amplified spontaneous emission was observed for excitation powers as low as ~ 4 μJ, indicating possibilities of low-threshold lasing.

In summary, the thesis highlights the usefulness of solution processed semiconductor and metals for printable electronics. Improvements observed in the polymer/metal adhesion and optical activity of solder alloys in presence of indium metal has been discussed. Charge transport in bilayer hybrid interface is limited by the interfacial states. Morphological modifications of hybrid perovskite thin films show large dependence on small molecules used in antisolvent treatment. The perovskite quantum dots demonstrate an increase in exciton-lattice coupling with particle size reduction. The one-dimensional core-shell fiber structure of perovskite quantum dots and Poly(methyl methacrylate) display large tunability in electronic property with density and composition of perovskite.

References

[1] L. Y. Lu, T. Y. Zheng, Q. H. Wu, A. M. Schneider, D. L. Zhao and L. P. Yu. Recent Advances in Bulk Heterojunction Polymer Solar Cells. *Chemical Reviews* **2015,** *115*, 12666-12731.

[2] G. Dennler, R. Gaudiana and C. J. Brabec. Conjugated Polymer Based Organic Solar Cells: State of the Art and Future Challenges. *Abstracts of Papers of the American Chemical Society* **2009,** *238*.

[3] S. Gunes, H. Neugebauer and N. S. Sariciftci. Conjugated Polymer-Based Organic Solar Cells. *Chemical Reviews* **2007,** *107*, 1324-1338.

[4] H. Hoppe and N. S. Sariciftci. Organic Solar Cells: An Overview. *Journal of Materials Research* **2004,** *19*, 1924-1945.

[5] J. Roncali. Molecular Bulk Heterojunctions: An Emerging Approach to Organic Solar Cells. *Accounts of Chemical Research* **2009,** *42*, 1719-1730.

[6] Q. S. An, F. J. Zhang, J. Zhang, W. H. Tang, Z. B. Deng and B. Hu. Versatile Ternary Organic Solar Cells: A Critical Review. *Energy & Environmental Science* **2016,** *9*, 281-322.

[7] T. Ameri, P. Khoram, J. Min and C. J. Brabec. Organic Ternary Solar Cells: A Review. *Advanced Materials* **2013,** *25*, 4245-4266.

[8] N. T. Kalyani and S. J. Dhoble. Organic Light Emitting Diodes: Energy Saving Lighting Technology-a Review. *Renewable & Sustainable Energy Reviews* **2012,** *16*, 2696-2723.

[9] S. Reineke, M. Thomschke, B. Lussem and K. Leo. White Organic Light-Emitting Diodes: Status and Perspective. *Reviews of Modern Physics* **2013,** *85*, 1245-1293.

[10] A. Dodabalapur. Organic Light Emitting Diodes. *Solid State Communications* **1997,** *102*, 259-267.

[11] C. D. Dimitrakopoulos and D. J. Mascaro. Organic Thin-Film Transistors: A Review of Recent Advances. *Ibm Journal of Research and Development* **2001,** *45*, 11-27.

[12] G. H. Gelinck, H. E. A. Huitema, E. Van Veenendaal, E. Cantatore, L. Schrijnemakers, J. B. P. H. Van der Putten, T. C. T. Geuns, M. Beenhakkers, J. B. Giesbers, B. H. Huisman, E. J. Meijer, E. M. Benito, F. J. Touwslager, A. W. Marsman, B. J. E. Van Rens and D. M. De Leeuw. Flexible Active-Matrix Displays and Shift Registers Based on Solution-Processed Organic Transistors. *Nature Materials* **2004,** *3*, 106-110.

[13] C. D. Dimitrakopoulos and P. R. L. Malenfant. Organic Thin Film Transistors for Large Area Electronics. *Advanced Materials* **2002,** *14*, 99-117.

[14] G. Gelinck, P. Heremans, K. Nomoto and T. D. Anthopoulos. Organic Transistors in Optical Displays and Microelectronic Applications. *Advanced Materials* **2010,** *22*, 3778-3798.

[15] D. Wöhrle and D. Meissner. Organic Solar Cells. *Advanced Materials* **1991,** *3*, 129-138.

[16] N. A. Azarova, J. W. Owen, C. A. McLellan, M. A. Grimminger, E. K. Chapman, J. E. Anthony and O. D. Jurchescu. Fabrication of Organic Thin-Film Transistors by Spray-Deposition for Low-Cost, Large-Area Electronics. *Organic Electronics* **2010,** *11*, 1960-1965.

[17] S. R. Forrest. The Path to Ubiquitous and Low-Cost Organic Electronic Appliances on Plastic. *Nature* **2004,** *428*, 911-918.

[18] S. R. Forrest and M. E. Thompson. Introduction: Organic Electronics and Optoelectronics. *Chemical Reviews* **2007,** *107*, 923-925.

[19] R. Po, C. Carbonera, A. Bernardi and N. Camaioni. The Role of Buffer Layers in Polymer Solar Cells. *Energy & Environmental Science* **2011,** *4*, 285-310.

[20] S. H. Ko, H. Pan, C. P. Grigoropoulos, C. K. Luscombe, J. M. J. Frechet and D. Poulikakos. All-Inkjet-Printed Flexible Electronics Fabrication on a Polymer Substrate by Low-Temperature High-Resolution Selective Laser Sintering of Metal Nanoparticles. *Nanotechnology* **2007,** *18*, 345202.

[21] F. Garnier, R. Hajlaoui, A. Yassar and P. Srivastava. All-Polymer Field-Effect Transistor Realized by Printing Techniques. *Science* **1994,** *265*, 1684-1686.

[22] H. Sirringhaus, T. Kawase, R. H. Friend, T. Shimoda, M. Inbasekaran, W. Wu and E. P. Woo. High-Resolution Inkjet Printing of All-Polymer Transistor Circuits. *Science* **2000,** *290*, 2123-2126.

[23] F. C. Krebs. Fabrication and Processing of Polymer Solar Cells: A Review of Printing and Coating Techniques. *Solar Energy Materials and Solar Cells* **2009,** *93*, 394-412.

[24] Y. S. Liu, C. C. Chen, Z. R. Hong, J. Gao, Y. Yang, H. P. Zhou, L. T. Dou, G. Li and Y. Yang. Solution-Processed Small-Molecule Solar Cells: Breaking the 10% Power Conversion Efficiency. *Scientific Reports* **2013,** *3*.

[25] N. Tessler, N. T. Harrison and R. H. Friend. High Peak Brightness Polymer Light-Emitting Diodes. *Advanced Materials* **1998,** *10*, 64-68.

[26] C. Kanimozhi, N. Yaacobi-Gross, K. W. Chou, A. Amassian, T. D. Anthopoulos and S. Patil. Diketopyrrolopyrrole-Diketopyrrolopyrrole-Based Conjugated Copolymer for High-Mobility Organic Field-Effect Transistors. *Journal of the American Chemical Society* **2012,** *134*, 16532-16535.

[27] S. P. Senanayak, A. Z. Ashar, C. Kanimozhi, S. Patil and K. S. Narayan. Room-Temperature Bandlike Transport and Hall Effect in a High-Mobility Ambipolar Polymer. *Physical Review B* **2015,** *91*, 115302.

[28] W. S. Yang, J. H. Noh, N. J. Jeon, Y. C. Kim, S. Ryu, J. Seo and S. Il Seok. High-Performance Photovoltaic Perovskite Layers Fabricated through Intramolecular Exchange. *Science* **2015,** *348*, 1234-1237.

[29] H. Cho, S. Jeong, M. Park, Y. Kim, C. Wolf, C. Lee, J. H. Heo, A. Sadhanala, N. Myoung, S. Yoo, S. H. Im, R. H. Friend and T-W Lee. Overcoming the Electroluminescence Efficiency Limitations of Perovskite Light-Emitting Diodes. *Science* **2015,** *350*, 1222-1225.

[30] S. P. Senanayak, B. Yang, T. H. Thomas, N. Giesbrecht, W. Huang, E. Gann, B. Nair, K. Goedel, S. Guha, X. Moya, C. R. McNeill, P. Docampo, A. Sadhanala, R. H. Friend and H. Sirringhaus. Understanding Charge Transport in Lead Iodide Perovskite Thin-Film Field-Effect Transistors. *Science Advances* **2017,** *3,* e1601935.

[31] C. H. M. Chuang, P. R. Brown, V. Bulovic and M. G. Bawendi. Improved Performance and Stability in Quantum Dot Solar Cells through Band Alignment Engineering. *Nature Materials* **2014,** *13,* 796-801.

[32] J. M. Caruge, J. E. Halpert, V. Wood, V. Bulovic and M. G. Bawendi. Colloidal Quantum-Dot Light-Emitting Diodes with Metal-Oxide Charge Transport Layers. *Nature Photonics* **2008,** *2*, 247-250.

[33] J. H. Noh, S. H. Im, J. H. Heo, T. N. Mandal and S. I. Seok. Chemical Management for Colorful, Efficient, and Stable Inorganic-Organic Hybrid Nanostructured Solar Cells. *Nano Letters* **2013,** *13*, 1764-1769.

[34] P. O. Anikeeva, J. E. Halpert, M. G. Bawendi and V. Bulovic. Quantum Dot Light-Emitting Devices with Electroluminescence Tunable over the Entire Visible Spectrum. *Nano Letters* **2009,** *9*, 2532-2536.

[35] D. Nath, P. Dey, D. Deb, J. K.Rakshit and J. N. Roy. Fabrication and Characterization of Organic Semiconductor Based Photodetector for Optical Communication. *CSI Transactions on ICT* **2017**, 5, 149-160.

[36] O. Mhibik, S. Forget, D. Ott, G. Venus, I. Divliansky, L. Glebov and S. Chenais. An Ultra-Narrow Linewidth Solution-Processed Organic Laser. *Light-Science & Applications* **2016,** *5*, e16026.

[37] J. Clark and G. Lanzani. Organic Photonics for Communications. *Nature Photonics* **2010,** *4*, 438-446.

[38] N. P. Vlannes, J. F. Mcdonald and T. M. Lu. Organic Photonics - a Materials and Devices Strategy for Computational and Communication-Systems. *Ntc-92* **1992**, J7-J15.

[39] H. Shirakawa, E. J. Louis, A. G. MacDiarmid, C. K. Chiang and A. J. Heeger. Synthesis of Electrically Conducting Organic Polymers: Halogen Derivatives of Polyacetylene, (Ch). *Journal of the Chemical Society, Chemical Communications* **1977**, 578-580.

[40] G. A. Chamberlain. Organic Solar Cells: A Review. *Solar Cells* **1983,** *8*, 47-83.

[41] D. Hertel and H. Bassler. Photoconduction in Amorphous Organic Solids. *Chemphyschem* **2008,** *9*, 666-688.

[42] J. C. S. Costa, R. J. S. Taveira, C. F. R. A. C. Lima, A. Mendes and L. M. N. B. F. Santos. Optical Band Gaps of Organic Semiconductor Materials. *Optical Materials* **2016,** *58*, 51-60.

[43] A. Köhler and H. Bässler. The Electronic Structure of Organic Semiconductors. In *Electronic Processes in Organic Semiconductors,* Wiley-VCH Verlag GmbH & Co. KGaA: 2015; pp 1-86.

[44] X. D. Yang, Q. K. Li and Z. G. Shuai. Theoretical Modelling of Carrier Transports in Molecular Semiconductors: Molecular Design of Triphenylamine Dimer Systems. *Nanotechnology* **2007,** *18*.

[45] A. Köhler and H. Bässler. Fundamentals of Organic Semiconductor Devices. In *Electronic Processes in Organic Semiconductors*, Wiley-VCH Verlag GmbH & Co. KGaA: 2015; pp 307-388.

[46] A. A. Zakhidov. Phototransformations of Polarons Bipolarons and Solitons Due to Interchain Transitions in Conducting Polymers. *Synthetic Metals* **1991,** *43*, 3649-3656.

[47] Z. Su and L. Yu. Soliton and Polaron Dynamics in Conducting Polymers. *Physica Scripta* **1987,** *T19a*, 231-238.

[48] C. J. Brabec. *Organic Photovoltaics*. 1 ed.; Springer-Verlag Berlin Heidelberg: Springer-Verlag Berlin Heidelberg, 2003; p XII, 300.

[49] J. Frenkel. On the Transformation of Light into Heat in Solids. I. *Physical Review* **1931,** *37*, 17-44.

[50] M. Knupfer. Exciton Binding Energies in Organic Semiconductors. *Applied Physics a-Materials Science & Processing* **2003,** *77*, 623-626.

[51] Y. Y. L. Jiarong, E. Peng and J. Huang. *Organic and Hybrid Solar Cells*. 1 ed.; Springer International Publishing: Switzerland, 2014; p VIII, 337.

[52] J. G. Xue, B. P. Rand, S. Uchida and S. R. Forrest. Mixed Donor-Acceptor Molecular Heterojunctions for Photovoltaic Applications. Ii. Device Performance. *Journal of Applied Physics* **2005,** *98*.

[53] B. P. Rand, J. G. Xue, S. Uchida and S. R. Forrest. Mixed Donor-Acceptor Molecular Heterojunctions for Photovoltaic Applications. I. Material Properties. *Journal of Applied Physics* **2005,** *98*.

[54] Y. Huang, E. J. Kramer, A. J. Heeger and G. C. Bazan. Bulk Heterojunction Solar Cells: Morphology and Performance Relationships. *Chemical Reviews* **2014,** *114*, 7006-7043.

[55] S. E. Shaheen, C. J. Brabec, N. S. Sariciftci, F. Padinger, T. Fromherz and J. C. Hummelen. 2.5% Efficient Organic Plastic Solar Cells. *Applied Physics Letters* **2001,** *78*, 841-843.

[56] A. Baumann, J. Lorrmann, C. Deibel and V. Dyakonov. Bipolar Charge Transport in Poly(3-hexyl Thiophene)/Methanofullerene Blends: A Ratio Dependent Study. *Applied Physics Letters* **2008,** *93*, 252104.

[57] Mcculloch I, M. Heeney, C. Bailey, K. Genevicius, Macdonald I, M. Shkunov, D. Sparrowe, S. Tierney, R. Wagner, W. M. Zhang, M. L. Chabinyc, R. J. Kline, M. D. Mcgehee and M. F. Toney. Liquid-Crystalline Semiconducting Polymers with High Charge-Carrier Mobility. *Nature Materials* **2006,** *5*, 328-333.

[58] H. Kim, H. Lee, D. Seo, Y. Jeong, K. Cho, J. Lee and Y. Lee. Regioregular Low Bandgap Polymer with Controlled Thieno[3,4-B]Thiophene Orientation for High-Efficiency Polymer Solar Cells. *Chemistry of Materials* **2015,** *27*, 3102-3107.

[59] H. Yan, Z. H. Chen, Y. Zheng, C. Newman, J. R. Quinn, F. Dotz, M. Kastler and A. Facchetti. A High-Mobility Electron-Transporting Polymer for Printed Transistors. *Nature* **2009,** *457*, 679-U1.

[60] B. Ebenhoch, S. A. J. Thomson, K. Genevicius, G. Juska and I. D. W. Samuel. Charge Carrier Mobility of the Organic Photovoltaic Materials PTB7 and PC71BM and Its Influence on Device Performance. *Organic Electronics* **2015,** *22*, 62-68.

[61] J. Wang, J. Liu, S. J. Huang, X. K. Wu, X. D. Shi, C. P. Chen, Z. C. Ye, J. G. Lu, Y. K. Su, G. F. He and Y. X. Zheng. High Efficiency Green Phosphorescent Organic Light-Emitting Diodes with a Low Roll-Off at High Brightness. *Organic Electronics* **2013,** *14*, 2854-2858.

[62] D. Qin and J. Zhang. *The Advanced Charge Injection Techniques Towards the Fabrication of High-Power Organic Light Emitting Diodes*. 2012.

[63] A. J. Das, C. Lafargue, M. Lebental, J. Zyss and K. S. Narayan. Three-Dimensional Microlasers Based on Polymer Fibers Fabricated by Electrospinning. *Applied Physics Letters* **2011,** *99*, 263303.

[64] A. J. Das and K. S. Narayan. Retention of Power Conversion Efficiency – from Small Area to Large Area Polymer Solar Cells. *Advanced Materials* **2013,** *25*, 2193-2199.

[65] H.-R. Wenk and A. Bulakh. *Minerals Their Constitution and Origin*. University Printing House, Cambridge, United Kingdom, 2004.

[66] T. Baikie, Y. N. Fang, J. M. Kadro, M. Schreyer, F. X. Wei, S. G. Mhaisalkar, M. Graetzel and T. J. White. Synthesis and Crystal Chemistry of the Hybrid Perovskite $(CH_3NH_3)PbI_3$ for Solid-State Sensitised Solar Cell Applications. *Journal of Materials Chemistry A* **2013,** *1*, 5628-5641.

[67] G. Kieslich, S. J. Sun and A. K. Cheetham. Solid-State Principles Applied to Organic-Inorganic Perovskites: New Tricks for an Old Dog. *Chemical Science* **2014,** *5*, 4712-4715.

[68] C. Motta, F. El-Mellouhi, S. Kais, N. Tabet, F. Alharbi and S. Sanvito. Revealing the Role of Organic Cations in Hybrid Halide Perovskite $CH_3NH_3PbI_3$. *Nature Communications* **2015,** *6*,7026.

[69] A. Miyata, A. Mitioglu, P. Plochocka, O. Portugall, J. T. W. Wang, S. D. Stranks, H. J. Snaith and R. J. Nicholas. Direct Measurement of the Exciton Binding Energy and Effective Masses for Charge Carriers in Organic-Inorganic Tri-Halide Perovskites. *Nature Physics* **2015,** *11*, 582-587.

[70] W. J. Yin, J. H. Yang, J. Kang, Y. F. Yan and S. H. Wei. Halide Perovskite Materials for Solar Cells: A Theoretical Review. *Journal of Materials Chemistry A* **2015,** *3*, 8926-8942.

[71] S. D. Stranks and H. J. Snaith. Metal-Halide Perovskites for Photovoltaic and Light-Emitting Devices. *Nature Nanotechnology* **2015,** *10*, 391-402.

[72] H. S. Jung and N. G. Park. Perovskite Solar Cells: From Materials to Devices. *Small* **2015,** *11*, 10-25.

[73] P. Fan, D. Gu, G. X. Liang, J. T. Luo, J. L. Chen, Z. H. Zheng and D. P. Zhang. High-Performance Perovskite $CH_3NH_3PbI_3$ Thin Films for Solar Cells Prepared by Single-Source Physical Vapour Deposition. *Scientific Reports* **2016,** *6*, 29910.

[74] C. Barugkin, J. Cong, T. Duong, S. Rahman, H. T. Nguyen, D. Macdonald, T. P. White and K. R. Catchpole. Ultralow Absorption Coefficient and Temperature Dependence of Radiative Recombination of $CH_3NH_3PbI_3$ Perovskite from Photoluminescence. *The Journal of Physical Chemistry Letters* **2015,** *6*, 767-772.

[75] O. Granas, D. Vinichenko and E. Kaxiras. Establishing the Limits of Efficiency of Perovskite Solar Cells from First Principles Modeling. *Scientific Reports* **2016,** *6*.

[76] J. Tilchin, D. N. Dirin, G. I. Maikov, A. Sashchiuk, M. V. Kovalenko and E. Lifshitz. Hydrogen-Like Wannier-Mott Excitons in Single Crystal of Methylammonium Lead Bromide Perovskite. *Acs Nano* **2016,** *10*, 6363-6371.

[77] Y. Li, W. B. Yan, Y. L. Li, S. F. Wang, W. Wang, Z. Q. Bian, L. X. Xiao and Q. H. Gong. Direct Observation of Long Electron-Hole Diffusion Distance in $CH_3NH_3PbI_3$ Perovskite Thin Film. *Scientific Reports* **2015,** *5*, 14485.

[78] Y. Chen, H. T. Yi, X. Wu, R. Haroldson, Y. N. Gartstein, Y. I. Rodionov, K. S. Tikhonov, A. Zakhidov, X. Y. Zhu and V. Podzorov. Extended Carrier Lifetimes and Diffusion in Hybrid Perovskites Revealed by Hall Effect and Photoconductivity Measurements. *Nature Communications* **2016,** *7*, 12253.

[79] S. D. Stranks, G. E. Eperon, G. Grancini, C. Menelaou, M. J. P. Alcocer, T. Leijtens, L. M. Herz, A. Petrozza and H. J. Snaith. Electron-Hole Diffusion Lengths Exceeding 1 Micrometer in an Organometal Trihalide Perovskite Absorber. *Science* **2013,** *342*, 341-344.

[80] D. Shi, V. Adinolfi, R. Comin, M. J. Yuan, E. Alarousu, A. Buin, Y. Chen, S. Hoogland, A. Rothenberger, K. Katsiev, Y. Losovyj, X. Zhang, P. A. Dowben, O. F. Mohammed, E. H. Sargent and O. M. Bakr. Low Trap-State Density and Long Carrier Diffusion in Organolead Trihalide Perovskite Single Crystals. *Science* **2015,** *347*, 519-522.

[81] C. Wehrenfennig, G. E. Eperon, M. B. Johnston, H. J. Snaith and L. M. Herz. High Charge Carrier Mobilities and Lifetimes in Organolead Trihalide Perovskites. *Advanced Materials* **2014,** *26*, 1584-1589.

[82] C. Motta, F. El-Mellouhi and S. Sanvito. Charge Carrier Mobility in Hybrid Halide Perovskites. *Scientific Reports* **2015,** *5*.

[83] B. Saparov and D. B. Mitzi. Organic-Inorganic Perovskites: Structural Versatility for Functional Materials Design. *Chemical Reviews* **2016,** *116*, 4558-4596.

[84] Y. X. Zhao and K. Zhu. Organic-Inorganic Hybrid Lead Halide Perovskites for Optoelectronic and Electronic Applications. *Chemical Society Reviews* **2016,** *45*, 655-689.

[85] M. R. Filip, G. E. Eperon, H. J. Snaith and F. Giustino. Steric Engineering of Metal-Halide Perovskites with Tunable Optical Band Gaps. *Nature Communications* **2014,** *5*.

[86] J. L. Knutson, J. D. Martin and D. B. Mitzi. Tuning the Band Gap in Hybrid Tin Iodide Perovskite Semiconductors Using Structural Templating. *Inorganic Chemistry* **2005,** *44*, 4699-4705.

[87] D. M. Jang, K. Park, D. H. Kim, J. Park, F. Shojaei, H. S. Kang, J. P. Ahn, J. W. Lee and J. K. Song. Reversible Halide Exchange Reaction of Organometal Trihalide Perovskite Colloidal Nanocrystals for Full-Range Band Gap Tuning. *Nano Letters* **2015,** *15*, 5191-5199.

[88] H. M. Zhu, Y. P. Fu, F. Meng, X. X. Wu, Z. Z. Gong, Q. Ding, M. V. Gustafsson, M. T. Trinh, S. Jin and X. Y. Zhu. Lead Halide Perovskite Nanowire Lasers with Low Lasing Thresholds and High Quality Factors. *Nature Materials* **2015,** *14*, 636-642.

[89] N. J. Jeon, J. H. Noh, Y. C. Kim, W. S. Yang, S. R. and S. I. Seok. Solvent Engineering for High-Performance Inorganic–Organic Hybrid Perovskite Solar Cells. *Nature Materials* **2014,** *13*, 897-903.

[90] P. Kumar, B. Zhao, R. H. Friend, A. Sadhanala and K. S. Narayan. Kinetic Control of Perovskite Thin-Film Morphology and Application in Printable Light-Emitting Diodes. *ACS Energy Letters* **2017,** *2*, 81-87.

[91] A. D. Yoffe. Semiconductor Quantum Dots and Related Systems: Electronic, Optical, Luminescence and Related Properties of Low Dimensional Systems. *Advances in Physics* **2001,** *50*, 1-208.

[92] A. M. Smith and S. M. Nie. Semiconductor Nanocrystals: Structure, Properties, and Band Gap Engineering. *Accounts of Chemical Research* **2010,** *43*, 190-200.

[93] D. Y. Wang, I. S. Wang, I. S. Huang, Y. C. Yeh, S. S. Li, K. H. Tu, C. C. Chen and C. W. Chen. Quantum Dot Light-Emitting Diode Using Solution-Processable Graphene Oxide as the Anode Interfacial Layer. *Journal of Physical Chemistry C* **2012,** *116*, 10181-10185.

[94] Y. Yin and A. P. Alivisatos. Colloidal Nanocrystal Synthesis and the Organic-Inorganic Interface. *Nature* **2005,** *437*, 664-670.

[95] B. O. Dabbousi, J. RodriguezViejo, F. V. Mikulec, J. R. Heine, H. Mattoussi, R. Ober, K. F. Jensen and M. G. Bawendi. (CdSe)ZnS Core-Shell Quantum Dots: Synthesis and Characterization of a Size Series of Highly Luminescent Nanocrystallites. *Journal of Physical Chemistry B* **1997,** *101*, 9463-9475.

[96] L. C. Schmidt, A. Pertegas, S. Gonzalez-Carrero, O. Malinkiewicz, S. Agouram, G. M. Espallargas, H. J. Bolink, R. E. Galian and J. Perez-Prieto. Nontemplate Synthesis of $CH_3NH_3PbBr_3$ Perovskite Nanoparticles. *Journal of the American Chemical Society* **2014,** *136*, 850-853.

[97] C. Muthu, S. R. Nagamma and V. C. Nair. Luminescent Hybrid Perovskite Nanoparticles as a New Platform for Selective Detection of 2,4,6-Trinitrophenol. *RSC Advances* **2014,** *4*, 55908-55911.

[98] J. Pan, S. P. Sarmah, B. Murali, I. Dursun, W. Peng, M. R. Parida, J. Liu, L. Sinatra, N. Alyami, C. Zhao, E. Alarousu, T. K. Ng, B. S. Ooi, O. M. Bakr and O. F. Mohammed. Air-Stable Surface-Passivated Perovskite Quantum Dots for Ultra-Robust, Single- and Two-Photon-Induced Amplified Spontaneous Emission. *Journal of Physical Chemistry Letters* **2015,** *6*, 5027-5033.

[99] Z. J. Ning, X. W. Gong, R. Comin, G. Walters, F. J. Fan, O. Voznyy, E. Yassitepe, A. Buin, S. Hoogland and E. H. Sargent. Quantum-Dot-in-Perovskite Solids. *Nature* **2015,** *523*, 324-328.

[100] H. Huang, A. S. Susha, S. V. Kershaw, T. F. Hung and A. L. Rogach. Control of Emission Color of High Quantum Yield $CH_3NH_3PbBr_3$ Perovskite Quantum Dots by Precipitation Temperature. *Advanced Science* **2015,** *2*, 1500194.

[101] Y. H. Kim, H. Cho and T. W. Lee. Metal Halide Perovskite Light Emitters. *Proceedings of the National Academy of Sciences of the United States of America* **2016,** *113*, 11694-11702.

[102] G. D. Scholes and G. Rumbles. Excitons in Nanoscale Systems. *Nature Materials* **2006,** *5*, 683-696.

[103] N. Ray. Charge Transport in Nanopatterned Pbs Colloidal Quantum Dot Arrays. Massachusetts Institute of Technology, Cambridge Massachusetts, 2015.

[104] A. G. MacDiarmid, R. J. Mammone, R. B. Kaner, S. J. Porter, R. Pethig, A. J. Heeger and D. R. Rosseinsky. The Concept of `Doping' of Conducting Polymers: The Role of Reduction Potentials [and Discussion]. *Philosophical Transactions of the Royal Society of London. Series A, Mathematical and Physical Sciences* **1985,** *314*, 3-15.

[105] J.-C. Chiang and A. G. MacDiarmid. 'Polyaniline': Protonic Acid Doping of the Emeraldine Form to the Metallic Regime. *Synthetic Metals* **1986,** *13*, 193-205.

[106] B. L. Groenendaal, F. Jonas, D. Freitag, H. Pielartzik and J. R. Reynolds. Poly(3,4-Ethylenedioxythiophene) and Its Derivatives: Past, Present, and Future. *Advanced Materials* **2000,** *12*, 481-494.

[107] F. Loffredo, A. D. Del Mauro, G. Burrasca, V. La Ferrara, L. Quercia, E. Massera, G. Di Francia and D. D. Sala. Ink-Jet Printing Technique in Polymer/Carbon Black Sensing Device Fabrication. *Sensors and Actuators B-Chemical* **2009,** *143*, 421-429.

[108] K. Kordas, T. Mustonen, G. Toth, H. Jantunen, M. Lajunen, C. Soldano, S. Talapatra, S. Kar, R. Vajtai and P. M. Ajayan. Inkjet Printing of Electrically Conductive Patterns of Carbon Nanotubes. *Small* **2006,** *2*, 1021-1025.

[109] L. Huang, Y. Huang, J. J. Liang, X. J. Wan and Y. S. Chen. Graphene-Based Conducting Inks for Direct Inkjet Printing of Flexible Conductive Patterns and Their Applications in Electric Circuits and Chemical Sensors. *Nano Research* **2011,** *4*, 675-684.

[110] K. Sun, S. P. Zhang, P. C. Li, Y. J. Xia, X. Zhang, D. H. Du, F. H. Isikgor and J. Y. Ouyang. Review on Application of PEDOT and PEDOT:PSS in Energy Conversion and Storage Devices. *Journal of Materials Science-Materials in Electronics* **2015,** *26*, 4438-4462.

[111] J. Ouyang, C. W. Chu, F. C. Chen, Q. F. Xu and Y. Yang. Polymer Optoelectronic Devices with High-Conductivity Poly(3,4-Ethylenedioxythiophene) Anodes. *Journal of Macromolecular Science-Pure and Applied Chemistry* **2004,** *A41*, 1497-1511.

[112] B. Y. Ouyang, C. W. Chi, F. C. Chen, Q. F. Xi and Y. Yang. High-Conductivity Poly (3,4-Ethylenedioxythiophene): Poly(Styrene Sulfonate) Film and Its Application in Polymer Optoelectronic Devices. *Advanced Functional Materials* **2005,** *15*, 203-208.

[113] A. M. Nardes, M. Kemerink and R. A. J. Janssen. Anisotropic Hopping Conduction in Spin-Coated PEDOT:PSS Thin Films. *Physical Review B* **2007,** *76*.

[114] S. P. Pang, H. N. Tsao, X. L. Feng and K. Mullen. Patterned Graphene Electrodes from Solution-Processed Graphite Oxide Films for Organic Field-Effect Transistors. *Advanced Materials* **2009,** *21*, 3488-3491.

[115] M. Schulze, M. Lorenz and T. Kaz. Xps Study of Electrodes Formed from a Mixture of Carbon Black and Ptfe Powder. *Surface and Interface Analysis* **2002,** *34*, 646-651.

[116] Z. Li, S. A. Kulkarni, P. P. Boix, E. Z. Shi, A. Y. Cao, K. W. Fu, S. K. Batabyal, J. Zhang, Q. H. Xiong, L. H. Wong, N. Mathews and S. G. Mhaisalkar. Laminated Carbon Nanotube Networks for Metal Electrode-Free Efficient Perovskite Solar Cells. *Acs Nano* **2014,** *8*, 6797-6804.

[117] J. B. Donnet. *Carbon Black: Science and Technology*. Marcel Dekker Inc: New York, 1993; p 461.

[118] R. C. Chiechi, E. A. Weiss, M. D. Dickey and G. M. Whitesides. Eutectic Gallium-Indium (Egain): A Moldable Liquid Metal for Electrical Characterization of Self-Assembled Monolayers. *Angewandte Chemie-International Edition* **2008,** *47*, 142-144.

[119] M. Bag, D. Gupta, N. Arun and K. S. Narayan. Deformation of Metallic Liquid Drop by Electric Field for Contacts in Molecular-Organic Electronics. *Proceedings of the Royal Society a-Mathematical Physical and Engineering Sciences* **2009,** *465*, 1799-1808.

[120] S. Linic, P. Christopher and D. B. Ingram. Plasmonic-Metal Nanostructures for Efficient Conversion of Solar to Chemical Energy. *Nature Materials* **2011,** *10*, 911-921.

[121] H. Heidarzadeh, A. Rostami, M. Dolatyari and G. Rostami. Plasmon-Enhanced Performance of an Ultrathin Silicon Solar Cell Using Metal-Semiconductor Core-Shell Hemispherical Nanoparticles and Metallic Back Grating. *Applied Optics* **2016,** *55*, 1779-1785.

[122] M. G. Kang, M. S. Kim, J. S. Kim and L. J. Guo. Organic Solar Cells Using Nanoimprinted Transparent Metal Electrodes. *Advanced Materials* **2008,** *20*, 4408-4413.

[123] D. H. Ko, J. R. Turnbleston, W. Schenck, R. Lopez and E. T. Samulski. Photonic Crystal Geometry for Organic Polymer:Fullerene Standard and Inverted Solar Cells. *Journal of Physical Chemistry C* **2011,** *115*, 4247-4254.

[124] D. H. Ko, J. R. Tumbleston, L. Zhang, S. Williams, J. M. DeSimone, R. Lopez and E. T. Samulski. Photonic Crystal Geometry for Organic Solar Cells. *Nano Letters* **2009,** *9*, 2742-2746.

[125] L. C. Oliveira, A. M. N. Lima, C. T. and H. F. Neff. *Surface Plasmon Resonance Sensors: A Materials Guide to Design and Optimization*. Springer International Publishing: 2015.

[126] D. Lupo and S. G. G. Nisato. *Organic and Printed Electronics - Fundamentals and Applications*. CRC Press, Taylor & Francis Group: Boca Raton, FL, 2016; p 580.

[127] W. Shockley and H. J. Queisser. Detailed Balance Limit of Efficiency of P-N Junction Solar Cells. *Journal of Applied Physics* **1961,** *32*, 510-519.

[128] C. H. Henry. Limiting Efficiencies of Ideal Single and Multiple Energy Gap Terrestrial Solar Cells. *Journal of Applied Physics* **1980,** *51*, 4494-4500.

[129] A. De Vos. Detailed Balance Limit of the Efficiency of Tandem Solar Cells. *Journal of Physics D: Applied Physics* **1980,** *13*, 839.

[130] K. Barnham, J. L. Marques, J. Hassard and P. O'Brien. Quantum-Dot Concentrator and Thermodynamic Model for the Global Redshift. *Applied Physics Letters* **2000,** *76*, 1197-1199.

[131] V. Sholin, J. D. Olson and S. A. Carter. Semiconducting Polymers and Quantum Dots in Luminescent Solar Concentrators for Solar Energy Harvesting. *Journal of Applied Physics* **2007,** *101*.

[132] M. C. Beard and R. J. Ellingson. Multiple Exciton Generation in Semiconductor Nanocrystals: Toward Efficient Solar Energy Conversion. *Laser & Photonics Reviews* **2008,** *2*, 377-399.

[133] T. Trupke, M. A. Green and P. Wurfel. Improving Solar Cell Efficiencies by up-Conversion of Sub-Band-Gap Light. *Journal of Applied Physics* **2002,** *92*, 4117-4122.

[134] T. Trupke, M. A. Green and P. Wurfel. Improving Solar Cell Efficiencies by Down-Conversion of High-Energy Photons. *Journal of Applied Physics* **2002,** *92,* 1668-1674.

[135] E. C. Greyson, B. R. Stepp, X. D. Chen, A. F. Schwerin, I. Paci, M. B. Smith, A. Akdag, J. C. Johnson, A. J. Nozik, J. Michl and M. A. Ratner. Singlet Exciton Fission for Solar Cell Applications Energy Aspects of Interchromophore Coupling. *Journal of Physical Chemistry B* **2010,** *114*, 14223-14232.

[136] S. M. Nie and S. R. Emery. Probing Single Molecules and Single Nanoparticles by Surface-Enhanced Raman Scattering. *Science* **1997,** *275*, 1102-1106.

[137] M. Moskovits. Surface-Enhanced Raman Spectroscopy: A Brief Retrospective. *Journal of Raman Spectroscopy* **2005,** *36*, 485-496.

[138] M. Moskovits. Surface-Enhanced Spectroscopy. *Reviews of Modern Physics* **1985,** *57*, 783-826.

[139] K. R. Catchpole and A. Polman. Plasmonic Solar Cells. *Optics Express* **2008,** *16*, 21793-21800.

[140] C. F. Bohren and D. R. Huffman. Absorption and Scattering by an Arbitrary Particle. In *Absorption and Scattering of Light by Small Particles*, Wiley-VCH Verlag GmbH: 2007; pp 57-81.

[141] F. J. Haug, T. Soderstrom, O. Cubero, V. Terrazzoni-Daudrix and C. Ballif. Plasmonic Absorption in Textured Silver Back Reflectors of Thin Film Solar Cells. *Journal of Applied Physics* **2008,** *104*, 064509.

[142] A. J. Morfa, K. L. Rowlen, T. H. Reilly, M. J. Romero and J. van de Lagemaat. Plasmon-Enhanced Solar Energy Conversion in Organic Bulk Heterojunction Photovoltaics. *Applied Physics Letters* **2008,** *92*, 013504.

[143] D. M. Schaadt, B. Feng and E. T. Yu. Enhanced Semiconductor Optical Absorption Via Surface Plasmon Excitation in Metal Nanoparticles. *Applied Physics Letters* **2005,** *86*, 063106.

[144] V. E. Ferry, L. A. Sweatlock, D. Pacifici and H. A. Atwater. Plasmonic Nanostructure Design for Efficient Light Coupling into Solar Cells. *Nano Letters* **2008,** *8*, 4391-4397.

[145] L. P. Zhang, X. Xing, L. L. Zheng, Z. J. Chen, L. X. Xiao, B. Qu and Q. H. Gong. Vertical Phase Separation in Bulk Heterojunction Solar Cells Formed by in Situ Polymerization of Fulleride. *Scientific Reports* **2014,** *4*, 5071.

[146] B. P. Lyons, N. Clarke and C. Groves. The Relative Importance of Domain Size, Domain Purity and Domain Interfaces to the Performance of Bulk-Heterojunction Organic Photovoltaics. *Energy & Environmental Science* **2012,** *5*, 7657-7663.

[147] B. Y. Huang, J. A. Amonoo, A. Li, X. C. Chen and P. F. Green. Role of Domain Size and Phase Purity on Charge Carrier Density, Mobility, and Recombination in Poly(3-hexylthiophene):Phenyl-C61-Butyric Acid Methyl Ester Devices. *Journal of Physical Chemistry C* **2014,** *118*, 3968-3975.

[148] J. U. Ha, S. W. Yoon, J. S. Lee and D. S. Chung. Organic-Inorganic Hybrid Inverted Photodiode with Planar Heterojunction for Achieving Low Dark Current and High Detectivity. *Nanotechnology* **2016,** *27*, 095203.

[149] X. F. Wang, W. F. Song, B. Liu, G. Chen, D. Chen, C. W. Zhou and G. Z. Shen. High-Performance Organic-Inorganic Hybrid Photodetectors Based on P3HT:CdSe Nanowire Heterojunctions on Rigid and Flexible Substrates. *Advanced Functional Materials* **2013,** *23*, 1202-1209.

[150] H. Kim, Q. Zhang, A. Nurmikko, Q. Sun and J. Han. Nitride/Organic Hybrid Heterostructures for Photodetector Devices. *2008 Conference on Lasers and Electro-Optics & Quantum Electronics and Laser Science Conference, Vols 1-9* **2008**, 354.

[151] N. Ikeda, T. Koganezawa, D. Kajiya and K. Saitow. Performance of Si/PEDOT:PSS Hybrid Solar Cell Controlled by PEDOT:PSS Film Nanostructure. *Journal of Physical Chemistry C* **2016,** *120*, 19043-19048.

[152] M. Carvelli, R. A. J. Janssen and R. Coehoorn. Determination of the Exciton Singlet-to-Triplet Ratio in Single-Layer Organic Light-Emitting Diodes. *Physical Review B* **2011,** *83*, 075203.

[153] L. Bergmann, G. J. Hedley, T. Baumann, S. Bräse and I. D. W. Samuel. Direct Observation of Intersystem Crossing in a Thermally Activated Delayed Fluorescence Copper Complex in the Solid State. *Science Advances* **2016,** *2*, e1500889.

[154] K. Goushi, K. Yoshida, K. Sato and C. Adachi. Organic Light-Emitting Diodes Employing Efficient Reverse Intersystem Crossing for Triplet-to-Singlet State Conversion. *Nature Photonics* **2012,** *6*, 253-258.

[155] C. Zhang, D. Sun, C. X. Sheng, Y. X. Zhai, K. Mielczarek, A. Zakhidov and Z. V. Vardeny. Magnetic Field Effects in Hybrid Perovskite Devices. *Nature Physics* **2015,** *11*, 428-435.

Chapter 2: Eutectic Metal Alloys for Large Area Solution-Processed Electrodes

2.1: Introduction

In lab efficiencies for solution-processed photovoltaics (PVs), have reached beyond 11% for OSC [1, 2] and 22% for organic-inorganic perovskite-based absorbers [3, 4]. To scale up the PVs, for large-area applications, low-temperature, printable metal inks which can be easily processed into anode-cathode and interconnects are essential [5-7]. Many conducting ink formulations (silver ink, carbon ink) have been made available for this application, however, it is always desired to minimize the losses by reducing the work function (W_F) mismatch and improve the conductivity [8, 9]. Meltable eutectic solder alloys can be doubled up as both electrodes and interconnects, where the mechanical and electronic properties can be tuned by varying the composition [10, 11]. The eutectic mixtures of the binary alloy (In-Ga alloy) have been explored as vacuum free electrodes for long [12, 13]. Other combinations of ternary and quaternary alloy systems have also shown to be useful for printable electrode applications [14-16]. However, the underlying mechanisms for establishing low resistance contacts for these alloys are not well understood, thereby requiring a thorough investigation for improving the performance and applicability.

The cathode and interconnects are characterized in terms of parameters like mechanical adhesion to the substrate, workfunction-W_F, conformability and sheet resistance. In plastic electronics, the ability of an electrode to withstand a certain degree of bending and flexing is also desirable. W_F plays a crucial role in maximizing the charge injection and collection efficiency of an electrode [17, 18]. In previous work, it was demonstrated that a quaternary eutectic alloy with low melting point (~ 58 ^{0}C) works at par with thermally evaporated cathodes like aluminum (Al) [15]. The alloy electrodes offered small series resistance compared to the evaporated electrodes. High efficiencies attained over a small area, can be retained over larger pixel size. In the organic bulk heterojunction (BHJ) system the lowest unoccupied molecular orbital (LUMO) of acceptor (A) molecule (PCBM-C70) is at 3.8 - 4.0 eV [19]. The metals with W_F close to ~ 4 eV are suitable as a cathode. One of the widely used cathode metal is Al as its W_F (~ 4.07 eV) is close to that of acceptor LUMO and is cost effective. However, a low W_F metal also suffers from the problem of rapid oxidation under ambient conditions. As the W_F increases, the stability towards oxidation improves, simultaneously the barrier for electron collection also increases and the interface changes from ohmic to Schottky. The indium (In) based solder alloys, where the W_F is below that of Al, demonstrate a superior stability towards oxidation while still forming an ohmic contact with the acceptor component. Thus the alloys (with low indium content) can suitably replace Al as a cathode layer in printable thin film devices.

The polymer bulk heterojunction system has been used in conjugation with alloy cathode to study the electrical properties of alloy/polymer interface. Low band gap donor polymer has been selected in particular for highlighting the optical activity of alloy as a function of indium concentration using surface enhanced Raman spectroscopic and photocurrent studies. Kelvin probe in conjugation with capacitance-voltage studies is used to estimate the work function of alloy cathode while the electrical quality of alloy/polymer interface is probed using current-voltage and impedance studies. Observations suggest that indium is essential for the efficient performance of alloy cathodes.

2.2: Overview of low-temperature meltable alloys

Eutectic solder alloys or fusible alloys can be a binary, ternary or quaternary mixture of post-transition metals like In, lead (Pb), bismuth (Bi), tin (Sn) and gallium. Alloys with different metal ratios demonstrate large variation in melting point, electrical and mechanical properties. Fusible alloys are characterized by their melting point which varies from a minimum of 35 ^{o}C to maximum of 250 ^{o}C. This range of melting temperature is ideal for printing on plastic substrates, which can become unstable above ~ 150 ^{0}C. The solder alloys have thermal and electrical conductivity (~ 4-5 %) comparable to that of metal inks made of silver (Ag), Al and copper. The ability to locally melt and form conformal contact with the underlying substrate gives a decisive advantage over commonly used metals.

Alloys used in the present study are a ternary or quaternary mixture of In, Sn, Bi and Pb mixed in the different weight ratio as is shown in Figure 2.1a. The melting point increases with a decrease in the indium content (below 21 %), while at a higher weight percentage of indium (21-51 wt %) the melting point does not vary significantly (~ 58 - 62 ^{o}C). For the ease of differentiation, alloys have been named based on their relative indium content. The melting point for various alloys used in this study lies in the range of 58 - 94 ^{o}C depending on the composition, as shown in the melting point curves in Figure 2.1b. Additionally, the Bi alloys feature some unique properties like an expansion upon cooling by ~ 3.3 %, such features are desirable for achieving a homogeneous contact without any gaps between metal and polymer layer.

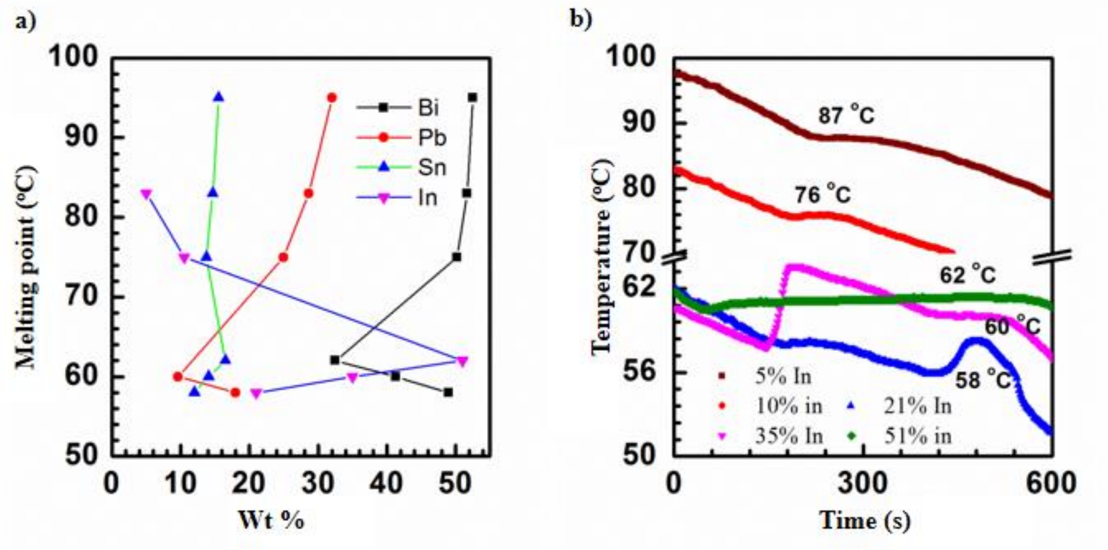

Figure 2.1: a) Composition vs. melting point curve for different alloys used, b) melting point estimated through temperature vs. time plot.

2.3: Experimental details

2.3.1: Materials

Semiconducting polymer PBDTTT-C-T (2,6-Bis(trimethyltin)-4,8-bis(5-(2 ethylhexyl) thiophen-2-yl) benzo[1,2-b :4,5-b']dithiophene) was procured from Solarmer, USA and PCBM-C70 ([6,6]-Phenyl C71 butyric acid methyl ester) was purchased from Luminescence Technology Corporation, Taiwan. Hole transporter PEDOT:PSS (Poly(3,4-ethylenedioxythiophene)-poly(styrenesulfonate)) (AI PVP 4083) was procured from Clevious. Conducting transparent electrode, ITO (indium tin oxide) coated glass substrates ($R_S = 8$ Ωcm) were purchased from Xin Yan Technology Limited, China. Low-temperature meltable alloys with 0%, 21% and 51% indium content were purchased from Roto Metals, USA, while the 5%, 10% and 35% indium content alloys were prepared in the laboratory.

2.3.2: Sample preparation

Substrate cleaning

Quartz and ITO substrates were cleaned using wet cleaning procedure as described below,

I. 10 min Sonication in surfactant and de-ionized water at 40 ^{o}C.
II. Rinsed and sonicated in di-ionized water for 10 min.
III. Rinsed and sonicated in acetone for 10 min.
IV. Rinsed and sonicated in Isopropyl alcohol 10 min
V. Blow dried using compressed air and treated in air plasma for 10 min.

Thin film fabrication

A solution of PBDTTT-C-T and PCBM-C70 was prepared in 1:1.5 wt ratio in 1,2-dichlorobenzene in different concentration (1 to 25 mg/ml) to obtain a range of film thicknesses (~ 10 to 120 nm).

Films for Raman and absorption measurement: All the thin films of pristine and blend semiconductors were spin coated at 1000 rpm on quartz substrates in the nitrogen filled glove box. PEDOT: PSS films were spin coated at 3000 rpm for 60 s in air followed by annealing at 180 ^{o}C for 15 min.

Solar cell fabrication: PEDOT: PSS films (film thickness ~ 40 nm) were spin coated on plasma cleaned ITO glass at 3000 rpm in air, followed by annealing on a hot plate at 180 ^{o}C for 15 min. Blend solution with different concentration was spin coated at 1000 rpm in nitrogen filled glove box, films were not annealed.

2.3.3: Metal electrode deposition

Metal electrodes like aluminum (Al), silver (Ag) and gold (Au) were thermally evaporated in a thermal evaporation chamber at ~ $5\text{-}6 \times 10^{-6}$ mbar pressure. The active area was controlled using a metal mask. Low-temperature alloy electrodes were deposited as a cathode on a hotplate, in air, using low-temperature injection technique as illustrated in Figure 2.2. The area was controlled using a perforated Polyethylene terephthalate (PET) mask with the active area ranging from 0.07 to 0.12 cm^2. The process of depositing alloy electrode involves three steps, (a) the nozzle is charged from a reservoir using a small vacuum pump, (b) the molten alloy is carefully dispensed on the perforated area and (c) the excess metal is removed using the nozzle. The alloy electrode thickness is typically $\cong$ 150 μm and is comparable to the thickness of PET sheet (~ 70 μm); thickness can be further reduced by using more controlled alloy deposition.

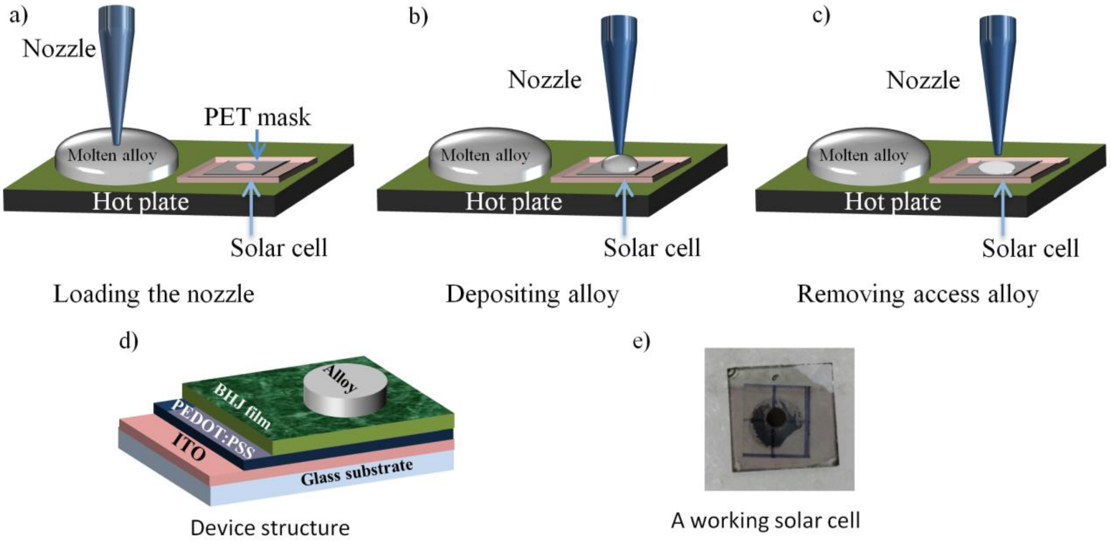

Figure 2.2: *An illustration of low-temperature injection deposition of alloy cathode, a0 charging of nozzle, b) dispensing alloy, c) removing access alloy, d) device schematic and e) actual working solar cell with mirror finish alloy electrode.*

2.3.4: Characterization

All characterizations were performed in air without any encapsulation, while the devices were stored in nitrogen filled glove box in between the measurements.

Raman: Surface enhanced Raman spectroscopy has been used as a tool to study the plasmonic and chemical nature of alloy/polymer interface; the results were compared with the standard electrodes like Al, Ag, and Au. A custom made Raman setup with 180° backscattering was used to collect the Raman signals [20]. An epi-fluorescent microscope was converted to work as a Raman microscope. A diode pumped frequency doubled (λ = 532 nm) Nd: YAG solid state laser (Photop Suwtech Inc., GDLM-5015 L) was used as an excitation source. Laser power at the sample was 8 mW without filters, and it was controlled using appropriate neutral density filters to prevent photobleaching of the sample. The incident light was focused onto the sample using a high numerical aperture (0.45) objective lens with a working distance of 17 mm. The entrance slit width to the monochromator defines the spectral resolution and it was typically set at 200 µm. 1800 grooves per mm grating were used to achieve a resolution of 0.7 cm^{-1}. The Raman spectrometer was equipped with a SPEX TRIAX 550 monochromator and a liquid nitrogen cooled CCD. Spectra were acquired in 100 cm^{-1} to 2000 cm^{-1} range with a typical accumulation time of 30 - 90 s, in general, multiple spectra were recorded for each system and averaged. Raman intensities were normalized using Raman intensity of first order Si optical mode as a reference.

Absorption and Reflection: Absorption and reflection measurements were performed on a Perkin Elmer UV-Vis spectrometer equipped with integrating sphere for accurate reflection and transmission measurements. Teflon disks were used as high reflective holders, where ever necessary, to reduce background signatures.

Atomic force microscopy (AFM): Topography and Kelvin probe (KPFM) measurement of pristine and blend films of PBDTTT-C-T and PCBM-C70 and alloy electrode was recorded using JPK Nanowizard 3 atomic force microscope. Topography and phase images were recorded in non-contact tapping mode using Si cantilever with platinum/iridium coating, the resonance frequency of 300 KHz and force constant of 40 N/m. thermally evaporated gold on the glass and highly oriented pyrolytic graphite (HOPG) were used as a calibration standard for estimating the W_F of the AFM cantilever.

Impedance and capacitance-voltage (C-V): Small signal impedance measurement was performed using a function generator (Tektronix) and a lock-in amplifier (SR830). A small sinusoidal varying voltage of ~ 100 mV was applied with 0 V DC bias across the device, and the current was recorded using a low noise preamplifier (SR570). The C-V measurement was performed at 10 kHz from -0.5 V to 1.5 V using a semiconductor parameter analyzer (Keithley SCS 4200).

Current-Voltage (J-V) and quantum efficiency (QE): Dark and under illumination measurements were performed on Newport solar simulator. Oriel Class 3 A solar simulator was used for 1 Sun illumination. Keithley 2400 source meter was used for J-V measurement. QE measurement was performed in a lab built facility; a tungsten lamp coupled with a monochromator (Zolix Omni 750) was used as a light source. Device photocurrent (I_{ph}) response was recorded in using lock-in amplifier (SR830). Incident optical power was calibrated using a calibrated detector (DS1-200, Zolix).

Photocurrent scanning: Large area scanning of photocurrent was performed on in lab developed facility. A red laser (λ = 632 nm) was focused through a 0.45 NA 50X objective. The samples were mounted on a stepper controlled X-Y-Z stage (Thor Labs). The samples were raster scanned at a resolution of 50 µm in X and Y axis for a total length of 4 mm by 4mm. Photocurrent signal was recorded using a lock-in amplifier (SR830) along with the low noise current preamplifier (FEMTO 2000).

2.4: Result and Discussion

2.4.1: Morphology and surface potential

The liquid alloy coated on a clean surface of ITO forms an optical quality interface. The roughness of alloy surface, at the peeled alloy/ITO interface, was mapped using non-contact AFM. Roughness map of alloy with different weight percentage of indium is indistinguishable, as shown in Figure 2.3 for 21%, 35% and 51% Alloys. Conformal mapping of the surface features of the ITO coated substrates, by molten alloy, is exhibited in the surface feature resembling grain size distribution. The average roughness of alloy surface is ~ 10 nm; highest features are ~ 20 nm. Low roughness observed over a large area is important for homogeneous charge extraction.

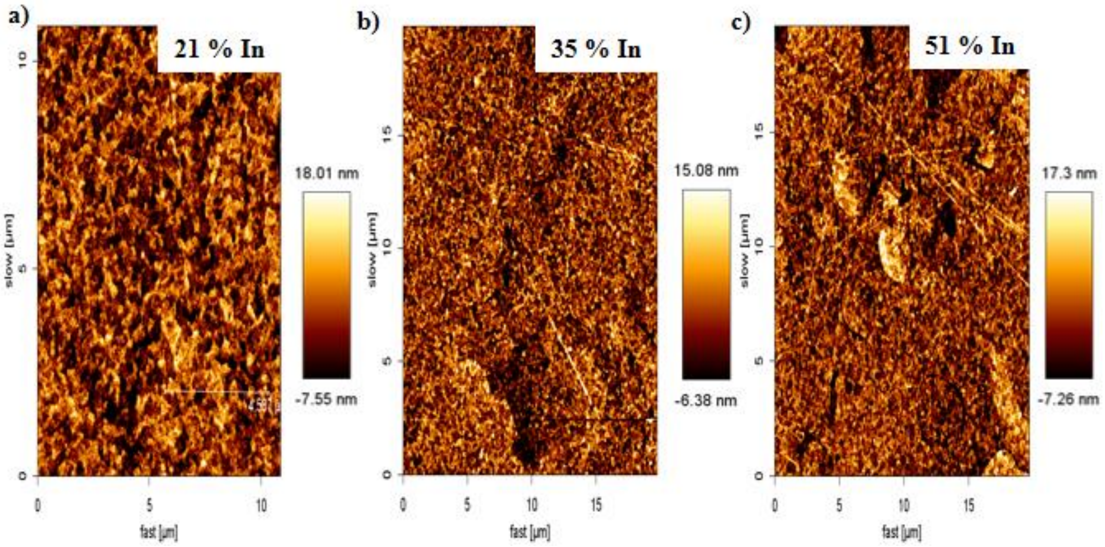

Figure 2.3: *Surface roughness measured on the surface of alloy with a) 21%, b) 35%, and c) 51% indium.*

Along with the roughness of alloy surface, the contact potentials were also mapped on the planar alloy surfaces cast on ITO-glass substrates. Use of oxide layer, like ITO, is helpful for avoiding any modification to surface potential, due to the residual polymer layer. The surface potential map shows a small average variation < 30 mV over an area of ~ $15 \times 15\ \mu m^2$. Variation in contact potential over the measured area remains small between alloys with different indium wt %, as is evident in Figure 2.4.

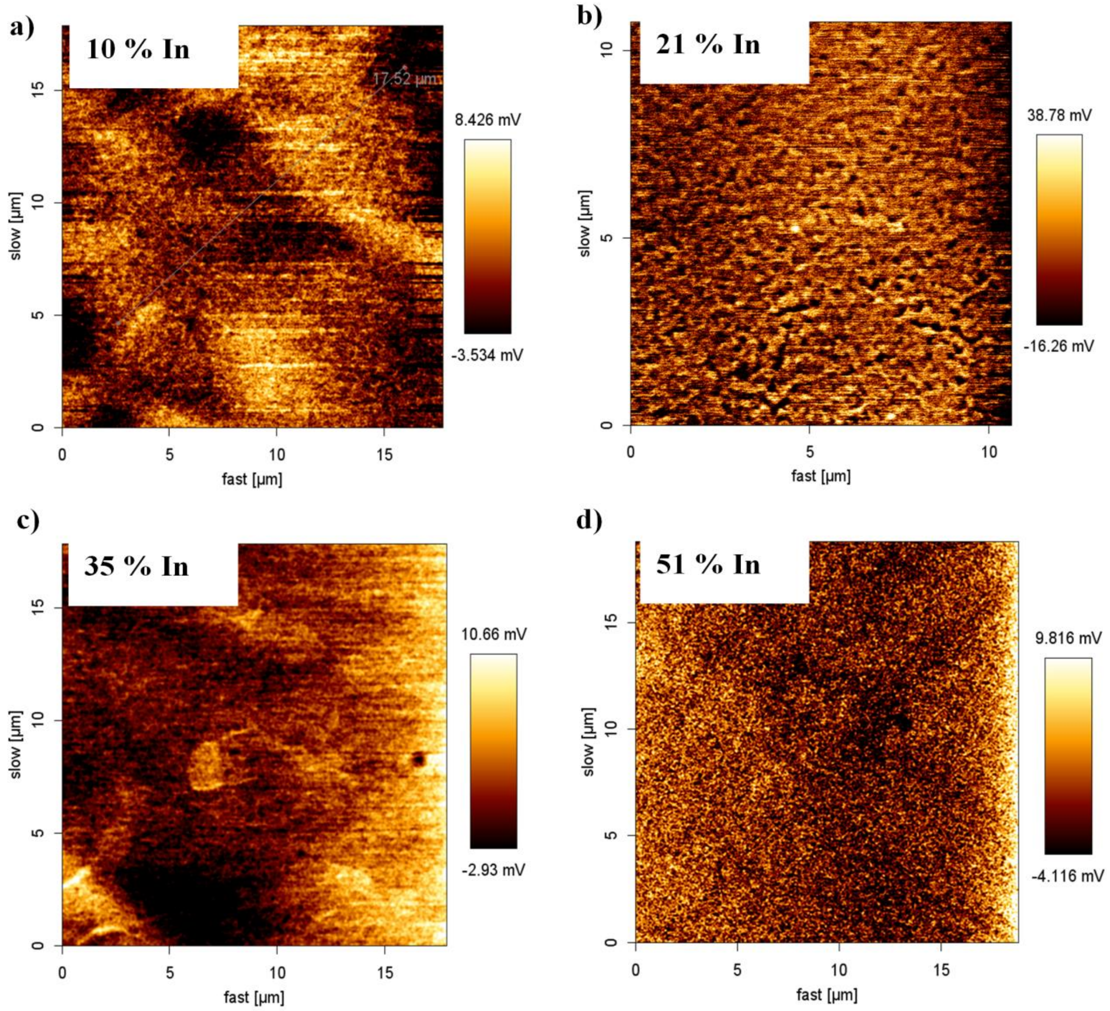

Figure 2.4: *Surface contact potential map for alloy with a) 10%, b) 21%, c) 35% and d) 51% indium.*

The absolute value of contact potential is ~ 435 mV (for 21%, 35% and 51% indium alloy), while for 10% indium alloy the value is ~ 470 mV (Figure 2.5). A variation in surface potential can be associated with two possible sources, i) The alloys used in this study are a ternary or quaternary mixture of solder metals (In, Pb, Bi and

Sn). The work function of In and Pb is ~ 4.0 eV while that of Bi and Sn is ~ 4.3 eV. Thus the work function of the alloy will be governed by the relative ratio of constituent metals, ii) The 10 % In alloy also demonstrates higher melting point temperature (> 15 ^{o}C) compared to 21%, 35% and 51%, the higher processing temperature is also associated with increased susceptibility towards oxide formation. The Kelvin Probe measurement used for determining the surface potential was performed on the alloy electrodes processed in air, which increases the possibility of surface modification due to the presence of oxides.

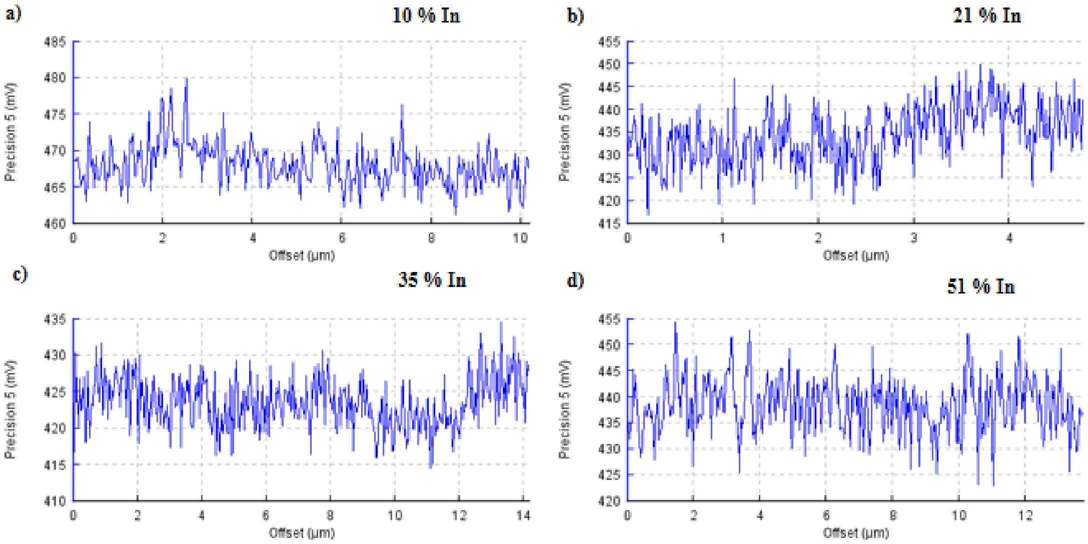

Figure 2.5: *Line scans representing absolute contact potential for alloy with, a) 10%, b) 21%, c) 35% and d) 51% indium respectively.*

Contact potential at the exposed surfaces is typically modified due to the formation of thin oxide layers and other carbon impurities, which makes it difficult to estimate the absolute W_F in air. However, the surface contact potential difference between different alloys can be used to estimate their W_F by comparing it with the known W_F of any alloy. The W_F for 21% indium alloy (~ 4.27 ± 0.03 eV), measured using ultraviolet photoelectron spectroscopy (UPS) is shown in Figure 2.6. Using the contact potential map for alloys with different indium wt % to that of 21% indium alloy, the absolute W_F for remaining alloys was estimated to be in the range of 4.25 - 4.30 eV, which is close to that of their constituent metals. The W_F show little modification across different alloys, which is beneficial for a stable, oxidation resistant cathode layer in polymer solar cells.

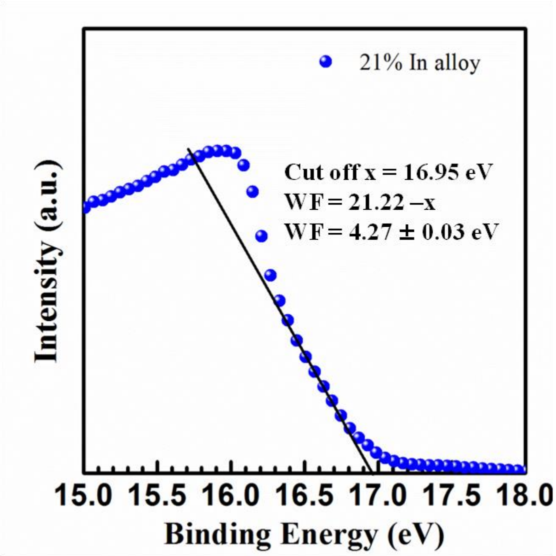

Figure 2.6: *Workfunction estimation using UPS for the alloy with 21% indium. (Reprinted with permission from P. Kumar, B. Zhao, R. H. Friend, A. Sadhanala, and K. S. Narayan, Kinetic Control of Perovskite Thin Film Morphology and Application in Printable Light Emitting Diodes, ACS Energy letters, 2, 1, 81-87, (2016). Copyright (2017) American Chemical Society).*

2.4.2: Surface adhesion properties of Indium alloys

Adequate adhesion between alloy and polymer surface is the minimum necessary criteria for ensuring a low loss charge collection. Alloys adhesion with polymer BHJ layer differs significantly with alloy composition. The alloys without indium, i.e. the ternary mixture of Pb, Bi, Sn, demonstrate the high melting point (> 90 ^{o}C) and negligible adhesion strength (delaminates instantaneously) with a polymer layer. Higher melting point alloys also pose difficulty in processing due to the higher cooling rates, solidifying very quickly in the nozzle. Alloys adhesion strength to polymer layer shows large improvements with the addition of a small fraction of indium (~ 5%) into the Bi, Sn, Pb alloy. The strength of adhesion is proportional to the content of indium; highest strength was observed for 51% indium alloy. Improvement in adhesion strength suggests the formation of alloy/polymer bond which is activated in the presence of indium.

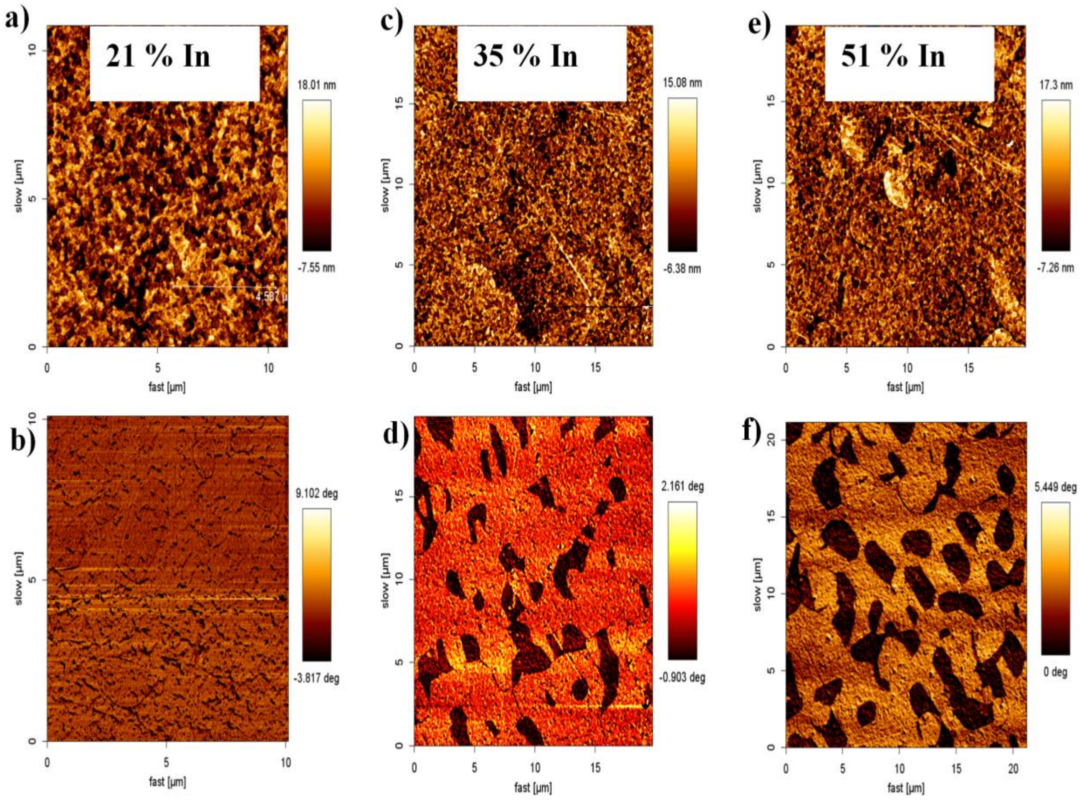

Figure 2.7: *a) Morphology and b) phase map of 21%, c) morphology and d) phase map of 35%, e) morphology and f) phase map of 51% indium alloy.*

The surface roughness map shows little variation between different alloys, however, the phase images show a significant modification. Small regions ~ 5-10 µm diameters can be consistently seen in the phase image of alloys with 35% and 51% indium (Figure 2.7). These regions do not show any correlation with topography or surface contact potential maps. The occurrence of such regions can be associated with the high indium content, which is likely to form indium rich regions. The small difference in tip-surface interaction for indium rich regions compared to that of the alloy as a whole can be easily picked in phase map. The presence of indium rich regions, at the surface, will result in a larger density of indium/polymer bond and hence a mechanically stronger contact.

The adhesion energy, which is defined as the minimum amount of energy per unit area required to separate the two surfaces in contact an infinite distance apart. The strength of adhesion (E_a) between a metal and polymer layer can be summed as,

$$E_a \propto \gamma_M + \gamma_p + \gamma_{MP} \tag{2.1}$$

Where, γ_M is the surface energy of metal, γ_p is the surface energy of polymer and γ_{MP} is interfacial energy between metal and polymer [21]. The term γ_{MP} is controlled by two factors: (i) nature of atomic/molecular bonding at the interface and (ii) the interfacial morphology. The physical nature of the bond between metal and polymer layer has been studied with respect to the overlap between atomic orbital of metal and molecular orbital of the polymer layer. Metals with a large number of vacant d-orbital like chromium and titanium are known to form strong metal-polymer bond [21, 22]. In the case of metals with a small number of free d-electrons like copper, the bond strength is weak, which is reflected in an island like deposition of metal and a small decrease in polymer carbonyl peak [21, 23]. The strength of the metal/polymer bond in metals with vacant p-orbital, like Al, is intermediate [21, 24, 25]. The indium belongs to the same group as Al, suggesting that the polymer/indium interface should have similar adhesion strength.

Apart from the metal-polymer bond, the interfacial microstructure plays a significant role in defining the strength of adhesion. The strength further amplifies with the increase in the amount of intermixing at the interface, which depends on the temperature of the interface. The higher melting point for indium-free alloys allows for higher intermixing. However, the increased diffusion does not help improve the adhesion due to the weak bond between the polymer and alloys. Due to the disordered nature of polymer semiconductors and lack of understanding of the lattice structure of alloy, a quantitative understanding of the adhesion has not been established. However, further qualitative insights are gained by probing the interfacial morphology of the delaminated films of alloy and underlying polymer surface.

The viscoelastic nature of the polymer and metal deformation energy, larger than the adhesion energy, makes it difficult to determine the adhesion energy accurately. Lateral elongation and peel test are generally used to estimate the adhesion energy; the elongation test can only be used for free-standing polymer films while the peel test is more suitable for polymer films coated on a stiff substrate like glass. Improved adhesion between alloy and polymer layer has been followed by peeling the alloy layer and probing the morphology of the surfaces, in contact, at the interface. Figure 2.8 shows the AFM surface topography and phase image of alloy and BHJ layer at the interface. The alloy electrode has a very low surface roughness (~ 2 nm) (Figure 2.8a), which is conformal with the surface roughness of BHJ layer. Phase image of the same region (Figure 2.8b) suggests a large variation in the material stiffness on and off the web-like network indicating that the web-like network is composed of the polymer layer. Thin layer of web-like network, visible on the alloy surface, has an average thickness of ~ 3nm and average feature size < 100 nm (Figure 2.8c) Along with the morphology, the W_F of the alloy surface also decreases by ~ 200 meV (Figure 2.8d) suggesting a surface modification of alloy by the polymer layer.

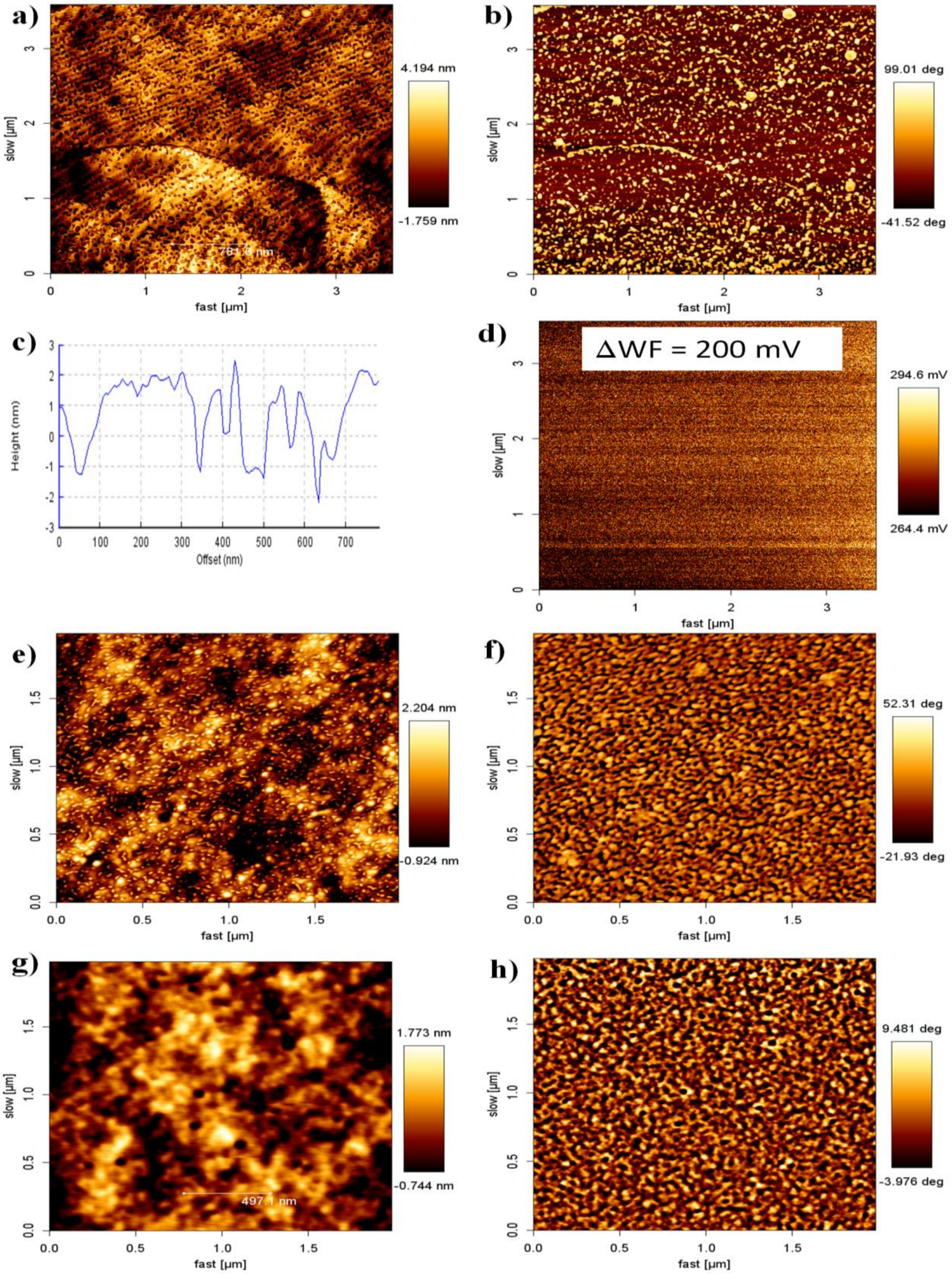

Figure 2.8: *a) Surface topography and b) phase map of peeled alloy surface, c) line scan showing the average thickness of polymer layer on alloy surface, d) surface*

contact potential map for alloy surface peeled from the working device. e) Topography and f) phase image of polymer surface below the alloy electrode. G) Surface roughness and h) phase for polymer layer outside the active area.

The polymer layer morphology, underneath the alloy electrode, is shown in Figure 2.8e, is a negative of alloy surface morphology. Small islands ~ 100 nm correlates well with the holes of similar dimension on alloy surface. The BHJ phase image shows a typical D-A separation, which is not correlated with the morphology (Figure 2.8f). The phase image map of fractured polymer layer represents sub-surface (~ 3 nm below the surface) D-A separation, which is expected to be unperturbed by the modifications introduced by the drying of the surface. The surface morphology and D-A separation for as spin coated BHJ layer are shown in Figure 2.8g and 2.8h. Delamination of alloy cathodes can also be used to probe the subsurface phase separation.

Above observations indicate that, upon peeling the alloy cathode, from the polymer layer, the fractures developed in polymer layer prior to the delamination of alloy/polymer interface. The intermolecular interaction within the polymer film is dominated by the π-π interaction of neighboring aromatic rings, which also defines the strength of interaction. Fracture in the polymer layer, before metal/polymer layer delimitation, suggests that the adhesion energy at the alloy/polymer layer is large when compared to the polymer π-π interaction energy. Similar adhesion strength is also expected at the metal/polymer interface of evaporated cathodes like Ag and Al, though; it is not obvious since the metal films are very thin (~ 200 nm). However, the importance of metal-polymer adhesion becomes evident in freestanding metal films which can peel off in the absence of sufficient adhesion strength. The improved adhesion is critical for printed electrodes as it ensures mechanical stability.

2.4.3: Light harvesting properties of indium alloys

2.4.3 I: Raman scattering of thin polymer films and charge-transfer state

Further understanding of the physical nature of the bond between polymer and alloy can be developed by using optical probes. Surface modified Raman spectroscopy measurements serves as a unique highly sensitive optical probe to study the charge transfer nature of bonds at the interface and the effect of the surface plasmon. Optical absorption techniques cannot be used in a meaningful way due to the opaque nature of the metal surface, making it difficult to separate the effects of absorption and total internal reflection. The alloy/BHJ interfaces were compared with standard metal electrodes like Ag, Au, and Al. Pristine and blend films were used to understand the optical activity of alloy surface and selective enhancement of polymer Raman. As the surface interactions are limited to few monolayers, a thin layer (~ 8-10 nm thickness) of pristine PBDTTT-C-T and PCBM-C70 was spin-coated on quartz substrates.

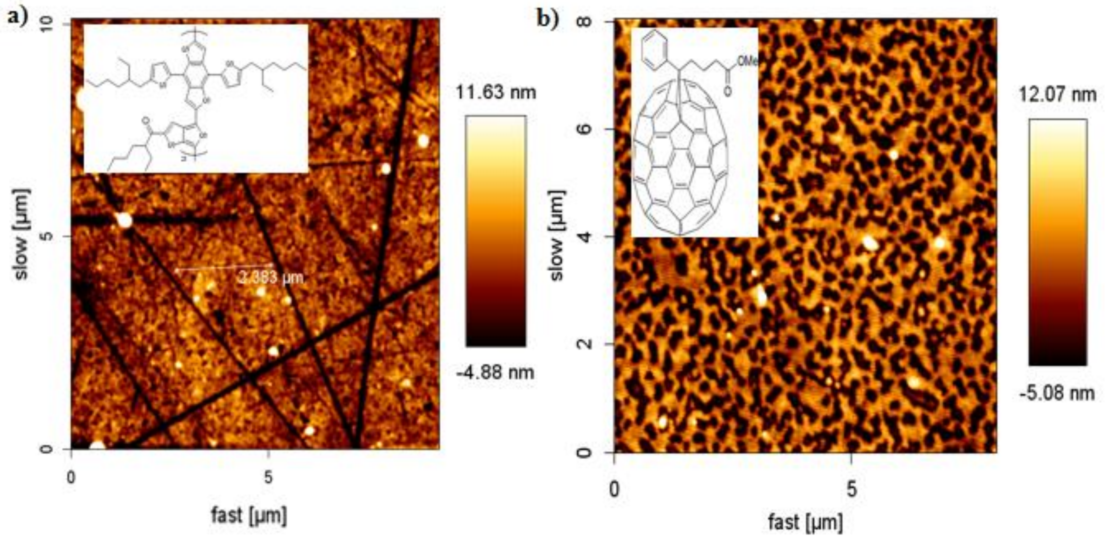

Figure 2.9: *Surface topography map of a) pristine PBDTTT-C-T and b) PCBM-C70, inset show the chemical structure.*

The AFM topography of pristine PBDTTT-C-T and PCBM-C70 shows high surface roughness, Figure 2.9a, and 2.9b respectively, the inset shows the chemical structure of the organic molecule. The Raman spectra for pristine PBDTTT-C-T films show asymmetric -C=C- stretching mode peak for thiophene rings at ~ 1472, 1508 and 1538 cm^{-1} as is shown by a black solid line in Figure 2.10a. With the Raman scattering, a strong fluorescence background is present, resulting from the finite absorption of PBDTTT-C-T at 532 nm excitation. An increase in the Raman cross-section of PBDTTT-C-T has been observed in presence of metal overlayers; the highest increase is seen for Al followed by Au and Ag.

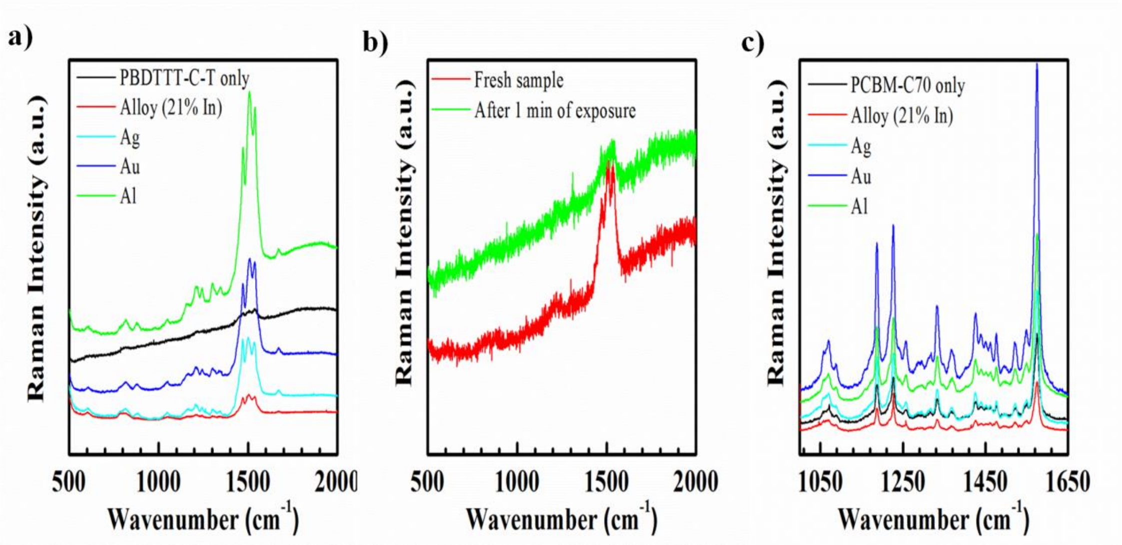

Figure 2.10: *Raman spectra for, a) pristine PBDTTT-C-T measured with a different metal electrode, the characteristic -C=C- peaks associated with thiophene rings at different positions have been marked. b) Raman spectra for PBDTTT-C-T measured without any metal contact, the two spectra were recorded with a delay of 1 min, c) Pristine PCBM-C70 measured with different metal electrodes.*

Large increase in Raman cross-section for Al can be related to larger cluster size formed due to rapid deposition during thermal evaporation of Al layer. However, in the case of alloy over-layer, the Raman cross-section decreases below the magnitude of the pristine film. The increase Raman cross-section could not be quantified due to the variable nature of Raman cross-section of pristine PBDTTT-C-T films (Figure 2.10b), when exposed to large excitation densities (~ 2.5 kW/cm^2), under ambient condition. This effect is suppressed considerably in presence of metal over-layer (Figure 2.10a). However, such observation is not new, donor polymers are well known to undergo rapid photo-oxidation under such large excitation densities. The decrease in Raman intensity was also seen for ~ 10 nm thick pristine PCBM-C70 films (Figure 2.10c); however, the Raman cross-section did not change significantly, over time, for PCBM-C70 films exposed to air. Origin of suppression in alloy electrode can be related purely to the local geometrical effects. During the cooling process of the alloy, the surface binds strongly with polymer layers, which along with high surface roughness of organic layer, can locally trap the Raman scattering, thereby reducing the out-coupled intensity.

In addition, the fluorescence background for PBDTTT-C-T gets suppressed significantly for alloy and Ag, while the level of suppression is less for Au and Al electrodes. The decrease in fluorescence is associated with the presence of metal-polymer charge-transfer (C-T) state (not a van-der-Waals interaction) at the metal/organic interface and a visual proof of chemical Raman enhancement [26-28]. These C-T states have also been highlighted as the possible mechanism for Raman enhancement in presence of metal electrodes like Ag, the enhancement gets suppressed by introducing a less active, monolayer thick Pb [29, 30]. The fluorescence quenching, equivalent to that of the Ag electrode, observed in alloy electrodes, suggests that the alloy surface can host a similar level of C-T states. The high density of C-T state at polymer/ alloy interface can also be related to improved energy of adhesion.

2.4.3 II: Chemical enhancement of Raman scattering in BHJ films

The Raman scattering in the blend of PBDTTT-C-T and PCBM-C70 show a significant increase in the presence of metal over-layer (Figure 2.11a), the level of increase changes significantly with different metal layers. The fluorescence of PBDTTT-C-T is completely quenched (~ 100%) in presence of PCBM-C70, resulting in no visible fluorescence background. Increases in Raman cross-section in the presence of metal over-layer have been frequently reported for metals like Ag and Au [31, 32]. The magnitude of enhancement observed for PBDTTT-C-T in the presence of alloy is similar to that of conventional metal electrodes, which suggests that a similar mechanism is active at the alloy/polymer interface. The increase in Raman cross-section is highest for Al, which again can be related to larger metal clusters formed during evaporation and the associated plasmonic nature of Al [33, 34].

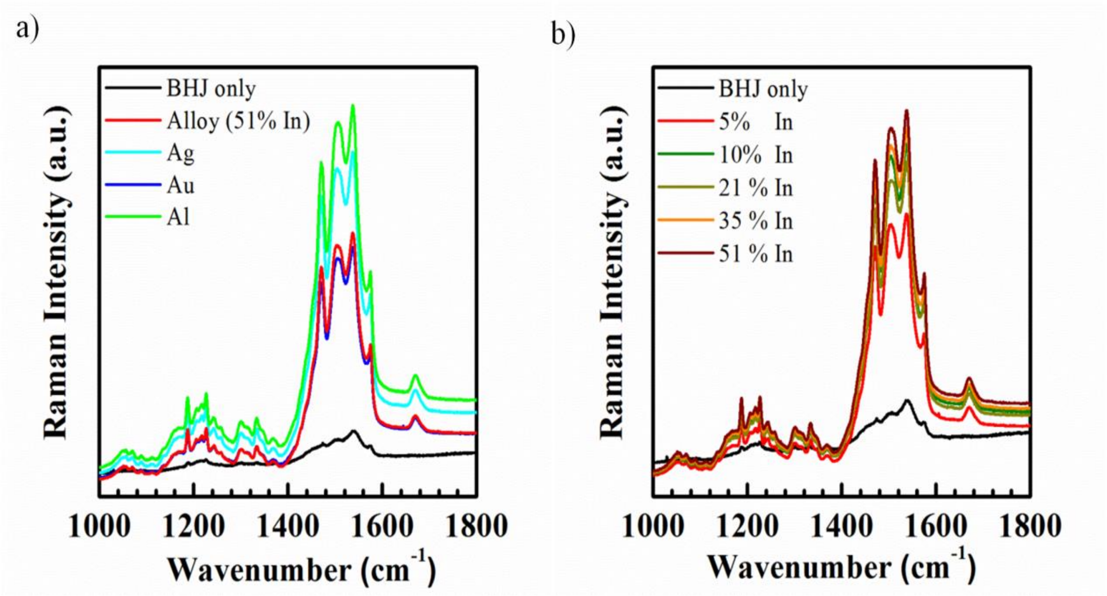

Figure 2.11: *Raman spectra measured for PBDTTT-C-T: PCBM-C70 BHJ with, a) Different metal electrodes and b) alloy with varying concentration of indium.*

Enhancement observed for flat Ag films is comparable to that of Al, which is linked to the large density of C-T state and the surface plasmon. The level of enhancement is comparable for Au and alloys, though Au is a better plasmonic substrate than the alloy; the enhancement is weak for Au, as the 532 nm excitation is off-resonance for Au. The Raman scattering cross-section improves with increasing ratio of indium in the alloy, as can be seen in Figure 6b. Scattering cross-section increases 1.5 times for 51% indium compared to that in 5% indium alloy.

A new mode is visible in the Raman spectra of PBDTTT-C-T at 1675 cm^{-1} for all metal electrodes, which represents a metal-polymer bond. The increase in PBDTTT-C-T Raman cross-section higher than that of PCBM-C70 suggests a better coupling of energy from alloy to D molecule. Above results indicate that the indium imparts the optical activity to the alloy. The increase in optical activity with higher wt % of indium is associated with an increase in the density of C-T state, which also gets reflected in the improvement of adhesion energy.

A possible mechanism by which the Raman scattering cross-section can increase has been shown in Figure 2.12. Other than resonance enhancement (Figure 2.12a), Raman scattering can also be enhanced by two possible mechanisms, namely by chemical enhancement (Figure 2.12b) and plasmon resonance enhancement (Figure 2.12c). Chemical enhancement results from the bonding at the metal/adsorbate interface which controls the density of C-T states at the interface. Also, known as first layer effect, it may lead to the formation of the surface-adsorbate complex. Charge transfer from metal to adsorbed molecule mimics the process of resonance Raman, thereby increasing the scattering cross section. In a chemical enhancement process, a photon is absorbed by the metal, this results in the ejection of the hot electron. Excited hot electron gets transferred into the organic LUMO, which when decays, emits stokes photon. The metallic surface does not require any nanostructure for this process and the scattering enhancement is ~ 10-100 times. Plasmon resonance enhancement requires formation of nanostructures for amplifying the electric field in the near vicinity of the molecule. Under plasmonic induced electromagnetic enhancement, the Raman scattering can be easily enhanced by ~ 10^6-10^7 times.

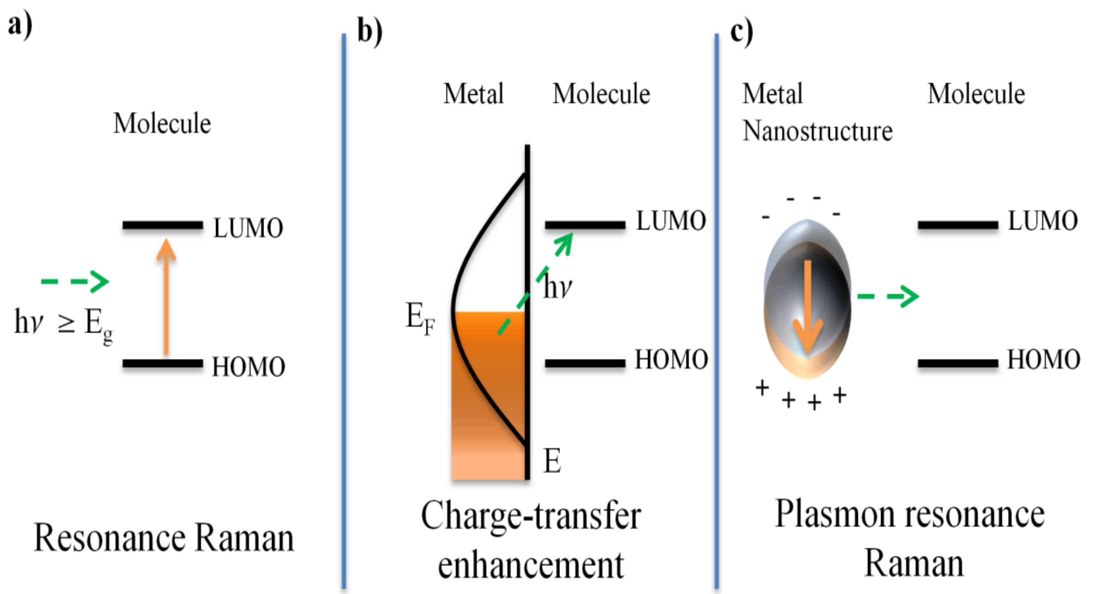

Figure 2.12: Schematic representation of possible enhancement mechanisms in SERS, a) resonance Raman, b) plasmon enhancement, c) chemical enhancement.

2.4.3 III: Plasmon enhanced SERS in PEDOT: PSS

Raman scattering cross-section of BHJ layer show an increase which is indicative of chemical enhancement and the scattering intensity increases by 6-8 times. However, a larger enhancement was recorded in the case of PEDOT: PSS layer, which is also used as a hole transporter in organic BHJ solar cells. The Raman scattering intensity of -C=C- stretching mode in thiophene ring shows ~ 10^4 - 10^5 times enhancement for multiple electrodes (Figure 2.13a).

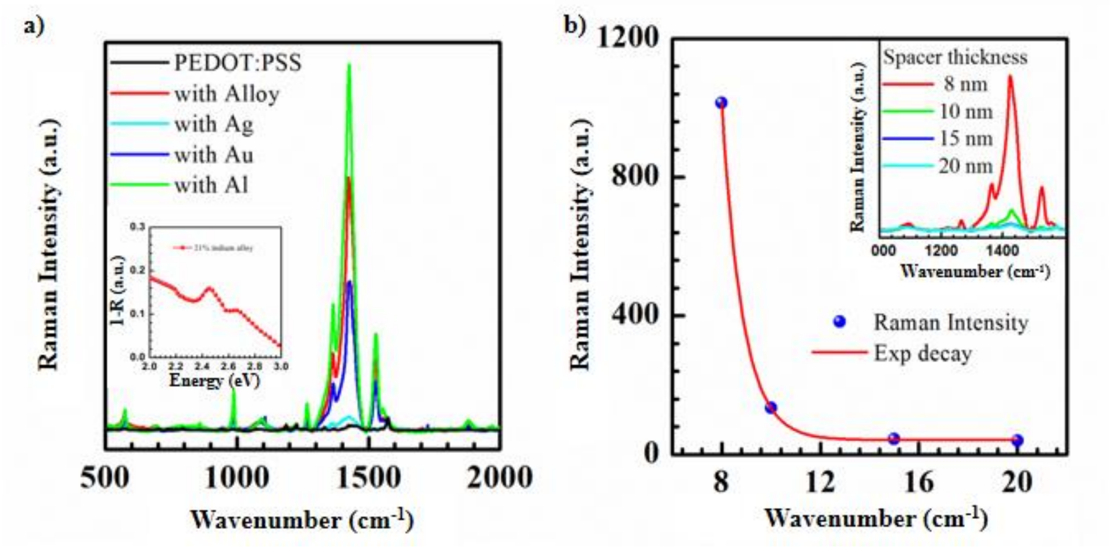

***Figure 2.13**: SERS spectra measured in PEDOT: PSS film, a) SERS in presence of different metal electrodes, the inset shows the alloy reflectance, b) SERS intensity as a function of the spacing between metal and PEDOT: PSS.*

Large increase in Raman cross-section suggests that the surface plasmon is active at the alloy surface [35] and in the presence of suitable nanostructures plasmon induced electromagnetic SERS can be easily realized. This is particularly useful for light harvesting in inverted OPV structure where derivatives of PEDOT is used as hole only transport layer for back contact [36, 37]. A thin layer of BHJ, coated between metal and PEDOT: PSS, can act both as a spacer and a roughness inducing medium. The roughness of ultra-thin BHJ layer (~ 10 nm) is higher than that in thick films (~ 1 - 2 nm), used in devices. Rough spacer layer helps in creating the nanostructure which can act as active dipole and enhance the EM field locally. Higher scattering cross-section in the case of Al can be related to the added effect of larger nanostructures formed during evaporation.

The Raman scattering cross-section for alloy shows higher enhancement compared to that of Au and Ag, which can be associated with the selective chemical interaction between metal/PEDOT: PSS. The Raman scattering does not show any improvement in presence of Ag metal, however, the PEDOT: PSS Raman signatures have been shown to improve in presence of Ag nanoparticle [38, 39]. The scattering cross-section decreases exponentially as the alloy metal surface is moved away from the PEDOT: PSS layer using a dielectric spacer (Figure 2.13b). Exponential decay of Raman scattering with an increase in spacer thickness is a strongly indicative of the EM origin of enhancement. The plasmon absorption is visible in the reflection spectra of alloy which has a significant overlap with the excitation energy ~ 2.33 eV (inset of Figure 2.13a).

2.4.4: Electrical characteristics of Alloy/polymer interface

2.4.4 I: Current-voltage characteristics

The electrical characteristic of alloy cathode is identical to that of thermally evaporated cathode like Al. The J-V response measured under dark, with alloys as a cathode, matches well with that of thermally evaporated Al electrode, as seen in Figure 2.14. The electrical properties of indium-free alloys could not be tested, due to the lack of adhesion. The dark I-V curves have been modeled using equation 2.2,

$$I = I_0 \left\{ exp\left(\frac{q(V - IR_s)}{nk_B T} \right) \right\} + \frac{(V - IR_s)}{R_{sh}} \qquad 2.2$$

where *n* is the diode ideality factor and *Rs* and *Rsh* represent series and shunt resistance respectively. A detailed analysis of the dependence on R_s, R_{sh}, and n is presented in Appendix I. The adhesion between the alloy and polymer layer allows enhanced mechanical stability and efficient electrical contact similar to that of Al. Thus the J-V characteristics of OPVs with alloy can be simulated using Shockley equation (equation1) without requiring any additional series resistance correction for adhesion.

The value of *n* is ~ 1.75 for all alloys and the Al cathode, a small difference in the forward current for different cathode can arise from a combination of R_S and *Rsh*, where R_{sh} has a larger influence on the magnitude of J. The similarity between the J-V characteristics of alloy and thermally evaporated Al suggests good interface quality and minimizing of transport losses. Better performance observed in the case of alloys with indium can be attributed to the thin oxide layer (~ 1-2 nm) formed at the interface during deposition [14]. Thin oxide interfacial layer, can function as a buffer layer, which improves the selective charge extraction and suppresses recombination losses, thereby reducing the number of steps in processing.

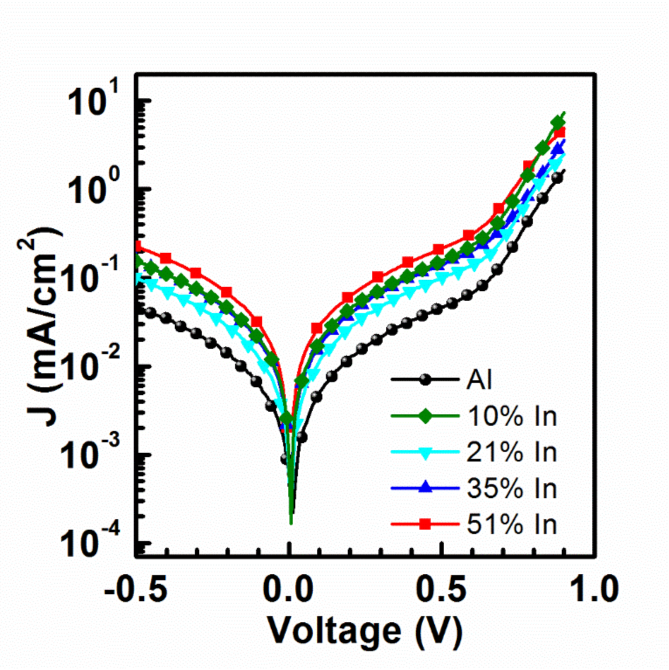

Figure 2.14: *Dark J-V curve for different metal cathodes.*

The R_{Sh} for alloy cathode is comparable to that of thermally evaporated Al. Low R_{Sh} is a signature of manufacturing defects, which can cause charge leakage pathways and reduce the performance of a PV cell. Origin of these defects can be traced to the manual fabrication process of alloy cathode, where the puncturing the polymer layer is very likely. However, quality of alloy cathode being comparable to that of Al suggests that the alloy conforms well to the underlying surface and does not form shorts or pinholes. The electrical characteristics of diodes with different alloys as a cathode are comparable; Variation between different alloy cathodes is within the device statistics. Above analysis supports the argument that a small quantity of indium can significantly improve the charge injection property, by improving adhesion.

2.4.4 II: Impedance and capacitance-voltage spectroscopy

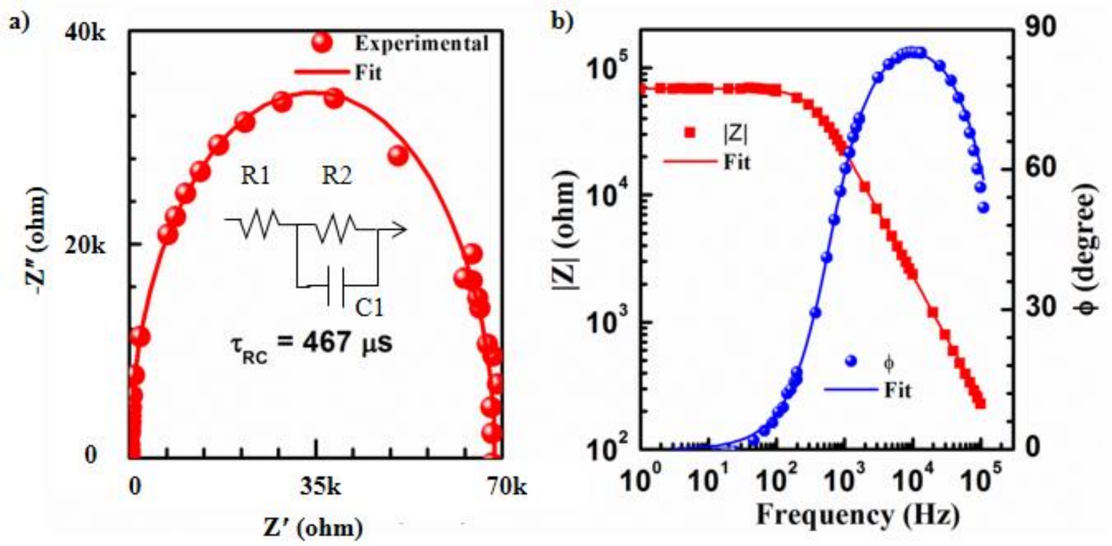

Figure 2.15: *a) Cole-Cole plot showing single RC nature of the device, the inset shows the equivalent circuit diagram, b) Typical impedance and phase response of BHJ solar cell.*

Small signal impedance was measured at short circuit ($V_{DC} = 0$) under no light illumination. The impedance curves were fitted using Zview impedance modeling software (Scribner Associates). The impedance cole-cole plot is a single semi-circle (Figure 2.15a) for Al as well as alloy cathode, which is representative of a single RC circuit. The impedance response was simulated using an RC circuit with an additional resistance (*R1*) (Figure 2.15a) which can be viewed as R_S. The trend in series resistance is consistent with the trend observed for R1. Typical impedance and phase behavior of a BHJ device as a function of frequency is shown in Figure 2.15b. The circuit parameters derived from model fit are summarized in table 1. The RC time constant for different cathodes are in the range of 50-400 μs. From the impedance plot, it can be inferred that the alloy electrode processed under ambient conditions have a low density of traps at the interfaces. Additionally, the thin oxide layer has no influence on the series resistance value, which is significantly lower for alloy cathodes.

Table 2.1: Impedance parameter fit for a solar cell with different cathodes.

Cathode	R1 (Ω)	R2 (KΩ)	C1 (nF)	τ (μs)
Aluminum	370±10	52.5±0.5	3.0±0.01	155±5
21% alloy	230±10	44.5±0.5	6.4±0.01	280±5
35% alloy	160±10	53.0±0.5	6.2±0.01	220±5
51% alloy	180±10	9.0±0.5	6.0±0.01	57±5

Capacitance-Voltage measurements

The capacitance-voltage plot for BHJ system shows a characteristic peak in the positive voltage region as is shown in Figure 2.16. Origin of this peak has been associated with the presence of built-in voltage in the device [40, 41]. The region below the peak voltage represents a diffusion limited transport, while the transport above the peak voltage it is drift mediated.

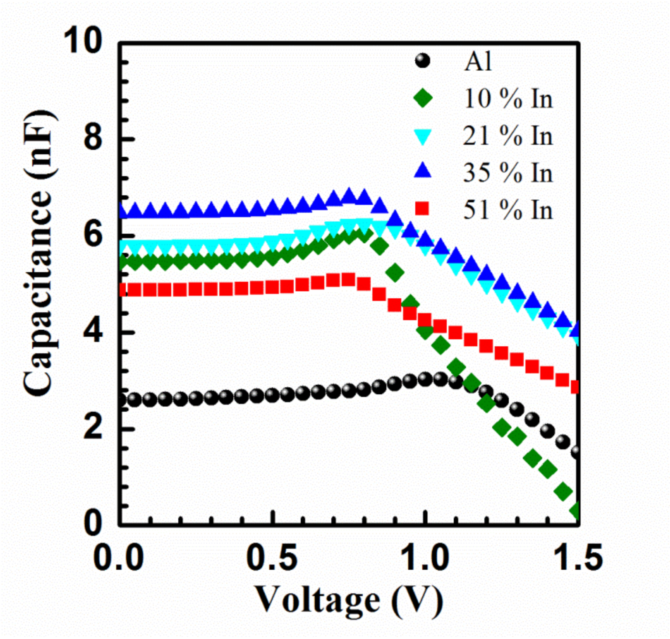

Figure 2.16: *Capacitance-voltage plot for PV cells with different metal cathodes.*

The built-in voltage has a significant dependence on the W_F difference between anode and cathode. Capacitance peak for Al devices is higher (ΔV ~ 0.25 V) than that for the devices with alloy cathodes. PV cells were composed of the identical layers with similar thicknesses, while the cathode layer was varied. Modification in the peak capacitance voltage, by replacing the Al cathode with alloy can be understood with respect to the difference in the W_F of alloys and Al. The W_F of Al is ~ 4.07 eV, a lower capacitance peak voltage for alloy indicates that the alloy W_F is 4.3 ± 0.3 eV, which matches very well with the values derived from KPFM and UPS plot.

2.4.5 Charge collection efficiency of Indium based alloys

2.4.5 I: Power conversion efficiency

Charge collection efficiency of the alloy is superior to that of Al cathode. The representative light J-V curves for Al and different alloy cathode is shown in Figure 2.17a.

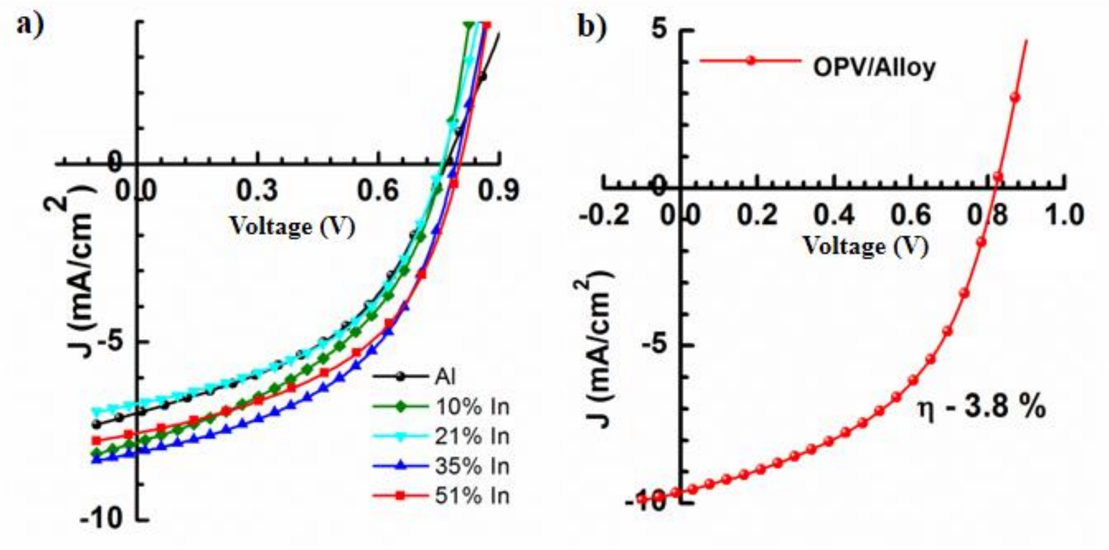

Figure 2.17: *a) Light J-V curve for PBDTTT-C-T: PCBM-C70 with Al and alloy with varying indium content, b) J-V curved for best OPV device with alloy cathode.*

The variations in V_{OC} for different cathodes are within the device statistics. Fill factor for alloy cathode is higher than that of Al, which arises from the improved collection efficiency of the alloy, owing to the thin oxide layer [9, 42]. While the J_{SC} and V_{OC} remain comparable. High fill factor contributes towards the higher efficiency for the alloy cathodes. Best efficiencies achieved in alloy based solar cells are only limited by the active layer material. Under optimized conditions (without additives), best device efficiencies achieved with alloy electrode in BHJ architecture was ~ 3.8% (Figure 2.17b). Efficiencies ~ 6% has been demonstrated in the previous report from our laboratory by using performance enhancing additives like di-iodooctane [15]. Performance variation and device statistics, in light J-V characteristics, is shown in table 2.2, parameters, averaged over ~ 10 devices have also been plotted in Figure 2.18 for ease of viewing. The average performance of 35% indium alloy is superior to that of other wt % alloys. Better performance can be related to relatively low melting temperature (~ 60 ^{o}C), which ensures fewer defects during manufacturing and a larger indium content which improves adhesion and charge collection.

Table 2.2: Light J-V parameters for PBDTTT-C-T: PCBM-C70 OPV with different metal cathodes.

Cathode	V_{OC} (V)	J_{Sc} (mA/cm^2)	FF (%)	PCE (%)	R at V_{OC} (Ω□)	R at J_{SC} (Ω□)
Al	0.74 ± 0.03	6.5 ± 0.4	41 ± 3	2.0 ± 0.2 **Best Efficiency** **BHJ - 2.36%^{a}**	50 ± 10	300 ± 50
10% In	0.76 ± 0.01	6.5 ± 0.9	43 ± 2	2.2 ± 0.4 **Best Efficiency** **BHJ - 2.57 %^{a}**	24 ±7	350 ± 60
21% In	0.74 ± 0.01	6.2 ± 0.8	46 ± 5	2.1 ± 0.5 **Best efficiency** **BHJ 3.8%^{b}** **OIP 7%**	31± 6	500± 100
35% In	0.75 ± 0.04	7.2 ± 0.5	46 ± 3	2.5 ± 0.4 **Best efficiency** **BHJ - 3.4%^{b}**	24 ±2	400 ± 100
51% In	0.72 ± 0.06	6.6 ± 0.6	42 ± 4	2.1 ± 0.5 **Best Efficiency** **BHJ - 2.9%^{a}**	36 ± 9	320 ± 70
a - 75 nm BHJ thickness, b - 120 nm BHJ thickness						

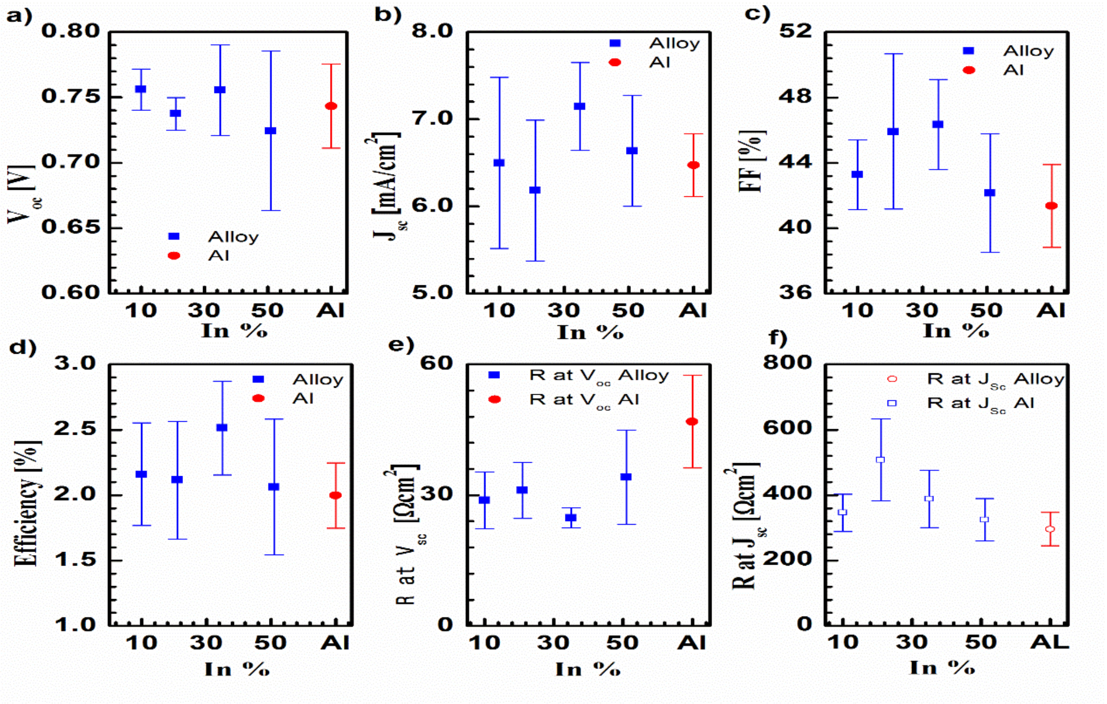

Figure 2.18: *Variation in light J-V characteristics for different metal cathodes in a) V_{OC}, b) J_{SC}, c) FF, d) PCE, e) R at V_{OC} and f) R at J_{SC}.*

2.4.5 II: Spectral photocurrent response ($I_{ph}(E)$)

Optical activity of alloy surface can be verified by using $I_{ph}(E)$ as a function of indium and the thickness of BHJ layer. Absolute and normalized EQE response for PVs with different cathodes is shown in Figure 2.19a and 2.19b respectively.

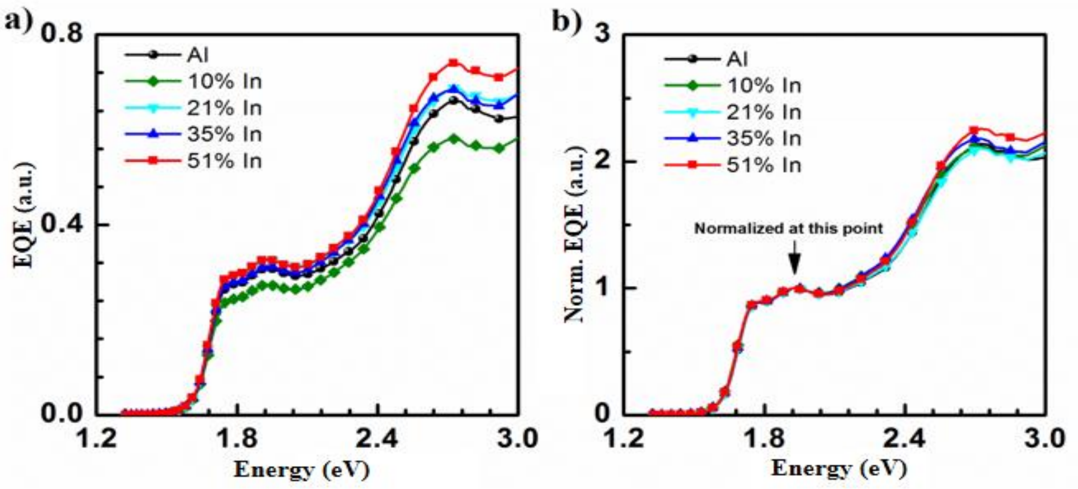

Figure 2.19: *a) absolute EQE and b) normalized EQE with the different cathode.*

The normalized EQE response shows a relative increase (~ 5-10%) at ~ 2.5 eV for 35% and 51% alloy while it remains similar to that of Al for 21% and 10% alloys. This observable increase in EQE can be attributed to the absorption contribution from alloy surface. Given that the optical improvements associated with the back metal layer are limited to only a few monolayers in the vicinity of polymer/alloy surface, the relative increase is significant. This observation is also consistent with the occurrence of indium rich regions in the phase image of 35% and 51% alloys.

The interfacial effects are further amplified by restricting the $I_{ph}(E)$ response from the BHJ bulk, by reducing the active layer thickness. Figure 2.20 shows the normalized EQE response for PV with alloy cathode at different BHJ thicknesses. As has been highlighted in Figure 2.20a, the sub-band gap EQE response shows a small shift (~ 0.025 eV) in peak position from that of D-AC-T state (~ 1.45 eV).

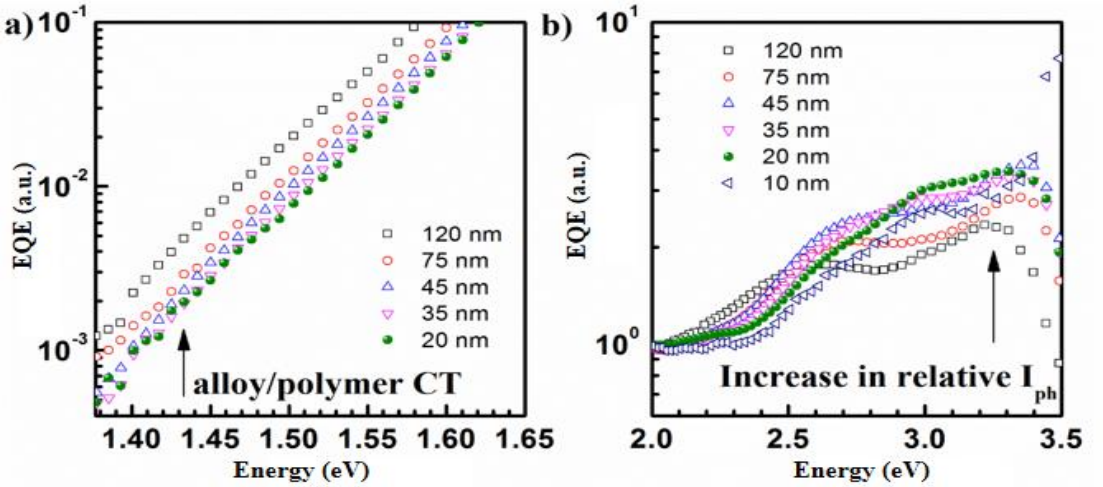

Figure 2.20: *Normalized EQE response for 21% indium alloy, a) near the band edge, b) at the alloy absorption.*

This shift can be related to the significant contribution from the metal/polymer C-T state present at the polymer/ alloy interface. However, the change in EQE is very small as the effect is only limited to a monolayer at the interface. The high energy region of the normalized EQE response is shown in Figure 2.20b. As the thickness of BHJ is reduced, the relative contribution from the interface increases, which can be viewed as a corresponding increase in the spectral feature of the EQE response between 2.5 - 3.0 eV. These changes observed in normalized EQE response are not similar to the effects originating purely from thickness variation [43, 44].

2.4.5 III: Large area photocurrent mapping

The ability of the alloy cathodes to form soft and conformal contact with polymer surface can be visualized better in the large area photocurrent maps. Soft contact with the active layer allows for a uniform, leakage free cathode layer. A uniform photocurrent response is visible across the electrode region as shown in Figure 2.21a and 2.21b.

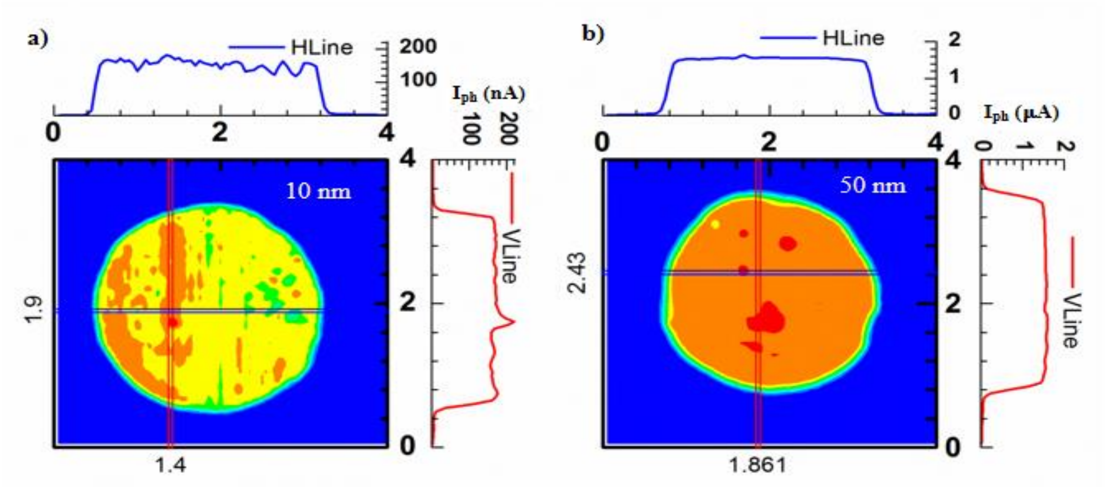

Figure 2.21: *Large are photocurrent map of OPV with alloy cathode, a) 10 nm thick BHJ layer and b) 60 nm thick BHJ layer.*

Homogeneous photocurrent response was observed for thin BHJ layer (~ 10 nm), which improves further with an increase in BHJ layer thickness (Figure 2.21a), uniform I_{Ph} response across the active area is essential for maximizing the efficiency.

2.4.6: Instability induced patterning in meltable alloys

Liquid alloys show cohesive behavior similar to that of a mercury droplet. Under suitable drying conditions the surface of the alloy, at the alloy/polymer interface, show formation of a regularly spaced circular pattern (diameter ~ 10 µm). Origin of these features can be related to surface instability present at alloy surface and high surface energy at the polymer surface. Such effects result in the self-patterning of alloy drops at µm scale on alloy/polymer interface, as is shown in Figure 2.22a. These structures are particularly useful for diffusing the reflected light at random angle inside the polymer layer [45-47]. Diffused reflection can result in increased path length for photons reflected in the polymer layer, resulting in increased absorption of reflected photons and hence improving the EQE.

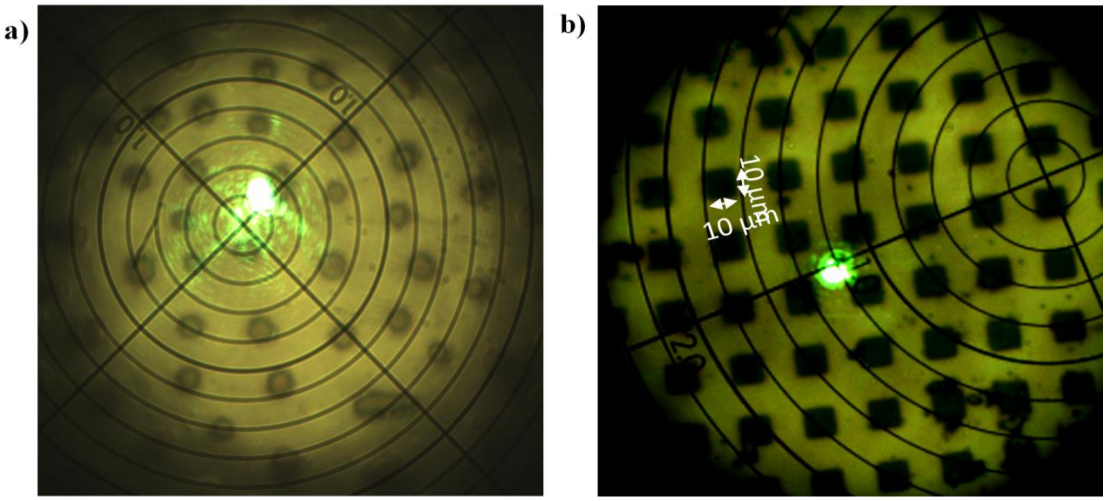

Figure 2.22: *a) Instability induced self-patterning of alloy droplets at the alloy/polymer interface, b) image of a calibration disk captured at same magnification; each square is of 10 µm × 10 µm area.*

2.5: Conclusions

In summary, the eutectic solder alloys provide a viable option as electrodes for printable electronics applications. It is observed that the indium present in the quaternary alloy plays a decisive role, in the perspective of thermal, mechanical and electronic aspect. Indium is instrumental in lowering the melting point and improving the adhesion of alloy, which is essential for easy fabrication and efficient charge transport. The optical activity of alloy surface also shows improvement with an increase in indium content, which is beneficial for light concentration at the reflective back surface. Improvements in optical activity are also translated into photocurrent improvements in BHJ solar cell. The work function of the alloy is well suited for the role of electron collection while being less susceptible to degradation related to rapid oxidation, as is seen in Al cathodes. The electrical purity of alloy/polymer interface fabricated in ambient is at par with thermally evaporated Al cathodes, providing a facile route for vacuum-free device fabrication. The ability to locally melt at moderate temperatures is beneficial for properties like self-healing of cracks, making them more desirable than traditional metal inks.

References

[1] J. D. Chen, C. H. Cui, Y. Q. Li, L. Zhou, Q. D. Ou, C. Li, Y. F. Li and J. X. Tang. Single-Junction Polymer Solar Cells Exceeding 10% Power Conversion Efficiency. *Advanced Materials* **2015,** *27*, 1035-1041.

[2] Y. S. Liu, C. C. Chen, Z. R. Hong, J. Gao, Y. Yang, H. P. Zhou, L. T. Dou, G. Li and Y. Yang. Solution-Processed Small-Molecule Solar Cells: Breaking the 10% Power Conversion Efficiency. *Scientific Reports* **2013,** *3*, 3356.

[3] W. S. Yang, J. H. Noh, N. J. Jeon, Y. C. Kim, S. Ryu, J. Seo and S. I. Seok. High-Performance Photovoltaic Perovskite Layers Fabricated through Intramolecular Exchange. *Science* **2015,** *348*, 1234-1237.

[4] H. P. Zhou, Q. Chen, G. Li, S. Luo, T. B. Song, H. S. Duan, Z. R. Hong, J. B. You, Y. S. Liu and Y. Yang. Interface Engineering of Highly Efficient Perovskite Solar Cells. *Science* **2014,** *345*, 542-546.

[5] F. C. Krebs. Fabrication and Processing of Polymer Solar Cells: A Review of Printing and Coating Techniques. *Solar Energy Materials and Solar Cells* **2009,** *93*, 394-412.

[6] F. C. Krebs. Polymer Solar Cell Modules Prepared Using Roll-to-Roll Methods: Knife-over-Edge Coating, Slot-Die Coating and Screen Printing. *Solar Energy Materials and Solar Cells* **2009,** *93*, 465-475.

[7] G. Schubert, F. Huster and P. Fath. Physical Understanding of Printed Thick-Film Front Contacts of Crystalline Si Solar Cells- Review of Existing Models and Recent Developments. *Solar Energy Materials and Solar Cells* **2006,** *90*, 3399-3406.

[8] S. Gatz, T. Dullweber and R. Brendel. Evaluation of Series Resistance Losses in Screen-Printed Solar Cells with Local Rear Contacts. *Ieee Journal of Photovoltaics* **2011,** *1*, 37-42.

[9] L. Yan, Y. X. Song, Y. Zhou, B. Song and Y. F. Li. Effect of Pei Cathode Interlayer on Work Function and Interface Resistance of Ito Electrode in the Inverted Polymer Solar Cells. *Organic Electronics* **2015,** *17*, 94-101.

[10] D. R. Frear. The Mechanical Behavior of Interconnect Materials for Electronic Packaging. *Jom-Journal of the Minerals Metals & Materials Society* **1996,** *48*, 49-53.

[11] J. Glazer. Metallurgy of Low-Temperature Pb-Free Solders for Electronic Assembly. *International Materials Reviews* **1995,** *40*, 65-93.

[12] R. C. Chiechi, E. A. Weiss, M. D. Dickey and G. M. Whitesides. Eutectic Gallium-Indium (Egain): A Moldable Liquid Metal for Electrical Characterization of Self-Assembled Monolayers. *Angewandte Chemie-International Edition* **2008,** *47*, 142-144.

[13] A. Tabatabai, A. Fassler, C. Usiak and C. Majidi. Liquid-Phase Gallium-Indium Alloy Electronics with Microcontact Printing. *Langmuir* **2013,** *29*, 6194-6200.

[14] M. Bag, D. Gupta, N. Arun and K. S. Narayan. Deformation of Metallic Liquid Drop by Electric Field for Contacts in Molecular-Organic Electronics. *Proceedings of the Royal Society a-Mathematical Physical and Engineering Sciences* **2009,** *465*, 1799-1808.

[15] A. J. Das and K. S. Narayan. Retention of Power Conversion Efficiency – from Small Area to Large Area Polymer Solar Cells. *Advanced Materials* **2013,** *25*, 2193-2199.

[16] P. Kumar, B. Zhao, R. H. Friend, A. Sadhanala and K. S. Narayan. Kinetic Control of Perovskite Thin-Film Morphology and Application in Printable Light-Emitting Diodes. *ACS Energy Letters* **2017,** *2*, 81-87.

[17] J. Baek, J. Lee, M. Joo, D. Han, H. Kim, H. Seong, J. Lee, J. Kim, S. Yoo, S. Jeon and S. G. Im. Tuning the Electrode Work Function Via a Vapor-Phase Deposited Ultrathin Polymer Film. *Journal of Materials Chemistry C* **2016,** *4*, 831-839.

[18] G. Jo, S. I. Na, S. H. Oh, S. Lee, T. S. Kim, G. Wang, M. Choe, W. Park, J. Yoon, D. Y. Kim, Y. H. Kahng and T. Lee. Tuning of a Graphene-Electrode Work Function to Enhance the Efficiency of Organic Bulk Heterojunction Photovoltaic Cells with an Inverted Structure. *Applied Physics Letters* **2010,** *97*, 213301.

[19] B. Ebenhoch, S. A. J. Thomson, K. Genevicius, G. Juska and I. D. W. Samuel. Charge Carrier Mobility of the Organic Photovoltaic Materials Ptb7 and Pc71bm and Its Influence on Device Performance. *Organic Electronics* **2015,** *22*, 62-68.

[20] G. V. P. Kumar and C. Narayana. Adapting a Fluorescence Microscope to Perform Surface Enhanced Raman Spectroscopy. *Current Science* **2007,** *93*, 778-781.

[21] P. S. Ho, R. Haight, R. C. White, B. D. Silverman and F. Faupel. Chemistry, Microstructure, and Adhesion of Metal—Polymer Interfaces. In *Fundamentals of Adhesion*, L.-H. Lee, Ed. Springer US: Boston, MA, 1991; pp 383-406.

[22] N. J. Chou and C. H. Tang. Interfacial Reaction During Metallization of Cured Polyimide: An Xps Study. *Journal of Vacuum Science & Technology A: Vacuum, Surfaces, and Films* **1984,** *2*, 751-755.

[23] R. C. White, R. Haight, B. D. Silverman and P. S. Ho. Cr-Polyimide and Cu-Polyimide Interface - Chemistry and Structure. *Applied Physics Letters* **1987,** *51*, 481-483.

[24] P. O. Hahn J. W. Bartha, F. LeGoues, and P. S. Ho. Photoemission Spectroscopy Study of Aluminum–Polyimide Interface. *Journal of Vacuum Science & Technology A: Vacuum, Surfaces, and Films* **1985,** *3*, 1390-1393.

[25] S. G. Anderson Lj. Atanasoska, H. M. Meyer III, Zhangda Lin, and J. H. Weaver. Aluminum/Polyimide Interface Formation: An X-Ray Photoelectron Spectroscopy Study of Selective Chemical Bonding. *Journal of Vacuum Science & Technology A: Vacuum, Surfaces, and Films* **1987,** *5*, 3325-3333.

[26] E. L. Ru and P. Etchegoin. *Principles of Surface-Enhanced Raman Spectroscopy*. Elsevier Science: Great Britain 2009.

[27] S. K. Ghosh, A. Pal, S. Kundu, S. Nath and T. Pal. Fluorescence Quenching of 1-Methylaminopyrene near Gold Nanoparticles: Size Regime Dependence of the Small Metallic Particles. *Chemical Physics Letters* **2004,** *395*, 366-372.

[28] T. Pal, N. R. Jana and T. Sau. Nanoparticle Induced Fluorescence Quenching. *Radiation Physics and Chemistry* **1997,** *49*, 127-130.

[29] M. Fleischmann and Z. Q. Tian. The Effects of the Underpotential and Overpotential Deposition of Lead and Thallium on Silver on the Raman-Spectra of Adsorbates. *Journal of Electroanalytical Chemistry* **1987,** *217*, 385-395.

[30] L. W. H. Leung and M. J. Weaver. Extending the Metal Interface Generality of Surface-Enhanced Raman-Spectroscopy - Underpotential Deposited Layers of Mercury, Thallium, and Lead on Gold Electrodes. *Journal of Electroanalytical Chemistry* **1987,** *217*, 367-384.

[31] D. Adil and S. Guha. Surface-Enhanced Raman Spectroscopic Studies of the Au-Pentacene Interface: A Combined Experimental and Theoretical Investigation. *Journal of Chemical Physics* **2013,** *139*, 044715.

[32] D. Adil and S. Guha. Surface-Enhanced Raman Spectroscopic Studies of Metal-Semiconductor Interfaces in Organic Field-Effect Transistors. *Journal of Physical Chemistry C* **2012,** *116*, 12779-12785.

[33] Y. Ekinci, H. H. Solak and J. F. Loffler. Plasmon Resonances of Aluminum Nanoparticles and Nanorods. *Journal of Applied Physics* **2008,** *104*, 083107.

[34] Q. Hao, C. X. Wang, H. Huang, W. Li, D. Y. Du, D. Han, T. Qiu and P. K. Chu. Aluminum Plasmonic Photocatalysis. *Scientific Reports* **2015,** *5*, 15288.

[35] M. G. Blaber, M. D. Arnold and M. J. Ford. A Review of the Optical Properties of Alloys and Intermetallics for Plasmonics. *Journal of Physics: Condensed Matter* **2010,** *22*, 143201.

[36] J. Weickert, H. Y. Sun, C. Palumbiny, H. C. Hesse and L. Schmidt-Mende. Spray-Deposited PEDOT:PSS for Inverted Organic Solar Cells. *Solar Energy Materials and Solar Cells* **2010,** *94*, 2371-2374.

[37] L. Z. Zhu, B. J. Richardson and Q. M. Yu. Inverted Hybrid CdSe-Polymer Solar Cells Adopting PEDOT:PSS/MoO3 as Dual Hole Transport Layers. *Physical Chemistry Chemical Physics* **2016,** *18*, 3463-3471.

[38] M. Stavytska-Barba and A. M. Kelley. Surface-Enhanced Raman Study of the Interaction of PEDOT:PSS with Plasmonically Active Nanoparticles. *Journal of Physical Chemistry C* **2010,** *114*, 6822-6830.

[39] M. Stavytska-Barba and A. M. Kelley. Surface Enhanced Raman Study of the Interaction of PEDOT:PSS with Silver and Gold Nanoparticles. *2010 Conference on Lasers and Electro-Optics (Cleo) and Quantum Electronics and Laser Science Conference (Qels)* **2010**.

[40] M. Eck, C. Van Pham, S. Zufle, M. Neukom, M. Sessler, D. Scheunemann, E. Erdem, S. Weber, H. Borchert, B. Ruhstaller and M. Kruger. Improved Efficiency of Bulk Heterojunction Hybrid Solar Cells by Utilizing CdSe Quantum Dot-Graphene Nanocomposites. *Physical Chemistry Chemical Physics* **2014,** *16*, 12251-12260.

[41] S. L. M. van Mensfoort and R. Coehoorn. Determination of Injection Barriers in Organic Semiconductor Devices from Capacitance Measurements. *Physical Review Letters* **2008,** *100*.

[42] R. Po, C. Carbonera, A. Bernardi and N. Camaioni. The Role of Buffer Layers in Polymer Solar Cells. *Energy & Environmental Science* **2011,** *4*, 285-310.

[43] Y. M. Nam, J. Huh and W. H. Jo. Optimization of Thickness and Morphology of Active Layer for High Performance of Bulk-Heterojunction Organic Solar Cells. *Solar Energy Materials and Solar Cells* **2010,** *94*, 1118-1124.

[44] G. L. C. Paulus, M. H. Ham and M. S. Strano. Anomalous Thickness-Dependence of Photocurrent Explained for State-of-the-Art Planar Nano-Heterojunction Organic Solar Cells. *Nanotechnology* **2012,** *23*, 095402.

[45] P. Campbell and M. A. Green. Light Trapping Properties of Pyramidally Textured Surfaces. *Journal of Applied Physics* **1987,** *62*, 243-249.

[46] Y. Ein-Eli, N. Gordon and D. Starosvetsky. Reduced Light Reflection of Textured Multicrystalline Silicon Via Npd for Solar Cells Applications. *Solar Energy Materials and Solar Cells* **2006,** *90*, 1764-1772.

[47] R. H. Franken, R. L. Stolk, H. Li, C. H. M. van der Werf, J. K. Rath and R. E. I. Schropp. Understanding Light Trapping by Light Scattering Textured Back Electrodes in Thin Film N-I-P-Type Silicon Solar Cells. *Journal of Applied Physics* **2007,** *102*, 014503.

Chapter 3: Hybrid n-GaN/Polymer Interface: Model System for Tunable Photodiodes

3.1: Introduction

The hybrid interface formed between semiconductors offers a range of interesting properties, which cannot be easily realized in pure organic or inorganic semiconductors. The understanding of solution-processed organic semiconductors has advanced rapidly and provides complementary technology for realizing flexible, wearable electronics. However, the applications of these amorphous semiconductors are limited by the slow charge transport owing to lower carrier mobility and diffusion length. Pairing organics with inorganic layer can significantly improve the charge transport properties while being able to process tunable devices with relative ease [1-4]. However these materials have very dissimilar properties, contrary to the crystalline and band type inorganic semiconductors, the polymeric semiconductors are disordered, low dielectric constant materials with high absorption coefficient ($\alpha(E)$). A hybrid p-n junction can be realized, given that the process at the organic-inorganic interface is not detrimental to the device performance.

The hybrid interface of large band gap n-doped gallium nitride (n-GaN) and low band gap p-type donor (D) polymeric semiconductors has been studied in this chapter. A comparison is drawn with n-type polymeric semiconductors which belong to the class of acceptors (A). The basic difference in the nature of optical excitations in organic (Frenkel exciton)[5] and inorganic (Wannier-Mott exciton)[6] semiconductors is expected to reveal phenomena such as splitting of the excitonic spectrum, dipole-dipole coupling, and enhancement of optical nonlinearities[7-11]. Similar to what has been observed in inorganic quantum-well/nanocrystal structures[12]. Furthermore, many studies have been reported on the fabrication and application of hybrid light-emitting diodes in microdisplays [13-15]. Hybrid interfaces for device applications are still at an emerging stage providing many unique directions for better device architectures in the area of photodetectors [16, 17], hybrid solar cells [18-20], emitters [21, 22], and transistors [23, 24]. Many recent reports have explored the hybrid devices using II-VI semiconductors such as ZnO [25] and other amorphous oxides [26] and organic layers. Although some of these oxide semiconductors provide low-temperature growth, their band gap energies are difficult to tune. The III-N semiconductors are very attractive in the regard since a wide range of band gap energies is achievable by changing the Al, Ga, and In composition [27-29]. Tunability is required for matching the energy levels of inorganic with the HOMO and LUMO energies in organic/polymeric semiconductors. The inorganic system, n-GaN, provides an ideal platform for creating an interface with the low band-gap organic semiconductors for understanding the charge and exciton transfer at the hybrid junction. Important advantages offered by III-V semiconductor system in general and n-GaN, in particular, are listed below.

i. The semiconductors of III-N family are intrinsically n-doped, which results from the nitrogen vacancies and the doping can be increased to achieve high carrier (electron) density (~ 10^{18}-10^{19} /cm^3). The difficulty to achieve p-doping in these systems makes them a suitable candidate for coupling with a large variety of donor polymers.

ii. Transmission of n-GaN films is > 80 % for the visible range of EM spectrum making them an excellent active window element for exciting low band gap polymers. Due to its large band gap, the applicability of n-GaN in visible light detection is limited. However, with a heterointerface with low gap semiconductors, the active detection window can be easily tuned for visible and near IR detection.

iii. By controlling the ratio of another element like aluminum and indium, the band gap of GaN can be easily tuned for required applications.

Our work explores the model system of n-GaN/polymer photodiodes for tuning the spectral detection by changing the polymer layer alone and keeping the n-GaN layer identical, providing a simple route for windowed photodetection.

3.2: Experimental details

3.2.1: Materials

Gallium polar, n-doped GaN films, with a thickness of 3μm, were grown on sapphire substrates using metal-organic chemical vapor deposition (MOCVD) technique [30] by the group of F. Shahedipour-Sandvik at Albany-State University of New York. Donor semiconducting polymers P3HT (Poly(3-hexylthiophene)) (M_W ~ 30,000-40,000 D) and PBTTT-C14 (Poly(2,5-bis(3-tetradecyllthiophene-2-yl)thieno[3,2-b]thiophene)) (M_W ~ 40,000-80,000 D) were procured from Luminescence Technology Inc. Taiwan. Acceptor semiconducting polymer Polyera ActiveInk N2200 (Poly{[N,N$^{'}$- bis(2-octyldodecyl)-napthalene-1,4,5,8-bis(dicarboximide)-2,6-diyl]-alt-5,5$^{'}$-(2,2$^{'}$-bithiophene) (P(NDI20D-T2))) (M_W ~ 1,20,000 D) was obtained from Polyera, USA. The organic soluble hole transporting buffer layer dihexyl-poly(3,4-propylenedioxythiophene) (PProDOT-Hx_2) was provided by Prof. Anil Kumar at IIT Mumbai [31].

3.2.2: Sample preparation

The n-GaN films were cleaned using wet chemical cleaning procedure as described below.

i. The n-GaN coated sapphire substrates were sonicated for 10 min in 2-propanol and acetone.

ii. Substrates were boiled in 2-propanol for 10 min and sonicated for 10 min.

iii. Following sonication, sapphire/n-GaN substrates were blow dried and treated with nitrogen plasma.

Polymer semiconductors were spin coated from a 20 mg/ml solution for P3HT and PBTTT-C14 and 10 mg/ml solution for N2200 in ortho-dichlorobenzene giving a film thickness of 100-120 nm for P3HT and PBTTT-C14 and 60-70 nm for N2200. P3HT films were annealed at 120 ^{o}C and PBTTT-C14 films were annealed at 180 ^{o}C for better crystallinity [32, 33]. A layer of hole transporting buffer, PProDOT-Hx$_2$, was spin coated on P3HT and PBTTT-CT from a 10 mg/ml solution in dichloromethane and chloroform respectively. The hole transporting layer was required primarily for avoiding the diffusion of gold in the organic layer. No buffer layer was required for N2200. Au was deposited as top contact for P3HT and PBTTT-C14 devices while Al was used as a top electrode for N2200 using thermal evaporation (~ 5×10^{-6} mbar pressure, 1 Å/s evaporation rate and 100 nm thickness). Active area ~ 0.06 cm^2 was controlled using a metal mask. The ohmic contact with n-GaN was formed using indium or indium alloy on the same side. This kind of geometry requires lateral charge transport in the n-GaN, which has a drawback of higher lateral series resistance which can influence the photoresponse.

3.2.3: Characterization

Optical: All absorption studies were performed in Perkin Elmer UV-Vis spectrometer; PL measurements were performed in a spectrofluorometer **(**Perkin Elmer**).**

Charge transport studies: Current-voltage measurement was performed using Keithley 4200 semiconductor characterization system. High power LED and the laser was used to study excitation energy and intensity dependence. Photocurrent response ($I_{ph}(E)$) with and without external bias was measured in an in lab developed setup as described in the previous chapter.

Structural: Stacking in thin films of P3HT and PBTTT-C14 coated on quarts and n-GaN substrates was studied using the P-XRD system.

3.3: Results and Discussion

3.3.1: Wannier-Frenkel hybrid excitons at n-GaN/polymer interface

The $\alpha(E)$ for organic semiconductors is two orders of magnitude higher than that of the inorganic n-GaN layer, as is shown in Figure 3.1a and 3.1b respectively. Large $\alpha(E)$ allows for a very thin layer (~ 100 nm) of an organic compound, compared to that of the n-GaN layer, which is an order of magnitude thicker (~ 3μm). The PL from n-GaN layer shows two peaks at ~ 3.3 eV and ~ 2.2 eV (Figure 3.1a). Emission near band gap (~ 3.4 eV) is related to the band edge emission of the n-GaN. The emission at ~ 2.2 eV arises from the defect states, which is inherent to, strain relaxed, epitaxially grown layers, the emission spans from ~ 2.76 - 1.95 eV.

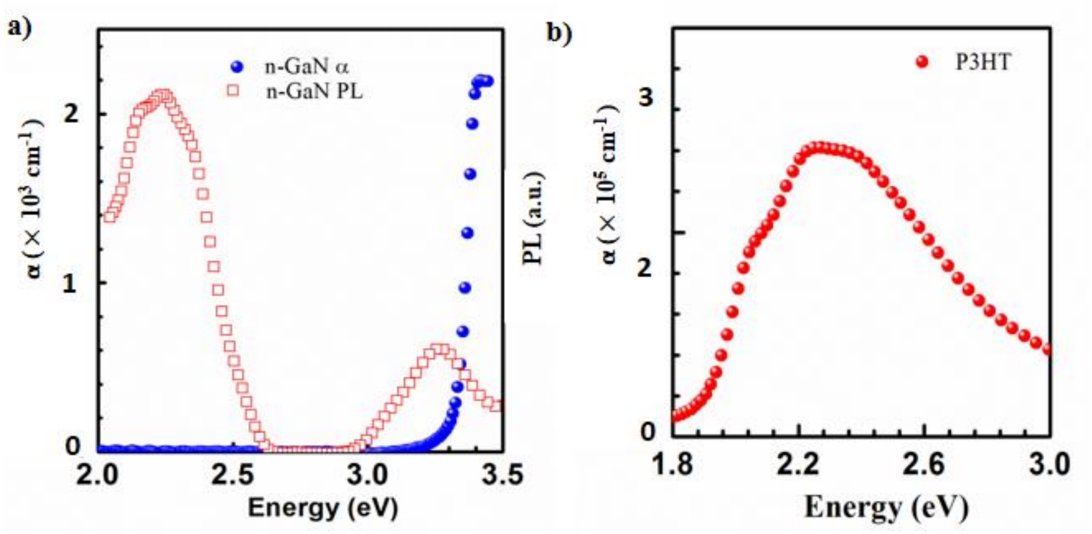

Figure 3.1: *a) α(E) and PL spectra of the n-GaN layer, b) α(E) spectra for the P3HT thin film.*

The defect state emission from n-GaN has a considerable spectral overlap with the PBTTT-C14 absorption (Figure 3.2a). The PL peak (~ 1.7 eV) of PBTTT-C14 is significantly Stoke shifted (~ 0.7 eV) from its absorption peak (~ 2.4 eV) (Figure 3.2b). The PL from n-GaN/PBTTT-C14 hybrid interface has a peak at ~ 1.96 eV which lies in between the organic and n-GaN emission maxima (Figure 3.2c). Simultaneously, the defect state emission from n-GaN is significantly quenched, suggesting that the defect state emission is coupled into the organic layer. The emission peak intensity, at ~ 1.96 eV, follows the intensity of defect state emission from n-GaN and is maximum at the band gap excitation of n-GaN (~ 3.4 eV) (inset of Figure 3.2c). The origin of this emission band can be associated with the charge-transfer state formed between organic HOMO and n-GaN CB at the hybrid interface, (Figure 3.2d). The internal recycling of defect state emission can be a contributing factor towards the photocurrent enhancement in the polymer layer.

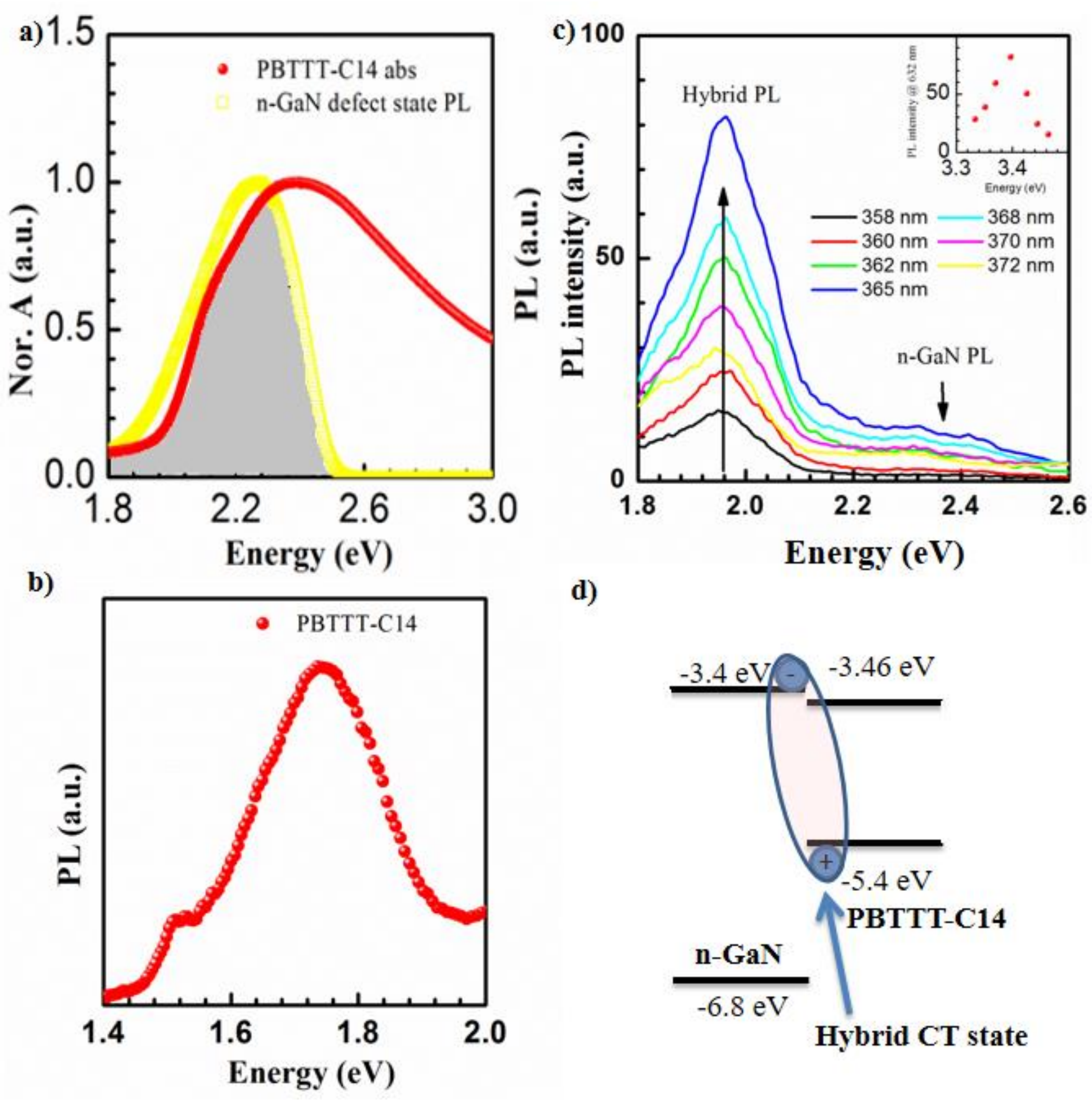

Figure 3.2: *a) Spectral overlap between defect state emission in the n-GaN and PBTTT-C14 absorption, b) PBTTT-C14 PL, c) PL from hybrid bilayer n-GaN/PBTTT-C14 structure, the inset shows PL intensity as a function of n-GaN excitation, d) Schematic representation of hybrid state between n-GaN/PBTTT-C14. (Reprinted from Organic Electronics, 14, 11, P. Kumar, K. Shadi, S. Guha and K. S. Narayan, Hybrid n-GaN and polymer interfaces: model systems for tunable photodiodes, 2818-2825, copyright (2013), with permission from Elsevier).*

3.3.2: Charge injection and transport at the hybrid interface

The bilayer structure formed between n-GaN and polymer, as is shown in Figure 3.3a, can be easily tuned into type I or type II heterostructure (Figure 3.3b). The J-V characteristic has a significant dependence on the energy level alignment across the hybrid interface. The n-GaN/D polymers form type II energy structure and n-GaN/A polymers form type I energy structure (specific to the choice of polymer).

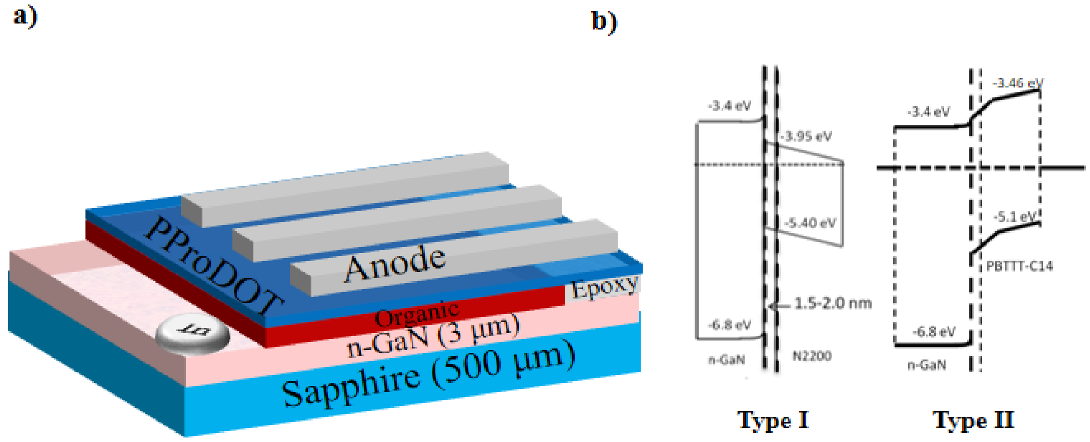

Figure 3.3: *a) Schematic representation of n-GaN/polymer bilayer hybrid device, b) type I and type II energy structure. (Reprinted from Organic Electronics, 14, 11, P. Kumar, K. Shadi, S. Guha and K. S. Narayan, Hybrid n-GaN and polymer interfaces: model systems for tunable photodiodes, 2818-2825, copyright (2013), with permission from Elsevier).*

The dark J-V characteristics for n-GaN/D(A) devices is shown in Figure 3.4a. A diode like behavior is seen for all device structure with good rectification. For devices with D polymer layer, a small positive offset in Voltage (at J=0) and a zero bias reverse current is seen in dark J-V characteristics (Figure 3.4b), such feature is not present for n-type polymer layer. The magnitude of the offset voltage of ~ 0.4 V shows no dependence on measurement history or prior conditioning. Origin of such offset voltage in J-V curve has been associated with the charging of traps present in organic BHJ system [34]. Alternatively, the traps can originate at the n-GaN/polymer interface sue to the large surface polarization in n-GaN [35, 36], which can modify the energy level of polymer in the vicinity, leading to the formation of charge carrier trap state at the interface.

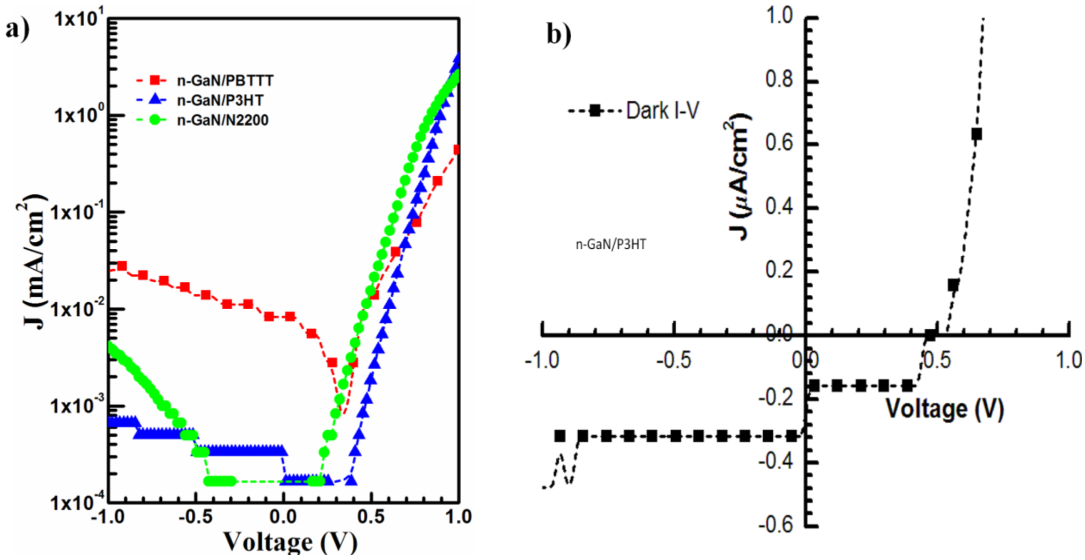

Figure 3.4: *a) Dark J-V characteristics for n-GaN/polymer hybrid diode, b) Positive offset voltage observed in n-GaN/Donor polymer hybrid diodes.* ***(****Reprinted from Organic Electronics, 14, 11, P. Kumar, K. Shadi, S. Guha and K. S. Narayan, Hybrid n-GaN and polymer interfaces: model systems for tunable photodiodes, 2818-2825, copyright (2013), with permission from Elsevier).*

The dark I-V responses were modeled using the thermionic emission model (equation 3.1), assuming that the charge density of n-GaN >> organic layer [37].

$$I = A^{*}T^{2}exp\left(\frac{-\phi_B}{nk_BT}\right)\left[exp\left(\frac{V_a - IR_s}{nk_BT}\right) - 1\right] \qquad (3.1)$$

Where A^* is Richardson constant and ϕ_B is Schottky barrier height, n is the diode ideality factor and R_s is the series resistance. Equation 3.1 is a transcendental equation, which requires further simplification into linear equations for model fitting [38].

$$\frac{dV}{d(lnI)} = \frac{nk_BT}{q} + IR_s \tag{3.2}$$

$$H(I) \equiv V - \left(\frac{nk_BT}{q}\right) ln\left(\frac{I}{A^*T^2}\right) = n\phi_B + IR_s \tag{3.3}$$

The fitting parameters derived from thermionic emission model are summarized in table 3.1. The reverse saturation current density and diode ideality factor calculated from dark I-V are higher than that of GaN/polymer hybrid systems reported previously [39, 40]. High reverse saturation current density originates from lower barrier height, which is a function of offset between n-GaN W_F and donors LUMO. The performance of a hybrid diode is dominated by the electronic nature of the interface; a higher value of *n* (non-ideal behavior) suggests large recombination losses. Interface traps and polarization induced effects from the n-GaN surface can contribute significantly towards higher *n*. The Schottky barrier height for both n-GaN/P3HT and n-GaN/PBTTT-C14 system is comparable, the small difference of ~ 0.08 eV can arise from the energy offset between the LUMO of two systems.

The hybrid diodes consisting of n-GaN and P3HT feature superior performance compared to the n-GaN/PBTTT-C14 hybrid diodes. This observation can be attributed to the energy level alignment, which is a type II for n-GaN/P3HT while for n-GaN/PBTTT-C14 the energy level alignment is at the boundary of type I and II structure. Observed effect can also be attributed to the increased stacking property of P3HT on the n-GaN surface, which is not the case for PBTTT-C14. The stacking in

P3HT and PBTTT-C14 on the n-GaN surface is controlled by the surface energy and steric effects. The XRD spectrum shows an ordering peak for P3HT at 2θ = 5.16 degree, which corresponds to the edge on stacking and the interchain spacing is ~ 1.6 nm (Figure 3.5). Similar features are absent in PBTTT-C14 films coated on the n-GaN layer, suggesting no favorable ordering.

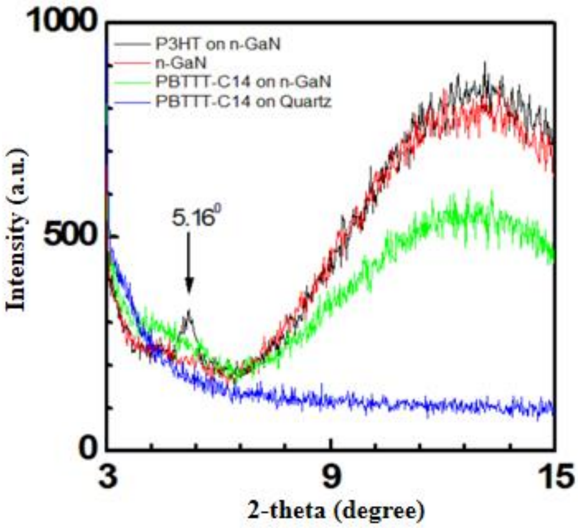

Figure 3.5: *XRD spectra of P3HT and PBTTT-C14 thin films coated on n-GaN and quartz substrates. (Reprinted from Organic Electronics, 14, 11, P. Kumar, K. Shadi, S. Guha and K. S. Narayan, Hybrid n-GaN and polymer interfaces: model systems for tunable photodiodes, 2818-2825, copyright (2013), with permission from Elsevier).*

Table 3.1: Thermionic emission model fit for n-GaN/D polymer hybrid diode.

Hybrid structure	n	Φ_b (V)
n-GaN/PBTTT-C14	3.8 ± 0.2	0.85 ± 0.01
n-GaN/P3HT	2.37 ± 0.01	0.93 ± 0.01

3.3.3: Photoresponse in bilayer hybrid diode

A typical photodiode response was observed upon illumination on n-GaN/D hybrid system as is shown in Figure 3.6a. The n-GaN serves as electron transport layer while holes are transported in the donor layer, as can be deduced from the polarity of J_{SC}. The n-GaN/N2200 system show much lower J_{SC}, than that of n-GaN/D system, which is related to the energy structure and the selective charge transport (n-type) nature of both layers (inset of Figure 3.6a).

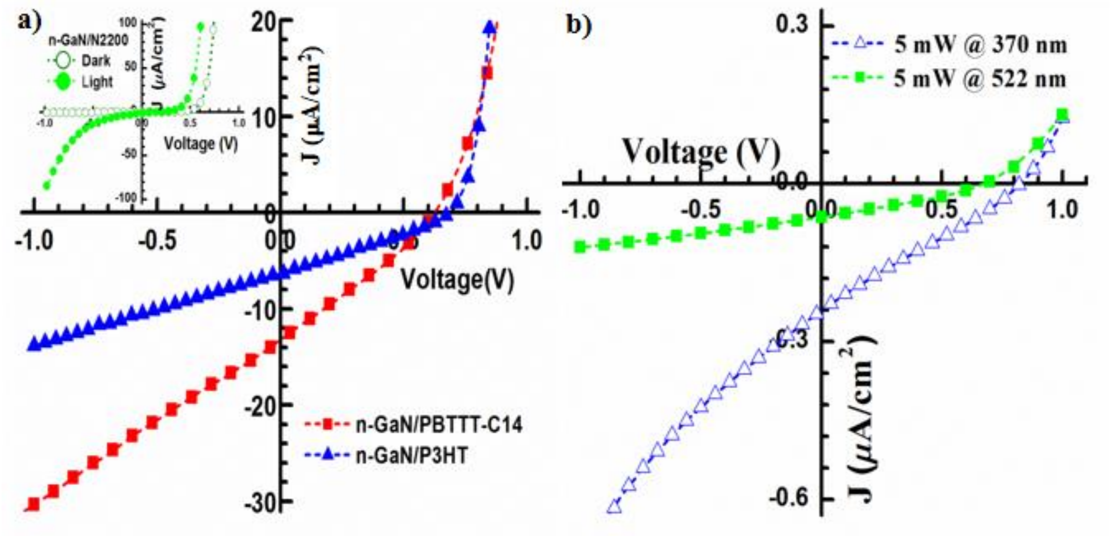

Figure 3.6: *a) The n-GaN/D polymer photodiode response, the inset shows the photodiode response for n-GaN/A polymer diode, b) photodiode response at excitation wavelengths for n-GaN and PBTTT-C14. (Reprinted from Organic Electronics, 14, 11, P. Kumar, K. Shadi, S. Guha and K. S. Narayan, Hybrid n-GaN and polymer interfaces: model systems for tunable photodiodes, 2818-2825, copyright (2013), with permission from Elsevier).*

Under larger reverse bias, the hybrid diode operates in photodiode mode. The fill factor in photovoltaic mode is ~ 25%, the photocurrent does not show saturation with increasing reverse bias. These observations imply a strong field dependence of charge carrier extraction resulting from large density of interface traps. In the absence of strong reverse bias, the carriers trapped at the hybrid interface will eventually be lost via recombination process.

From the dark J-V response, it can be concluded that P3HT forms a better hybrid interface with n-GaN, which facilitates better charge transport compared to PBTTT-C14. Extraction of the photogenerated carrier is relatively easy in the n-GaN/P3HT system, compared to that of n-GaN/PBTTT-C14 system, under the driving force of built-in electric field. This can also be inferred from the stronger field dependence of photocurrent in the n-GaN/PBTTT-C14 system. In a given hybrid system the charge generation and transport are asymmetric across the hybrid interface (Figure 3.6b). It is observed that the photocurrent from the hybrid device is higher for 365 nm illumination compared to that of 532 nm illumination (similar incident power ~ 5 mW/cm^2). The J-V at 365 nm excitation shows a strong, nonlinear field response in reverse bias. This indicates the presence of larger barrier for charge injection from n-GaN to D layer. The asymmetry in charge transport can be related to the large offset between the energy levels of n-GaN and the organic layer.

The intensity dependence of V_{OC} shows a logarithmic dependence on incident photon intensity (Figure 3.7a). The J_{SC} vs. Intensity ($J_{SC} \propto I^{\varphi}$) shows a sublinear response for both n-GaN ($\varphi \approx 0.73$) and D polymer ($\varphi \approx 0.85$) suggesting a bimolecular recombination (Figure 3.7b). Further insights on charge transport across the hybrid interface were obtained by spectrally tuning the incident light and direction of illumination, which allows for selecting the spatial zone of photocarrier generation.

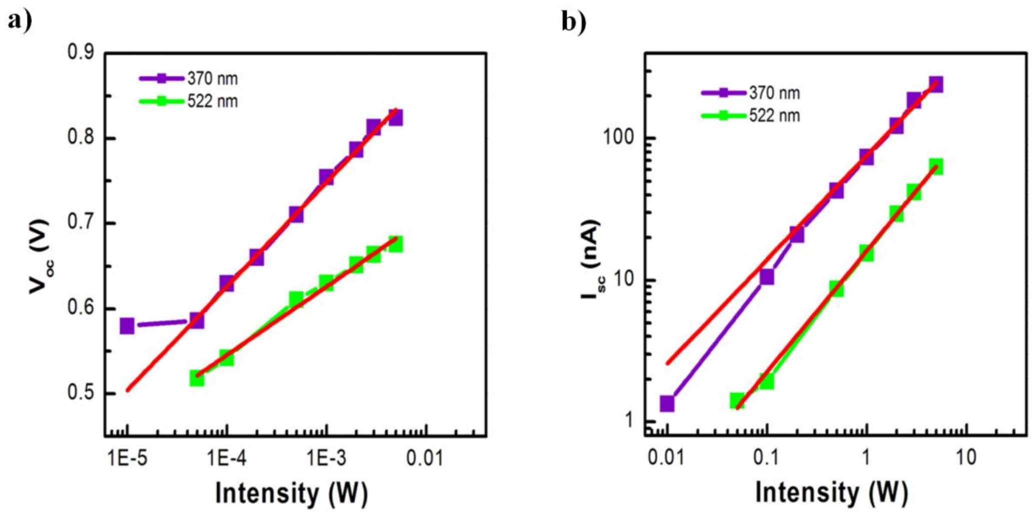

Figure 3.7: *a) Intensity dependence of* V_{OC} *and b) Intensity dependence of* J_{SC}*, at n-GaN and PBTTT-C14 excitation. (Reprinted from Organic Electronics, 14, 11, P. Kumar, K. Shadi, S. Guha and K. S. Narayan, Hybrid n-GaN and polymer interfaces: model systems for tunable photodiodes, 2818-2825, copyright (2013), with permission from Elsevier).*

3.3.4: Spectral photocurrent response in hybrid photodiodes

The $I_{ph}(E)$, in the hybrid photodiode, shows a characteristic dependence on the energy level of the polymer layer and the direction of illumination. The responsivity for n-GaN and the different organic layer is shown in Figure 3.8a and 3.8b respectively. The responsivity of the n-GaN layer (~ 2.5 mW at -2.0V) is an order of magnitude higher than that of the polymer layer. The responsivity for an inorganic and organic layer under selective excitation is expected to be different. The carrier generation in organic layer is hindered by large exciton binding energy (~ 0.2-0.3 eV) compared to that of the n-GaN layer (~ 10-15 meV). The superior charge transport in the n-GaN layer is associated with high charge carrier mobility (~300 cm^2/Vs), which is much slower in the organic layer.

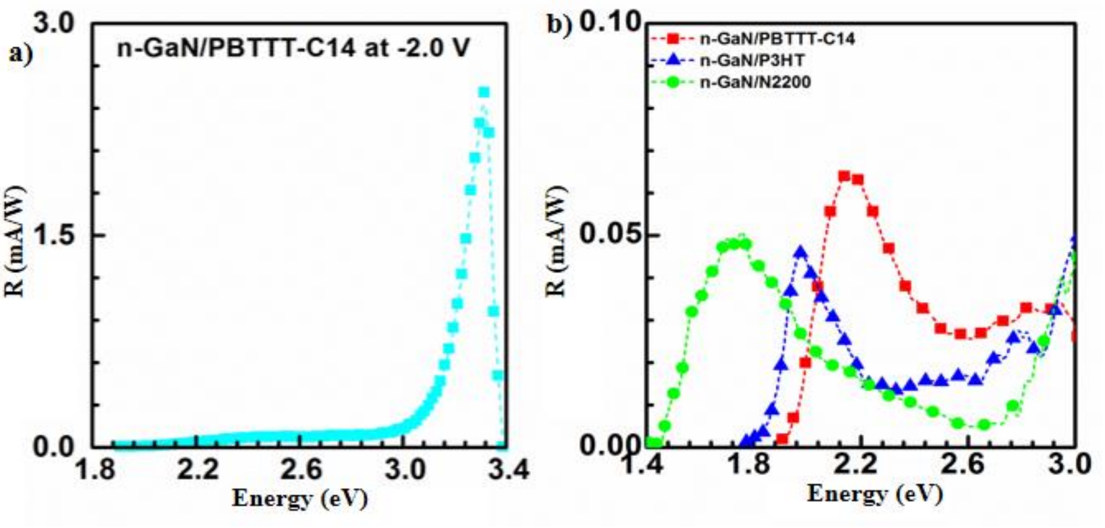

Figure 3.8: *Spectral I_{ph} response for a) n-GaN layer and b) polymer layers. (Reprinted from Organic Electronics, 14, 11, P. Kumar, K. Shadi, S. Guha and K. S. Narayan, Hybrid n-GaN and polymer interfaces: model systems for tunable photodiodes, 2818-2825, copyright (2013), with permission from Elsevier).*

The affinity (driving force) for electron transport towards n-GaN and hole transport towards organic layer shows a significant difference. The origin of this behavior can be related to large asymmetry in the offset between CB-LUMO and VB-HOMO. An $I_{ph}(E)$ response in organic semiconductor sandwiched between ohmic and Schottky contacts show a strong dependence on the direction of illumination [41, 42].

The $I_{ph}(E)$ for donor polymer shows a characteristics peak at lower $\alpha(E)$, while the $I_{ph}(E)$ is lower at the $\alpha(E)$ maximum when illuminated from the n-GaN side (antibatic response). This behavior is consistent for n-GaN/PBTTT-C14 (Figure 3.9a) and n-GaN/P3HT (Figure 3.9b) and contrary to the trends observed for conventional bilayer polymer devices. When illuminated through the thin gold anode, the $I_{ph}(E) \propto \alpha(E)$ (symbatic response). However for n-GaN/N2200 system the $I_{ph}(E) \propto \alpha(E)$ when illuminated from the n-GaN side (Figure 3.9c), which is the ideal expected behavior.

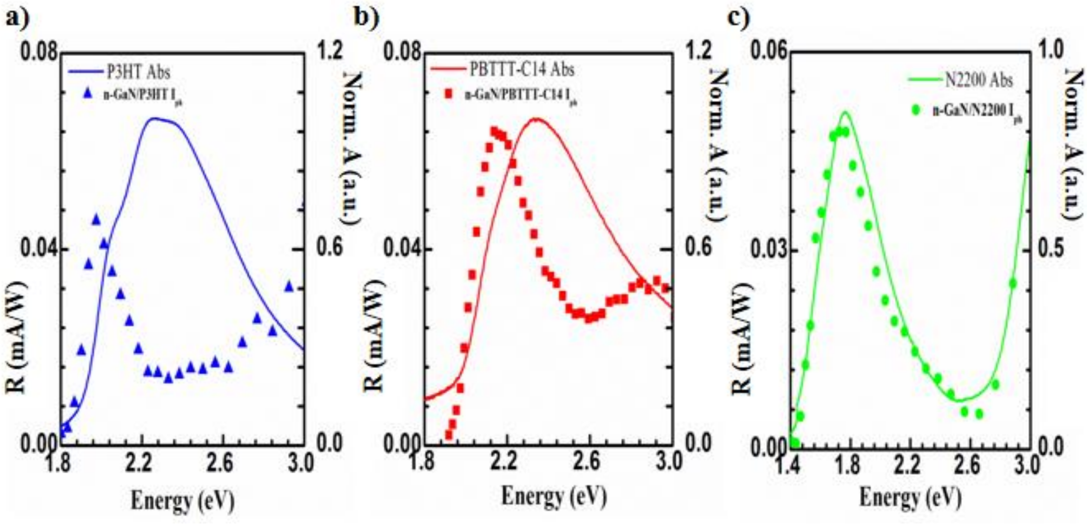

Figure 3.9: *I_{ph} response along with the absorption of, a) P3HT, b) PBTTT-C14 and c) N2200 polymer layer*. *(Reprinted from Organic Electronics, 14, 11, P. Kumar, K. Shadi, S. Guha and K. S. Narayan, Hybrid n-GaN and polymer interfaces: model systems for tunable photodiodes, 2818-2825, copyright (2013), with permission from Elsevier).*

Normalized symbatic and antibatic response measured for type II energy structure, n-GaN/PBTTT-C14 and n-GaN/P3HT diode, when illuminated from thin Au and the n-GaN sides, shows a consistent behavior (Figure 3.10). The antibatic response is more pronounced in the n-GaN/P3HT system, which can be related to higher LUMO in P3HT (~ 3.0 eV) compared to that of PBTTT-C14 (~ 3.46 eV). The n-GaN/polymer interface is the rectifying junction in hybrid diodes, the $I_{ph}(E)$ response for light illuminated through n-GaN is expected to be symbatic. Which is also the case for bilayer polymer devices, where light incident through rectifying junction $I_{ph}(E) \propto \alpha(E)$[41]. The origin of such a behavior can be related to surface polarization present in the n-GaN layer.

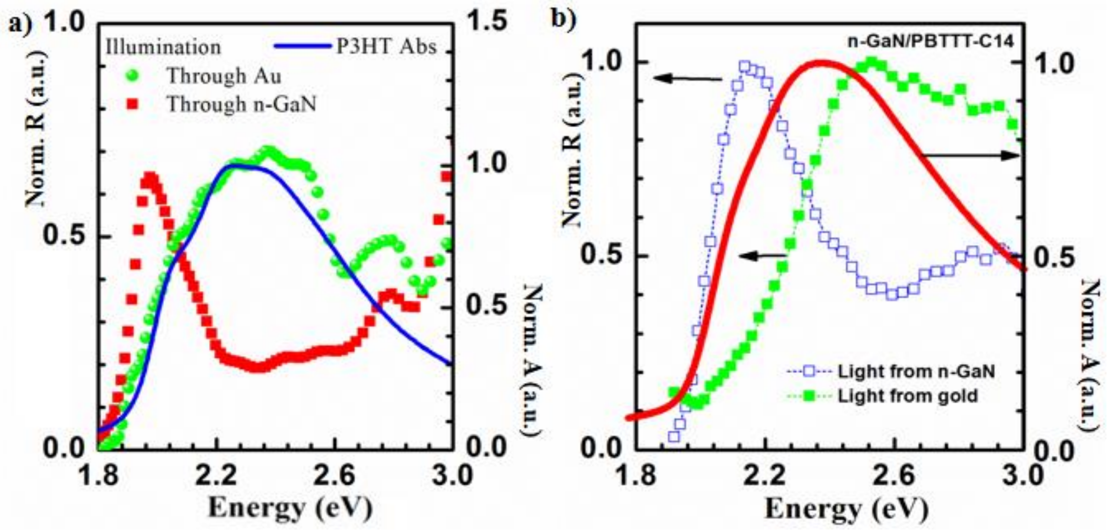

Figure 3.10: *Dependence of I_{ph} (E) response on the direction of illumination in a)n-GaN/ P3HT and b) n-GaN/PBTTT-C14 hybrid diodes. (Reprinted from Organic Electronics, 14, 11, P. Kumar, K. Shadi, S. Guha and K. S. Narayan, Hybrid n-GaN and polymer interfaces: model systems for tunable photodiodes, 2818-2825, copyright (2013), with permission from Elsevier).*

The observation of symbatic and antibatic response in $I_{ph}(E)$ can be understood by using the energy diagram shown in Figure 3.11. The energy structure of the semiconductor layer is such that electron transport towards metal-A is favored, while holes move towards metal-B. Upon illumination from the direction of metal-A, a maximum number of photons, at the $\alpha(E)$ maxima, will be absorbed close to metal-A/polymer interface. The charge carriers can easily move towards the respective electrode, contributing towards a symbatic $I_{ph}(E)$ response. However, when the light is illuminated from the metal-B side, the maximum amount of photons is absorbed close to metal-B/polymer interface. The free charges generated have an unfavorable energy condition, restricting the movement towards their respective electrodes, resulting in a decrease in $I_{ph}(E)$ at $\alpha(E)$ maxima. However, the photons, in the low $\alpha(E)$ region, can penetrate deeper into the polymer films and can generate e-h pair close to metal-

A/polymer interface, which can contribute towards $I_{ph}(E)$ response. Hence the $I_{ph}(E)$ response is higher at low $\alpha(E)$ and lower at high $\alpha(E)$, giving rise to an antibatic response [41, 42].

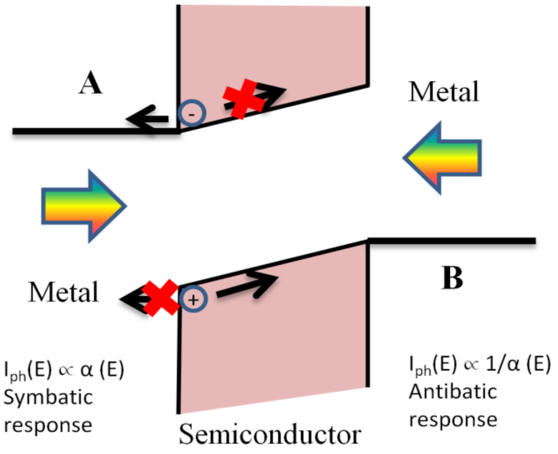

Figure 3.11: *Schematic depicting the origin of symbatic and antibatic response.*

Bias dependence of $I_{ph}(E)$ in the n-GaN/PBTTT-C14 hybrid devices, for illumination from the n-GaN side is shown in Figure 3.12. For n-GaN excitation, the $I_{ph}(E)$ increases linearly with applied reverse bias (Figure 3.12a). The responsivity for the n-GaN layer is an order of magnitude higher than that of the polymer layer. A gradual shift, in $I_{ph}(E)$ of the PBTTT-C14 layer, is observed under steady-state external bias. The maxima in $I_{ph}(E)$ shifts from lower $\alpha(E)$ under forward bias (~ 0.75V) (Figure 3.12b) to $I_{ph}(E) \propto \alpha(E)$ under reverse bias (~ -2.0V) (Figure 3.12c). The ability to control the $I_{ph}(E)$ response with external bias, suggests the energy level modification at the n-GaN/polymer interface. In presence of n-GaN surface polarization and the built in voltage, the energy level at the hybrid interface can be significantly modified.

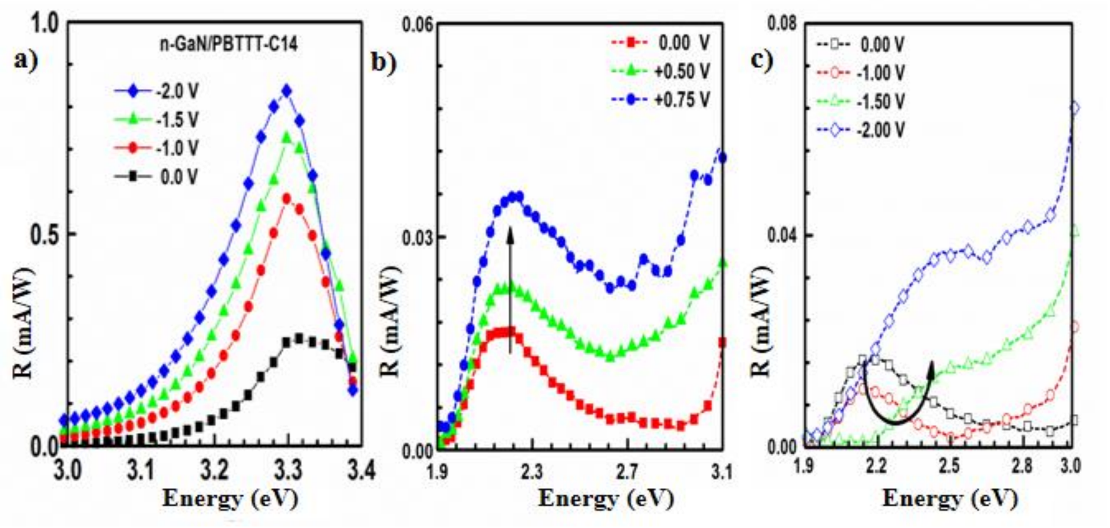

Figure 3.12: *Spectral I_{ph} response for a) n-GaN layer under reverse bias, b) polymer layer under forward bias and c) polymer layer under reverse bias. (Reprinted from Organic Electronics, 14, 11, P. Kumar, K. Shadi, S. Guha and K. S. Narayan, Hybrid n-GaN and polymer interfaces: model systems for tunable photodiodes, 2818-2825, copyright (2013), with permission from Elsevier).*

Thin films of n-GaN, grown using epitaxial growth technique, show a strong surface polarization ($\vec{P}$) which is a cumulative of spontaneous and strain induced polarization [43, 44]. In the case of Ga-polar n-GaN films, grown using MOCVD, the surface polarization is directed away from the surface, into the n-GaN film [45]. In the hybrid bilayer device structure an additional built in field ($\overrightarrow{E_{\mathrm{Bi}}}$) is present, which arises from the workfunction restructuring across the device. Net field ($\vec{D}$) present at the hybrid interface is a sum of built in voltage and polarization, as given in 3.4,

$$\vec{D} = \varepsilon_0 \varepsilon_r \vec{E}_{Bl} + \vec{P} \tag{3.4}$$

Where, ε_r is relative permittivity of the organic layer, $\vec{D}$ is directed from polymer towards n-GaN layer.

Presence of $\vec{D}$ at the interface modifies the polymer energy level in the vicinity of hybrid interface. It is assumed that the band bending effect of $\vec{D}$ is equal for both electrons and holes. Modification in polymer energy level gives rise to an energy hill for hole transport towards Au electrode. The holes created at hybrid interface, at the peak $\alpha(E)$, will be trapped and will not contribute to $I_{ph}(E)$response. At the absorption edge the photons are weakly absorbed, which increases the penetration depth. These photons can reach the polymer/Au interface, chargers generated at this interface does not experience the energy level restructuring. Hence the contribution towards $I_{ph}(E)$ response is higher from polymer/Au interface compared to n-GaN/polymer interface, which gives rise to antibatic response. Alternatively, when the light is incident through Au side, the charges generated at peak $\alpha(E)$ contribute towards $I_{ph}(E)$, giving rise to symbatic response. In case of type I energy structure between n-GaN and n-type N2200, the energy structure does not seems to have an identical effect of $\vec{D}$.

The bias dependence of spectral feature can be understood better by considering the effect of external bias in renormalizing $\vec{D}$. The spontaneous polarization induced in strain relaxed n-GaN film is ~ 29 mC/m^2 [44, 46]. Assuming that the polarization effect extends over the polymer thickness of ~ 2 - 3 nm [47], the magnitude of external field required to reverse the effect can be easily estimated. In order to estimate the magnitude of external field, the required condition is $\vec{D} = 0$.

$$\vec{P} = \varepsilon_0 \varepsilon_r \left(\vec{E}_{Bl} + \vec{E}_{ext} \right) \tag{3.5}$$

From dark J-V, the built in voltage for n-GaN/PBTTT-C14 structure is 0.85±0.01 V and ε_r for polymer layer is assumed to be ≈ 2.7. Thus the minimum external bias required to create a zero field condition and reverse the polarization induced effect is ~ - 1.3 ± 0.2 V. As can be noticed in Figure 3.12c, the spectral feature shows a transition from antibatic to symbatic between -1.0 to -1.5 V, which is well in the range of calculation. A schematic representation of expected energy structure in hybrid device structure is shown in Figure 3.13a.

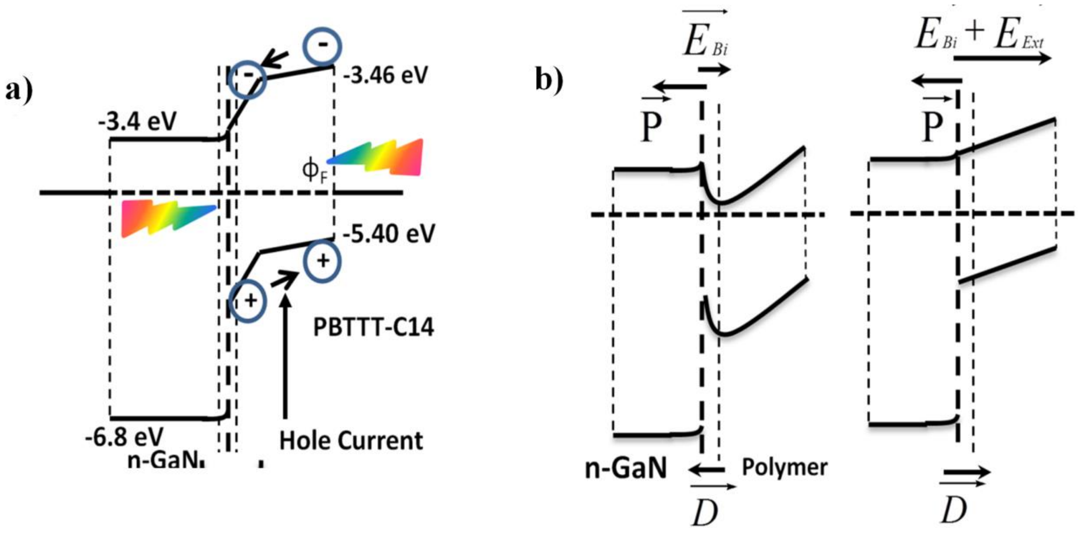

Figure 3.13: *Schematic representation of a) ideal energy structure and b) energy structure under applied external bias. (Reprinted from Organic Electronics, 14, 11, P. Kumar, K. Shadi, S. Guha and K. S. Narayan, Hybrid n-GaN and polymer interfaces: model systems for tunable photodiodes, 2818-2825, copyright (2013), with permission from Elsevier).*

The distortion at the hybrid interface under the influence of polarization and built-in electric field is shown in Figure 3.13b. Upon applying forward bias, the zero bias energy structure gets amplified, giving rise to higher antibatic response. However, under reverse bias, the energy structure gets renormalized towards ideal bilayer structure, which is also reflected in a shift from antibatic to symbatic response. The $I_{ph}(E)$ response measured for different organic layers, suggests, that by using different polymers, a wide and well defined spectral range can be accessed. Above highlighted strategy, of using polymer layers with variable spectral sensitivity, is possibly more effective and facile than approaches involving alloying of n-GaN using indium and aluminum.

3.3.5: Background illumination and thickness dependence of photocurrent

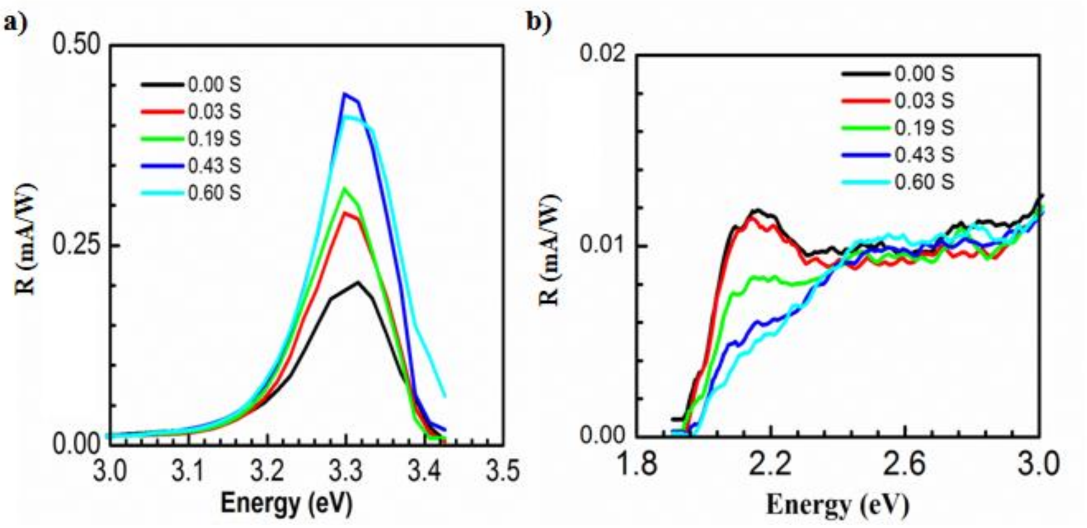

Figure 3.14: *Spectral* I_{ph} *response under background light illumination for a) n-GaN layer and a b) polymer layer.*

Using external DC background light, a situation analogous to the external field can be created. Figure 3.14a and 3.14b shows the response in presence of background light illumination for n-GaN and polymer layer, respectively. The background charges trapped at the interface can create an additional field at the interface, which can compensate for polarization effects. This result is a decrease in antibatic response with an increase in background charge density, which is proportional to the background light intensity (Figure 3.14b). The internal filter effect shows strong thickness dependence as is shown in Figure 3.15. With an increase in polymer layer thickness, the photons at peak $\alpha(E)$ is filtered more efficiently, and the $I_{ph}(E)$ response decreases further at peak $\alpha(E)$. While the carrier generated at polymer/Au edge still contribute towards $I_{ph}(E)$, which results in a narrower peak at the *α(E)* edge. A strong antibatic response is visible for P3HT/n-GaN hybrid device for 130 nm thick films compared to 90 nm thick film.

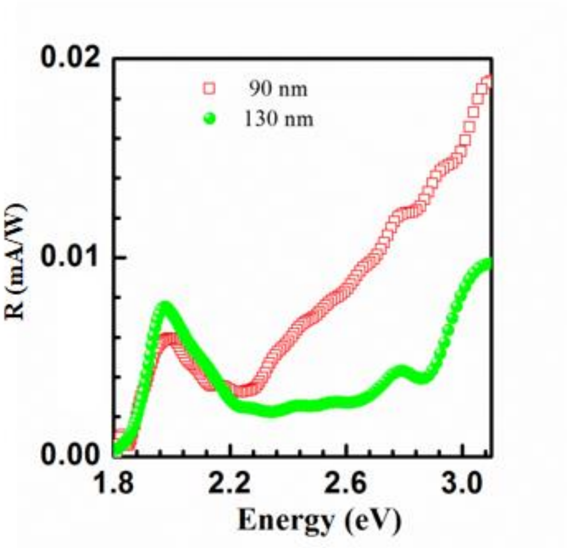

Figure 3.15: *Thickness dependence of* $I_{ph}(E)$ *response in n-GaN/P3HT hybrid.*

3.4: Conclusions

The hybrid diode formed using large band gap (no response in visible range) n-GaN and low band gap organic donor/acceptor polymers provide a model system to study charge transport across the hybrid interface. Polarization at n-GaN surface strongly affects the energy level bending in the polymer layer, in the vicinity of the n-GaN layer. The modification in polymer energy level is reflected in the deviation of $I_{ph}(E)$ response from the polymer absorption. The use of external field and light bias to realign the polymer energy structure results in a normal $I_{ph}(E)$ response. This study indicates that the interfacial modifications are essential to passivate the surface states and the polarization induced effects to improve the charge transport and photodetection.

References

[1] Y. Li, S. Calder, O. Yaffe, D. Cahen, H. Haick, L. Kronik and H. Zuilhof. Hybrids of Organic Molecules and Flat, Oxide-Free Silicon: High-Density Monolayers, Electronic Properties, and Functionalization. *Langmuir* **2012,** *28*, 9920-9929.

[2] A. S. Erickson, N. K. Kedem, A. E. Haj-Yahia and D. Cahen. Aluminum Oxide-N-Si Field Effect Inversion Layer Solar Cells with Organic Top Contact. *Applied Physics Letters* **2012,** *101*, 233901.

[3] P. Judeinstein and C. Sanchez. Hybrid Organic-Inorganic Materials: A Land of Multidisciplinarity. *Journal of Materials Chemistry* **1996,** *6*, 511-525.

[4] S. R. Wang, Y. F. Kang, L. W. Wang, H. X. Zhang, Y. S. Wang and Y. Wang. Organic/Inorganic Hybrid Sensors: A Review. *Sensors and Actuators B-Chemical* **2013,** *182*, 467-481.

[5] J. Frenkel. On the Transformation of Light into Heat in Solids. I. *Physical Review* **1931,** *37*, 17-44.

[6] G. H. Wannier. The Structure of Electronic Excitation Levels in Insulating Crystals. *Physical Review* **1937,** *52*, 191-197.

[7] S. Blumstengel, S. Sadofev, C. Xu, J. Puls and F. Henneberger. Converting Wannier into Frenkel Excitons in an Inorganic/Organic Hybrid Semiconductor Nanostructure. *Physical Review Letters* **2006,** *97*, 237401.

[8] V. M. Agranovich, D. M. Basko, G. C. La Rocca and F. Bassani. Excitons and Optical Nonlinearities in Hybrid Organic-Inorganic Nanostructures. *Journal of Physics-Condensed Matter* **1998,** *10*, 9369-9400.

[9] G. Itskos, G. Heliotis, P. G. Lagoudakis, J. M. Lupton, N. P. Barradas, E. Alves, S. Pereira, I. M. Watson, M. D. Dawson, J. Feldmann, R. Murray and D. D. C. Bradley. Efficient Dipole-Dipole Coupling of Mott-Wannier and Frenkel Excitons in (Ga,In)N Quantum Well/Polyfluorene Semiconductor Heterostructures. *Physical Review B* **2007,** *76*, 035344.

[10] Q. Zhang, T. Atay, J. R. Tischler, M. S. Bradley, V. Bulovic and A. V. Nurmikko. Highly Efficient Resonant Coupling of Optical Excitations in Hybrid Organic/Inorganic Semiconductor Nanostructures. *Nature Nanotechnology* **2007,** *2*, 555-559.

[11] G. Itskos, C. R. Belton, G. Heliotis, I. M. Watson, M. D. Dawson, R. Murray and D. D. C. Bradley. White Light Emission Via Cascade Forster Energy Transfer in (Ga, In) N Quantum Well/Polymer Blend Hybrid Structures. *Nanotechnology* **2009,** *20*, 275207.

[12] M. Achermann, M. A. Petruska, S. Kos, D. L. Smith, D. D. Koleske and V. I. Klimov. Energy-Transfer Pumping of Semiconductor Nanocrystals Using an Epitaxial Quantum Well. *Nature* **2004,** *429*, 642-646.

[13] C. Zhang and A. J. Heeger. Gallium Nitride Conjugated Polymer Hybrid Light Emitting Diodes: Performance and Lifetime. *Journal of Applied Physics* **1998,** *84*, 1579-1582.

[14] G. Heliotis, P. N. Stavrinou, D. D. C. Bradley, E. Gu, C. Griffin, C. W. Jeon and M. D. Dawson. Spectral Conversion of InGaN Ultraviolet Microarray Light-Emitting Diodes Using Fluorene-Based Red-, Green-, Blue-, and White-Light-Emitting Polymer Overlayer Films. *Applied Physics Letters* **2005,** *87*, 103505.

[15] B. Guilhabert, Z. Gong, H. Zhang, C. Belton, A. MackIntosh, E. Gu, M. Campoy-Quiles, P. N. Stavrinou, D. D. C. Bradley, R. A. Pethrick and M. D. Dawson.

Patterning and Integration of Polyfluorene Polymers on Micro-Pixellated UV AlInGaN Light-Emitting Diodes. *Journal of Physics D: Applied Physics* **2008,** *41*, 094008.

[16] L. D. Wang, D. X. Zhao, Z. S. Su, F. Fang, B. H. Li, Z. Z. Zhang, D. Z. Shen and X. H. Wang. High Spectrum Selectivity Organic/Inorganic Hybrid Visible-Blind Ultraviolet Photodetector Based on ZnO Nanorods. *Organic Electronics* **2010,** *11*, 1318-1322.

[17] X. F. Wang, W. F. Song, B. Liu, G. Chen, D. Chen, C. W. Zhou and G. Z. Shen. High-Performance Organic-Inorganic Hybrid Photodetectors Based on P3HT:CdSe Nanowire Heterojunctions on Rigid and Flexible Substrates. *Advanced Functional Materials* **2013,** *23*, 1202-1209.

[18] W. J. E. Beek, M. M. Wienk and R. A. J. Janssen. Efficient Hybrid Solar Cells from Zinc Oxide Nanoparticles and a Conjugated Polymer. *Advanced Materials* **2004,** *16*, 1009.

[19] A. Guchhait, A. K. Rath and A. J. Pal. Near-Ir Activity of Hybrid Solar Cells: Enhancement of Efficiency by Dissociating Excitons Generated in PbS Nanoparticles. *Applied Physics Letters* **2010,** *96*, 073505.

[20] D. Gebeyehu, C. J. Brabec, N. S. Sariciftci, D. Vangeneugden, R. Kiebooms, D. Vanderzande, F. Kienberger and H. Schindler. Hybrid Solar Cells Based on Dye-Sensitized Nanoporous TiO_2 Electrodes and Conjugated Polymers as Hole Transport Materials. *Synthetic Metals* **2001,** *125*, 279-287.

[21] H. J. Bolink, E. Coronado, D. Repetto and M. Sessolo. Air Stable Hybrid Organic-Inorganic Light Emitting Diodes Using ZnO as the Cathode. *Applied Physics Letters* **2007,** *91*, 223501.

[22] J. Bruckbauer, C. Brasser, N. J. Findlay, P. R. Edwards, D. J. Wallis, P. J. Skabara and R. W. Martin. Colour Tuning in White Hybrid Inorganic/Organic Light-Emitting Diodes. *Journal of Physics D-Applied Physics* **2016,** *49*, 405103.

[23] C. R. Kagan, D. B. Mitzi and C. D. Dimitrakopoulos. Organic-Inorganic Hybrid Materials as Semiconducting Channels in Thin-Film Field-Effect Transistors. *Science* **1999,** *286*, 945-947.

[24] S. Dutta, S. D. Lewis and A. Dodabalapur. Hybrid Organic/Inorganic Ambipolar Thin Film Transistor Chemical Sensor. *Applied Physics Letters* **2011,** *98*, 213504.

[25] J. Smith, A. Bashir, G. Adamopoulos, J. E. Anthony, D. D. C. Bradley, M. Heeney, I. McCulloch and T. D. Anthopoulos. Air-Stable Solution-Processed Hybrid Transistors with Hole and Electron Mobilities Exceeding 2 Cm^2 V^{-1} S^{-1}. *Advanced Materials* **2010,** *22*, 3598-3602.

[26] K. Nomura, T. Aoki, K. Nakamura, T. Kamiya, T. Nakanishi, T. Hasegawa, M. Kimura, T. Kawase, M. Hirano and H. Hosono. Three-Dimensionally Stacked Flexible Integrated Circuit: Amorphous Oxide/Polymer Hybrid Complementary Inverter Using N-Type a-In-Ga-Zn-O and P-Type Poly-(9,9-Dioctylfluorene-Co-Bithiophene) Thin-Film Transistors. *Applied Physics Letters* **2010,** *96*, 263509.

[27] T. Kuykendall, P. Ulrich, S. Aloni and P. Yang. Complete Composition Tunability of Ingan Nanowires Using a Combinatorial Approach. *Nature Materials* **2007,** *6*, 951-956.

[28] M. A. D. Poisson, M. Magis, M. Tordjman, N. Sarazin and J. di Persio. Mocvd Growth of Group Iii Nitrides for High Power, High Frequency Applications. *E-MRS 2004 Fall Meeting Symposia C and F* **2005,** *2*, 947-955.

[29] M. A. Sanchez-Garcia, J. L. Pau, F. Naranjo, A. Jimenez, S. Fernandez, J. Ristic, F. Calle, E. Calleja and E. Munoz. Plasma-Assisted Mbe Growth of Group-Iii Nitrides:

From Basics to Device Applications. *Materials Science and Engineering B-Solid State Materials for Advanced Technology* **2002,** *93*, 189-196.

[30] J. R. Grandusky, M. Jamil, F. Shahedipour-Sandvik, J. A. DeLuca, S. F. LeBoeuf, X. A. Cao and S. D. Arthur. Optimization of the Active Region of InGaN/GaN 405 nm Light Emitting Diodes Using Statistical Design of Experiments for Determination of Interaction Effects. *Journal of Vacuum Science & Technology B* **2005,** *23*, 1576-1581.

[31] A. Kumar and A. Kumar. Single Step Reductive Polymerization of Functional 3,4-Propylenedioxythiophenes Via Direct C-H Arylation Catalyzed by Palladium Acetate. *Polymer Chemistry* **2010,** *1*, 286-288.

[32] S. Lilliu, T. Agostinelli, E. Pires, M. Hampton, J. Nelson and J. E. Macdonald. Dynamics of Crystallization and Disorder During Annealing of P3HT/PCBM Bulk Heterojunctions. *Macromolecules* **2011,** *44*, 2725-2734.

[33] Mcculloch I, M. Heeney, C. Bailey, K. Genevicius, Macdonald I, M. Shkunov, D. Sparrowe, S. Tierney, R. Wagner, W. M. Zhang, M. L. Chabinyc, R. J. Kline, M. D. Mcgehee and M. F. Toney. Liquid-Crystalline Semiconducting Polymers with High Charge-Carrier Mobility. *Nature Materials* **2006,** *5*, 328-333.

[34] C. F. Zhang, S. W. Tong, C. X. Zhu, C. Y. Jiang, E. T. Kang and D. S. H. Chan. Enhancement in Open Circuit Voltage Induced by Deep Interface Hole Traps in Polymer-Fullerene Bulk Heterojunction Solar Cells. *Applied Physics Letters* **2009,** *94*, 103305.

[35] A. Bykhovski, B. Gelmont and M. Shur. The Influence of the Strain-Induced Electric-Field on the Charge-Distribution in GaN-AlN-GaN Structure. *Journal of Applied Physics* **1993,** *74*, 6734-6739.

[36] J. P. Ibbetson, P. T. Fini, K. D. Ness, S. P. DenBaars, J. S. Speck and U. K. Mishra. Polarization Effects, Surface States, and the Source of Electrons in AlGaN/GaN Heterostructure Field Effect Transistors. *Applied Physics Letters* **2000,** *77*, 250-252.

[37] E.H. Rhoderick and R.H. Williams. *Metal-Semiconductor Contacts*. Clarendon Press: 1988.

[38] N. W. Cheung S. K. Cheung. Extraction of Schottky Diode Parameters from Forward Current-Voltage Characteristics. *Applied Physics Letters* **1986,** *49*, 85-87.

[39] N. Matsuki, Y. Irokawa, T. Matsui, M. Kondo and M. Sumiya. Photovoltaic Action in Polyaniline/N-GaN Schottky Diodes. *Applied Physics Express* **2009,** *2*, 092201.

[40] M. Lozac'h, Y. Nakano, L. W. Sang, K. Sakoda and M. Sumiya. Fabrication of Transparent Conducting Polymer/GaN Schottky Junction for Deep Level Defect Evaluation under Light Irradiation. *Physica Status Solidi a-Applications and Materials Science* **2013,** *210*, 470-473.

[41] M. G. Harrison, J. Gruner and G. C. W. Spencer. Analysis of the Photocurrent Action Spectra of MEH-PPV Polymer Photodiodes. *Physical Review B* **1997,** *55*, 7831-7849.

[42] K. S. Narayan and T. B. Singh. Nanocrystalline Titanium Dioxide-Dispersed Semiconducting Polymer Photodetectors. *Applied Physics Letters* **1999,** *74*, 3456-3458.

[43] E. T. Yu, X. Z. Dang, P. M. Asbeck, S. S. Lau and G. J. Sullivan. Spontaneous and Piezoelectric Polarization Effects in III-V Nitride Heterostructures. *Journal of Vacuum Science & Technology B* **1999,** *17*, 1742-1749.

[44] F. Bernardini, V. Fiorentini and D. Vanderbilt. Spontaneous Polarization and Piezoelectric Constants of III-V Nitrides. *Physical Review B* **1997,** *56*, 10024-10027.

[45] M. Sumiya and S. Fuke. Review of Polarity Determination and Control of GaN. *MRS Internet Journal of Nitride Semiconductor Research* **2004,** *9*.

[46] O. Ambacher, J. Smart, J. R. Shealy, N. G. Weimann, K. Chu, M. Murphy, W. J. Schaff, L. F. Eastman, R. Dimitrov, L. Wittmer, M. Stutzmann, W. Rieger and J. Hilsenbeck. Two-Dimensional Electron Gases Induced by Spontaneous and Piezoelectric Polarization Charges in N- and Ga-Face AlGaN/GaN Heterostructures. *Journal of Applied Physics* **1999,** *85*, 3222-3233.

[47] M. J. Panzer and C. D. Frisbie. High Carrier Density and Metallic Conductivity in Poly(3-hexylthiophene) Achieved by Electrostatic Charge Injection. *Advanced Functional Materials* **2006,** *16*, 1051-1056.

Chapter 4: Kinetic Control of Perovskite Thin Film Morphology

4.1: Introduction

In contrast to the hybrid bilayer structure, the bulk hybrid active layers harbor greater potential. Hybrid organic-inorganic perovskites (OIP) have come into view as high-efficiency materials for their applications in low-cost, flexible, light weight PVs and display devices [1-6]. These materials can be easily solution proceed into thin films and have a low enthalpy of formation [7-9]. Charge transport characteristics in OIPs, like charge carrier mobility and diffusion length, are analogous to that of pure inorganic semiconductors [10-12]. Hybrid OIP show many notable properties like easy tunability of band gap [13, 14], geometrical structure and dimensionality tuning [15, 16] and high PL quantum yield (PLQY) [17]. The ability to easily form various nanostructures, along with the emission spanning over entire visible and infrared range of the electromagnetic spectrum is advantageous for various optoelectronic applications [3, 17-21].

Morphology tuning of polycrystalline thin films of OIP has shown to improve the device efficiencies considerable [3, 22, 23]. Decreasing the average size of OIP grains from tens of micron to tens of nanometer have resulted in remarkable enhancements in PL and EL of the films [3]. Simultaneously, the reduced grain size is also useful in a homogeneous distribution of OIP grains across the film which is inhomogeneously distributed in bulk films [24]. One of the ways highlighted for modifying the morphology of OIP thin films is by the use of antisolvent treatment. Cho et al. have used this technique in conjugation with the addition of organic small molecule additive to fabricate high-efficiency LEDs [3].

This chapter discusses the role of small molecule additives in defining the morphology of methylammonium lead bromide ($MAPbBr_3$) thin films. The kinetic control of thin film crystallization results into the formation of dendritic and maze-like structures composed of sub-micron OIP grains [24]. Such structures are advantageous for applications in a narrow channel or anisotropic charge transport such as field effect transistors [25, 26], high photoconductive gain and array based photodetectors [27, 28]. The choice of $MAPbBr_3$ is motivated by the visible range band edge emission which is useful for display and lighting applications [6]. The low-temperature meltable eutectic alloy is used as a cathode, with the modified OIP films, to realize a vacuum free, printable, all solution processed LED structure [29, 30].

4.2: Experimental Details

4.2.1: Materials

Methylammonium bromide (MABr) was procured from Dyesol, Australia, and $PbBr_2$ (99.999% metal basis) was bought from Alfa Asear and used as it is. Small molecule TPBi (2,2′,2"-(1,3,5-Benzinetriyl)-tris(1-phenyl-1-*H*-benzimidazole)) was purchased from Sigma-Aldrich. Low conductivity poly(3,4-ethylenedioxythiophene)-poly(styrene sulfonate)) (PEDOT:PSS) (Clevios P VP AI 4083, resistivity 500 – 5000 Ωcm) was obtained from Heraeus. The eutectic alloy was bought from Roto Metals, USA.

4.2.2: Sub-micron crystal (SMC) and device fabrication

Quartz and ITO-coated glass substrates were cleaned following the procedure described in section 2.3.2. OIP films for optical characterization were prepared on quartz substrates. For devices, low conductivity PEDOT: PSS was spin-coated at 3000 rpm on pre-cleaned ITO coated glass substrates and annealed at 180 ^{o}C for 10 min in a nitrogen atmosphere. SMCs were formed using microcrystal pinning (MCP) process via two different routes. When only the anti-solvent ($CHCl_3$) was used (described as solvent assisted sub-micron crystal (S-SMC)) the grain sizes were larger compared to that of the films made using small molecule additives, mixed in anti-solvent (A-SMC). The grain size and film morphology show a strong dependence on the solubility and concentration of additive. An n-type small molecule like PTCDA (perylene-3,4,9,10-tetracarboxylic dianhydride) or TPBi was dissolved in chloroform ($CHCl_3$) at very low concentration (~ 0.2 wt %) to be used as an additive. The OIP layer was spin coated on PEDDOT: PSS/ITO/Glass substrates from a 40 wt % solution of $PbBr_2$ and MABr (1:1.05 molar ratio) in dimethyl sulfoxide (DMSO). After the 60s, while the OIP film is still spinning, the additive mixed antisolvent is added in quick continuous drops. A thick layer of TPBi (50-60 nm) was coated on SMC at 2000 rpm from a 30 mg/ml solution in $CHCl_3$.The SMC and TPBi films did not require any annealing and the entire process was carried out at room temperature. Alloy cathode was deposited by following the procedure described in section 2.3.3.

4.2.3: Characterization

Optical and structural: Unmodified and morphologically modified SMC films were coated on quartz substrates for optical measurements. PL and PLQY measurements were performed in a custom integrated quantum yield setup. PL was collected using a fiber coupled Si CCD-based spectrometer. 405 nm laser (~100 mW) was used for excitation. Sub-bandgap absorption studies were carried out using photothermal deflection spectroscopy. Crystallization properties of thin films of untreated OIP and SMC were studied using powder X-ray diffractometer, where 2θ was varied from 10 - 90 degree.

Microscopy: AFM and confocal microscopy were carried out on an integrated confocal (LSM 700) - AFM (Nano wizard 3) setup from Carl Zeiss and JPK Instruments, Germany. AFM topography and phase images were recorded in non-contact tapping mode using a 300 KHz cantilever (force constant ~ 40 N/m). Localized emission map was recorded using 100× oil immersion objective, and 488 nm excitation. Emission was recorded using a photomultiplier tube (PMT), for spectral emission map the emission was split into two channels via a variable dichroic. SEM and energy dispersive x-ray spectroscopy (EDAX) were performed in a Bruker Instrument.

Electrical characterization: LEDs fabricated using A-SMC as an active layer and meltable alloy as a cathode were characterized in a custom built LED characterization set-up. Keithley 2400 source meter used as a voltage source, the LED emission was recorded using a calibrated Si detector in reverse biased configuration. EL spectrum was captured using a fiber coupled Si CCD-based spectrometer (Ocean Optics).

“All measurements were performed in air without any encapsulation layer.”

4.3: Result and Discussion

4.3.1: Crystallization of sub-micron OIP crystals

The process of the formation of sub-micron crystals is governed by the kinetic control factors like drying of solvent and the movement of OIP grains during the solvent drying process. Thermodynamically, the crystallization process is controlled by the minimization of Gibbs free energy of the system. Crystallization from the solution phase is known to result in the formation of ordered structures, where the symmetry of crystal plays a crucial role in controlling the large-scale morphology [31, 32]. Such process happens over an extended period and results in a structure representing local minima in the free energy curve. Figure 4.1a shows one such microscopic image of $MAPbBr_3$ OIP grains crystallized thermodynamically, inherent cubic symmetry is replicated as large cubes over micron scale. The film shows high roughness (~ micrometer) and contains large voids, where the OIP thickness is very less as can be inferred from topography and the phase mapping (Figure 4.1b). Such films are not suitable for optoelectronic devices, due to the large density of electrical shorts between anode and cathode.

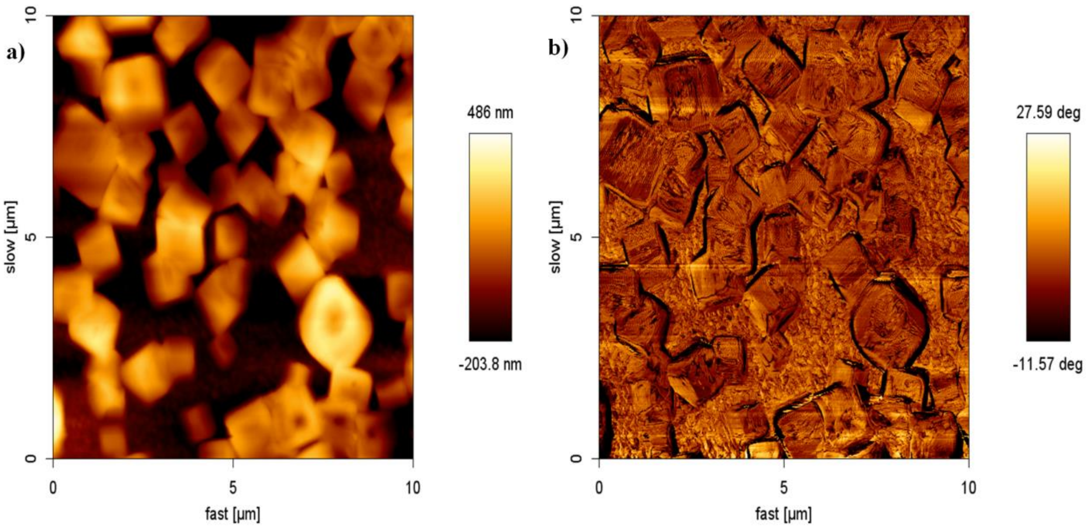

Figure 4.1: *a) AFM topography image of OIP grains crystallized from solution in spin-coated thin films, b) phase image of OIP grains. (Reprinted with permission from P. Kumar, B. Zhao, R. H. Friend, A. Sadhanala, and K. S. Narayan, Kinetic Control of Perovskite Thin Film Morphology and Application in Printable Light Emitting Diodes, ACS Energy letters, 2, 1, 81-87, copyright (2017) American Chemical Society).*

However, the crystallization can be altered by introducing certain kinetic elements during the process which can result in entirely different morphology [15]. In the case of OIP thin films, use of solvent extraction by using orthogonal solvents/antisolvent has been reported to modify the morphology and the quality of the thin films for electronic applications. By the use of orthogonal solvents the solubilizing medium, which is DMSO or DMF in the case of OIP, is rapidly expelled from the film. This process initiates formation of multiple nucleation sites which can rapidly grow into small grains, due to the drying of solvent [33].

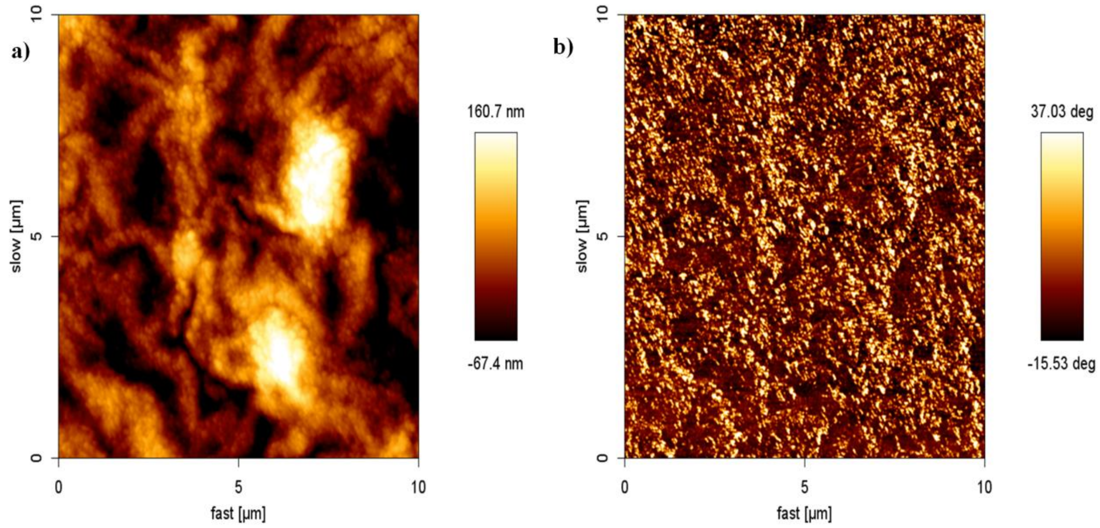

Figure 4.2: *a) AFM topography image of OIP thin film after treatment with* $CHCl_3$*, b) phase image of S-SMC film. (Reprinted with permission from P. Kumar, B. Zhao, R. H. Friend, A. Sadhanala, and K. S. Narayan, Kinetic Control of Perovskite Thin Film Morphology and Application in Printable Light Emitting Diodes, ACS Energy letters, 2, 1, 81-87, copyright (2017) American Chemical Society).*

Large scale crystallization and rapid growth results in the reduction of the OIP grain size from tens of micron to tens of nanometer. Such processes are controlled by the kinetics of solvent evaporation, which also results in large scale homogeneous distribution of SMC OIP grains. Figure 4.2 shows the effect of $CHCl_3$ as an orthogonal solvent on the thin film morphology of $MAPbBr_3$. As can be easily noticed, the micron-sized grains have been reduced to a sub-micron level (200-400 nm) (Figure 4.2a), while the surface coverage has been greatly improved (Figure 4.2b).

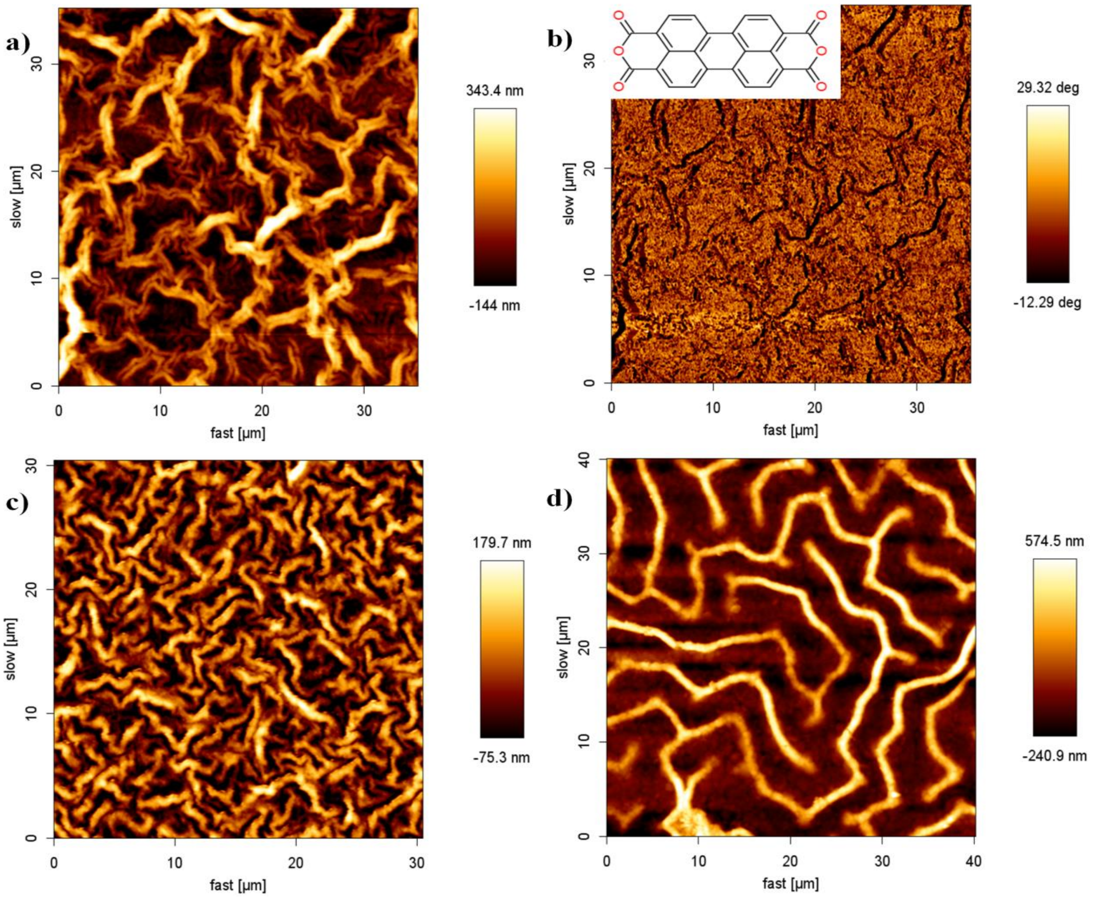

Figure 4.3: *a) AFM topography and b) phase image of PTCDA additive based A-SMC films. c) and d) morphology variation by changing the processing parameters. (Reprinted with permission from P. Kumar, B. Zhao, R. H. Friend, A. Sadhanala, and K. S. Narayan, Kinetic Control of Perovskite Thin Film Morphology and Application in Printable Light Emitting Diodes, ACS Energy letters, 2, 1, 81-87, copyright (2017) American Chemical Society).*

The morphology can be further tuned by using small molecule additive mixed in antisolvent. Small molecules used as additives are n-type organic molecules which can be easily dissolved or dispersed in $CHCl_3$. It has been shown that when blended with the OIP precursor, the small molecules can easily get trapped at the grain boundaries [34]. Preferential orientation resulting from the stacking of small molecules and kinetics introduced by the solvent evaporation can tailor the macroscopic morphology. Figure 4.3 shows the topography image of OIP A-SMC films fabricated using 0.2 wt % PTCDA in $CHCl_3$. The origin of such structure can be associated with the nature of PTCDA to stack and form fibrillar networks [35].

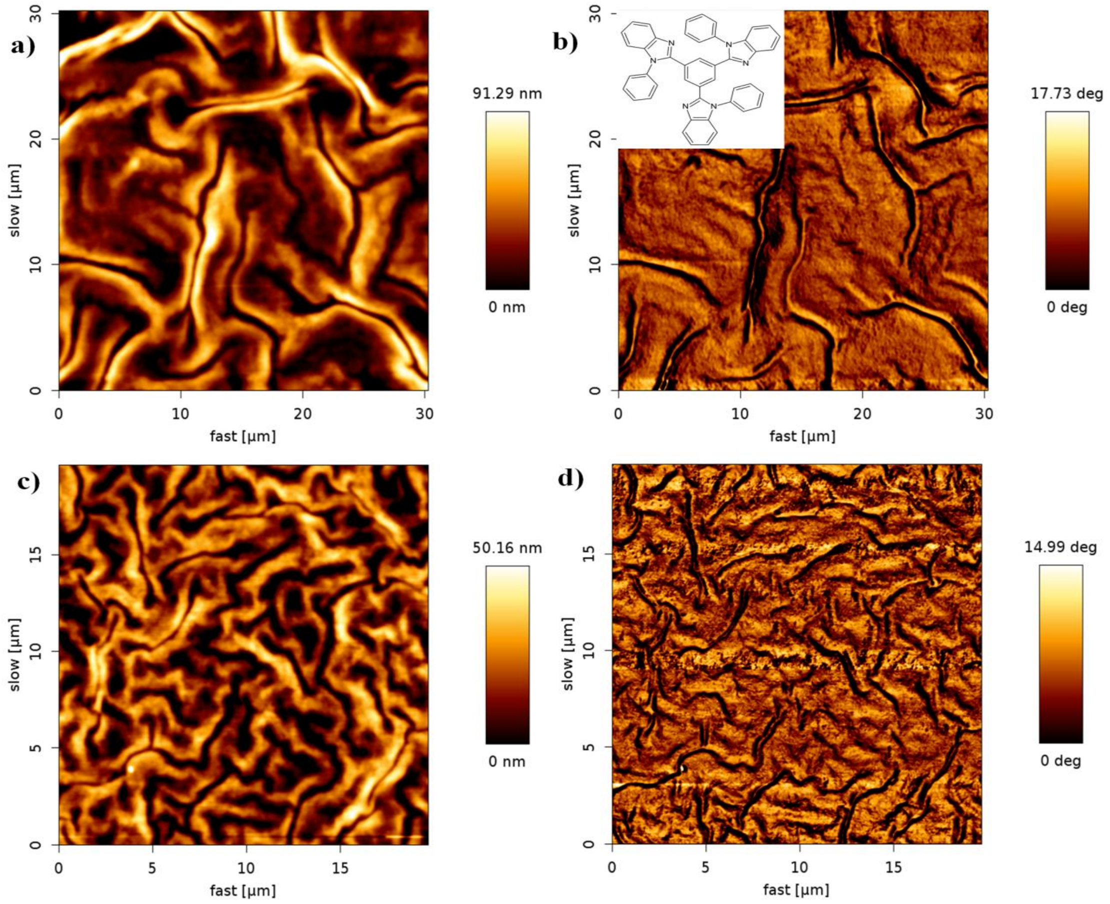

Figure 4.4: *A-SMC films based on TPBi additives, a) and c) topography and b) and d) phase treated with the small and large volume of 0.2 wt % TPBi mixed* $CHCl_3$.

The sub-micron grain size is further reduced (~ 100-300 nm) as compared to that of $CHCl_3$ treated S-SMC films. The phase image shows a uniform distribution of OIP grains across the scan area. The formation of the fibrillar network is sensitive to the processing conditions and can yield a different morphology by changing the time delay before the additive is added. Figure 4.3c and 4.3d show the effect of altering the delay time by at most 20s. The solubility and structure of additive also influence the overall morphology of the film, as can be seen in Figure 4.4.

A small molecule like TPBi, which has different solubility in $CHCl_3$ results in much planar, wrinkled and folded like morphology with much less surface roughness. By changing the volume of additive the size of wrinkles can be tuned as is seen in Figure 4.4a and 4.4c. The phase image shows a much smooth distribution and a further decrease in pinhole density. By increasing the concentration of TPBi from 0.2 wt % to 1.3 wt %, the morphology shows a large modification, with no observable surface microstructures (Figure 4.5a).

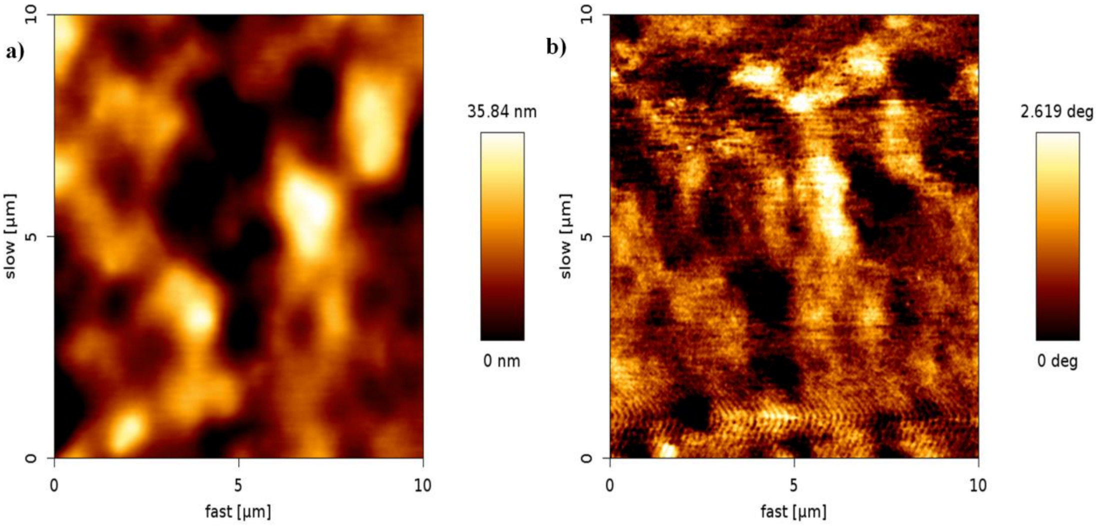

Figure 4.5: *The AFM a) topography and b) phase image of OIP films treated with 1.3 wt % TPBi dissolved in* $CHCl_3$.

This can be attributed to large density of TPBi molecules which can homogenize the surface variations underneath. Simultaneously the phase image also shows a much less variation (Figure 4.5b) as compared to that of OIP surface seen previously.

Above highlighted morphologies represent local minima along the free energy curve and can go under further modification upon thermal treatment. Figure 4.6a shows the AFM topography of PTCDA modified A-SMC films annealed for 5 min at 100 ^{0}C under a nitrogen atmosphere. As can be noticed, the grains are homogeneously distributed, similar to the unannealed films, however, the unique fibrillar network gets modified to a much smoother surface with an average surface roughness < 50 nm. Though the overall morphology gets significantly modified, the average grain size remains similar to the un-annealed film. Simultaneously the phase image (Figure 4.6b) shows a smaller variation as compared to the unannealed films.

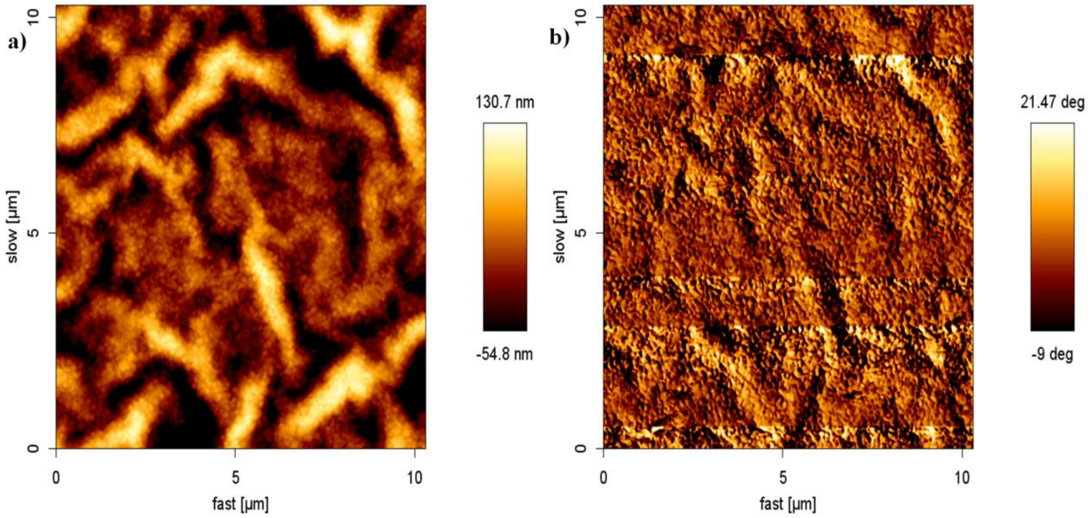

Figure 4.6: *a) AFM topography and b) phase image of PTCDA based A-SMC after annealing.*

4.3.1 I: Crystallization kinetics

The kinetics of crystallization, in solution growth of crystalline materials, is governed by the minimization of Gibbs free energy. In the equilibrium crystallization process, like controlled evaporation of the solvent, the concentration of solute increases with solvent evaporation. The difference in the chemical potential (μ) in solution (μ_L) and crystallite phase (μ_S) is the thermodynamic driving force for crystallization. As one moves along the pressure axis in the P-V phase diagram (Figure 4.7a), the $\Delta\mu = \mu_L - \mu_S$ increases, resulting in a supersaturation. The nucleation rate depends exponentially on supersaturation (Figure 4.7b). During the equilibrium growth process, the shape of the crystallite is governed by the Wulff plot [36]. The equilibrium shape is controlled by the minimization of the surface tension over all faces. However, under non-equilibrium cooling processes, the growth of one face can be preferred, leading to morphological instabilities and dendritic growth. Further, the presence of organic ligands during the crystallization process can significantly influence the growth and morphological arrangement of grains. The organic ligands can bind with the surface of the grain and restrict further growth, thereby controlling the size of the grain. These ligands can also interact within themselves to form unique morphologies which can be a representative of the stacking nature of the organic ligands (Figure 4.7c). The fibrillar structure observed in the case of PTCDA additive can be related to the inherent nature of perylene to form fibers [35], while similar behavior is not present in TPBi films.

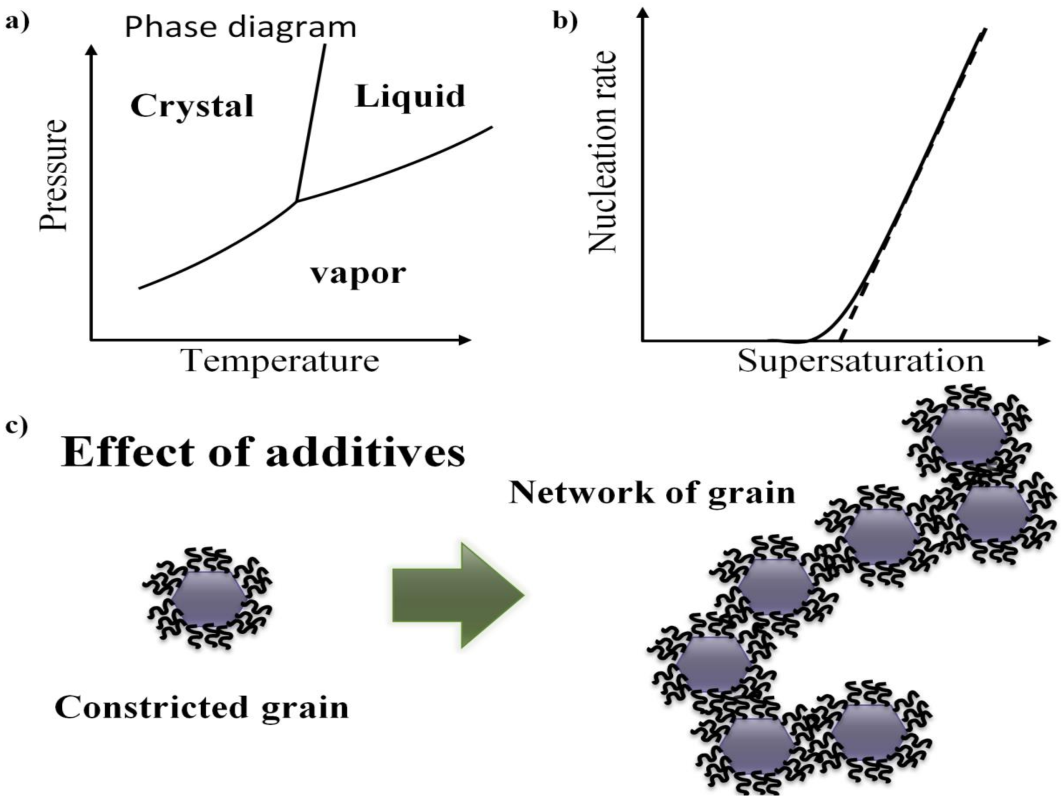

Figure 4.7: *a) Schematic P-V phase diagram, b) nucleation rate as a function of super saturation and c) schematic depicting the formation of the fibrillar network in presence of organic ligands.*

4.3.2: Crystal structure of sub-micron grains

The large scale modifications observed in OIP thin film morphology does not alter the inherent crystal structure. Cubic symmetry is prevalent in untreated and PTCDA treated A-SMC thin films alike, as is shown in Figure 4.8. The 2θ peak for PTCDA modified A-SMC grains at 14.9^0 (100), 21.14^0 (110), 30.11^0 (200), 33.77^0 (210), 37.12^0 (211), 43.11^0 (220) and 45.9^0 (300) represent cubic symmetry identical to the literature values. Lattice constant (*a*) calculated from 2θ is ~ 5.95 Å which is in good agreement with the previous reports [37, 38]. The XRD peak for untreated OIP grains are shifted by 0.07^0 towards lower θ as compared to PTCDA treated A-SMC peaks suggesting a small shift in "lattice constant-*a*", as shown in the inset of Figure 4.8).

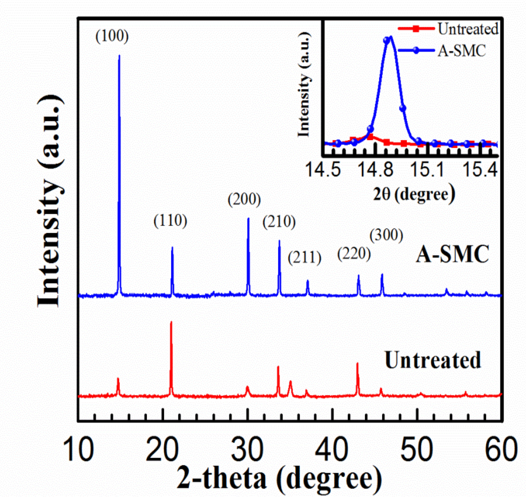

Figure 4.8: *Powder X-Ray diffraction of untreated OIP grains (red) and PTCDA treated A-SMC, inset is a zoom in on (100) peak. (Reprinted with permission from P. Kumar, B. Zhao, R. H. Friend, A. Sadhanala, and K. S. Narayan, Kinetic Control of*

Perovskite Thin Film Morphology and Application in Printable Light Emitting Diodes, ACS Energy letters, 2, 1, 81-87, copyright (2017) American Chemical Society).

The origin of a shift in XRD peak can be related to the stoichiometry imbalance in OIP structure where, *a,* is smaller than expected. Compressive stress in large crystals has also been associated with such shifts when the grain size is reduced such strains can get relaxed. The stoichiometry of the OIP precursor was altered from the standard 1:1 to 1:1.05 molar ratios of $PbBr_2$ and MABr. Higher content of MABr has been shown to be helpful in a complete conversion of the lead salt into perovskite structure, which otherwise can be present as metallic Pb centers, acting as exciton quenching sites [3]. Untreated and PTCDA modified A-SMC were fabricated from same precursor solution to maintain an identical stoichiometry. The boundary conditions involved during the crystallization of large grains can bring in strain in the crystallites.

4.3.3: Reduced disorder in S-SMC and A-SMC films

As the average crystallite size is reduced by ~ 100 times, the associated disorder and PL is expected to be modified. To probe the variation in sub-band gap states, Photo Thermal Deflection (PDS) technique was used (*PDS measurements were performed by Dr. Aditya Sadhanala, at Prof. Sir Richard Friend's Laboratory, at Cavendish Laboratory, Cambridge, UK*). PDS is known for its 4-5 orders of the dynamic range of measurement compared to standard absorption which is limited to 2-3 orders [38, 39]. Absorbance measured through PDS shows more than an order of magnitude decrease in subgap absorption compared to the untreated films. The order of decrease is identical for S-SMC and A-SMC (Figure 4.9a), suggesting that the grain size reduction is the only factor responsible for the decrease in subgap absorption. The presence of additives does not have any additional influence unless the additive itself does not absorb in the subgap region. As can be seen in Figure 4.8a, the subgap absorption for PTCDA based A-SMC shows an additional shoulder which is not present for S-SMC absorption. The origin of this feature has been related to tail state absorption in PTCDA used as the additive which overlaps well with the observed feature as shown in Figure 4.9b. This suggests that the small molecules are embedded at the grain boundaries, a similar observation has been reported with other OIP/small molecule blend system as well [34].

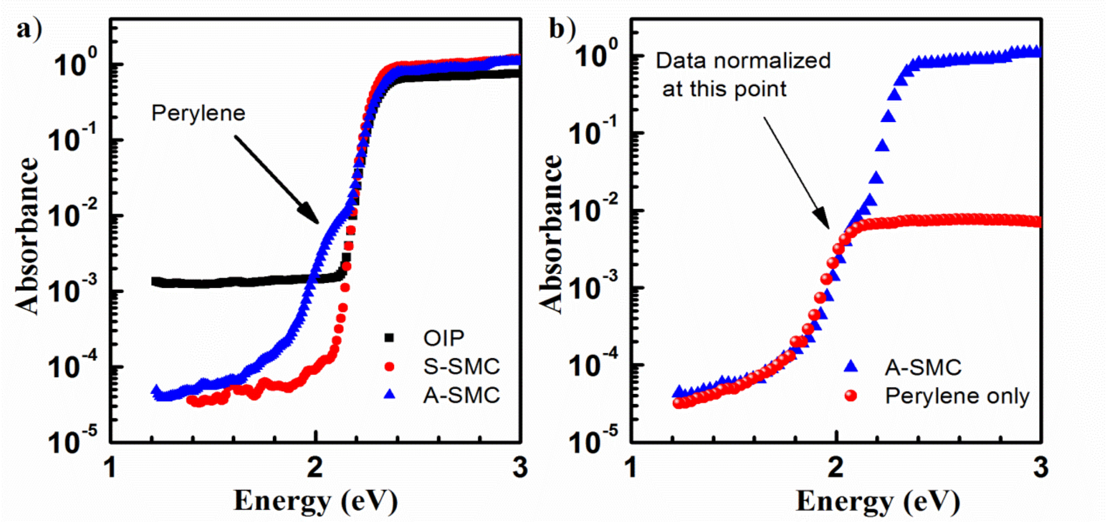

Figure 4.9: a) PDS absorbance measured for untreated OIP, S-SMC and A-SMC, b) A-SMC absorbance plotted against absorbance of PTCDA only films. (Reprinted with permission from P. Kumar, B. Zhao, R. H. Friend, A. Sadhanala, and K. S. Narayan, Kinetic Control of Perovskite Thin Film Morphology and Application in Printable Light Emitting Diodes, ACS Energy letters, 2, 1, 81-87, copyright (2017) American Chemical Society).

4.3.4: Photoluminescence and lifetime improvements in A-SMC

The reduced average grain size of OIP and accompanied decrease in disorder in the absorbance is also followed by an increase in PL yield. The PL intensity increases by ~ 6 times, while the PLQY increases from 1-2%, for untreated film, to 25% for PTCDA, treated A-SMC. The increase in PL intensity is partially attributed to the confinement of charge carriers in the sub-micron grains which results in increased bulk and surface radiative recombination due to the increased localization of carriers [3]. Factors such as a decrease in non-radiative defect density are also helpful in increasing the PL intensity. The PL peak emission does not shift with a decrease in crystallite size suggesting that the average crystallite size is still in bulk domain (Figure 4.10a). PL lifetime (τ) shows a similar increase from ~ 2 ns for untreated OIP film to ~ 36 ns for PTCDA treated A-SMC films (Figure 4.10b).

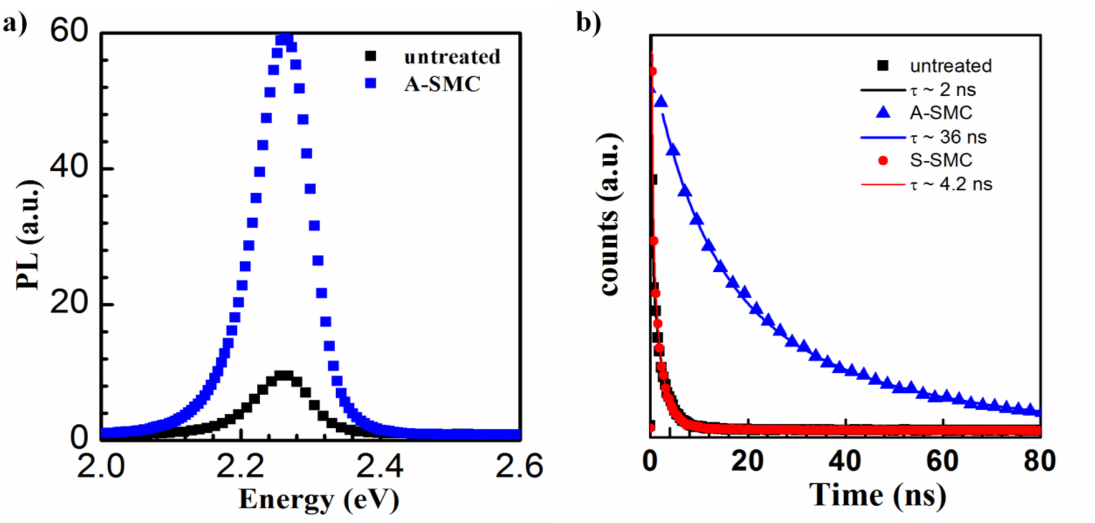

Figure 4.10: a) *PL from untreated OIP films (black) and PTCDA treated A-SMC (blue) and b) PL lifetime decay curve. (Reprinted with permission from P. Kumar, B. Zhao, R. H. Friend, A. Sadhanala, and K. S. Narayan, Kinetic Control of Perovskite Thin Film Morphology and Application in Printable Light Emitting Diodes, ACS Energy letters, 2, 1, 81-87, copyright (2017) American Chemical Society).*

The decrease in sub-band gap absorption can be attributed to the reduction in the non-radiative defect state density which can also be estimated from τ and PLQY. PLQY and τ can be written in terms of radiative (k_r) and non-radiative (k_{nr}) decay rates as,

$$PLQY = \frac{k_r}{(k_r + k_{nr})} \tag{4.1}$$

and

$$\tau = \frac{1}{(k_r + k_{nr})} \tag{4.2}$$

The k_r shows slight increases from ~ 5×10^6/s, for untreated OIP films, to ~7×10^6/s for PTCDA treated A-SMC. A large decrease, of an order of magnitude, is observed for k_{nr} which decreases from ~ 2.5×10^8/s, for untreated OIP films, to ~ 2.3×10^7/s for A-SMC films. Factors, like increased outcoupling and reduced internal re-absorption processes, can also add to the observed increase in PL quantum yield.

4.3.5: Localized photoluminescence spectral imaging

Emission at sub-micron scale can provide critical information about the distribution of luminous OIP grains. Emission variation from point to point can be mapped and the overall luminescence quality of the OIP film can be established. Using confocal technique and sequential gating of emission to two separate PMT channels, it is possible to create a detailed emission spectral plot with sub-micron spatial resolution giving a distribution in emission spectral profile. The major fraction of PL in untreated OIP films remains restricted to large cube like grains, which sharply decreases outside the region (Figure 4.11a). The emission peak energy for 3 distinct regions, marked as 1,2 and 3 in Figure 4.10a, shows a large variation from ~ 2.20 - 2.32 eV around the far field emission ~ 2.26 eV (Figure 4.11b). Large contrast in dark and bright regions can be associated with the concentration of OIP in the region. The emission for A-SMC is homogeneous and closely resembles the morphology (Figure 4.11c), while the peak energy for 3 distinct regions, marked as 1, 2 and 3 in Figure 4.11c, shows a much smaller spread compared to that of untreated OIP films (Figure 4.11d).

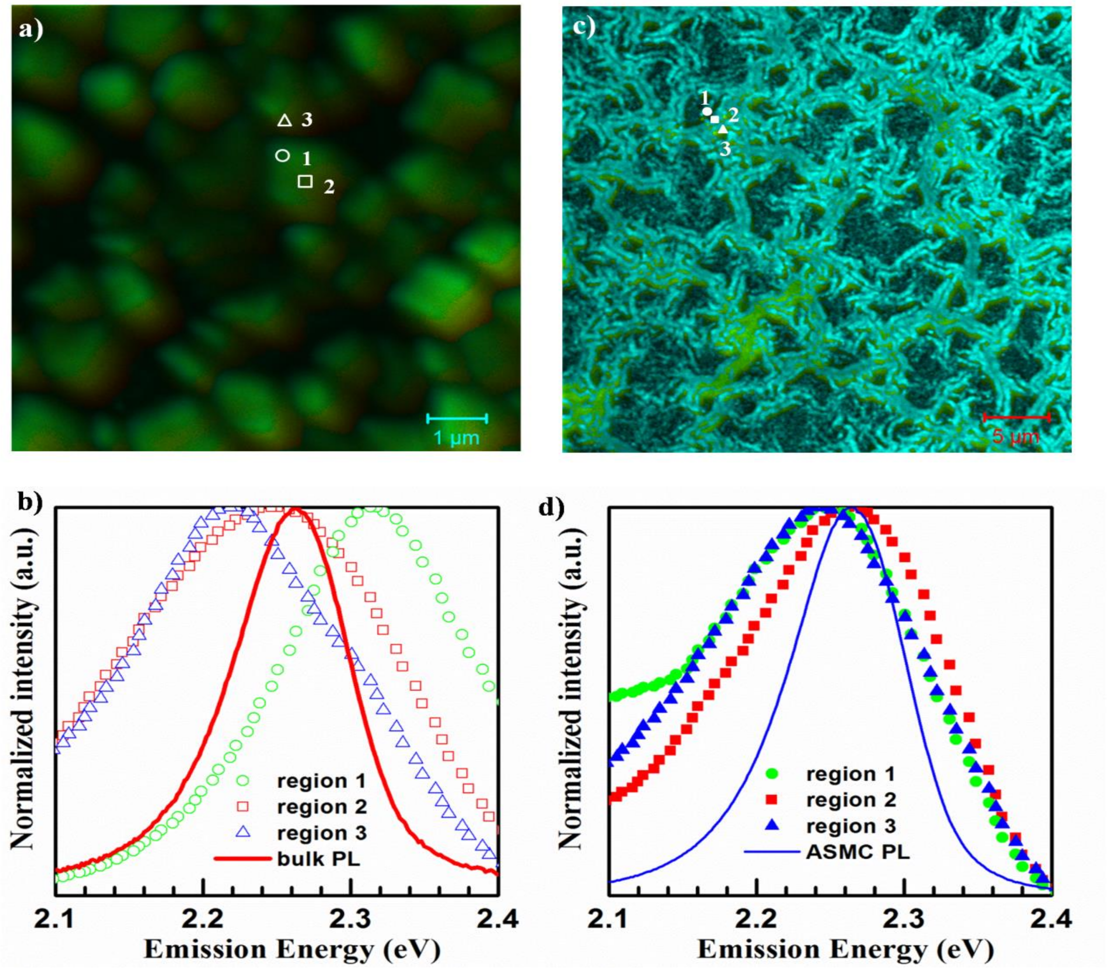

Figure 4.11: ***a****) Localized spectral emission map for untreated OIP films, b) Emission profile across 3 distinct regions (1, 2 and 3) market in (a), c) Confocal spectral map of PTCDA treated A-SMC thin film, d) emission profile across 3 distinct regions (1,2 and 3) marked in (c). (Reprinted with permission from P. Kumar, B. Zhao, R. H. Friend, A. Sadhanala, and K. S. Narayan, Kinetic Control of Perovskite Thin Film Morphology and Application in Printable Light Emitting Diodes, ACS Energy letters, 2, 1, 81-87, copyright (2017) American Chemical Society).*

Emission peak shift can be related to the effects of internal re-absorption or photon recycling processes previously reported in OIP films and crystals [40]. Larger variation in untreated films can arise from the larger difference in path length present from point to point due to the bigger grain size. Multiple internal re-absorption can modify the far-field PL. In the case of A-SMC film, where the grain size is much smaller and more homogeneously distributed, the variation in peak energy is much smaller. Small variations can still arise from the morphology related effects. The large width of PL, observed in confocal, arises from the instrument response function and has no material origin.

Emission map for S-SMC films does not show any correlation with the morphology, simultaneously, the emission distribution is inhomogeneous (Figure 4.12a). The annealed films show the distribution of emission similar to the PTCDA treated A-SMC without any structural features (Figure 4.12b).

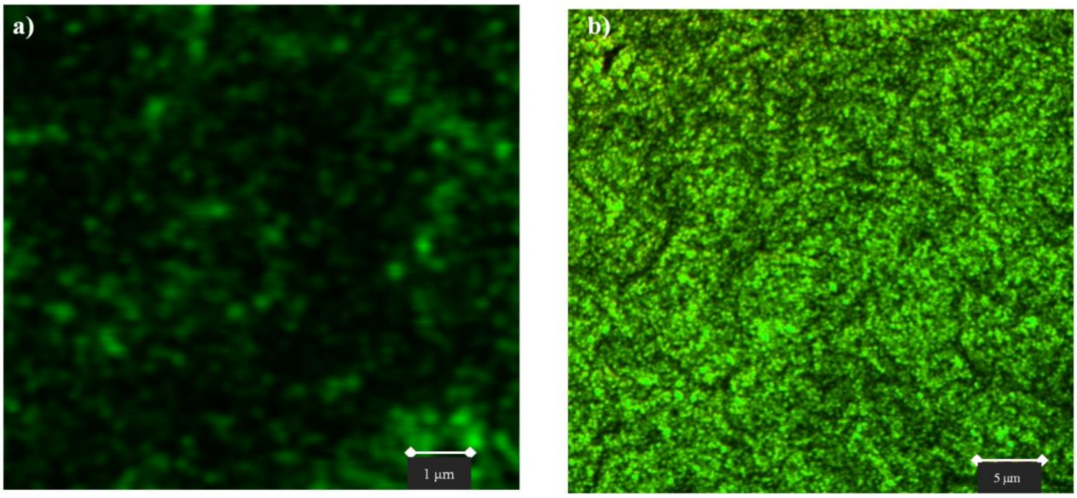

Figure 4.12: *Localized emission map for a) S-SMC and b) PTCDA based A-SMC after annealing at 100 ^{0}C for 5 min.*

Emission distribution in TPBi based A-SMC is homogeneous over the entire scan area as shown in Figure 4.13. The average particles size is smaller than that of PTCDA based A-SMC. The fibrillar structures visible in emission spectra can be seen as the edges of folded, wrinkle like structure where OIP concentration is higher resulting in stronger emission compared to the uniform background. Such improvements in emission are ideally suited for EL devices like LEDs.

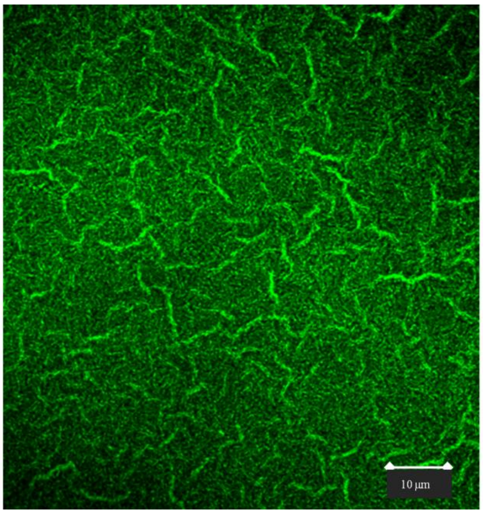

Figure 4.13: *Emission map of A-SMC films prepared using 0.2 wt % TPBi.*

4.3.6: Low-temperature printable light emitting diode

Large improvements observed in morphology and emission of OIP films fabricated using additive-assisted process can be easily integrated into efficient device structures. A schematic of printable LED and vacuum level energy diagram along with two step A-SMC fabrication has been shown in Figure 4.14.

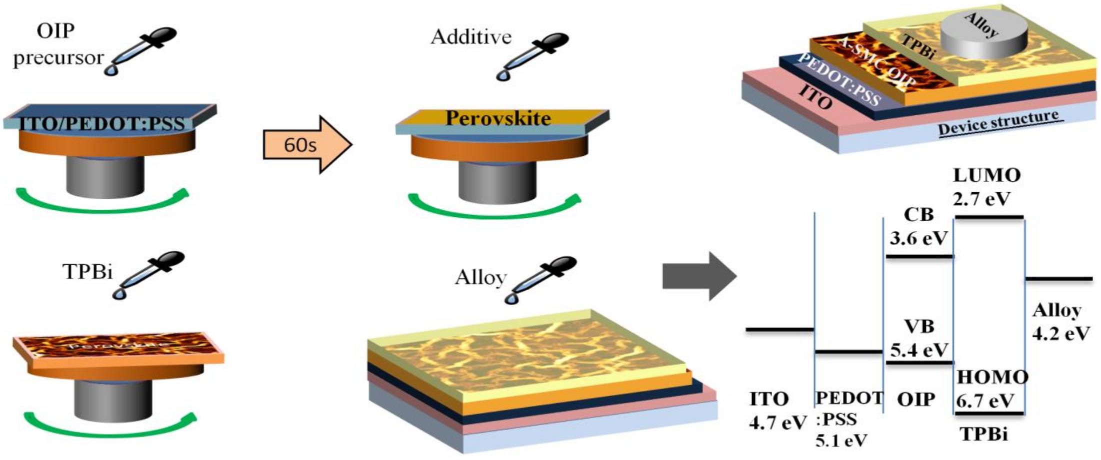

Figure 4.14: *Schematic of fabrication of A-SMC OIP based printable LED structure.*

The innate surface variation observed in A-SMC films makes the eutectic alloys more suitable candidate for cathode layer. These alloys, being able to stick conformally with the underneath layer can preserve the microstructures while forming a smooth contact for charge injection [30]. The morphology of alloy cathode in contact with the TPBi layer is imaged in SEM, after carefully peeling it off and washing with chloroform. Sub-micron sized surface roughness can be seen in the active region as shown in Figure 4.15.

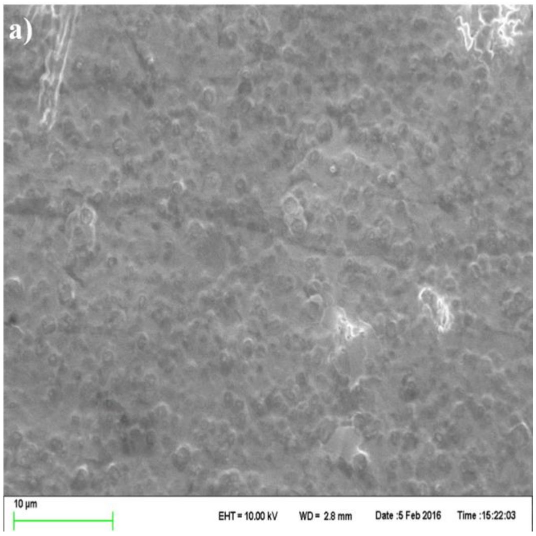

Figure 4.15: *SEM micrograph of alloy cathode in contact with TPBi layer. (Reprinted with permission from P. Kumar, B. Zhao, R. H. Friend, A. Sadhanala, and K. S. Narayan, Kinetic Control of Perovskite Thin Film Morphology and Application in Printable Light Emitting Diodes, ACS Energy letters, 2, 1, 81-87, copyright (2017) American Chemical Society).*

Along with the uniform coverage and improved PL, balanced charge mobility is essential to ensure that the recombination occurs in the OIP bulk, leading to a color pure electroluminescence (EL). Charge transport mobility in electron and hole only devices were measured in ITO/TiO_2/OIP/TPBi/Alloy and ITO/PEDOT: PPS/OIP/PTB7/Au configuration respectively. Space charge limited current (SCLC) method is suitable for estimating mobility in pristine semiconductors of thickness greater than 200-300 nm. The Current-voltage curve for electron only and hole only devices is shown in Figure 4.16. The bulk charge transport mobility for electron and hole was estimated to be ~ 10^{-2} cm^2/Vs. While the transport is balanced; a low value can result from a large number of grain boundaries and the additional layers which can limit the measured average bulk mobility.

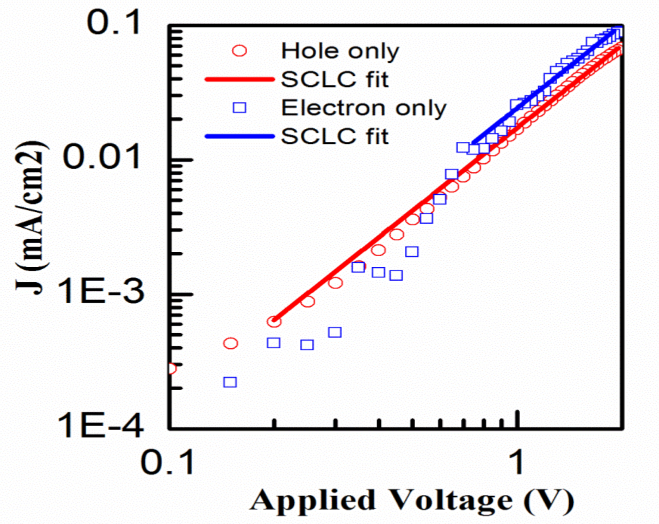

Figure 4.16: *J-V curve for hole only (red circle) and electron only (blue square) devices and respective SCLC fit. (Reprinted with permission from P. Kumar, B. Zhao, R. H. Friend, A. Sadhanala, and K. S. Narayan, Kinetic Control of Perovskite Thin Film Morphology and Application in Printable Light Emitting Diodes, ACS Energy letters, 2, 1, 81-87, copyright (2017) American Chemical Society).*

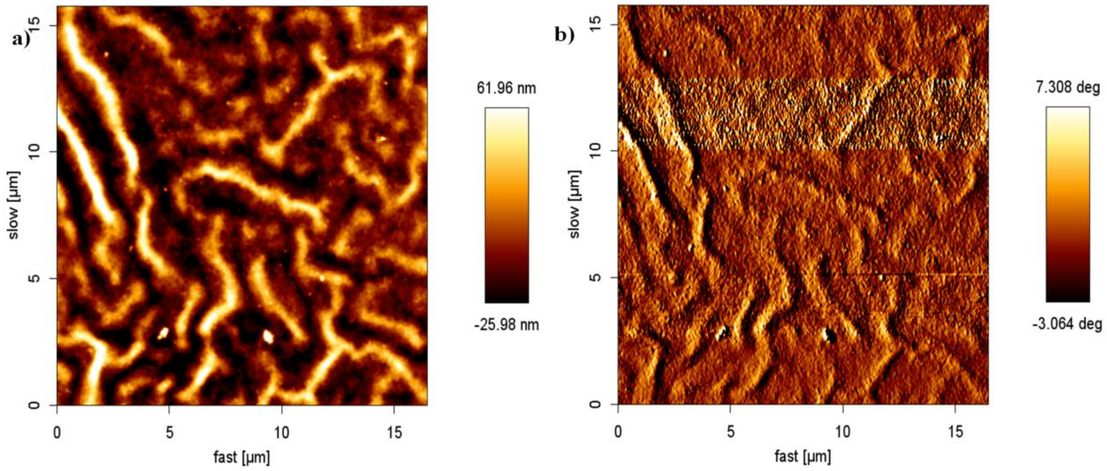

__Figure 4.17:__ Passivation of the fibrillar network in the presence of additional transport layer a) morphology and b) phase map.

The top transport layer can easily passivate the microfibrillar network observed in the case of A-SMC. Figure 4.17 shows a representative image of reduced surface roughness in PTCDA based A-SMC films after coating thin films of the transport layer, which is essential for homogeneous injection of charges. The A-SMC EL and PL have an identical width, as shown in Figure 4.18.

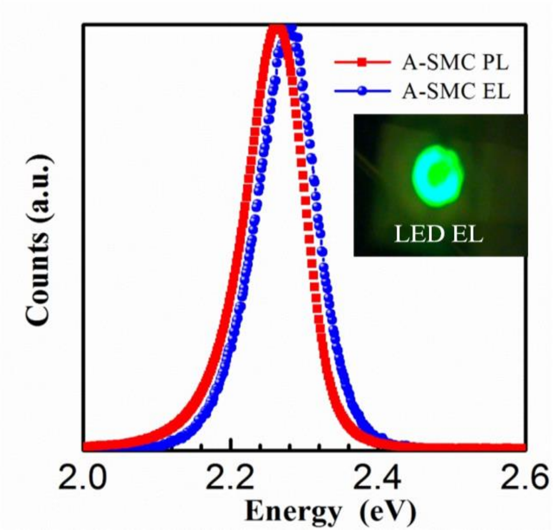

__Figure 4.18:__ PL (red, square) and EL (blue, circles) from a typical A-SMC film. The inset shows an image of the working pixel. (Reprinted with permission from P. Kumar,

B. Zhao, R. H. Friend, A. Sadhanala, and K. S. Narayan, Kinetic Control of Perovskite Thin Film Morphology and Application in Printable Light Emitting Diodes, ACS Energy letters, 2, 1, 81-87, copyright (2017) American Chemical Society).

The LEDs fabricated using A-SMC as an active layer with PTCDA and TPBi as additives show comparable electrical characteristics. The PTCDA based devices show an early rise in current compared to TPBi based devices as seen in Figure 4.19a.

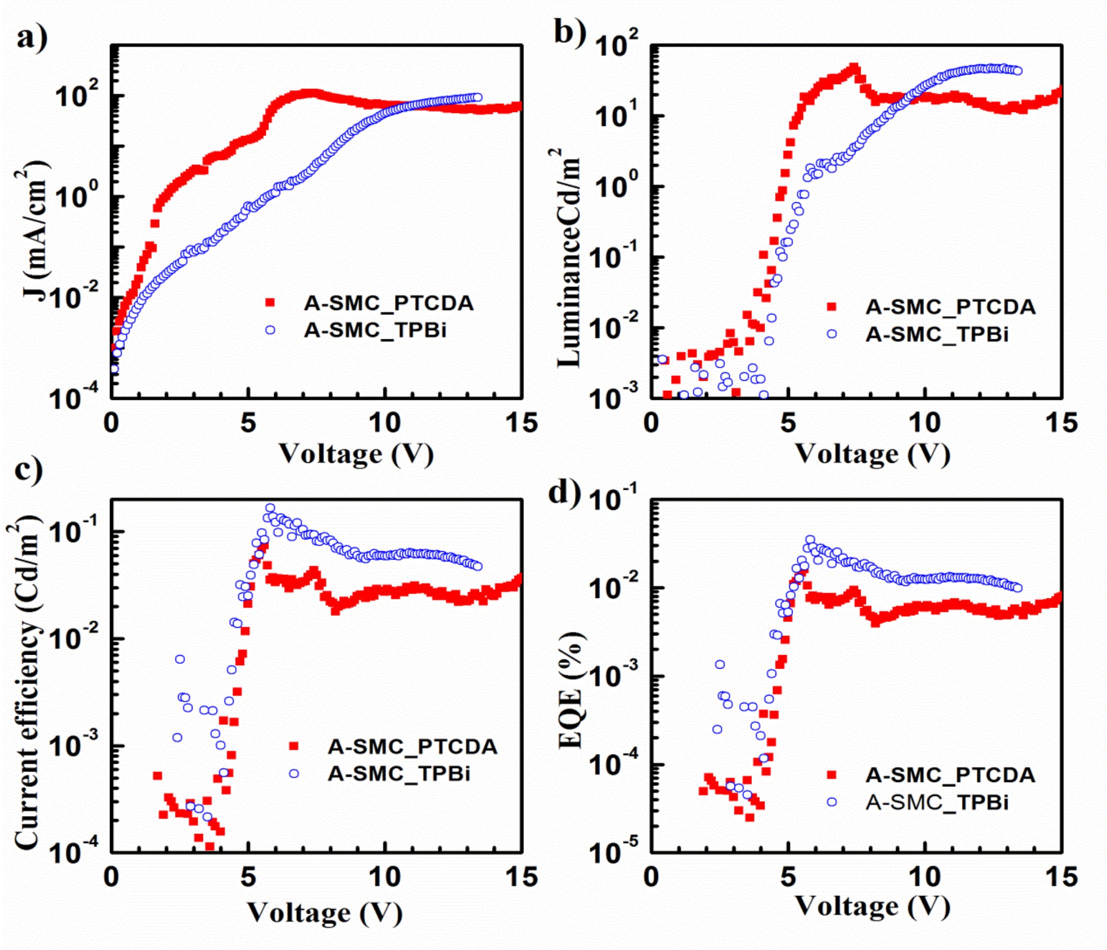

Figure 4.19: *LED characteristics of A-SMC fabricated using PTCDA and TPBi, a) J-V, b) Luminance, c) Current efficiency and d) EQE plot. (Reprinted with permission from P. Kumar, B. Zhao, R. H. Friend, A. Sadhanala, and K. S. Narayan, Kinetic Control of Perovskite Thin Film Morphology and Application in Printable Light*

Emitting Diodes, ACS Energy letters, 2, 1, 81-87, copyright (2017) American Chemical Society).

This observation can be linked to the fibrillar network which can act as percolation pathways. Which results in peak luminance at a lower voltage for PTCDA based devices (Figure 4.19b). However, the smaller grain size and better PLQY for TPBi based A-SMC is reflected in higher current efficiency and EQE compared to that of PTCDA based A-SMC. For both the A-SMC films the maximum performance is achieved at ~ 5V forward bias after which the output steadily drops to ~ 35% of maximum.

The decrease in performance after an early saturation is a result of thermal burn in noticed for all devices [41]. This process was driven by a unique feature specific to the OIP A-SMC films, after the coating of TPBi layer as electron transporter.

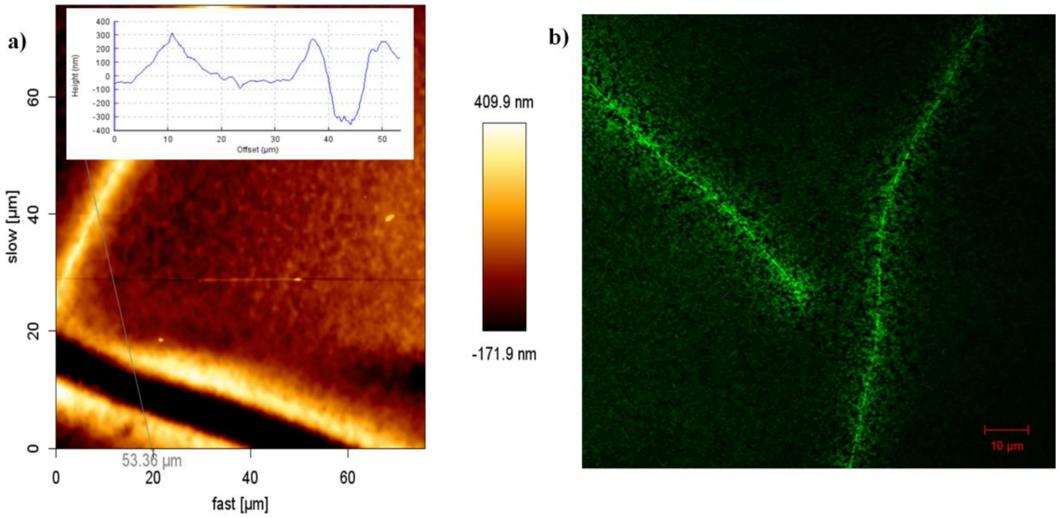

Figure 4.20: *Crack formation in OIP film after spin coating a thick layer of TPBi, a) AFM height image and b) confocal fluorescence map of cracked film.*

The drying of TPBi layer introduces strain in the films which result in the formation of uneven cracks and hill like structures as shown in the AFM topography

(Figure 4.20a). Fluorescence mapping suggests that the uneven structures are largely composed of OIP grains which have emission similar to the bulk (Figure 4.20b). These structures act as the sites of failure for the entire device by forming electrical short circuit at large forward bias. It is interesting to note that the crystalline films can be modulated with such an ease under solvent processing.

Low-melting alloys can perform suitably with a variety of active layers as charge injection and collection layer. Apart from the LEDs, the OIP PVs fabricated using liquid alloy electrode demonstrate efficient devices with PCE as high as 11% (figure 4.21).

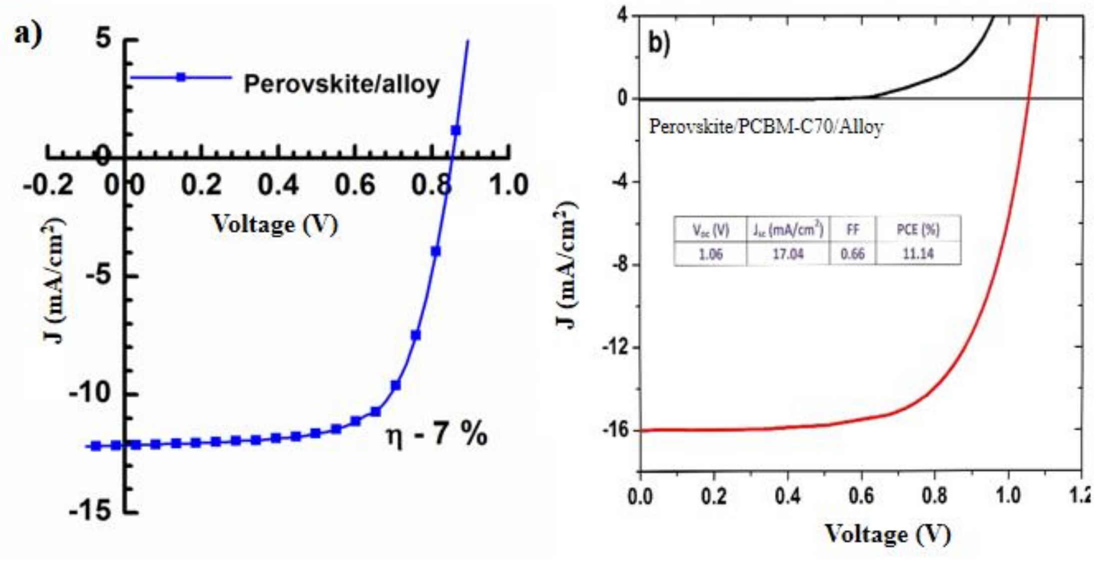

V_{oc} (V)	J_{sc} (mA/cm^2)	FF	PCE (%)
1.06	17.04	0.66	11.14

Figure 4.21: *J-V characteristics for PVs with $MAPbI_3$ absorber, a) cells made at JNCASR and b) cells made at Cambridge.*

4.4: Conclusion

Large-scale morphological modification of OIP polycrystalline thin film was demonstrated using additive mixed antisolvent mediated kinetic control of crystal growth. The organic small molecule like PTCDA and TPBi results in very different morphologies which are controlled by the intermolecular interaction. The morphology of A-SMC OIP shows sensitivity towards the stacking nature of additive, solubility, and concentration. The subgap disorder reduces in A-SMCs, while the PL yield improves owing to reduced non-radiative decay rates. Modifications in localized emission spectra as a function of morphology suggest that internal re-absorption of photons contributes significantly to PL. Morphologically modified films show better EL and pinhole free charge transport which allows for realizing printable LED structures using low-temperature metal cathodes.

References

[1] M. Saliba, T. Matsui, J. Y. Seo, K. Domanski, J. P. Correa-Baena, M. K. Nazeeruddin, S. M. Zakeeruddin, W. Tress, A. Abate, A. Hagfeldt and M. Gratzel. Cesium-Containing Triple Cation Perovskite Solar Cells: Improved Stability, Reproducibility and High Efficiency. *Energy & Environmental Science* **2016,** *9,* 1989-1997.

[2] W. S. Yang, J. H. Noh, N. J. Jeon, Y. C. Kim, S. Ryu, J. Seo and S. I. Seok. High-Performance Photovoltaic Perovskite Layers Fabricated through Intramolecular Exchange. *Science* **2015,** *348,* 1234-1237.

[3] H. Cho, S-H Jeong, M-H Park, Y-H Kim, C. Wolf, C-L Lee, J. H. Heo, A. Sadhanala, N. Myoung, S. Yoo, S. H. Im, R. H. Friend and T-W Lee. Overcoming the Electroluminescence Efficiency Limitations of Perovskite Light-Emitting Diodes. *Science* **2015,** *350,* 1222-1225.

[4] Y. C. Ling, Z. Yuan, Y. Tian, X. Wang, J. C. Wang, Y. Xin, K. Hanson, B. W. Ma and H. W. Gao. Bright Light-Emitting Diodes Based on Organometal Halide Perovskite Nanoplatelets. *Advanced Materials* **2016,** *28,* 305-311.

[5] Z. K. Tan, R. S. Moghaddam, M. L. Lai, P. Docampo, R. Higler, F. Deschler, M. Price, A. Sadhanala, L. M. Pazos, D. Credgington, F. Hanusch, T. Bein, H. J. Snaith and R. H. Friend. Bright Light-Emitting Diodes Based on Organometal Halide Perovskite. *Nature Nanotechnology* **2014,** *9,* 687-692.

[6] S. D. Stranks and H. J. Snaith. Metal-Halide Perovskites for Photovoltaic and Light-Emitting Devices. *Nature Nanotechnology* **2015,** *10,* 391-402.

[7] M. M. Lee, J. Teuscher, T. Miyasaka, T. N. Murakami and H. J. Snaith. Efficient Hybrid Solar Cells Based on Meso-Superstructured Organometal Halide Perovskites. *Science* **2012,** *338,* 643-647.

[8] H. S. Kim, C. R. Lee, J. H. Im, K. B. Lee, T. Moehl, A. Marchioro, S. J. Moon, R. Humphry-Baker, J. H. Yum, J. E. Moser, M. Gratzel and N. G. Park. Lead Iodide Perovskite Sensitized All-Solid-State Submicron Thin Film Mesoscopic Solar Cell with Efficiency Exceeding 9%. *Scientific Reports* **2012,** *2,* 591.

[9] J. B. You, Z. R. Hong, Y. Yang, Q. Chen, M. Cai, T. B. Song, C. C. Chen, S. R. Lu, Y. S. Liu, H. P. Zhou and Y. Yang. Low-Temperature Solution-Processed Perovskite Solar Cells with High Efficiency and Flexibility. *Acs Nano* **2014,** *8,* 1674-1680.

[10] C. S. Ponseca, T. J. Savenije, M. Abdellah, K. B. Zheng, A. Yartsev, T. Pascher, T. Harlang, P. Chabera, T. Pullerits, A. Stepanov, J. P. Wolf and V. Sundstrom. Organometal Halide Perovskite Solar Cell Materials Rationalized: Ultrafast Charge Generation, High and Microsecond-Long Balanced Mobilities, and Slow Recombination. *Journal of the American Chemical Society* **2014,** *136*, 5189-5192.

[11] S. D. Stranks, G. E. Eperon, G. Grancini, C. Menelaou, M. J. P. Alcocer, T. Leijtens, L. M. Herz, A. Petrozza and H. J. Snaith. Electron-Hole Diffusion Lengths Exceeding 1 Micrometer in an Organometal Trihalide Perovskite Absorber. *Science* **2013,** *342*, 341-344.

[12] C. S. Ponseca, Y. X. Tian, V. Sundstrom and I. G. Scheblykin. Excited State and Charge-Carrier Dynamics in Perovskite Solar Cell Materials. *Nanotechnology* **2016,** *27*.

[13] N. K. Kumawat, A. Dey, A. Kumar, S. P. Gopinathan, K. L. Narasimhan and D. Kabra. Band Gap Tuning of $CH_3NH_3Pb(Br_{1-X}Cl_X)_3$ Hybrid Perovskite for Blue Electroluminescence. *ACS Applied Materials & Interfaces* **2015,** *7*, 13119-13124.

[14] J. H. Noh, S. H. Im, J. H. Heo, T. N. Mandal and S. I. Seok. Chemical Management for Colorful, Efficient, and Stable Inorganic-Organic Hybrid Nanostructured Solar Cells. *Nano Letters* **2013,** *13*, 1764-1769.

[15] P. C. Zhu, S. Gu, X. P. Shen, N. Xu, Y. L. Tan, S. D. Zhuang, Y. Deng, Z. D. Lu, Z. L. Wang and J. Zhu. Direct Conversion of Perovskite Thin Films into Nanowires with Kinetic Control for Flexible Optoelectronic Devices. *Nano Letters* **2016,** *16*, 871-876.

[16] J. H. Im, J. S. Luo, M. Franckevicius, N. Pellet, P. Gao, T. Moehl, S. M. Zakeeruddin, M. K. Nazeeruddin, M. Gratzel and N. G. Park. Nanowire Perovskite Solar Cell. *Nano Letters* **2015,** *15*, 2120-2126.

[17] F. Deschler, M. Price, S. Pathak, L. E. Klintberg, D. D. Jarausch, R. Higler, S. Huttner, T. Leijtens, S. D. Stranks, H. J. Snaith, M. Atature, R. T. Phillips and R. H. Friend. High Photoluminescence Efficiency and Optically Pumped Lasing in Solution-Processed Mixed Halide Perovskite Semiconductors. *Journal of Physical Chemistry Letters* **2014,** *5*, 1421-1426.

[18] Y. J. Fang, Q. F. Dong, Y. C. Shao, Y. B. Yuan and J. S. Huang. Highly Narrowband Perovskite Single-Crystal Photodetectors Enabled by Surface-Charge Recombination. *Nature Photonics* **2015,** *9*, 679-686.

[19] X. Y. Chin, D. Cortecchia, J. Yin, A. Bruno and C. Soci. Lead Iodide Perovskite Light-Emitting Field-Effect Transistor. *Nature Communications* **2015,** *6*, 7383.

[20] J. S. Luo, J. H. Im, M. T. Mayer, M. Schreier, M. K. Nazeeruddin, N. G. Park, S. D. Tilley, H. J. Fan and M. Gratzel. Water Photolysis at 12.3% Efficiency Via Perovskite Photovoltaics and Earth-Abundant Catalysts. *Science* **2014,** *345*, 1593-1596.

[21] S. Yakunin, M. Sytnyk, D. Kriegner, S. Shrestha, M. Richter, G. J. Matt, H. Azimi, C. J. Brabec, J. Stangl, M. V. Kovalenko and W. Heiss. Detection of X-Ray Photons by Solution-Processed Lead Halide Perovskites. *Nature Photonics* **2015,** *9*, 444-449.

[22] G. E. Eperon, V. M. Burlakov, P. Docampo, A. Goriely and H. J. Snaith. Morphological Control for High Performance, Solution-Processed Planar Heterojunction Perovskite Solar Cells. *Advanced Functional Materials* **2014,** *24*, 151-157.

[23] G. R. Li, Z. K. Tan, D. W. Di, M. L. Lai, L. Jiang, J. H. W. Lim, R. H. Friend and N. C. Greenham. Efficient Light-Emitting Diodes Based on Nanocrystalline Perovskite in a Dielectric Polymer Matrix. *Nano Letters* **2015,** *15*, 2640-2644.

[24] P. Kumar, B. Zhao, R. H. Friend, A. Sadhanala and K. S. Narayan. Kinetic Control of Perovskite Thin-Film Morphology and Application in Printable Light-Emitting Diodes. *ACS Energy Letters* **2017,** *2*, 81-87.

[25] M. J. Lee, D. Gupta, N. Zhao, M. Heeney, I. McCulloch and H. Sirringhaus. Anisotropy of Charge Transport in a Uniaxially Aligned and Chain-Extended, High-Mobility, Conjugated Polymer Semiconductor. *Advanced Functional Materials* **2011,** *21*, 932-940.

[26] L. H. Jimison, M. F. Toney, I. McCulloch, M. Heeney and A. Salleo. Charge-Transport Anisotropy Due to Grain Boundaries in Directionally Crystallized Thin Films of Regioregular Poly(3-Hexylthiophene). *Advanced Materials* **2009,** *21*, 1568-1572.

[27] Na Ai, Yan Zhou, Yina Zheng, Haibo Chen, Jian Wang, Jian Pei and Yong Cao. Achieving High Sensitivity in Single Organic Submicrometer Ribbon Based Photodetector through Surface Engineering. *Organic Electronics* **2013,** *14*, 1103-1108.

[28] Yuping Zhang, Xudi Wang, Yiming Wu, Jiansheng Jie, Xiwei Zhang, Yuliang Xing, Haihua Wu, Bin Zou, Xiujuan Zhang and Xiaohong Zhang. Aligned Ultralong Nanowire Arrays and Their Application in Flexible Photodetector Devices. *Journal of Materials Chemistry* **2012,** *22*, 14357-14362.

[29] A. J. Das and K. S. Narayan. Retention of Power Conversion Efficiency – from Small Area to Large Area Polymer Solar Cells. *Advanced Materials* **2013,** *25*, 2193-2199.

[30] M. Bag, D. Gupta, N. Arun and K. S. Narayan. Deformation of Metallic Liquid Drop by Electric Field for Contacts in Molecular-Organic Electronics. *Proceedings of the Royal Society a-Mathematical Physical and Engineering Sciences* **2009,** *465*, 1799-1808.

[31] R. M. Hooper, B. J. McArdle, R. S. Narang and J. N. Sherwood. Chapter 10 - Crystallization from Solution at Low Temperatures A2 - Pamplin, Brian R. In *Crystal Growth (Second Edition)*, Pergamon: 1980; Vol. 16, pp 395-420.

[32] P. Christian and P. O'Brien. Thermodynamic and Kinetic Control of Crystal Growth in Cds Nanomaterials. *Journal of Materials Chemistry* **2008,** *18*, 1689-1693.

[33] N. J. Jeon, J. H. Noh, Y. C. Kim, W. S. Yang, S. Ryu and S. I. Seok. Solvent Engineering for High-Performance Inorganic–Organic Hybrid Perovskite Solar Cells. *Nature Materials* **2014,** *13*, 897-903.

[34] J. Xu, A. Buin, A. H. Ip, W. Li, O. Voznyy, R. Comin, M. Yuan, S. Jeon, Z. Ning, J. J. McDowell, P. Kanjanaboos, J-P Sun, X. Lan, L. N. Quan, D. H. Kim, I. G. Hill, P. Maksymovych and E. H. Sargent. Perovskite–Fullerene Hybrid Materials Suppress Hysteresis in Planar Diodes. *Nature Communications* **2015,** *6*, 7081.

[35] K. Yan, B. X. Chen, H. W. Hu, S. Chen, B. Dong, X. Gao, X. Y. Xiao, J. B. Zhou and D. C. Zou. First Fiber-Shaped Non-Volatile Memory Device Based on Hybrid Organic-Inorganic Perovskite. *Advanced Electronic Materials* **2016,** *2*, 1600160.

[36] W. G. Zur Frage Der Geschwindigkeit Des Wachstums Und Der Auflösung Der Krystallflagen. *Zeitsch. für Kristall* **1901,** *34*, 449–480.

[37] J. H. Noh, S. H. Im, J. H. Heo, T. N. Mandal and S. I. Seok. Chemical Management for Colorful, Efficient, and Stable Inorganic–Organic Hybrid Nanostructured Solar Cells. *Nano Letters* **2013,** *13*, 1764-1769.

[38] A. Sadhanala, F. Deschler, T. H. Thomas, S. E. Dutton, K. C. Goedel, F. C. Hanusch, M. L. Lai, U. Steiner, T. Bein, P. Docampo, D. Cahen and R. H. Friend. Preparation of Single-Phase Films of $CH_3NH_3Pb(I_{1-X},Br_X)_3$ with Sharp Optical Band Edges. *Journal of Physical Chemistry Letters* **2014,** *5*, 2501-2505.

[39] S. D. Wolf, J. Holovsky, S. J. Moon, P. Loper, B. Niesen, M. Ledinsky, F. J. Haug, J. H. Yum and C. Ballif. Organometallic Halide Perovskites: Sharp Optical

Absorption Edge and Its Relation to Photovoltaic Performance. *Journal of Physical Chemistry Letters* **2014,** *5*, 1035-1039.

[40] L. M. Pazos-Outón, M. Szumilo, R. Lamboll, J. M. Richter, M. Crespo-Quesada, M. Abdi-Jalebi, H. J. Beeson, M. Vrućinić, M. Alsari, H. J. Snaith, B. Ehrler, R. H. Friend and F. Deschler. Photon Recycling in Lead Iodide Perovskite Solar Cells. *Science* **2016,** *351*, 1430-1433.

[41] M. H. Chang, D. Das, P. V. Varde and M. Pecht. Light Emitting Diodes Reliability Review. *Microelectronics Reliability* **2012,** *52*, 762-782.

Chapter 5: Quantum Confinement Effects in Perovskite Nanocrystals

5.1: Introduction

` Hybrid perovskites are similar to inorganic semiconductors, as is demonstrated using efficient PVs and LEDs [1-12]. However, they do not demonstrate comparable stability, which results from its low formation energy and a larger degree of freedom associated with organic cation [13-15]. In order to improve the stability, numerous studies have suggested the use of encapsulating layers like that of PMMA or polyaniline to prevent the OIP films from reacting with ambient oxygen and moisture [16, 17]. Other approaches involve creating nano-dimensional crystals with the inert capping of long chain alkyls or surfactant groups [18, 19]. Interesting observations have been reported with a decrease in average crystallite size, which include a shift in absorption edge [20, 21], an increase in photoluminescence (PL) [22] and formation of nanosheets and platelets [23]. NCs are suitable for applications in devices compared to the bulk polycrystalline methylammonium lead bromide ($MAPbBr_3$) films (bulk), primarily due to the enhanced stability and high luminescence [24]. Thus it is important to understand the electronic and optical properties of nanocrystals (NCs) for realizing efficient and stable devices.

In this chapter, the optical and charge transport properties of highly luminescent NC of methylammonium lead bromide ($MAPbBr_3$) perovskite thin films have been studied. The diameter of NCs varies from 4 - 10 nm, while the majority of crystals have ~ 6 nm diameter, simultaneously the luminescence quantum yield (PLQY) of NCs in solution and film is high (> 50 %). The presence of a layer of large alkyl chain on the surface acts as an encapsulation, which is efficient is protecting the OIP against the moisture. Reduced sizes are linked to quantum confinement, which has been studied using the temperature dependence of emission; the lattice-exciton interaction was investigated, which is significantly different when compared to the bulk counterpart. The choice of system is driven by the fact that $MAPbBr_3$ has band edge in the visible (~ 540 nm) part of the electromagnetic spectrum, which is beneficial for lighting and display applications. The emission and absorption also mimic human vision response making them an interesting system for fabricating detectors replicating human eye response.

5.2: Experimental details

5.2.1: Materials

$MAPbBr_3$ NCs were fabricated using the template-free synthesis route as reported by Schmidt et al. [19]. NCs were synthesized by the group of Prof. Vijayakumar C. Nair at National Institute for Interdisciplinary Science and Technology, Trivandrum. The distribution in particle diameter, as observed in TEM analysis, suggests variation in particle size from 3 to 10 nm, a major fraction of particles have average diameter ~ 6 nm [18]. Semiconducting N-type polymer N2200 (Activeink-N2200 (P(NDI2OD-T2)) (M_w ~ 84,000 g/mol)) was procured from Polyera Corporation and PCBM-C70 (Phenyl-C71-butyric acid methyl ester) was purchased from Luminescence Technology Inc., Taiwan. Low sheet resistance (8 Ωsq) indium tin oxide (ITO) coated glass slides were procured from Xin Yan Technology, China. High conductivity PEDOT:PSS ((Poly(3,4-ethylenedioxythiophene)-poly(styrene sulfonate)) (Clevios PH – 1000, specific conductivity ~ 800 S/cm) was procured from Heraeus.

5.2.2: Device Fabrication

Quartz and ITO-coated glass substrates were cleaned using wet cleaning procedure as described in section 2.3.2. The $MAPbBr_3$ NCs were suspended in toluene at 20 mg/ml concentration. Bulk OIP films were fabricated from 1:1.05 molar ratios of MABr and $PbBr_2$, dissolved in dimethylformamide, at 20 wt %. Films for optical measurement were fabricated by spin coating the bulk precursor and NC suspension on quartz substrates. Devices were fabricated on ITO coated glass substrates, PEDOT: PSS layer was spin coated at 3000 rpm in the air and annealed for 30 min at 150 ^{o}C. NC and bulk thin films were deposited in nitrogen filled glove box at 1000 and 2000 rpm respectively. Following the OIP layer, an organic n-type semiconductor layer of thickness ~ 40 - 50 nm of N2200 (PCBM-C70) was spin coated at 1000 rpm from 10 mg/ml (20 mg/ml) solution in chlorobenzene. A reflective Al back contact (~ 150 - 200 nm) was evaporated at an evaporation rate of ~ 0.5 - 1.0 Å/s in a thermal evaporator at ~ 10^{-6} mbar pressure, the active area was controlled using a metal mask.

5.2.3: Characterization

Absorption (*α(E)*)

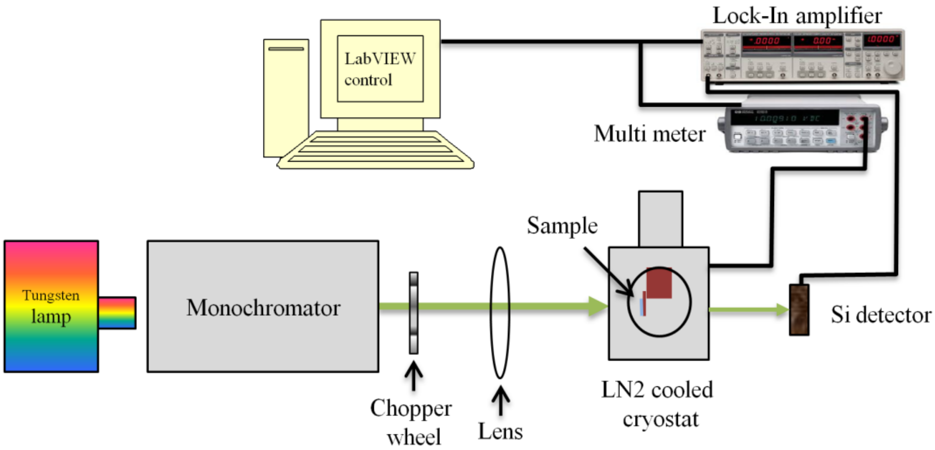

Figure 5.1: *Schematic for α(E) measured as a function of temperature.*

All absorption studies were performed in liquid N_2 cooled cryostats, flushed with dry nitrogen; measurements were performed at ~ 10^{-2} mbar pressure. Schematic of the setup is shown in Figure 5.1. Temperatures of substrates were recorded using a calibrated Pt-100 RTD and a multimeter (HP 2600). Tungsten lamp in conjugation with a monochromator (Zolix Omni 500) was used as a monochromatic light source; a calibrated Si detector (UDT sensors) along with lock-in amplifier (SR830) was used to measure transmission. The $\alpha(E)$ at 300K was also verified in UV-Vis spectrometer (Perkin Elmer).

Photoluminescence

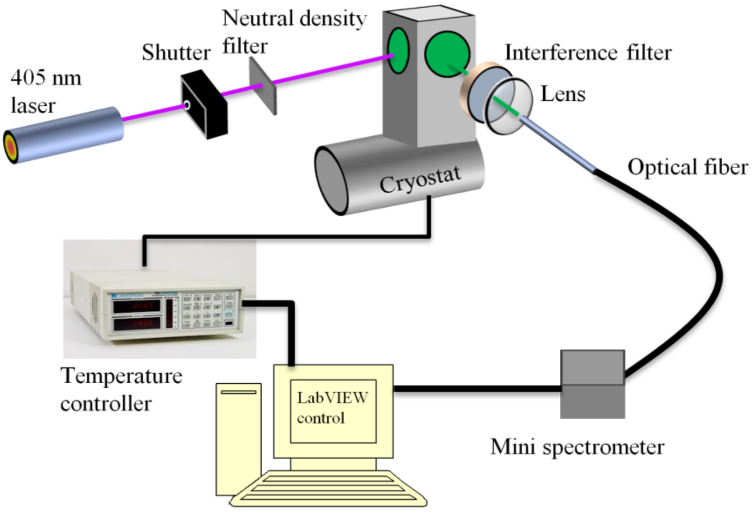

Figure 5.2: *Schematics for PL measured as a function of Temperature.*

PL measurements at different temperatures were carried out in a temperature-controlled cryostat (CTI cryogenics) cooled using a closed cycle helium pump. A 405 nm laser (output power ~ 100 mW) was used as an excitation source; PL was collected at 90-degree reflection, using a fiber coupled Si CCD-based spectrometer (Hamamatsu high sensitivity mini spectrometer C10083CA). The excitation wavelength was filtered out using 450 nm long pass interference filter. The substrate temperature was recorded using calibrated Pt-100 RTD and electrometer (Keithley 6514). Schematic of low-temperature PL setup is shown in Figure 5.2.

Electroluminescence (EL)

The EL was measured using a fiber-coupled Si CCD-based spectrometer. Voltage was applied through Keithley 2400 source meter. EL at low temperatures was measured in a Liquid N2 cooled cryostat, similar to the one used for absorption; substrate temperature was recorded using Pt-100 RTD and Keithley 6514 electrometer.

Photocurrent ($I_{ph}(E)$)

The $I_{ph}(E)$ was recorded in a device architecture identical to the one used for EL measurements. A monochromator (Zolix, Omni-λ500) coupled with tungsten lamp was used as light source. $I_{ph}(E)$ signals were recorded using lock-in amplifier (Stanford Research Systems- SR830) and the lamp power was calibrated using a UV-enhanced Si photodetector (DSi-200, Zolix).

5.3: Result and Discussion

5.3.1: Crystal structure

The NCs demonstrate cubic symmetry (at 300K), as is seen in Figure 5.4, where the (100) and (200) peaks match well with that of bulk, the absence of higher order peaks suggests that the long-range order is missing. The XRD peak shows a very small increase in width compared to that of bulk, the width increases at the bottom of the peak, suggesting a range of particle sizes present in the film. Narrower peaks predominantly arise from larger NCs.

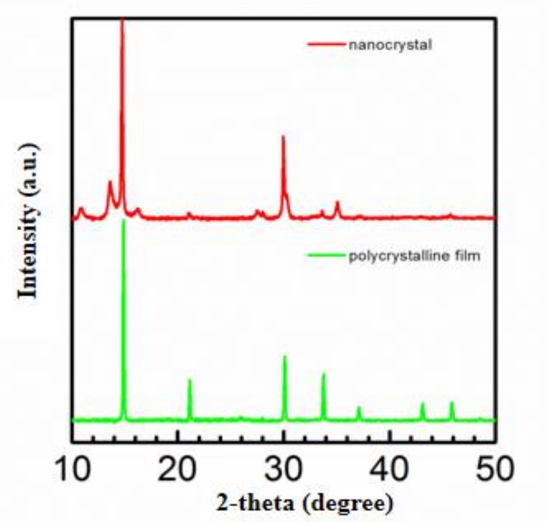

Figure 5.3: *XRD spectra of bulk and NC films coated on quartz substrates.*

5.3.2: Quantum confinement effect on optical band gap

The recorded $\alpha(E)$ for bulk and NC were corrected for scattering related artifacts [25] using the technique introduced by S.J. Leach and H. A. Scheraga [26]. The estimate of the band gap (E_g) was obtained from the modeled $\alpha(E)$, close to the band edge using the Elliot' theory of Wannier excitons as was reported by Saba et al. [27]. Which is more accurate for band gap estimation as compared to the values obtained using Tauc plot ($\alpha(E) \approx (E - E_g)^{1/2}$) [1], because of the excitonic peak present at the band edge. The normalized $\alpha(E)$ response measured for bulk and NC $MAPbBr_3$ thin films, at 300 K, is shown in Figure 5.3(a) and 5.3(b) respectively, modeled $\alpha(E)$ is shown in solid line. The E_g estimates from the model fit to modified Elliot's formula (described in appendix I) is ≈ 2.36 eV for bulk and ≈ 2.39 eV for NC, which agrees well with the previously reported values [28, 29].

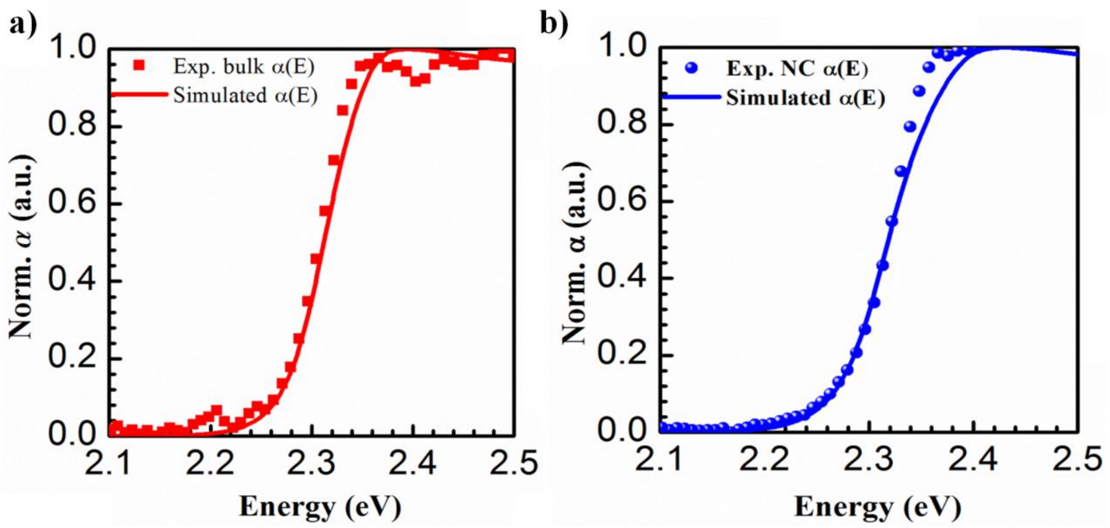

Figure 5.4: *a) experimental (red square) and modeled (solid red line) absorption of bulk, b) experimental (blue circles) and modeled (solid blue line) absorption of NC films. (Reprinted with permission from P. Kumar, C. Muthu, V. C Nair, and K. S. Narayan, Quantum Confinement Effects in Organic Lead Tribromide Perovskite Nanoparticles, J. Phys. Chem. C, 120, 32, 18333-18339, Copyright (2016) American Chemical Society).*

In the high energy region of $\alpha(E)$, above the E_g, additional peaks are visible, which are absent in the case of bulk. Origin of these peaks can be related to the NCs of dimension smaller than ~ 6 nm, present in a small fraction. A small shift observed in E_g (ΔE_g ~ 0.03 eV) signifies the onset of confinement effects in NCs (average radius ~ 3 nm) Using the effective mass approximation, the exciton Bohr radius (r_B) can be estimated using 5.1,

$$r_B = \frac{\varepsilon h^2}{\mu \pi e^2} \tag{5.1}$$

Where μ is effective mass and ε is the dielectric constant. The value for $r_B is \approx 3\ nm$ in MAPbBr$_3$ system, estimated using $\mu \approx 0.117m_e$ and $\varepsilon \approx 7.5$ [30], which is very close to the average NCs radius. Thus the excitons will experience a weak confinement in NCs giving rise to a small shift in energy gap. The band gap as a function of particle size can be calculated from effective mass approximation,

$$E_{g,NC} = E_{g,bulk} + \frac{\hbar^2\pi^2}{2\mu r^2} - 1.786\frac{e^2}{4\pi\varepsilon r} \tag{5.2}$$

Where second terms represent confinement induced shift and the third term represents Coulomb interaction between electron-hole pair [31]. $E_{g,NC}$ estimated using equation 5.2 gives an overestimated value of ΔE_g (≈ 0.3 eV). An order of magnitude increase in calculated ΔE_g can be associated with other complex interactions like spin-orbit coupling [32], which is not included in effective mass approximation. Confinement effects are stronger in NCs of smaller diameter (< 6 nm), seen as distinct peaks in $\alpha(E)$ in higher energy regime.

5.3.3: Temperature dependence of absorption

The $\alpha(E)$ spectra go through a sizable change with a decrease in temperature. The excitonic peak, which is seen as a shoulder feature at the band edge (at 300K), gets resolved into a well-defined peak (Figure 5.5). The local maxima at the $\alpha(E)$ band edge is an indicative of excitonic transition, which is prominent at low temperature (T ≈ 105 K) for both bulk and NC films, as shown in Figure 5.5a and 5.5b respectively. The excitonic peak is more sizable for NC, suggesting a larger binding energy. The procedure for estimating the exciton binding energy (E_B) using $\alpha(E)$ response has been well described in the literature of inorganic band type semiconductors like GaAs [33, 34]. To estimate the E_B for bulk and NCs, from $\alpha(E)$ response measured at 300K, the modified Elliot's theory for $\alpha(E)$ is used, as shown in Figure 5.3a and 5.3b respectively. The E_B for bulk, at 300K, is ≈ 50 meV which lies within the range of previous reports [35]. In the case of NCs, the E_B value is ≈ 75 meV, which is ~ 1.5 times higher than that of bulk. The excitonic transitions, for particles of a size smaller than 6 nm, show a redshift of ~ 50 - 60 meV at 105 K. This behavior is analogous to the band-edge excitonic peak and is consistent with the typical band-edge excitonic transitions.

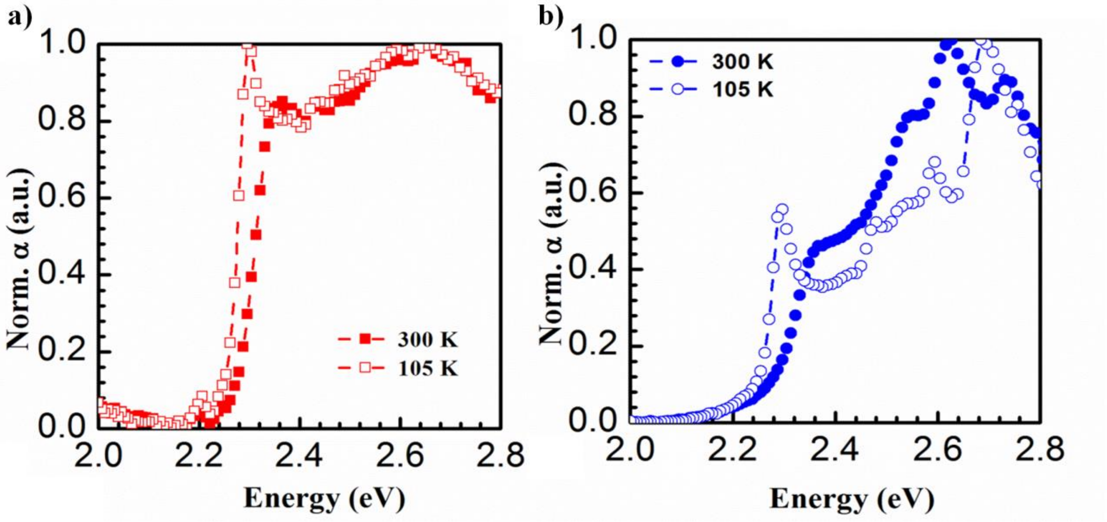

Figure 5.5: *Low temperature (~ 105 K) α(E) for a) bulk and b) NC OIP film. (Reprinted with permission from P. Kumar, C. Muthu, V. C Nair, and K. S. Narayan, Quantum Confinement Effects in Organic Lead Tribromide Perovskite Nanoparticles, J. Phys. Chem. C, 120, 32, 18333-18339, Copyright (2016) American Chemical Society).*

5.3.4: Photoluminescence in bulk and NC films

The larger effects of quantum confinement, observed in the temperature dependence of *α(E)*, is also evident in the PL measurements as a function of temperature. Normalized PL spectra for bulk and NC thin films, measured at 300K, are shown in Figure 5.6. The NC PLQY is significantly higher than that of bulk as shown in the inset of Figure 5.6. This effect is related to the increased radiative recombination and higher outcoupling due to the increased surface area, which agrees well with a previous report [36]. The blue shift, arising from the increase in E_g, in emission profile of NC, is inhomogeneous compared that of the bulk PL. The shift in emission peak ($\Delta E_{peak} \approx 0.037$ eV) is smaller than the shift at the edge of the PL ($\Delta E_{edge} \approx 0.076$ eV), towards higher energy, at FWHM. Incidentally, the ΔE_{peak} is similar to the ΔE_g (≈ 0.03 eV), calculated from $\alpha(E)$ measurements. The spectral line width (FWHM) for PL is broader for NCs (≈ 0.145 eV) compared to that of bulk (≈ 0.102 eV). Higher FWHM observed in NC PL can be attributed to processes like Förster resonance energy transfer from smaller (< 6nm) to the larger particles (~ 6 nm), re-absorption losses and direct emission from smaller NCs.

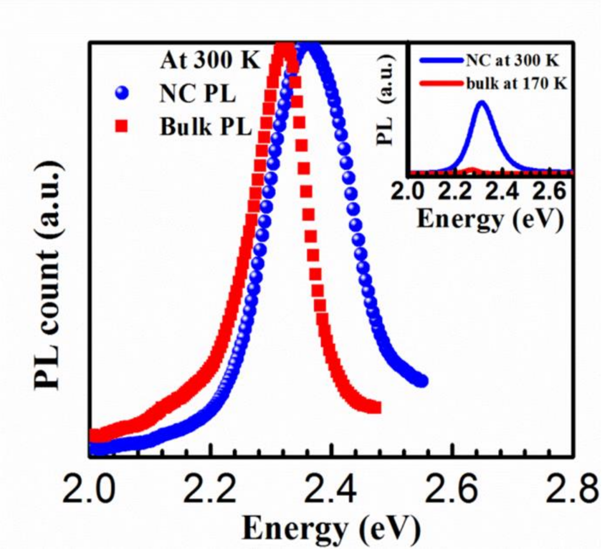

Figure 5.6: *PL spectra for bulk (red squares) and NC (blue circles) films. The inset shows the absolute PL magnitudes of bulk and NC. (Reprinted with permission from P. Kumar, C. Muthu, V. C Nair, and K. S. Narayan, Quantum Confinement Effects in Organic Lead Tribromide Perovskite Nanoparticles, J. Phys. Chem. C, 120, 32, 18333-18339, Copyright (2016) American Chemical Society).*

5.3.5: Temperature dependence of photoluminescence

The PL shows a large dependence on temperature, as is shown in Figure 5.7. The general trend of a red shift in peak position (E_{peak}), an increase in peak intensity and a decrease in FWHM is seen for both bulk (Figure 5.7a) and NC (Figure 5.7b), as the temperature is lowered. Along with the increase in intensity, the bulk PL becomes asymmetric below 155 K (orthorhombic phase) (Figure 5.7c). The PL intensity and its increase, with lowering of temperature, are sizably higher for NC. Large PL yield in NC is consistent with the increase in the excitonic nature, which originates from quantum confinement. The local maxima, observed in the absorbing region, at low-temperatures in NC PL(*E*) (Figure 5.7d), can be associated with NCs of smaller diameter (< 6 nm). This observation is consistent with the occurrence of local maxima in $\alpha(E)$, which suggests larger confinement effects for smaller NCs.

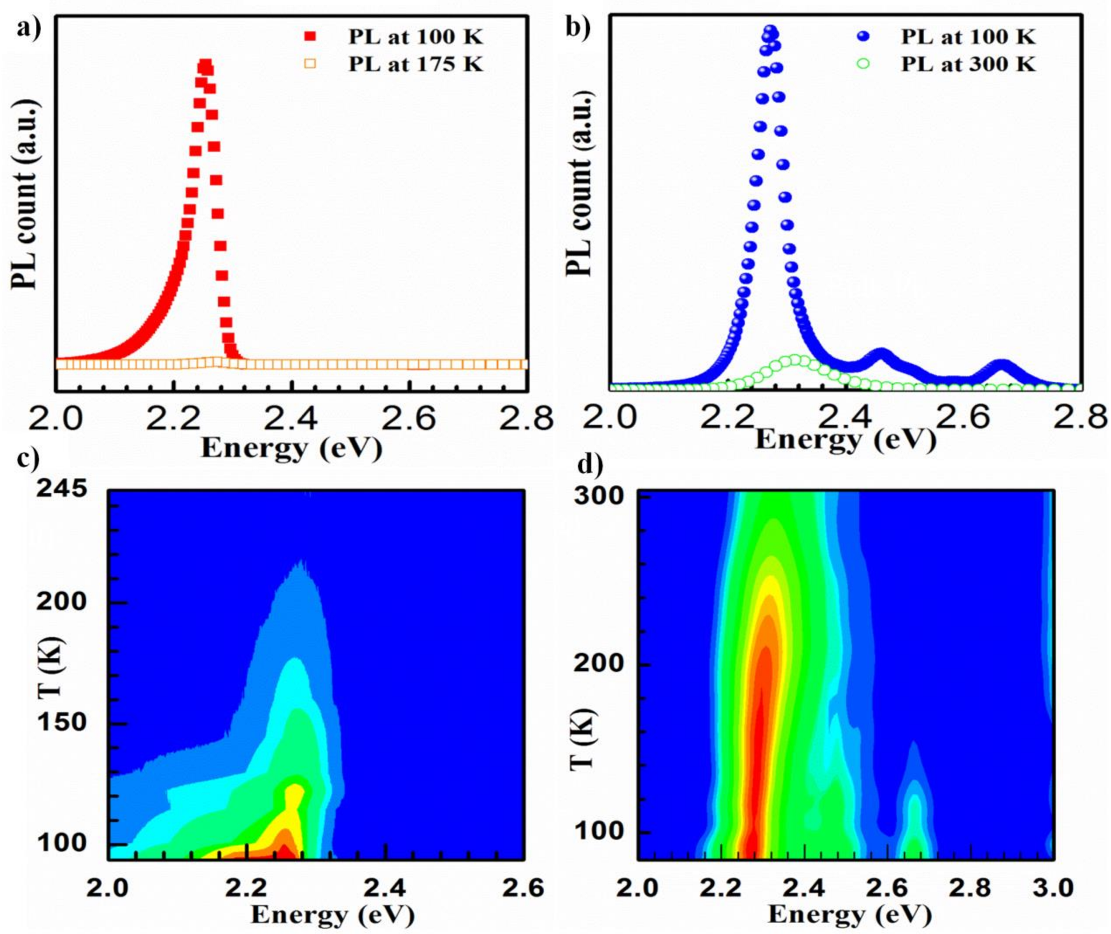

Figure 5.7: *PL spectra for a) bulk and b) NC films as a function of temperature, emission contour plot for measured temperature range for c) bulk and d) NC. (Reprinted with permission from P. Kumar, C. Muthu, V. C Nair, and K. S. Narayan, Quantum Confinement Effects in Organic Lead Tribromide Perovskite Nanoparticles,*

J. Phys. Chem. C, 120, 32, 18333-18339, Copyright (2016) American Chemical Society).

5.3.5 I: Emission peak shift

The red shift observed for E_{peak}, as the temperature is lowered, for both bulk and NC films are shown in Figure 5.8. The E_{peak} vs. T plot for NC exhibits a linear response with a slope ≈ 0.3 meV/K, which is comparable with the slope for a red shift in E_g [28]. In the case of bulk films, a discontinuity is observed in $E_{peak}(T)$ across the orthorhombic to tetragonal phase transition (T ≈ 155 K). Similar discontinuity has not been observed in $\alpha(E, T)$. The Slope of linear variation is ≈ 0.55 meV/K in orthorhombic phase (T < 155 K) and decreases to a lower value of ≈ 0.1 meV/K in tetragonal phase (T > 155 K). The phase transition from orthorhombic (low temperature) to tetragonal (high temperature) occurs at 155 K for $MAPbBr_3$ perovskite system. The phase transition is attributed to the decrease in the rotational degree of freedom of organic cation [37, 38]. It is interesting to note the presence of discontinuity in $E_{peak}(T)$ characteristics, across phase transition, in bulk, while it remains absent in NCs for much lower temperatures. Previously, many systems have been reported where the phase transitions temperature decreases with particle size. This structural stability of NC system, in general, has been highlighted in perovskite 2D layers, CuS and CdSe QDs [39-41].

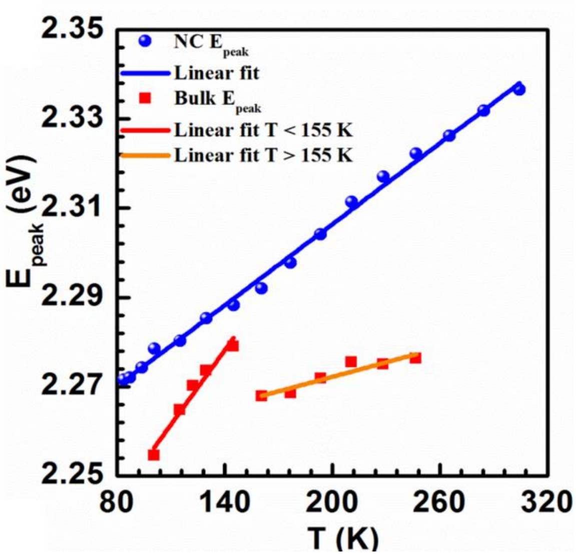

Figure 5.8: *PL peak shift for bulk (red square) and NC (blue circle). (Reprinted with permission from P. Kumar, C. Muthu, V. C Nair, and K. S. Narayan, Quantum Confinement Effects in Organic Lead Tribromide Perovskite Nanoparticles, J. Phys. Chem. C, 120, 32, 18333-18339, Copyright (2016) American Chemical Society).*

5.3.5 II: Integrated photoluminescence intensity

The integrated PL intensity ($I_{int}(T)$) can be used to estimate the binding energy by using the standard expression for thermal quenching of PL, which is given as,

$$I_{int}(T) = \frac{I_{int}(0)}{1 + Ae^{-E_B/k_B T}} \tag{5.3}$$

Where $I_{int}(0)$ is intensity at 0 K and A is a constant [42]. The $I_{int}(T)$, calculated by integrating PL over entire emission spectrum has been plotted as a function of 1/T in Figure 5.9a. The fitting has been limited to the temperature range in which cubic-tetragonal phase is prevalent. Bulk emission becomes very weak above 250 K, thus the $I_{int}(T)$ fit for bulk is limited in the temperature range from ≈ 155 K – 250 K. In the case of NC, the fitting range is ≈ 193 K – 300 K.

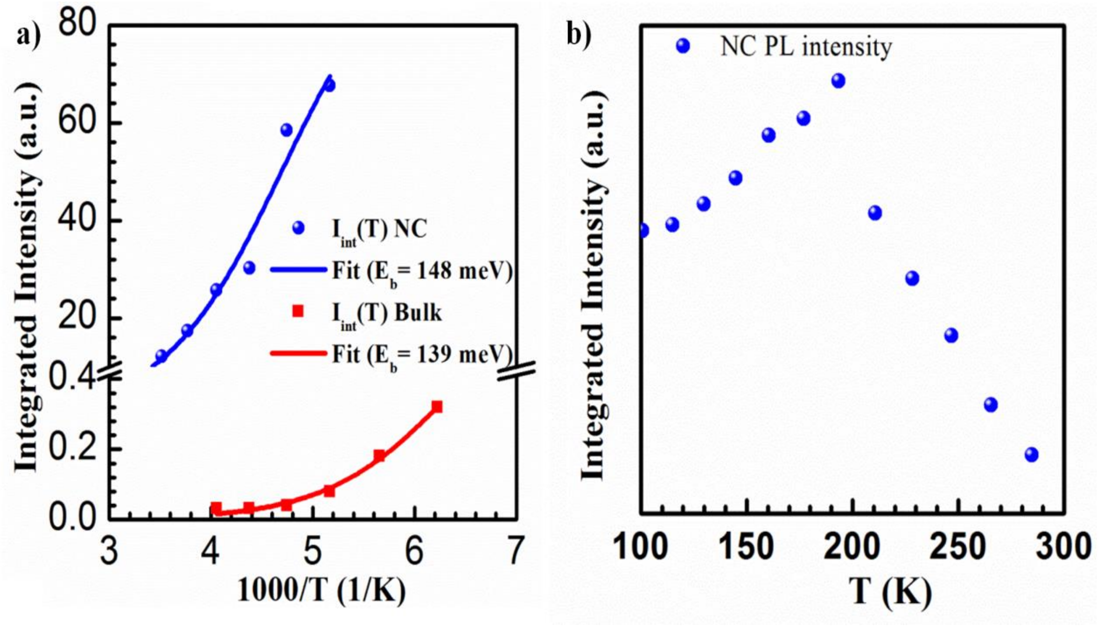

Figure 5.9: *a) Integrated PL intensity for bulk (red square) and NC (blue circle), b) Integrated PL intensity for NC showing anomalous behavior below 192 K. (Reprinted with permission from P. Kumar, C. Muthu, V. C Nair, and K. S. Narayan, Quantum Confinement Effects in Organic Lead Tribromide Perovskite Nanoparticles, J. Phys. Chem. C, 120, 32, 18333-18339, Copyright (2016) American Chemical Society).*

Anomalous behavior in $I_{int}(T)$ of NC PL was observed below $\approx$ 193 K, where the $I_{int}(T)$ decreases as the temperature is lowered, this trend persists till 100 K (Figure 5.9b), similar observation has been reported previously [43], however, the reason for such a behavior is unknown. The observed decrease in $I_{int}(T)$, can be attributed to the presence of non-radiative decay channel, which may get activated below ~ 190 K. The E_B calculated from thermal quenching model (equation 5.4) is 139 meV for bulk and 148 meV for NC. The value derived for E_B is significantly overestimated for both bulk and NC as compared to that estimated from $\alpha(E)$ at $\approx$ 300 K. This suggests that the OIP perovskite system may require correction to the thermal quenching model and may not be applicable in its current form.

5.3.5 III: Thermal broadening of Photoluminescence

The emission attributes as a function of temperature can be analyzed using exciton model of Toyazawa [42]. The FWHM shows a monotonic increase with temperature for both bulk and NC films. FWHM for bulk and NC emission, as a function of *1/T,* is shown in Figure 5.10. The increase in PL peak width is associated with the phonon-assisted thermal broadening. The FWHM for both NC and bulk has been fitted for temperature > 155 K, using independent boson model which is given as,

$$\Gamma(T) = \Gamma_0 + \sigma T + \frac{\Gamma_{op}}{e^{\hbar\omega_{op}/k_B T} - 1} \tag{5.4}$$

Where Γ_0 is the inhomogeneous broadening contribution, σ and Γ_{op} are related to the exciton-acoustic phonon interaction and exciton-optical phonon interactions, respectively [44].

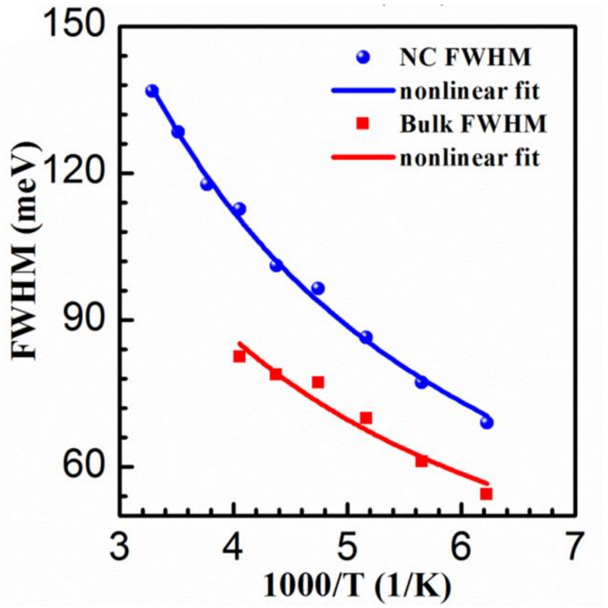

Figure 5.10: *FWHM as a function of temperature for bulk (red square) and NC (blue circle). (Reprinted with permission from P. Kumar, C. Muthu, V. C Nair, and K. S. Narayan, Quantum Confinement Effects in Organic Lead Tribromide Perovskite*

Nanoparticles, J. Phys. Chem. C, 120, 32, 18333-18339, Copyright (2016) American Chemical Society).

The quality of fit is not sensitive to the variation of σT, which suggests that acoustic phonons have a negligible contribution towards the thermal broadening of line-width at high temperatures (> 155 K), which agrees well with a previous report [43]. The Γ_0 value for NC and bulk is around ≈ 10 meV. The energy of optical phonon associated with the broadening ($\hbar\omega_{op}$) is around ≈ 6 meV for NC while for bulk it is ≈ 4 meV. The $\hbar\omega_{op}$ value for NC is closer to the values reported for longitudinal optical phonon energy [28], which can be associated with pure perovskite phase in NC, without the defect and grain boundary effects. The Γ_{op} value for NC (≈ 32 meV) is greater as compared to that of bulk (≈ 14 meV), which suggests a strong exciton – optical phonon interaction, which will result in an increased PL quenching with temperature.

5.3.5 IV: Spectral line shape analysis

Temperature dependence of spectral line shape for $\alpha(E)$ and PL(E) indicates the extent of phonon-exciton coupling [45]. The PL line shape for NC shows a significant variation with temperature. At low temperature (T < 155 K), in orthorhombic phase, the line shape is a Lorentzian as shown in Figure 5.11a. A Lorentzian profile has been associated with the weak exciton-lattice interaction. The line shape broadening is associated with the reciprocal of the excited state lifetime [46].

At temperature close to and above orthorhombic-tetragonal phase transition (T ~ 155 K), the spectral emission profile is a pseudo-Voigt (Figure 5.11b), which is a convolution of Lorentzian and Gaussian. This suggests an onset of thermal related broadening, as the Gaussian profile is related to thermal induced broadening [47]. In the cubic phase (T ~ 230 - 300 K) the emission profile is purely Gaussian (Figure 5.11c), which suggests a strong exciton-lattice interaction and leads to a characteristics reduction of PL intensity upon heating. Such observations are not new and have been observed in traditional inorganic QDs like CdSe [46].

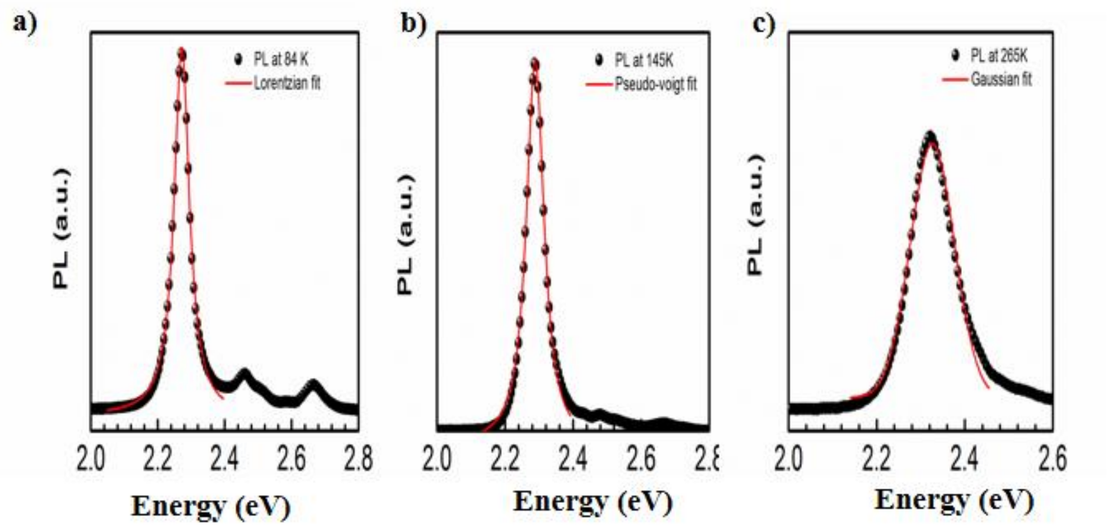

Figure 5.11: *Line shape fit for NC PL is a) a Lorentzian below 155K b) a pseudo-Voigt above 155K and c) a Gaussian in cubic phase. (Reprinted with permission from P. Kumar, C. Muthu, V. C Nair, and K. S. Narayan, Quantum Confinement Effects in Organic Lead Tribromide Perovskite Nanoparticles, J. Phys. Chem. C, 120, 32, 18333-18339, Copyright (2016) American Chemical Society).*

The observed feature of spectral line shape variation with temperature is consistent with the calculated higher value of Γ_{op} for NCs. The PL(E) for bulk film, in orthorhombic phase (T < 155 K), is asymmetric around the maxima. The emission tail is extended towards the low energy side as is shown in Figure 5.12a. The origin of asymmetric emission can be associated with localized exciton states [48]. Alternatively, it can also be related to the internal re-absorption process which can cause the emission to redshift [49]. This effect is less pronounced at a higher temperature (T > 155 K) and the peak shape is a Lorentzian (Figure 5.12b). The presence of Lorentzian emission profile at higher temperature is an indicative of small exciton-lattice interaction. This is concurrent with the lower value of Γ_{op} for bulk, inferred from independent boson model.

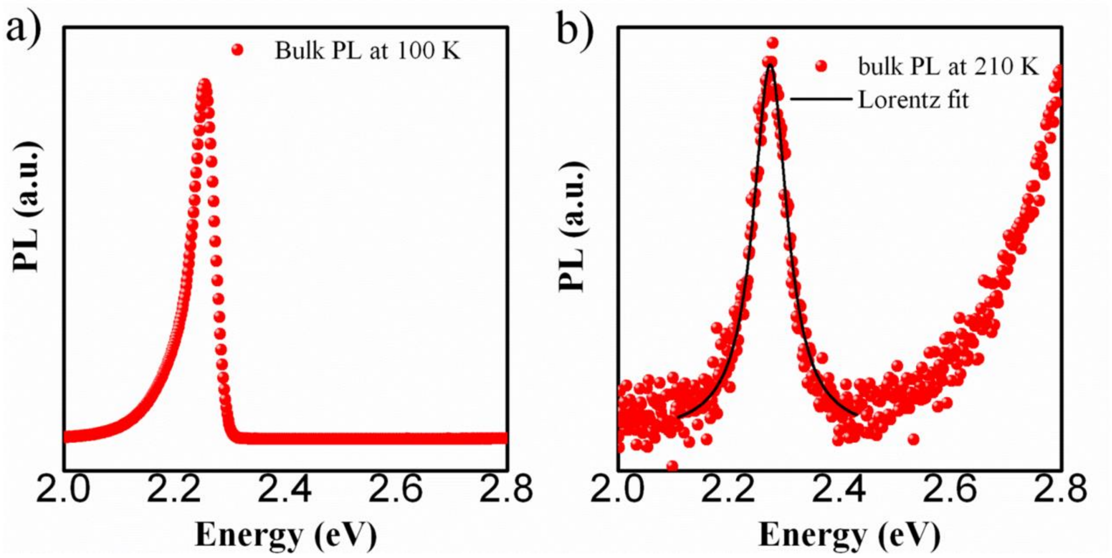

Figure 5.12: *Line shape fit for bulk PL in a) orthorhombic phase and b) tetragonal-cubic phase. (Reprinted with permission from P. Kumar, C. Muthu, V. C Nair, and K. S. Narayan, Quantum Confinement Effects in Organic Lead Tribromide Perovskite Nanoparticles, J. Phys. Chem. C, 120, 32, 18333-18339, Copyright (2016) American Chemical Society).*

5.3.5V: Temperature dependence of Emission is strongly confined particles

The additional blue shifted peaks, visible in the PL(E) spectra, at low temperature, for NC films are related to NCs of size < 6 nm. At high temperatures, the emissions from these NCs are very weak, arising from low PL yield, reabsorption, and energy transfer process. Multiple peak parameters, in the temperature range of $\approx$ 90 K – 300 K, have been derived using peak-fit software (fitky [50]). The variation in E_{peak}, $I_{int}(T)$ and FWHM with temperature has a different behavior compared to the dominant particle size ~ 6 nm. E_{peak} shows a consistent trend for different emission band, where weak temperature dependence is observed from 84 - 190 K, followed by a sharp increase of ≈ 70 – 100 meV (Figure 5.13a). The presence of internal conversion processes alters the trend in the temperature dependence of intensity and FWHM of the emission in this spectral regime (Figure 5.13b and 5.13c respectively).

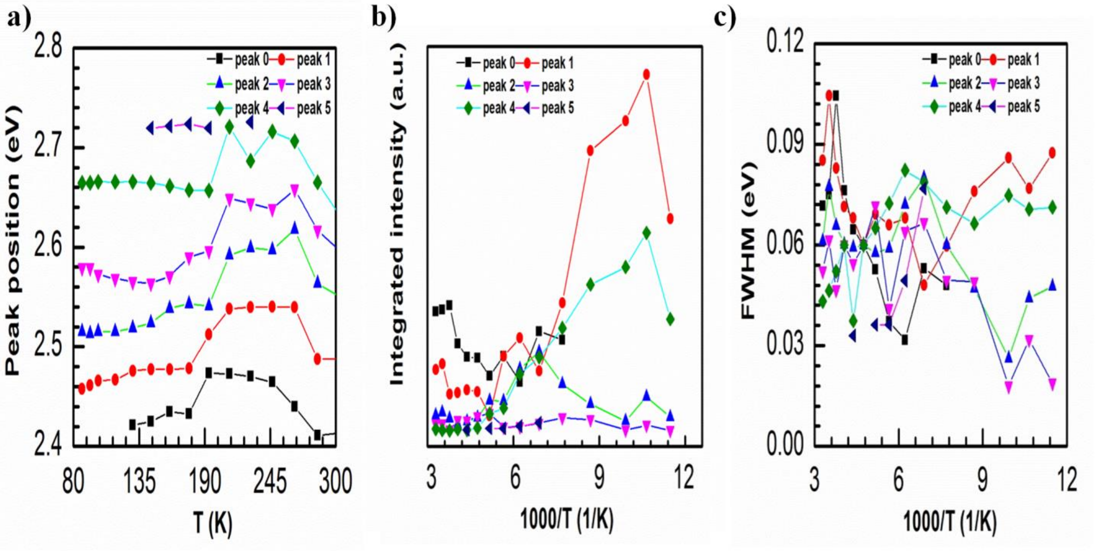

Figure 5.13: *Temperature dependence of a) peak position, b) integrated intensity and c) FWHM for strongly confined particles. (Reprinted with permission from P. Kumar, C. Muthu, V. C Nair, and K. S. Narayan, Quantum Confinement Effects in Organic Lead Tribromide Perovskite Nanoparticles, J. Phys. Chem. C, 120, 32, 18333-18339, Copyright (2016) American Chemical Society).*

5.3.6: Bilayer thin film devices

5.3.6 I: Surface coverage and roughness

The increase in PL intensity and size controlled energy gap in NCs open up the possibility of tailored devices. The devices, consisting of both NC and bulk form of hybrid OIP as an active layer, were studied for their emission and photodetection properties. The NCs can be dispersed in a variety of common non-polar organic solvents, which allows coating of very thin layers of perovskite over a wide range of substrates. While in the case of bulk, suitable solvents (DMF and DMSO) and hydrophilic surface are required. The surface energy plays a dominant role in film formation process of the bulk, which is considerably relaxed in NCs. The surface topography map of a thin film of NCs is shown in Figure 5.14a. High surface roughness results from the aggregation of NCs. To obtain an efficient charge transport across the interface, the NC layer has been further planarized using organic acceptor layer to reduce surface roughness. The emission is homogeneous across the area, which suggests a uniform surface coverage (Figure 5.14b).

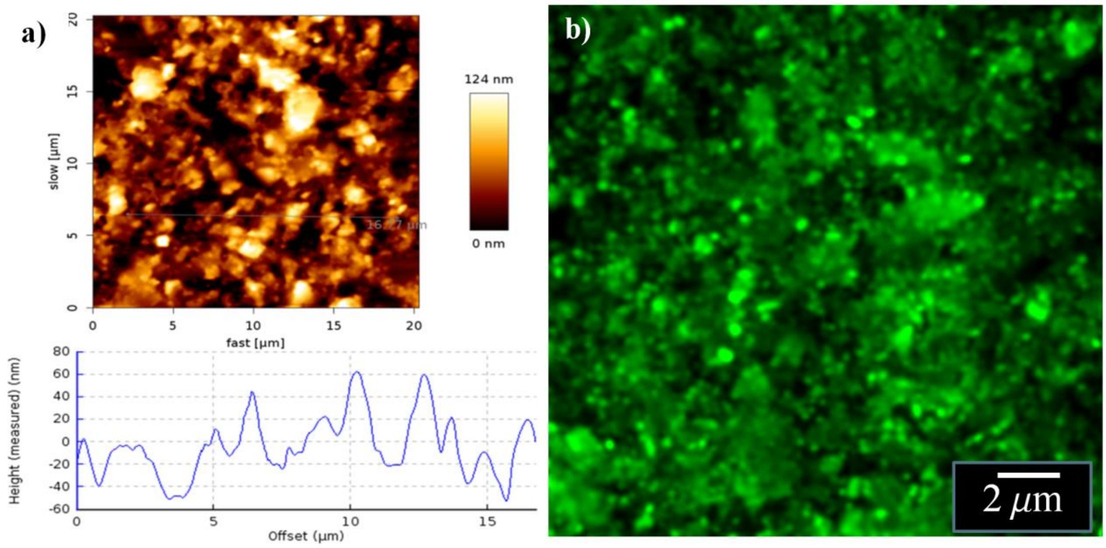

Figure 5.14: a) Surface roughness and, b) localized PL map of NC film.

5.3.6 II: Electroluminescence in bulk and NC devices

The NC surface roughness is planarized to a certain extent in a bilayer structure using acceptor layers like N2200 and PCBM-C70. A schematic of bilayer device is shown in Figure 5.15a, the bilayer devices of NC/acceptor exhibit characteristic $I_{ph}(E)$ and EL. The acceptor layer (N2200) does not contribute to the emission, which was separately verified. I-V response for both photodiode and LED is shown in Figure 5.15b and 5.15c respectively. As can be noticed that the NC devices demonstrate high V_{OC} but low I_{ph} and FF. Simultaneously, the LED characteristics show high turn-on voltage for NC/N2200 structure. This suggests that the NC forms a lossy interface with N2200, which can be associated with the large chain alkyls present at the surface of NC. To facilitate efficient charge transport long chain alkyl needs to be engineered using conjugated molecules.

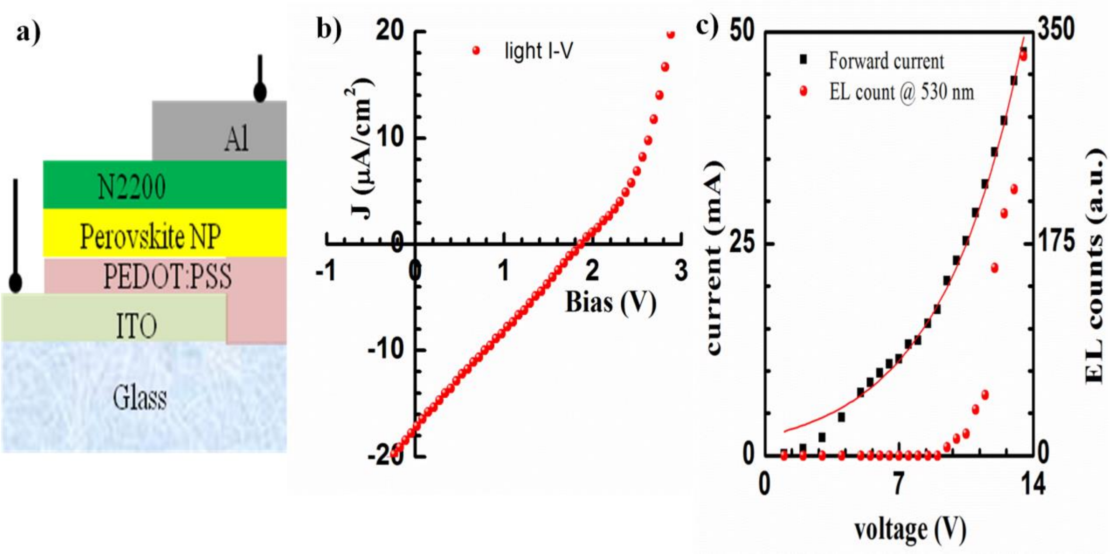

Figure 5.15: *a) Schematic of bilayer device structure, b) photoresponse of NC/N2200 bilayer device and c) LED I-V characteristics. (Reprinted with permission from P. Kumar, C. Muthu, V. C Nair, and K. S. Narayan, Quantum Confinement Effects in Organic Lead Tribromide Perovskite Nanoparticles, J. Phys. Chem. C, 120, 32, 18333-18339, Copyright (2016) American Chemical Society).*

The EL in a device is controlled by the bimolecular recombination process in the bulk of emissive layer. The exciton formation depends on the carrier density, carrier mobility, and capture cross section. As a result, EL becomes a useful tool to investigate the band edge radiative recombination process. The EL spectrum shows a good overlap with the PL of OIP layer, suggesting that the centers of bimolecular recombination are located in the NC layer (Figure 5.16a). Significant overlap between EL and PL suggests that the electron and hole transport are balanced in case of both NC and bulk films. A working pixel of NC bilayer LED is shown in the inset of Figure 5.16a, the devices exhibit uniform EL throughout the active area (~ 8 mm^2), measured over multiple devices (~ 30 in number).

The EL spectra for bulk and NC show comparable features. The E_{peak} in NC EL is blue shifted by ≈ 0.040 eV compared to that of bulk, this shift is similar to the shift observed between bulk and NC PL (≈ 0.037 eV). The FWHM for NC EL is ≈ 0.114 eV which is much less than that of NC PL (≈ 0.145 eV) and comparable to that of bulk PL and EL (≈ 0.102 eV) at 300 K. The observed narrowing in EL line width for NCs can be related to the low energy, band edge transition from larger crystals (~ 6 nm). The EL spectral shape for bulk and NC fits well to a Voigt function at 300 K, while the PL line shape for NC is a Gaussian. A Voigt profile implies contribution from lifetime and thermal broadening is a responsible broadening of EL. At low temperatures (~ 100 K) the NC EL spectra become increasingly asymmetric, which is similar to the bulk PL, the EL spectra also fits well with a Lorentzian profile (Figure 5.16b). The red shift in E_{peak} by ≈ 0.047 eV, is smaller than that in the case of NC PL (≈ 0.058 eV), at temperature ~ 100 K. The smaller shift in E_{peak} can be associated with local Joules heating. The high energy peaks visible in low-temperature PL, in the case of NC, are not visible in low-temperature EL spectra, suggesting that the smaller crystals (< 6 nm) are not accessed and do not contribute towards EL. Processes like internal re-absorption and energy transfer can also mask the contribution from smaller particles.

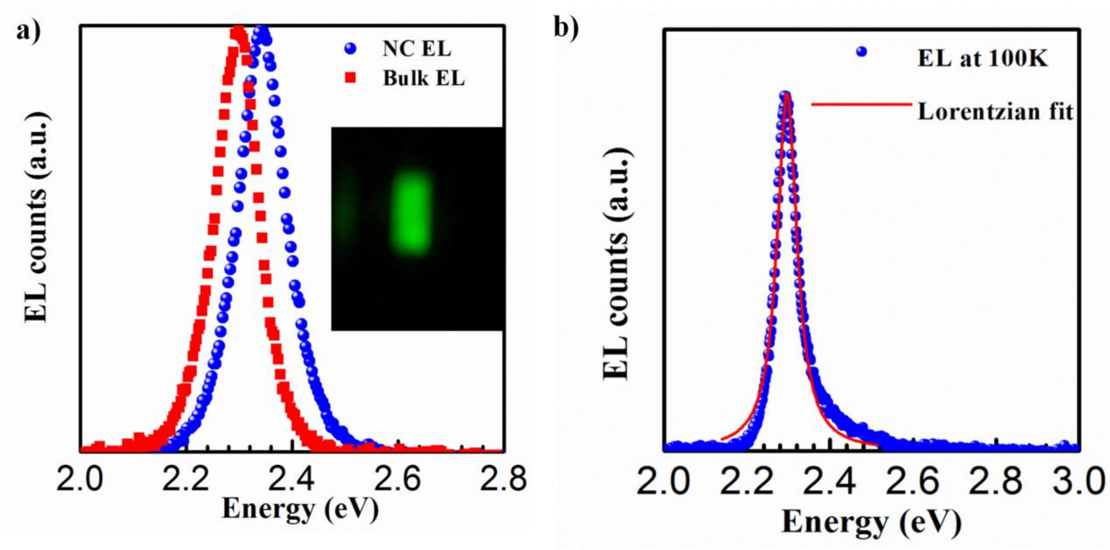

Figure 5.16: *a) EL from bulk (red square) and NC (blue circle) films, b) Low-temperature NC EL profile. (Reprinted with permission from P. Kumar, C. Muthu, V. C Nair, and K. S. Narayan, Quantum Confinement Effects in Organic Lead Tribromide Perovskite Nanoparticles, J. Phys. Chem. C, 120, 32, 18333-18339, Copyright (2016) American Chemical Society).*

5.3.6 III: Photocurrent ($I_{ph}(E)$) response from bulk and NC devices

The $I_{ph}(E)$ response along with the $\alpha(E)$, in the band edge region, can provide additional insight into the free carrier generation process. The excitonic nature of semiconductor can appear as a shift between the onset of $\alpha(E)$ and $I_{ph}(E)$, provided that the extrinsic processes such as interface or defects so not alter the carrier generation process. The spectral responsivity (R) of bulk and NC devices, measured in a bilayer structure, with N2200 and PCBM-C70 as n-type layers are shown in Figure 5.17a and 5.17b respectively. The $I_{ph}(E)$ edge for NC is blue shifted from the bulk $I_{ph}(E)$ by a magnitude (≈ 0.01 eV) as shown in the inset of Figure 5.17a. However, the $I_{ph}(E)$ exhibits only a negligible shift from the respective $\alpha(E)$ edge in both sets of devices.

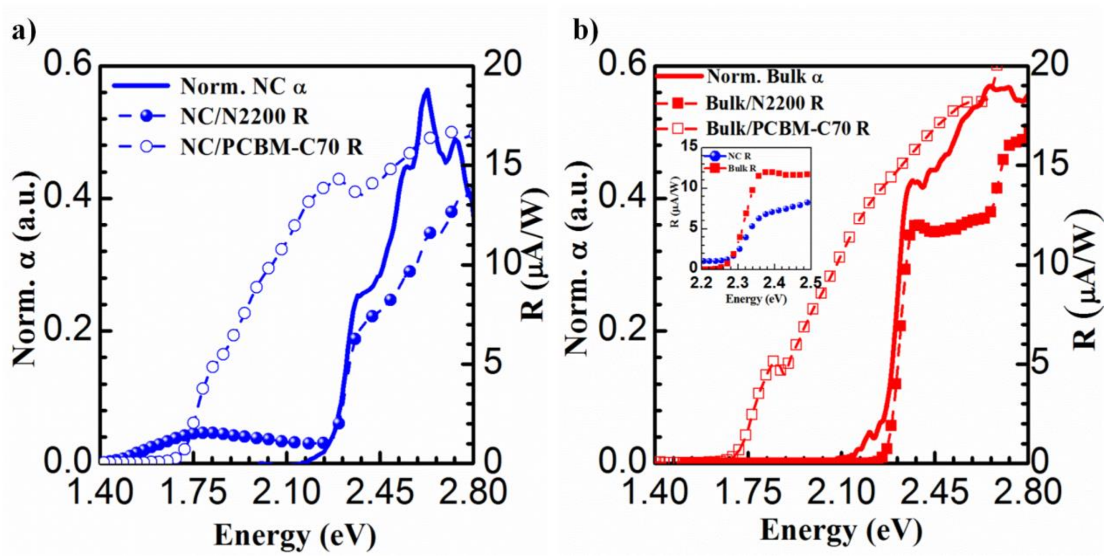

Figure 5.17: *I_{ph} (E) for bulk and NC films with a) N2200 and b) PCBM acceptor layers. The inset shows the shift in bulk and NC I_{ph}(E) response. (Reprinted with permission from P. Kumar, C. Muthu, V. C Nair, and K. S. Narayan, Quantum Confinement Effects in Organic Lead Tribromide Perovskite Nanoparticles, J. Phys. Chem. C, 120, 32, 18333-18339, Copyright (2016) American Chemical Society).*

The $I_{ph}(E)$ contribution from the organic layer is visible in NC based devices, which suggests that the charge transfer between perovskite NC layer and the organic layer is favored to a larger degree (which is not the case in bulk films). At the band edge, both bulk and NC films exhibit R ≈ 10 μA/W, which increases to ≈ 40 μA/W at a excitation energy of ~ 3 eV. Compared to the OIP layer, the n-type layers of N2200 and PCBM-C70 show low R (< 10 μA/W) for NC devices.

The observed selectivity, for charge transfer, in bulk perovskite can be related to the well-defined energy levels with low surface and gap states. This condition is relaxed in the case of NC, due to the quantum size effects and presence of surface states in significant number. Large surface states can result in the energy level pinning, giving rise to a greater flexibility for charge transfer in bilayer structure. In addition to the spectral response, the intensity dependence of $I_{ph}(E)$ in NC/N2200 devices has been studied at various excitation wavelengths (405 nm, 543 nm, and 632 nm) corresponding to the selective absorption of OIP and the organic layer. The $I_{ph}(E)$ shows linearly variation at low photon flux (~ 10^{11} – 10^{15} photons/s) (Figure 5.18).

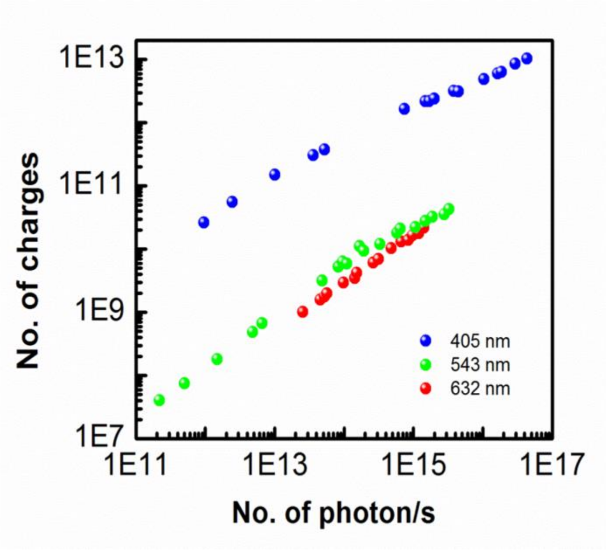

Figure 5.18: *Intensity dependence of I_{ph} (E) in NC/N2200 bilayer device for 405 nm (blue), 543 nm (green) and 632 nm (red) excitation. (Reprinted with permission from P. Kumar, C. Muthu, V. C Nair, and K. S. Narayan, Quantum Confinement Effects in Organic Lead Tribromide Perovskite Nanoparticles, J. Phys. Chem. C, 120, 32, 18333-18339, Copyright (2016) American Chemical Society).*

A linear $I_{ph}(E)$ response over a large range of photon flux is desirable for sensing applications. The observed property in OIP NC bilayer devices is advantageous for enhancing the optical window of detection beyond the band gap of perovskite. The additional option of acceptor characteristics featuring in the photodiode spectral response of the NC perovskite device can extend the optical window to NIR region.

5.4: Conclusions

To summarize, quantum confinement effects, optical properties, and charge transport were investigated in depth in the NCs of organic-inorganic hybrid perovskites. The size dependence, higher E_B, and improved stability are the key attributes of the NC systems. Estimates for E_B are arrived independently both from examining the temperature dependence of PL and $\alpha(E)$. Temperature dependence of emission shows a clear signature of structural phase transitions in bulk while such changes are not observed for NC system. Additionally, an increase in exciton-lattice coupling is observed with decrease in particle size. The two-fold increase in exciton-optical phonon coupling in NC also reflects in the modification of emission spectral profile which evolves from a Lorentzian at low temperature to a Gaussian at high temperature. The sizable PL observed in the NCs is translated in a device form where EL is readily observed, along with $I_{ph}(E)$ showing well-separated spectral features from NC and acceptor polymer. The bilayer device architecture shows potential to be employed as a single pixel emitter and detector in visible-NIR range.

References

[1] M. A. Green, A. Ho-Baillie and H. J. Snaith. The Emergence of Perovskite Solar Cells. *Nature Photonics* **2014,** *8*, 506-514.

[2] H. J. Snaith. Perovskites: The Emergence of a New Era for Low-Cost, High-Efficiency Solar Cells. *Journal of Physical Chemistry Letters* **2013,** *4*, 3623-3630.

[3] B. Saparov and D. B. Mitzi. Organic–Inorganic Perovskites: Structural Versatility for Functional Materials Design. *Chemical Reviews* **2016,** *116*, 4558-4596.

[4] D. B. Mitzi. Synthesis, Structure, and Properties of Organic-Inorganic Perovskites and Related Materials. *Progress in Inorganic Chemistry, Vol 48* **1999,** *48*, 1-121.

[5] A. Kojima, K. Teshima, Y. Shirai and T. Miyasaka. Organometal Halide Perovskites as Visible-Light Sensitizers for Photovoltaic Cells. *Journal of the American Chemical Society* **2009,** *131*, 6050-6051.

[6] H. S. Kim, S. H. Im and N. G. Park. Organolead Halide Perovskite: New Horizons in Solar Cell Research. *Journal of Physical Chemistry C* **2014,** *118*, 5615-5625.

[7] W. S. Yang, J. H. Noh, N. J. Jeon, Y. C. Kim, S. Ryu, J. Seo and S. I. Seok. High-Performance Photovoltaic Perovskite Layers Fabricated through Intramolecular Exchange. *Science* **2015,** *348*, 1234-1237.

[8] H. P. Zhou, Q. Chen, G. Li, S. Luo, T. B. Song, H. S. Duan, Z. R. Hong, J. B. You, Y. S. Liu and Y. Yang. Interface Engineering of Highly Efficient Perovskite Solar Cells. *Science* **2014,** *345*, 542-546.

[9] M. Saliba, T. Matsui, J-Y Seo, K. Domanski, J-P Correa-Baena, M. K. Nazeeruddin, S. M. Zakeeruddin, W. Tress, A. Abate, A. Hagfeldt and M. Gratzel. Cesium-Containing Triple Cation Perovskite Solar Cells: Improved Stability, Reproducibility and High Efficiency. *Energy & Environmental Science* **2016**, 9, 1989-1997.

[10] H. Cho, S-H Jeong, M-H Park, Y-H Kim, C Wolf, C-L Lee, J. H. Heo, A. Sadhanala, N. Myoung, S. Yoo, S. H. Im, R. H. Friend and T-W Lee. Overcoming the Electroluminescence Efficiency Limitations of Perovskite Light-Emitting Diodes. *Science* **2015,** *350*, 1222-1225.

[11] J. C. Yu, D. B. Kim, E. D. Jung, B. R. Lee and M. H. Song. High-Performance Perovskite Light-Emitting Diodes Via Morphological Control of Perovskite Films. *Nanoscale* **2016,** *8*, 7036-7042.

[12] Z. K. Tan, R. S. Moghaddam, M. L. Lai, P. Docampo, R. Higler, F. Deschler, M. Price, A. Sadhanala, L. M. Pazos, D. Credgington, F. Hanusch, T. Bein, H. J. Snaith and R. H. Friend. Bright Light-Emitting Diodes Based on Organometal Halide Perovskite. *Nature Nanotechnology* **2014,** *9*, 687-692.

[13] D. Li, P. Z. Liao, X. X. Shai, W. C. Huang, S. S. Liu, H. Li, Y. Shen and M. K. Wang. Recent Progress on Stability Issues of Organic-Inorganic Hybrid Lead Perovskite-Based Solar Cells. *RSC Advances* **2016,** *6*, 89356-89366.

[14] Q. Chen, H. N. Liu, H. S. Kim, Y. C. Liu, M. J. Yang, N. L. Yue, G. Ren, K. Zhu, S. Z. Liu, N. G. Park and Y. Zhang. Multiple-Stage Structure Transformation of Organic-Inorganic Hybrid Perovskite $CH_3NH_3PbI_3$. *Physical Review X* **2016,** *6*, 031042.

[15] X. Guo, C. McCleese, W. Gao, M. Wang, L. Sang and C. Burda. Investigation of Moisture Stability and PL Characteristics of Terpineol-Passivated Organic–

Inorganic Hybrid Perovskite. *Materials for Renewable and Sustainable Energy* **2016,** *5*, 17.

[16] N. Rajamanickam, S. Kumari, V. K. Vendra, B. W. Lavery, J. Spurgeon, T. Druffel and M. K. Sunkara. Stable and Durable $CH_3NH_3PbI_3$ Perovskite Solar Cells at Ambient Conditions. *Nanotechnology* **2016,** *27*, 235404.

[17] J. Cui, P. F. Li, Z. F. Chen, K. Cao, D. Li, J. B. Han, Y. Shen, M. Y. Peng, Y. Q. Fu and M. K. Wang. Phosphor Coated Nio-Based Planar Inverted Organometallic Halide Perovskite Solar Cells with Enhanced Efficiency and Stability. *Applied Physics Letters* **2016,** *109*, 171103.

[18] C. Muthu, S. R. Nagamma and V. C. Nair. Luminescent Hybrid Perovskite Nanoparticles as a New Platform for Selective Detection of 2,4,6-Trinitrophenol. *RSC Advances* **2014,** *4*, 55908-55911.

[19] L. C. Schmidt, A. Pertegas, S. Gonzalez-Carrero, O. Malinkiewicz, S. Agouram, G. M. Espallargas, H. J. Bolink, R. E. Galian and J. Perez-Prieto. Nontemplate Synthesis of $CH_3NH_3PBr_3$ Perovskite Nanoparticles. *Journal of the American Chemical Society* **2014,** *136*, 850-853.

[20] J. A. Sichert, Y. Tong, N. Mutz, M. Vollmer, S. Fischer, K. Z. Milowska, R. G. Cortadella, B. Nickel, C. Cardenas-Daw, J. K. Stolarczyk, A. S. Urban and J. Feldmann. Quantum Size Effect in Organometal Halide Perovskite Nanoplatelets. *Nano Letters* **2015,** *15*, 6521-6527.

[21] V. D'Innocenzo, A. R. S. Kandada, M. De Bastiani, M. Gandini and A. Petrozza. Tuning the Light Emission Properties by Band Gap Engineering in Hybrid Lead Halide Perovskite. *Journal of the American Chemical Society* **2014,** *136*, 17730-17733.

[22] S. Gonzalez-Carrero, R. E. Galian and J. Perez-Prieto. Maximizing the Emissive Properties of $CH_3NH_3PbBr_3$ Perovskite Nanoparticles. *Journal of Materials Chemistry A* **2015,** *3*, 9187-9193.

[23] R. Naphade, S. Nagane, G. S. Shanker, R. Fernandes, D. Kothari, Y. Y. Zhou, N. P. Padture and S. Ogale. Hybrid Perovskite Quantum Nanostructures Synthesized by Electrospray Antisolvent-Solvent Extraction and Intercalation. *ACS Applied Materials & Interfaces* **2016,** *8*, 854-861.

[24] M. F. Ayguler, M. D. Weber, B. M. D. Puscher, D. D. Medina, P. Docampo and R. D. Costa. Light-Emitting Electrochemical Cells Based on Hybrid Lead Halide Perovskite Nanoparticles. *Journal of Physical Chemistry C* **2015,** *119*, 12047-12054.

[25] Yuxi Tian and Ivan G. Scheblykin. Artifacts in Absorption Measurements of Organometal Halide Perovskite Materials: What Are the Real Spectra? *The Journal of Physical Chemistry Letters* **2015,** *6*, 3466-3470.

[26] S. J. Leach and H. A. Scheraga. Effect of Light Scattering on Ultraviolet Difference Spectra1. *Journal of the American Chemical Society* **1960,** *82*, 4790-4792.

[27] M. Saba, M. Cadelano, D. Marongiu, F. P. Chen, V. Sarritzu, N. Sestu, C. Figus, M. Aresti, R. Piras, A. G. Lehmann, C. Cannas, A. Musinu, F. Quochi, A. Mura and G. Bongiovanni. Correlated Electron-Hole Plasma in Organometal Perovskites. *Nature Communications* **2014,** *5*.

[28] A. M. Soufiani, F. Huang, P. Reece, R. Sheng, A. Ho-Baillie and M. A. Green. Polaronic Exciton Binding Energy in Iodide and Bromide Organic-Inorganic Lead Halide Perovskites. *Applied Physics Letters* **2015,** *107*, 231902.

[29] R. Sheng, A. Ho-Baillie, S. J. Huang, S. Chen, X. M. Wen, X. J. Hao and M. A. Green. Methylammonium Lead Bromide Perovskite-Based Solar Cells by Vapor-Assisted Deposition. *Journal of Physical Chemistry C* **2015,** *119*, 3545-3549.

[30] K. Galkowski, A. Mitioglu, A. Miyata, P. Plochocka, O. Portugall, G. E. Eperon, J. T. W. Wang, T. Stergiopoulos, S. D. Stranks, H. J. Snaith and R. J. Nicholas.

Determination of the Exciton Binding Energy and Effective Masses for Methylammonium and Formamidinium Lead Tri-Halide Perovskite Semiconductors. *Energy & Environmental Science* **2016,** *9*, 962-970.

[31] W. J. Parak, L. Manna, F. C. Simmel, D. Gerion and P. Alivisatos. Quantum Dots. In *Nanoparticles*, Wiley-VCH Verlag GmbH & Co. KGaA: 2005; pp 4-49.

[32] W. Gao, X. Gao, T. A. Abtew, Y-Y Sun, S. Zhang and P. Zhang. Quasiparticle Band Gap of Organic-Inorganic Hybrid Perovskites: Crystal Structure, Spin-Orbit Coupling, and Self-Energy Effects. *Physical Review B* **2016,** *93*, 085202-085207.

[33] M. D. Sturge. Optical Absorption of Gallium Arsenide between 0.6 and 2.75 Ev. *Physical Review* **1962,** *127*, 768-773.

[34] W. J. Turner, W. E. Reese and G. D. Pettit. Exciton Absorption and Emission in Inp. *Physical Review* **1964,** *136*, A1467-A1470.

[35] N. Sestu, M. Cadelano, V. Sarritzu, F. P. Chen, D. Marongiu, R. Piras, M. Mainas, F. Quochi, M. Saba, A. Mura and G. Bongiovanni. Absorption F-Sum Rule for the Exciton Binding Energy in Methylammonium Lead Halide Perovskites. *Journal of Physical Chemistry Letters* **2015,** *6*, 4566-4572.

[36] J. M. Richter, M. Abdi-Jalebi, A. Sadhanala, M. Tabachnyk, J. P. H. Rivett, L. M. Pazos-Outon, K. C. Godel, M. Price, F. Deschler and R. H. Friend. Enhancing Photoluminescence Yields in Lead Halide Perovskites by Photon Recycling and Light out-Coupling. *Nature Communications* **2016,** *7*, 13941.

[37] H. S. Jung and N. G. Park. Perovskite Solar Cells: From Materials to Devices. *Small* **2015,** *11*, 10-25.

[38] W. J. Yin, J. H. Yang, J. Kang, Y. F. Yan and S. H. Wei. Halide Perovskite Materials for Solar Cells: A Theoretical Review. *Journal of Materials Chemistry A* **2015,** *3*, 8926-8942.

[39] D. Li, G. Wang, H-C Cheng, C-Y Chen, H. Wu, Y. Liu, Y. Huang and X. Duan. Size-Dependent Phase Transition in Methylammonium Lead Iodide Perovskite Microplate Crystals. *Nature Communications* **2016,** *7*, 11330.

[40] C. C. Chen, A. B. Herhold, C. S. Johnson and A. P. Alivisatos. Size Dependence of Structural Metastability in Semiconductor Nanocrystals. *Science* **1997,** *276*, 398-401.

[41] J. B. Rivest, L. K. Fong, P. K. Jain, M. F. Toney and A. P. Alivisatos. Size Dependence of a Temperature-Induced Solid-Solid Phase Transition in Copper(I) Sulfide. *Journal of Physical Chemistry Letters* **2011,** *2*, 2402-2406.

[42] H. K. M. Ueta, K. Kobayashi, Y. Toyozawa, E. Hanamura. *Excitonic Processes in Solids*. Springer Berlin Heidelberg: 1986.

[43] F. Zhang, H. Zhong, C. Chen, X-G Wu, X. Hu, H. Huang, J. Han, B. Zou and Y. Dong. Brightly Luminescent and Color-Tunable Colloidal $CH_3NH_3PbX_3$ (X = Br, I, Cl) Quantum Dots: Potential Alternatives for Display Technology. *Acs Nano* **2015,** *9*, 4533-4542.

[44] S. Rudin, T. L. Reinecke and B. Segall. Temperature-Dependent Exciton Linewidths in Semiconductors. *Physical Review B* **1990,** *42*, 11218-11231.

[45] Y. Toyozawa. Theory of Line-Shapes of the Exciton Absorption Bands. *Progress of Theoretical Physics* **1958,** *20*, 53-81.

[46] L. Besombes, K. Kheng, L. Marsal and H. Mariette. Acoustic Phonon Broadening Mechanism in Single Quantum Dot Emission. *Physical Review B* **2001,** *63*, 155307.

[47] D. Gammon, E. S. Snow, B. V. Shanabrook, D. S. Katzer and D. Park. Homogeneous Linewidths in the Optical Spectrum of a Single Gallium Arsenide Quantum Dot. *Science* **1996,** *273*, 87-90.

[48] S. A. Lourenco, I. F. L. Dias, J. L. Duarte, E. Laureto, V. M. Aquino and J. C. Harmand. Temperature-Dependent Photoluminescence Spectra of Gaassb/Algaas and Gaassbn/Gaas Single Quantum Wells under Different Excitation Intensities. *Brazilian Journal of Physics* **2007,** *37*, 1212-1219.

[49] L. M. Pazos-Outón, M. Szumilo, R. Lamboll, J. M. Richter, M. Crespo-Quesada, M. Abdi-Jalebi, H. J. Beeson, M. Vrućinić, M. Alsari, H. J. Snaith, B. Ehrler, R. H. Friend and F. Deschler. Photon Recycling in Lead Iodide Perovskite Solar Cells. *Science* **2016,** *351*, 1430-1433.

[50] M. Wojdyr. Fityk: A General-Purpose Peak Fitting Program. *Journal of Applied Crystallography* **2010,** *43*, 1126-1128.

Chapter 6: Perovskite Quantum Dot Infused Polymer Fiber Emitters

6.1: Introduction

Nanostructures of low temperature, solution-processed organic-inorganic hybrid perovskites (OIPs) have been well recognized as luminous emitters (bright PL and EL) with wide-range in band gap tunability [1-5]. It has also been experimentally proven that the emission quantum yield improves manyfold with a decrease in average grain size [3, 6] and maximizes for quantum dots (QDs) with yield ~ 80-90 %) [7, 8] (as was also discussed in chapter 4 and 5). However, the OIP QDs still remains vulnerable to degradation due to the inefficient shielding, which can modify the perovskite framework and quench the luminescence [9, 10]. The core-shell QD geometry has been explored extensively for selectively modifying the reaction kinetics of QDs, similar architecture can be utilized to control the reaction with moisture and oxygen [11, 12]. Polymer matrices like Poly(methyl methacrylate) (PMMA) and polystyrene (PS) is commonly used for encapsulating the OIP core [13-15]. Use of a low refractive index material, as a shell, can also improve the light out-coupling (depending on the structure) by reducing the total internal reflection [16, 17].

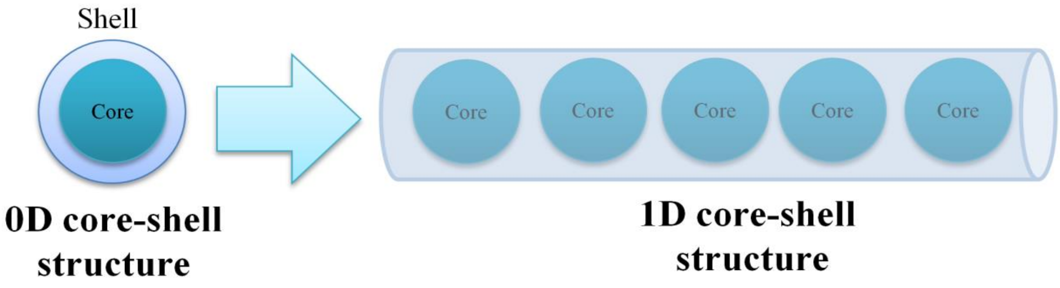

Figure 6.1: *Schematic representation of 0-D and 1-D core-shell structure of QDs.*

The concept of a 0-D core-shell QD framework can be extended to 1-D structures, where the shell is in the form of a linear fiber with OIP QDs homogeneously distributed [18, 19]. High molecular weight (~ 100 kDa) and low refractive index polymers like PMMA and PS can be pulled into thin fibers of diameter varying from 0.1 - 10 μm and several millimeters in length, using electrospinning [20-22]. Electrospun fibers are of interest for many applications including 3D microcavity for lasers [22, 23], aligned channels for field effect transistors [24, 25] and photodetectors [26-28]. 3-D geometries like in electrospun fibers are also known to host whispering gallery modes and allows for high quality-factors and dynamic tuning range [29, 30]. In this study the fibers of PMMA were electrospun along with the organic methylammonium bromide (MABr) and inorganic lead bromide ($PbBr_2$) salt, the OIP QDs were formed in situ by the phase separation of OIP precursor from PMMA matrix [31, 32]. The fibers show very high fluorescence quantum yield (> 50 %) along with a tunable emission width. Simultaneously, the fibers also demonstrate very high stability against moisture and negligible decay in PL yield when stored in ambient conditions (no observable change in PL intensity for over 6 months at relative humidity ~ 65%).

6.2: Experimental details

6.2.1: Materials

Methylammonium bromide (MABr) and methylammonium iodide (MAI) were purchased from Dyesol, Australia. Lead bromide ($PbBr_2$) (~ 98 % metal basis) was purchased from Alfa Aesar and lead iodide (PbI_2) (~99.9% metal basis) was obtained from Sigma-Aldrich. PMMA and PS were procured locally.

6.2.2: Electrospinning

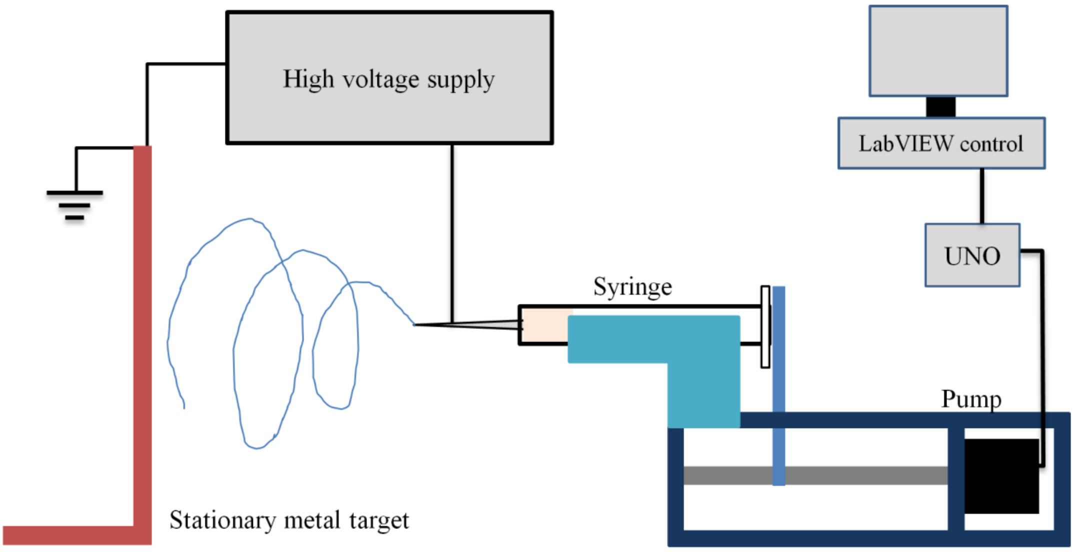

Figure 6.2: *A schematic representation of electrospinning setup.*

OIP infused PMMA fibers were electrospun in a custom made setup. The pump was driven using a 1/16 micro stepped stepper motor controlled using an Arduino Uno and the LabVIEW Interface for Arduino (LIFA). The high voltage supply (A push-pull amplifier coupled with a Cockcroft–Walton generator) was supplied by Zeonics Systech, Bangalore. A metal plate was used as a stationary collector (Figure 6.1). Fibers were spun from 17.5 wt % solution of PMMA in DMF or DMF/THF (1:1, v/v) mixture. The OIP precursor, dissolved in DMF was added to the PMMA solution at weight ratio varying from 0.16 to 5 wt %. All fibers were spun at 15 KV at a target distance of 15 cm.

6.2.3: Characterization

For characterization purpose, all fiber samples were sandwiched between a microscope glass slide (1.1mm thickness) and a cover slip (170 µm thickness).

Photoluminescence: PL measurements were performed on a laser PL setup using a UV-blue LED (365 nm) or laser (405 nm). The emission was collected using a fiber-coupled CCD spectrometer (Hamamatsu low noise TM CCD). Temperature dependent PL measurements were performed on a temperature controlled, liquid nitrogen cooled microscope stage (Linkam LTS420). A 405 nm laser was coupled to an upright microscope and focused on fibers using a 0.45 numerical aperture, 50× objective. Emission was collected in 180-degree reflection geometry through a fiber-coupled CCD spectrometer and a 430 nm long pass filter was used to filter the laser emission at the collection end. PLQY was measured in a lab built system using BWtek spectrometer and Newport integrating sphere.

Absorption: Absorption measurements were performed on a Perkin Elmer UV-Vis spectrometer equipped with an integrating sphere. Integrating sphere based absorption measurement is necessary to decrease the contribution from scattering.

Localized Confocal map: Localized emission and the vertical Z-stack map were recorded on Zeiss LSM 700 microscope where a 480 nm laser was used for excitation while the emission was collected using PMT. An oil immersion 100× objective was used for excitation and collection of emission. The localized spectral map was created by splitting the emission into two PMT channels using variable dichroic.

X-Ray Diffraction: Powder X-Ray diffraction was performed on the fiber samples sandwiched between two glass slides on a Bruker instrument. 2θ was varied from 10 to 60 degree.

Fiber structure: Localized surface topography and fiber structures were measured using JPK nano wizard AFM. Free standing fibers were adhered to a PDMS substrate to reduce the degree of freedom while the tip scans over the fiber. Images were recorded through tapping mode scanning using a Si cantilever of resonance frequency ~ 300 KHz and force constant ~ 40 N/m.

PL lifetime: Emission lifetime for different fiber samples were measured on a Time-correlated single photon counting (TCSPC) setup (Horiba). 450 nm laser was used for excitation, while the photons were counted at peak emission wavelength for fibers with different wt % of OIP.

Amplified spontaneous emission (ASE)

Optical ASE measurements were performed at Prof. Reji Philip's laboratory at Raman Research Institute, Bangalore. A high energy per pulse (> 200 μJ), femtosecond pulse width, Ti-Sapphire laser was frequency doubled (second harmonic generation) to 400 nm as the excitation source. The light source was focused in order to increase the power per pulse for 400 nm excitation. The emission was collected using a fiber-coupled CCD spectrometer (Hamamatsu TM CCD) at 90-degree geometry.

6.3: Results and Discussion

6.3.1: Electrospinning OIP quantum dot infused polymer fibers

The solution of PMMA and OIP precursors ($PbBr_2$: MABr in 1:1.05 molar ratio), dissolved in DMF, forms a homogeneous mixture without any crystallization of OIP particles. Figure 6.3 shows the solution of 17.5 wt % PMMA with different wt % of OIP precursor. The solution marked as A and B contains micron sized OIP crystals formed using solvent extraction technique, which shows fluorescence in the yellow-orange region (at 365 nm excitation). Similar behavior was not observed in PMMA/OIP solution mixture were weak purple-blue fluorescence was observed upon excitation at 365 nm. The 17.5 wt % solution of PMMA in DMF was ideal for spinning uniform fibers of diameter ~ 5 - 10 μm, without any beads being formed. For the pristine PMMA, the fiber thickness increased with concentration, while the shape changed from strings (cylindrical) to tapes (flat).

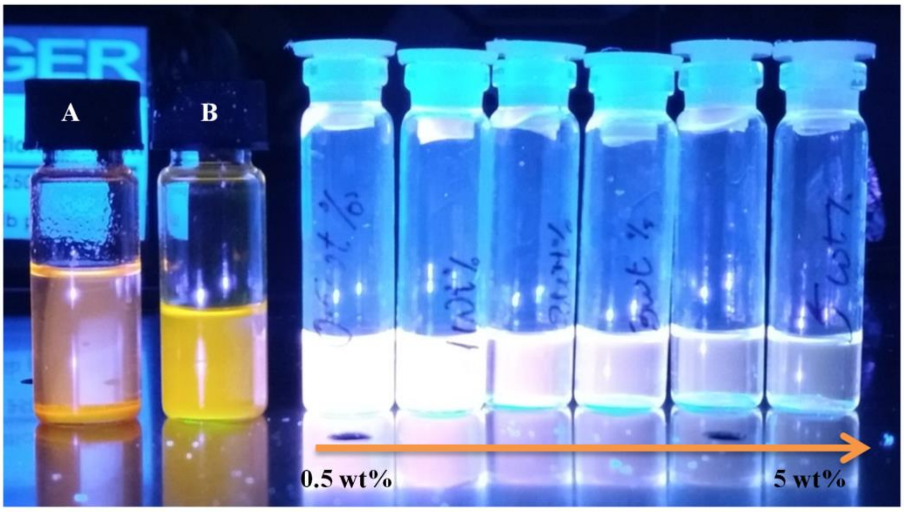

Figure 6.3: *PMMA solutions (17.5 wt %) in DMF with OIP concentration varying from 0.5wt % to 5 wt % (from left to right).*

The conductivity of electrospinning solution plays an important role in controlling the fiber diameter, salts and acids have been readily used to decrease the fiber diameter and surface roughness [33-35]. On addition of OIP precursor salt, the $PbBr_2$ and MABr ionizes into Pb^{2+}, MA^+, and Br^-, these ions increases the conductance of the electrospinning solution. In electrospinning, the solution is drawn into a cone-like structure at the tip of the needle, this is known as Taylor cone [36], which is assumed as an equipotential surface, from which jets of charged particles originate. The charges of the same polarity, collected in the solution, repel each other which results in stretching of the solution. Increasing the conductance of electrospinning solution allows more charges to be carried by the jets. The increase in the stretching of solution causes thinning of fibers [37, 38] while the surface becomes smooth [39].

A number of forces like electric field, Coulombic, surface tension, viscoelastic, air drag and gravitational are involved in the electrospinning process. Increasing the net charge density (σ) modifies the strength of Coulombic forces, the charge conservation equation can be written as [40],

$$I_t = \pi R^2 KE + 2\pi R\nu\sigma \tag{6.1}$$

Where I_t is the constant total current in the jet, R is the jet radius, K is solution conductance and E is vertical component of the electric field. In presence of additional ions, the K and σ get modified which results in increased stretching force. Additional ions present in the solution also reduce the required field strength for electrospinning. Since the electrospinning process is driven by the repulsion of like charges, the positive and negative ions do not separate spatially, which is also evident by the formation of OIP QDs in the PMMA fibers. Effects of an increase in solution conductance can be realized at a very small fraction (~ 0.01-0.1 wt %) or ions.

The fiber diameter shows negligible dependence on PMMA at large OIP concentration. The fiber diameter decreases significantly (~ 1 - 2 μm) upon addition of OIP precursor to the PMMA, compared to that of pristine PMMA fibers (5-10 μm). Upon electrospinning; colorless fibers get collected onto the stationary substrate, as shown in Figure 6.4a. The pristine PMMA fibers get deposited as a uniform layer, while the ability to form a uniform, porous film decreases with an increase in OIP precursor wt %. At low OIP wt % (~ 0.16 -1 wt %), the fibers form dense films, while for OIP concentration > 2 wt %, mid-air fiber formation and drying prior to deposition is observed. Upon excitation, at 365 nm, the OIP/PMMA fibers, show high luminescence in green (~ 530 nm), which is comparable to that of OIP QDs, as is shown in Figure 6.4b. The emission intensity increases with the wt % of OIP precursor, resulting in larger density of OIP particles. High PL is a signature of QDs getting formed in PMMA fibers in-situ during the electrospinning process.

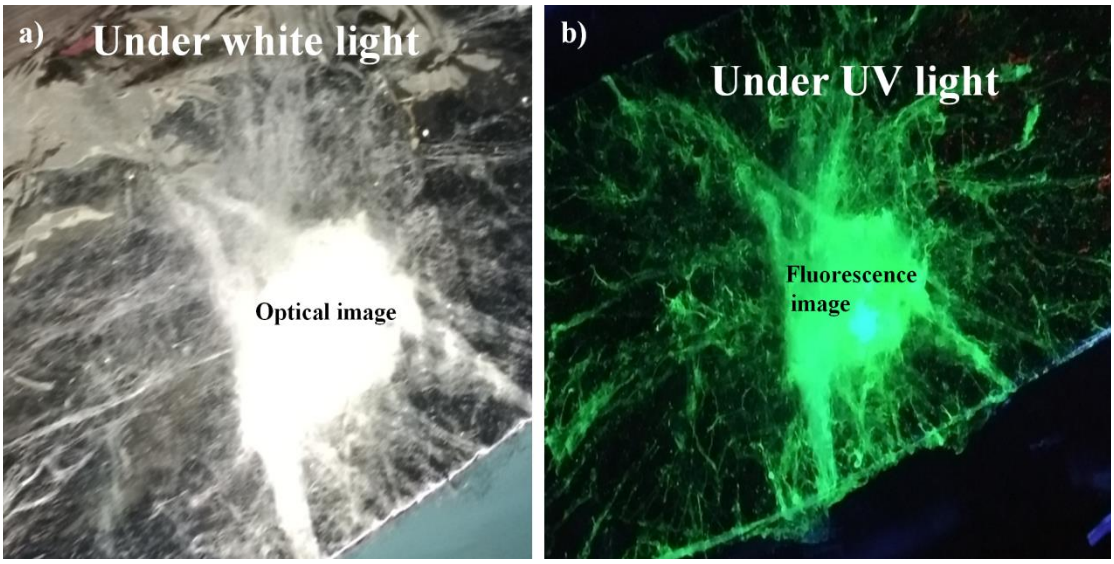

Figure 6.4: *OIP infused PMMA fibers in a) room light and b) UV (365 nm) light.*

6.3.2: In-situ formation of OIP quantum dots

AFM is used as a tool to further understand the formation process of OIP QDs. The optical and fluorescence image of a randomly picked fiber bundle is shown in Figure 6.5a and 6.5b respectively. In the far field, a uniform fluorescence emission for all the fibers is observed (λ_{exc} ~ 480 nm) which points towards the homogeneous distribution of OIP QDs.

The AFM surface topography of a small region, highlighted in the optical image in Figure 6.5a, is shown in Figure 6.5c. The fiber diameter measured using the AFM cross-section profile shows a variation from 0.5 - 2 μm. The fiber shape can vary from cylindrical to ribbon like depending on the concentration of the spinning solution. The phase image (Figure 6.5d) shows a large variation across the fiber, suggesting the presence of materials with different stiffness.

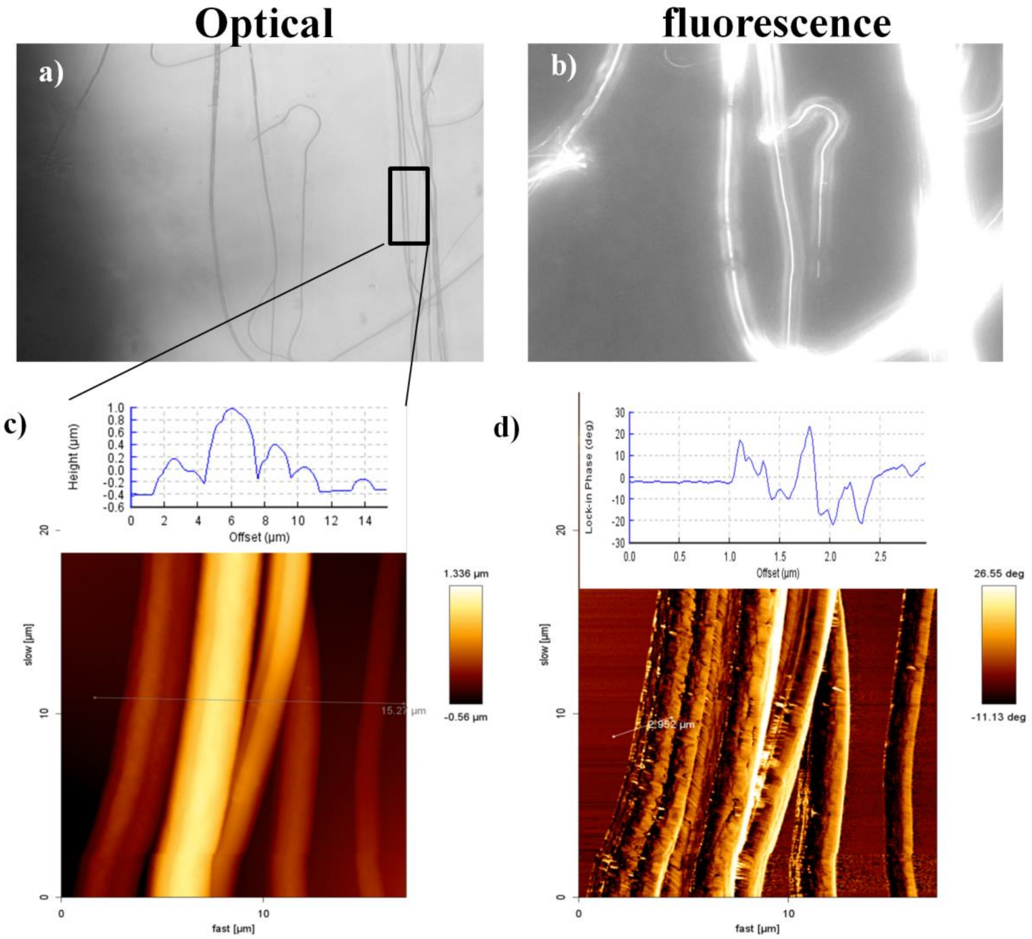

Figure 6.5: *a) Optical and b) fluorescence image of a bundle of fibers, c) topography and d) phase image of the OIP infused PMMA fibers shows large change on the edges.*

A zoomed image of a single fiber in morphology is shown in Figure 6.6a. The surface morphology is homogeneous with low roughness; however, the phase image shows long ellipsoidal grains along the length of the fiber, with major axis across the fiber length (Figure 6.6b). The ellipsoidal grain, visible in phase image depicts the OIP QDs embedded in the PMMA matrix. The presence of ellipsoidal OIP grains, embedded in PMMA matrix, can be further explored by probing the dissolved fiber remnants. The PMMA matrix readily dissolves in toluene leaving behind the OIP grains, which do not solubilize in toluene. Figure 6.6c shows the AFM morphology of a thin film spin coated from fibers dissolved in toluene. The needle-like grains are clearly seen in the surface topography image, while these grains were not visible in the fiber topography. The grain size varies from 50 - 100 nm in length and 20-50 nm in width. The large grain size is an indicative of aggregated crystallites and the individual crystal domain is expected to be much lower (~ 4 - 6 nm).

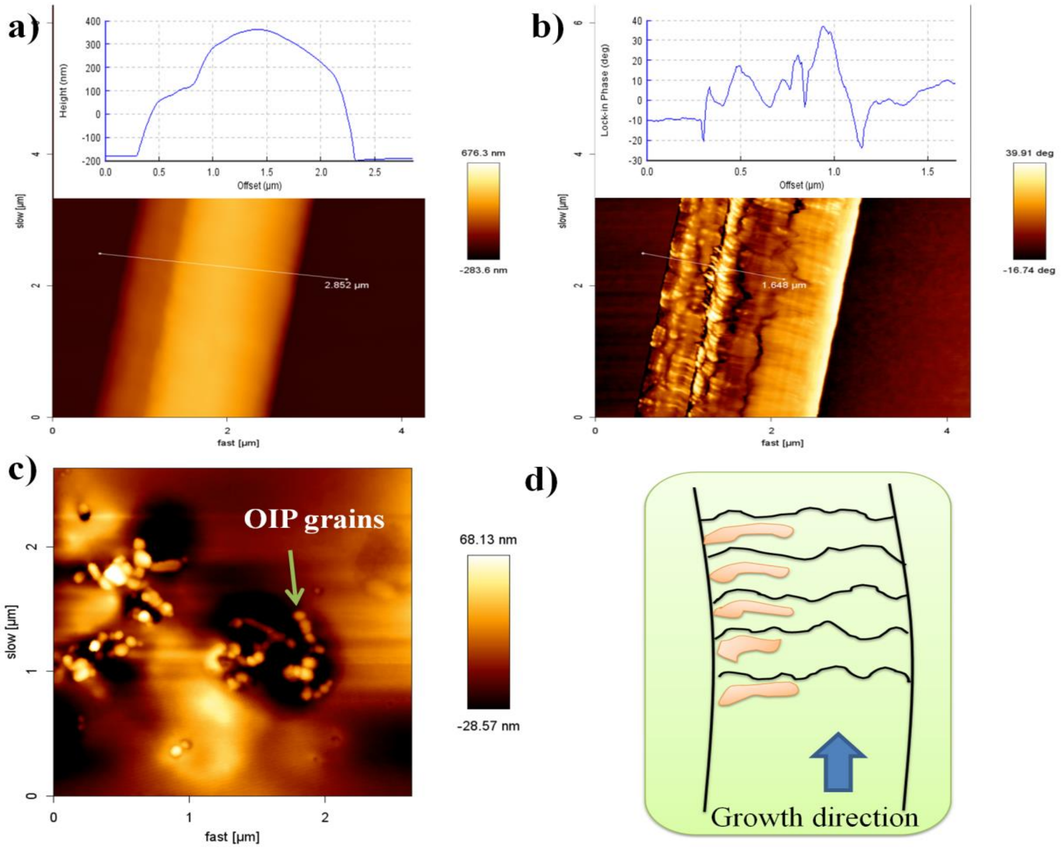

Figure 6.6: *a) Surface topography image of single fiber b) corresponding phase image, c) Topography of thin film formed by spin coating from fibers dissolved in toluene and d) schematic illustration of the possible growth mechanism of PMMA fibers infused with OIP QDs.*

From the above observation is can be concluded that the fibers are composed primarily of PMMA matrix with the OIP grains distributed along the periphery of the fiber (embedded below the surface). The long axis, of OIP grain, is aligned perpendicular to the direction of fiber growth; such growth patterns are rather unlikely and originate from the inhomogeneous phase separation. A schematic of the in-situ formation of OIP crystallite during the fiber growth process is shown in Figure 6.6d.

The dielectric constant of OIP (~ 7) is large compared to PMMA (~ 3.5); this can result in phase separation of two systems upon drying of solvent. The process of nanocrystal formation within the PMMA fiber is speculated to be governed by the supersaturation of precursor solution during electrospinning. A similar process has been observed for nanostructure formed while electrospinning of sol-gel solution of oxides like TiO_2, $BaTiO_3$. As the fiber gets pulled towards the target, the edge of fiber dries in a sequential order, where each segment is ~ 100-200 nm, creating a supersaturated state which drives rapid nucleation and crystallization of nanocrystals. Looking at the AFM phase images, we can understand the alignment of perovskite nanocrystals clusters is parallel to the fiber growth axis suggesting that the nanocrystals are getting formed at the drying edge of the precursor.

6.3.3: Crystal structure of OIP quantum dots

The XRD spectra of PMMA fibers with OIP QDs demonstrate very few diffraction peaks, indicative of small range order, as shown in Figure 6.7a. The 2θ value for (100) peak position is shifted by ~ 2.03 degree from that of bulk, suggesting a large decrease in lattice constant (~ 11.6%), which can also be related to stoichiometry imbalance. The shift in 2θ value for (100) peak, from that of bulk, shows trends similar to that for submicron crystals and nanocrystals [6]. A limited number of diffraction peaks observed in powder XRD restricts further structure analysis of QDs. The width of the diffraction peak is significantly larger for QDs embedded in fiber, compared to that of bulk and nanocrystal. Increased broadening suggests smaller crystallite domain (diameter ~ 2 - 4 nm) for the QDs. The width and 2θ value of diffraction peak show minimal variation with an increase in the concentration of OIP QDs (Figure 6.7b). This suggests that the particle size has small distribution and is limited to < 6 nm. Alternatively, the broadening can also be dominated by the smallest particles.

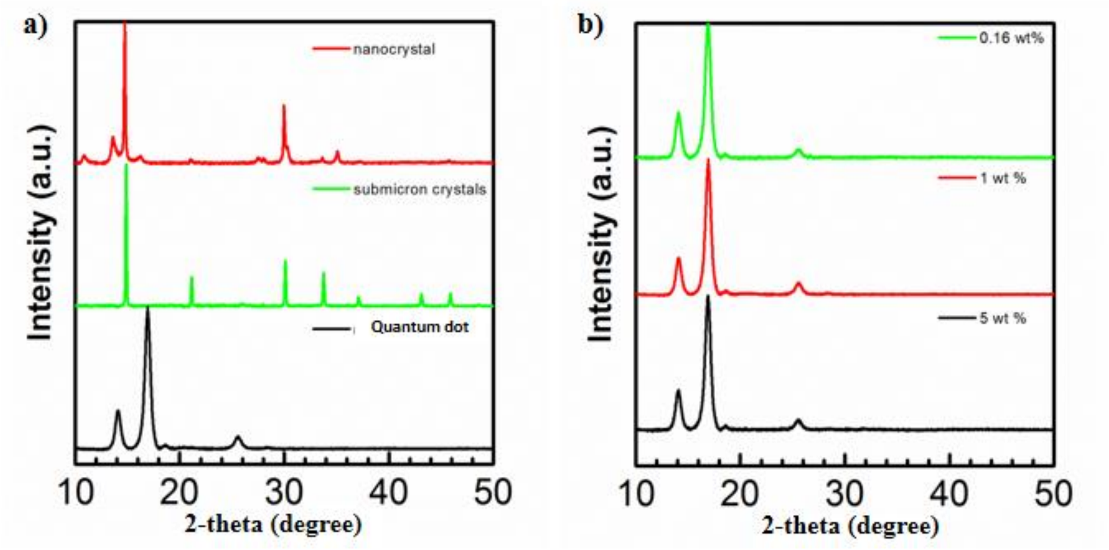

Figure 6.7: *XRD spectra of a) OIP QDs plotted against that of the nanocrystal and polycrystalline film, b) fibers spun with different OIP concentration.*

6.3.4: Confinement effects in OIP quantum dots

The small size of OIP QDs should lead to quantum confinement effect, which can be probed using optical techniques. The absorption and emission as a function of OIP concentration were used to estimate the extent of quantum confinement effects.

6.3.4 I: Increase in the optical band gap

The absorption of OIP QDs embedded in PMMA fiber matrix is measured in an integrating sphere-based spectrometer to minimize the scattering losses. Due to the porous nature of fiber bundle and low OIP content, the amount of light scattered is larger than the absorption, thereby masking the absorption signal, making it weak for further detection. Normalized absorption for different concentrations of OIP, along with bulk and NC absorption, is shown in Figure 6.8a. The absorption edge and the excitonic peak get blue-shifted with a decrease in OIP concentration, which indicates an increase in the optical band gap. The Larger band gap is associated with particles of smaller diameters, where the confinement effects are stronger. The band gap estimates from absorption spectra have been summarized in table 6.1. Upon dissolving the fibers in toluene, OIP grains are no longer capped, which results in loosely aggregated crystallites. The *α(E)* features of dissolved fiber grains are similar to that of bulk (excitonic peak at same energy), which indicates weak aggregation (Figure 6.8b).

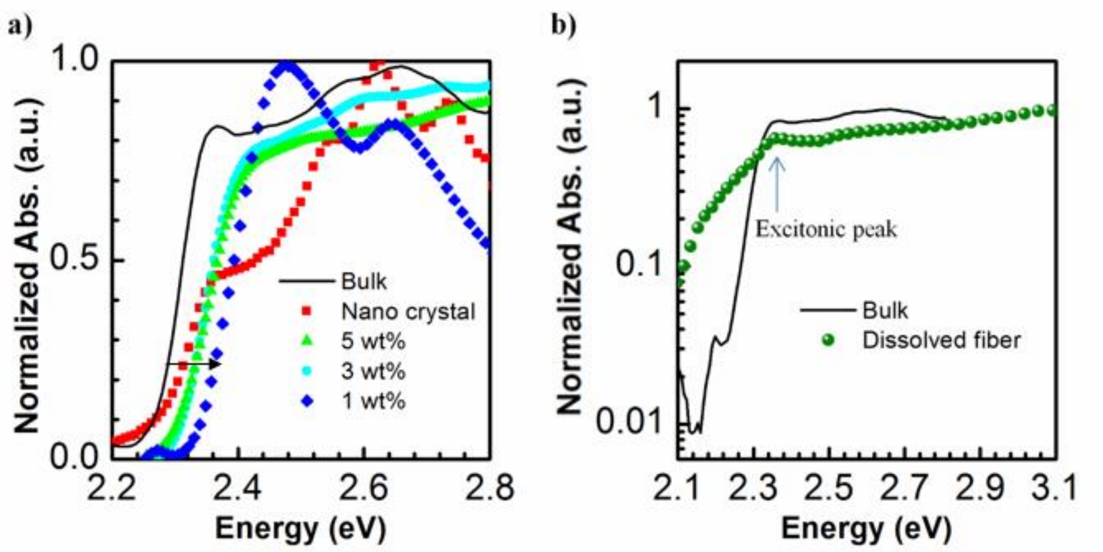

Figure 6.8: *a) absorption spectrum of OIP QDs infused in PMMA fibers, bulk and nanocrystal absorption has been plotted for reference, b) Absorption spectrum of thin film spin coated from fibers dissolved in toluene.*

Table 6.1: Band gap for different ratio of OIP QD in PMMA fiber matrix.

System	Band gap (eV)
Bulk	~ 2.36
Nanocrystal	~ 2.39
5 wt % OIP	~ 2.40
3 wt % OIP	~ 2.40
1 wt % OIP	~ 2.43

6.4.3 II: Blue shift in PL

The PL quantum yield in OIP QD infused PMMA fibers is much higher than that of bulk perovskite films. High PL efficiency can result from factors like quantum confinement, increased radiative surface recombination and improved light out-coupling. The emission intensity increases with an increase in OIP concentration from 0.16 wt % to 5 wt %, as can be seen in Figure 6.9a. It should be noted that the OIP QDs size and density both are low at lower concentrations. The blue shift in energy gap, seen in *α(E)* measurement, is also visible in PL(E) spectra. The peak position (E_{peak}) of emission, at 300K, shows a large blue shift with a decrease in OIP concentration (Figure 6.9b).

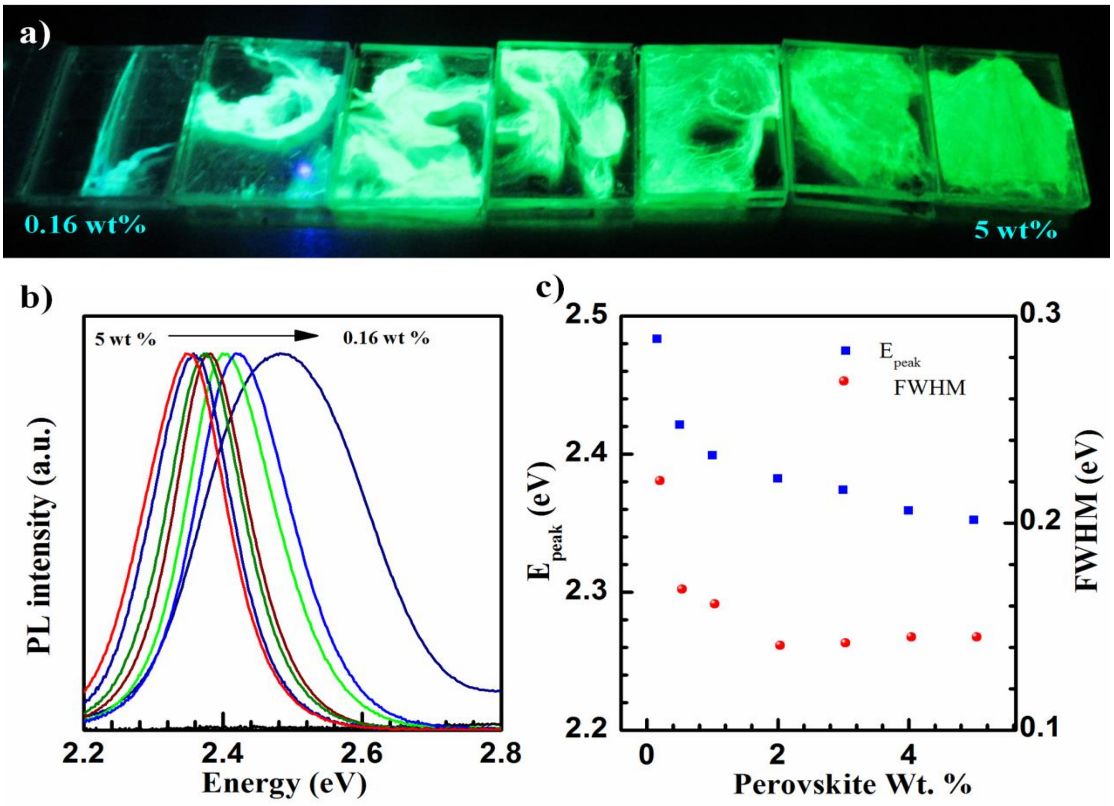

Figure 6.9: *a) Fluorescence image of PMMA fiber with varying OIP concentration, b) Emission spectral profile and c)* E_{peak} *and FWHM as a function of OIP concentration.*

The shift in E_{peak} and an increase in FWHM show a similar trend as a function of OIP concentration, as is shown in Figure 6.9c. The larger shift for lower concentration can be related to a large decrease in particles size, which exponentially decreases with increase in OIP concentration. This suggests that the confinement related effects can significantly dominate the nature of emission below the exciton Bohr radius (~ 3 nm) [41]. At lower concentration, the broadening of spectral width is observed, which can be attributed to poly-dispersity in QDs size. The PLQY increases from 20% for 0.5 wt% OIP to 80% for 3 wt% OIP, the QY decreases with further increase in OIP wt%. The initial rise in QY is also accompanied by rise in PL lifetime (τ), however the lifetime continues to increase with OIP wt%. For OIP QDs embedded PMMA fibers the τ of emission increases from ~ 0.5 ns for 0.16 wt % system to ~ 16 ns for 5 wt % OIP concentration (Figure 6.10). A large increase in PLQY, in comparison to τ suggests an increase in the radiative (k_r) recombination rate [6].

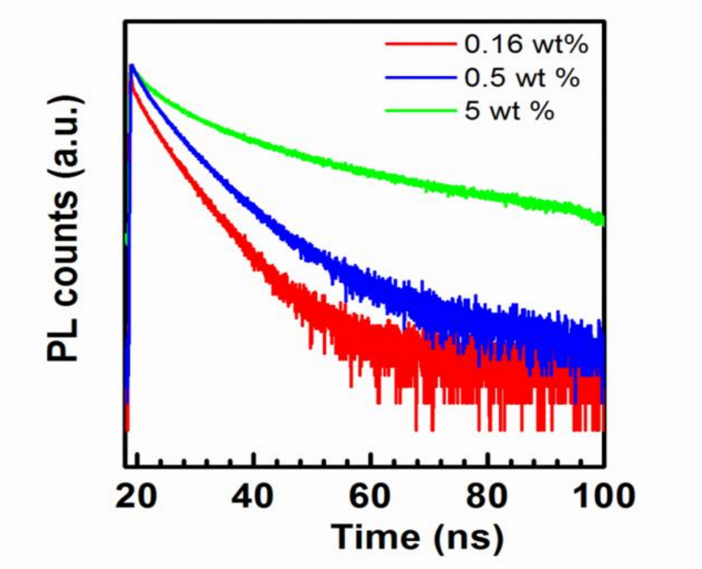

Figure 6.10: *Fluorescence lifetime measured for PMMA fibers with different OIP concentration.*

The matrix suspending the OIP QDs also acts as a surface passivation layer, which inhibits aggregation and quenching of emission. However, when the PMMA is selectively dissolved in toluene, the emission characteristics change noticeably. The emission intensity reduces significantly (PLQY ~ 6%) upon dissolving the fiber backbone in toluene, as shown in Figure 6.11. Along with the decrease in intensity, the E_{peak} of emission redshifts, this can again be linked to a weak aggregation.

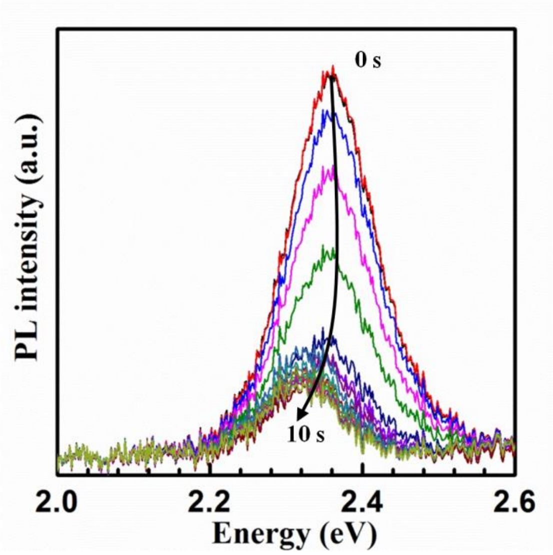

Figure 6.11: *Emission profile as a function of time after adding toluene, each spectrum has been acquired for an integration time of 100 ms.*

6.3.5: Localized emission map

Localized emission, mapped at µm resolution, using confocal microscopy can be used to investigate the microscopic homogeneity of emission across the fiber relating to QDs distribution. The emission map for a single fiber is shown in Figure 6.12a. The emission is homogeniously distributed across the length of the fiber, suggesting a uniform distribution of OIP QDs. The emission spatial width measured across the fiber is shown in Figure 6.12b. The typical emission width is ~ 2 µm, which is in agreement with the fiber width measured using AFM topography. This suggests that the QDs are equally distributed across the fiber, which allows for a continuous emission without any dead zone in between the QIP QDs.

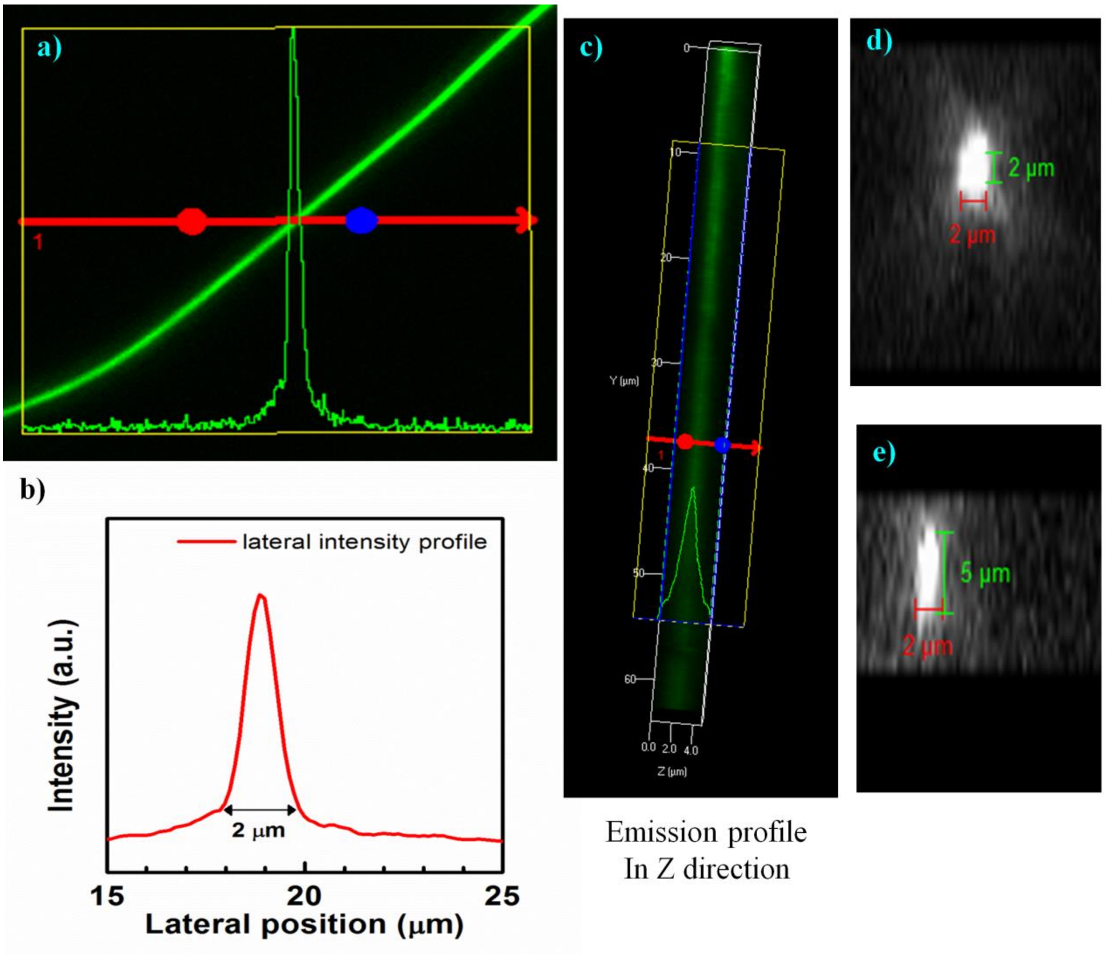

Figure 6.12: *a) localized emission map of a single fiber, b) Emission spatial profile, c) vertical emission profile, and fiber cross-section showing d) circular and e) elliptical profile.*

The transverse emission from the fiber can show uniformity in emission in the z-direction; this emission is mapped using vertical z-stack scanning. The vertical emission profile as a Z-stack for fiber is shown in Figure 6.12c. As can be noticed, the spatial width of emission along z direction is similar to the width of the fiber. This suggests that the fibers are cylindrical in construction and have a 360^0 isotropic emission. However, the shape of the fiber depends upon the spinning conditions and the cross-section can vary from circular (cylindrical) to elliptical (ribbons like) as shown in Figure 6.12d and 6.12e. This change of shape has been related to the concentration of the spinning solution which plays a significant role in controlling the shape of the fiber.

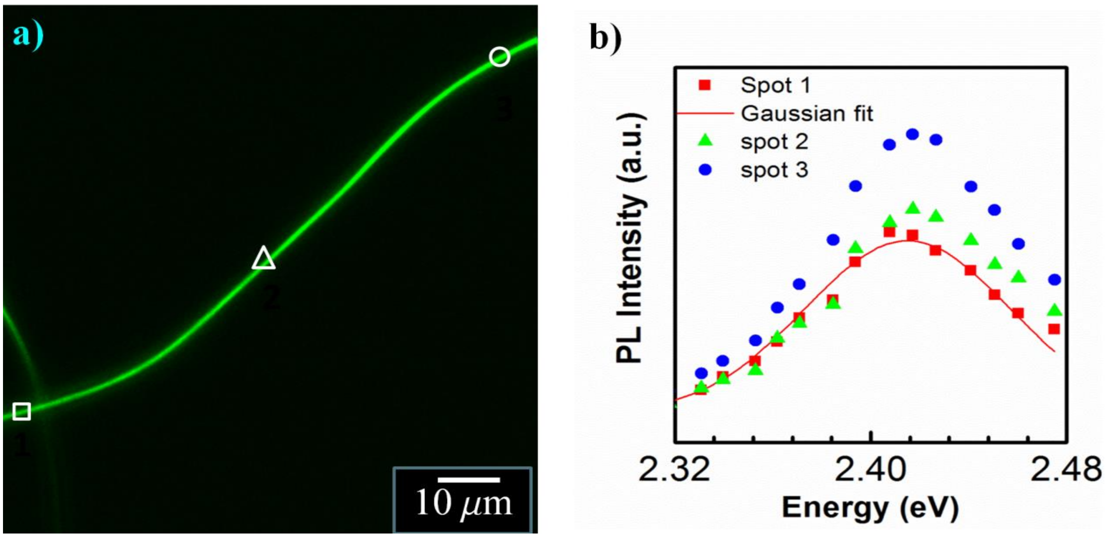

Figure 6.13: *a) localized spectral emission map and b) spectral profile at 3 regions highlighted as square, triangle, and circle.*

The localized emission spectral profile for a given fiber shows a smaller variation of emission E_{peak} from point to point, which is desirable of a color pure emitter for display applications. The local emission profile was measured using confocal lambda scan, for 3 distinct spots, as shown in Figure 6.13a, the emission E_{peak} shows negligible variation (6.13b). A small variation in emission peak over a large length scale of fiber suggests that the OIP QDs have very similar size across any given single fiber. The larger width of emission is associated with larger instrument response function, which can be reduced by using the grating-based technique for spectral measurement. The uniform emission with very small variation indicates towards a color pure emission from OIP QDs embedded PMMA fibers.

6.3.6: Waveguiding properties of luminescent fibers

A material of higher refractive index compared to the surrounding can suitably act as a waveguiding medium, given that the refractive index is significantly lower and the light does not get absorbed. The PMMA fibers can act as one such medium, allowing for the wave guiding of OIP emission. The QDs act as localized emission centers within the PMMA fiber, which forms an interesting system for studying waveguiding effect. The propagation of OIP emission in OIP/PMMA fiber is shown in Figure 6.14. The excitation spot of ~ 25 μm, is localized at the lower end of the fiber, while the emission propagates through the fiber. In general, the emission gets propagated into the fiber for 100's of μm. The fiber tip appears to be brighter than the side which is a clear signature of wave guiding.

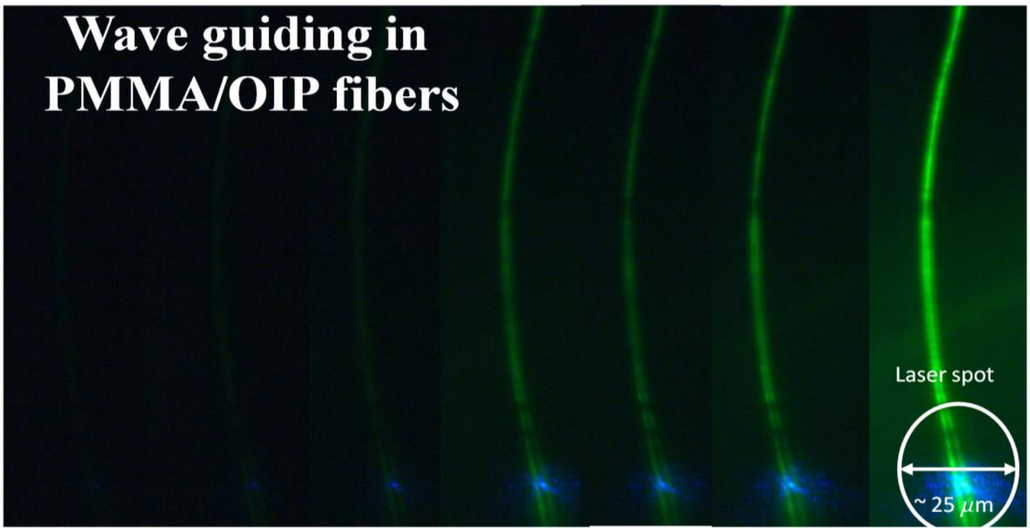

Figure 6.14: *Waveguiding of OIP emission in PMMA fiber as a function of pimp power.*

Longitudinal (ellipsoidal) OIP grains, as observed in this work, are preferred for waveguiding while the spherical grains results in improved out-coupling of emission. The difference can be associated with the direction of emission between longitudinal and spherical grains. In the case of longitudinal grains, arranged perpendicular to the fiber axis, the emission wavefront is directed parallel to the fiber axis, resulting in a larger coupling with the internal modes of the fiber. However, for spherical grains, the emission is more isotropic, resulting in a small fraction of emission getting coupled into the fiber as waveguided modes. This is also visualized in finite-domain time-difference (FDTD) simulation, where out-coupling is higher for spherical point source while the intensity of waveguided mode increases in longitudinal grains (Figure 6.15a and b). Simultaneously, the emission decay length in fiber is almost double for longitudinal particle (Figure 6.15c). (Simulation details are summarized in appendix III).

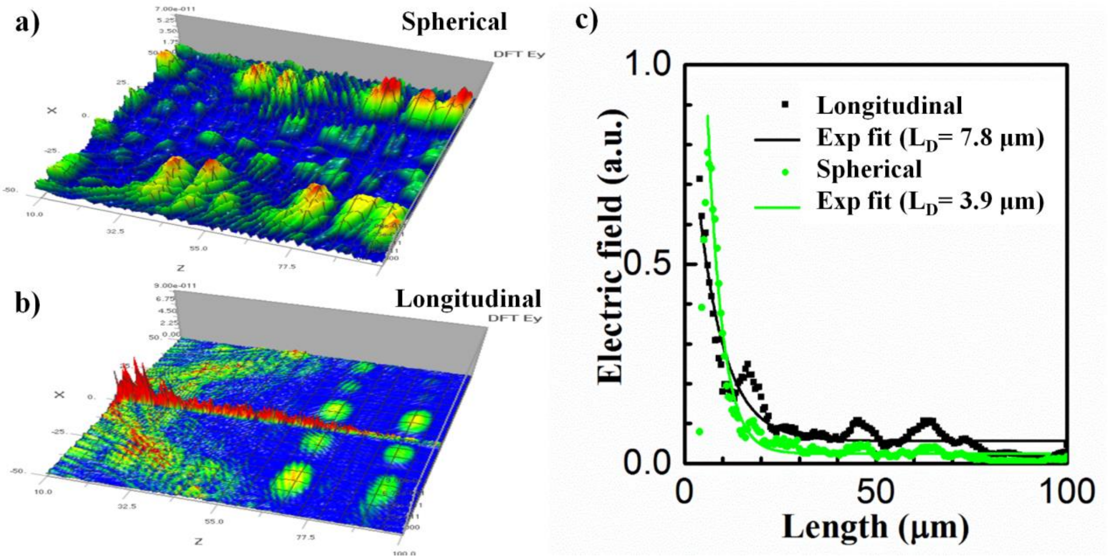

Figure 6.15: *Electric field map for a)spherical and b) longitudinal OIP grains in PMMA fiber, c) emission decay curve for spherical (circle) and longitudinal (square) grain.*

The PMMA fibers embedded with OIP QDs form an interesting system for investigating effects of photon recycling. The Stokes shift in OIP is very small (~ 10 nm) which allows for a significant absorption of emitted energy. This mechanism has been used to explain the very long distance (~ μm) propagation of photons [42]. In a bulk crystal, the mechanism involves propagation of emission accompanied by the diffusion of a free charge pair. However, in the fibers, the free carrier movement is restricted due to the localized QDs. The emission gets channeled through the fiber due to waveguiding nature, which allows for selectively investigating the effect of internal re-absorption. Additionally, the re-absorption effect can be useful for optical communication in fibers, where the emission signal can persist over a large distance.

6.3.7: Size dependence of exciton-lattice interaction

The OIP QDs demonstrate a size-dependent variation in the emission properties [41]. Modifications in the nature of emission can be explained based on effects like quantum confinement and associated lattice-exciton interaction. However, the size-tunability is difficult to achieve via non-template synthesis of OIP NCs (chapter 5) which gives a large variation of particle size. By changing the ratio of octyl ammonium bromide and methylammonium bromide, the particle shape changes from spherical to sheet-like, which make the comparison difficult [43]. In the case of OIP QDs infused PMMA fibers, the average size can be varied based on the OIP concentration. This allows for a systematic study of the size dependence of quantum confinement effect in emission, which has been followed by looking at the temperature dependence of emission. The emission as a function of temperature for different OIP concentrations is shown as a contour plot in Figure 6.16. The E_{peak}, FWHM, and integrated intensity variation, as a function of temperature, shows a strong dependence on QDs size.

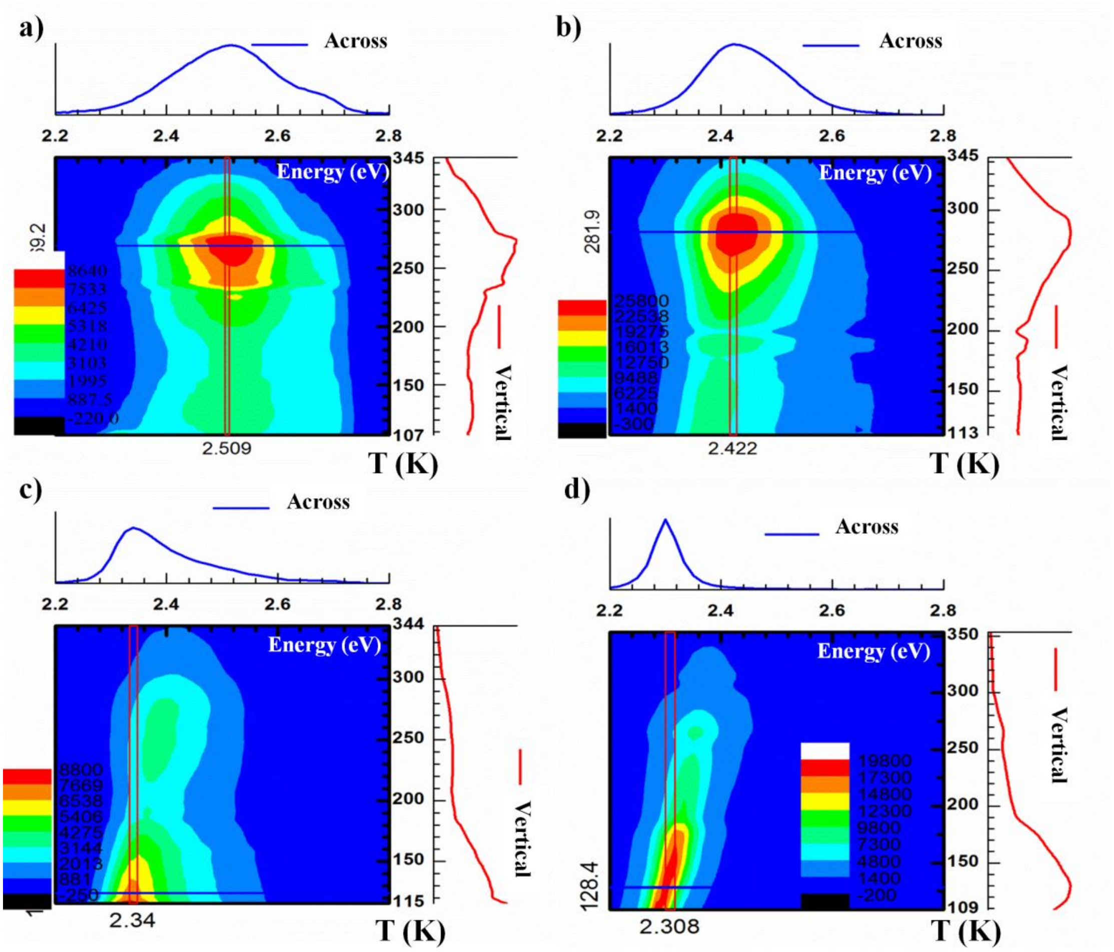

Figure 6.16: *Emission contour plot as a function of temperature for a) 0.16 wt %, b) 0.5 wt %, c) 1 wt % and d) 5 wt % of OIP.*

Some of the important points to note are,

i. The E_{peak} for 0.16 wt % QDs does not show any shift in the entire temperature range (100-350 K) (Figure 6.16a), however, the shift becomes visible at 0.5 wt % (Figure 6.16b) and is highest for 5 wt % (Figure 6.16d).

ii. The emission width (~ 0.2 eV) is constant for 0.16 wt %, throughout the temperature range. The FWHM decreases with an increase in QDs size and is almost half (~ 0.1 eV) at 5 wt %.

iii. One of the most interesting features to note is the variation in the integrated intensity which peaks at ~ 273 K for 0.16 and 0.5 wt %. However at higher concentration of 1 wt % (Figure 6.16c), the maxima in emission shifts to the lowest temperature, which overlaps with the bulk emission feature.

The nature of emission can be explained as the exciton-lattice interaction in the QDs. As was discussed in chapter 5, the emission properties of NCs get modified in presence of a stronger exciton-lattice interaction. This results in the red shift of E_{peak} and an increase in spectral broadening. A Similar feature is observed in OIP QDs which suggests an identical mechanism being responsible for the temperature dependence of emission. At low OIP concentration, the small shift in E_{peak} and FWHM is indicative of small lattice-exciton interaction which increases with QDs size. These observations support the fact that quantum confinement strengthens the exciton-lattice interactions at the nanoscale. The modification in the temperature dependence of emission at smallest QDs size (< 1-2 nm diameter) can be associated with the decrease in the interaction strength due to the reduction in the size, below a critical limit, of the crystalline domain.

6.3.8: Intensity dependence of emission

The intensity of PL as a function of excitation power is a useful tool to understand the nature of recombination. It has been argued that the recombination in bulk polycrystalline films, at low excitation densities, is dominated by the free or bound excitons [44]. The PL intensity shows a power law behavior with excitation power ($I_{incident} \propto I^{\phi}_{output}$). The exponent $1< \phi < 2$ for free or bound exciton recombination [45], $\phi = 2$ represents free carrier recombination (band-to-band transition)[46], $\phi < 1$ is an indicative of free-to-bound or donor-acceptor pair recombination [44]. In bulk OIP, at high excitation densities, the low-lying states are passivated which results in a decrease in the exciton binding energy, the magnitude of exponent ϕ increases from 1 to 2, which results from free carrier recombination [46]. A contour plot of emission vs. excitation power for OIP QDs embedded in PMMA fiber is shown in Figure 6.17a. The three distinct peaks visible in the emission spectrum can be related to particles of different size. Emission measurement was performed at ~ 100 K under a microscope based setup to ensure local excitation. The first peak from the right (peak 1) is associated with particles of larger diameter, the emission of these particles show strong quenching with temperature. Simultaneously, the emission as a function of excitation power has an exponent > 1, suggesting a free or bound exciton recombination (Figure 6.17b).

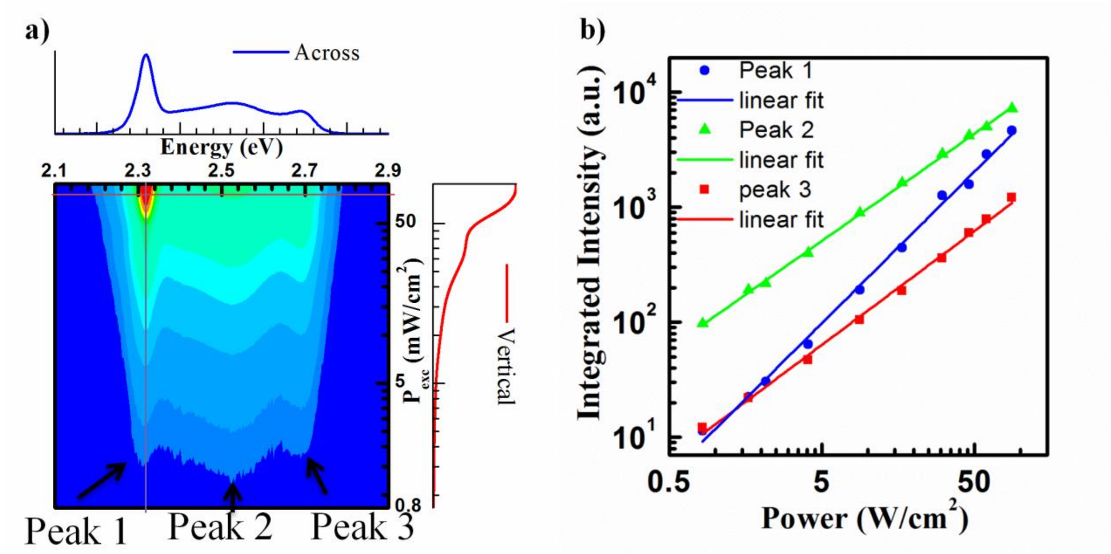

Figure 6.17: *a) Emission contour plot as a function excitation power and b) Integrated PL intensity as a function of excitation power.*

However, the emission intensity from the smaller particles, seen as peak 2 and 3, has weak temperature dependence. The integrated PL shows a sub-linear dependence ($\phi < 1$) on excitation power, suggesting a free-to-bound or donor-acceptor type recombination. Above observation is in accordance with the stronger confinement effect in smaller QDs. It is interesting to note that the value of ϕ remains constant for all the QDs over a large range of excitation density, suggesting a large exciton binding energy. This feature is advantageous for emissive layers for a linear down conversion efficiency in a wide excitation range. The OIP QD/PMMA fiber emitters show structural stability for large excitation densities (no noticeable burnout) at both room temperature and low temperature, which is useful for large power output. Excitons in QDs are localized, which can be advantageous for emission in LEDs. Excitons weakly localized can also contribute towards optical gain as they can be filled easily, unless their density is not very high, resulting in low threshold lasers [44].

6.3.9: Amplified spontaneous emission (ASE)

One of the advantages of confined morphologies, like the PMMA fibers being studied here, is the formation of internal cavities which can host interesting properties like the formation of cavity modes which can show lasing under carefully tuned cavities. Along with the confined geometric morphologies, a necessary requirement is the presence of a lasing medium like organic lasing dyes [22, 47] or other host materials [48, 49]. The OIP materials have been known to show narrowing of emission above critical excitation power. This suggests that the OIP QDs embedded in PMMA matrix can also act as a lasing medium, which can result in narrowing of emission due to the formation of cavity modes in the cylindrical PMMA fiber.

The emission from QD embedded PMMA fiber, as a function of excitation energy, is shown in Figure 6.18a. The fibers were trimmed at the edges and placed on CYTOP coated glass substrates, which forms a cylindrical cavity a few mm long. Emission was recorded at 90 degrees of the direction of excitation; the narrowing of emission being visible only in this configuration.

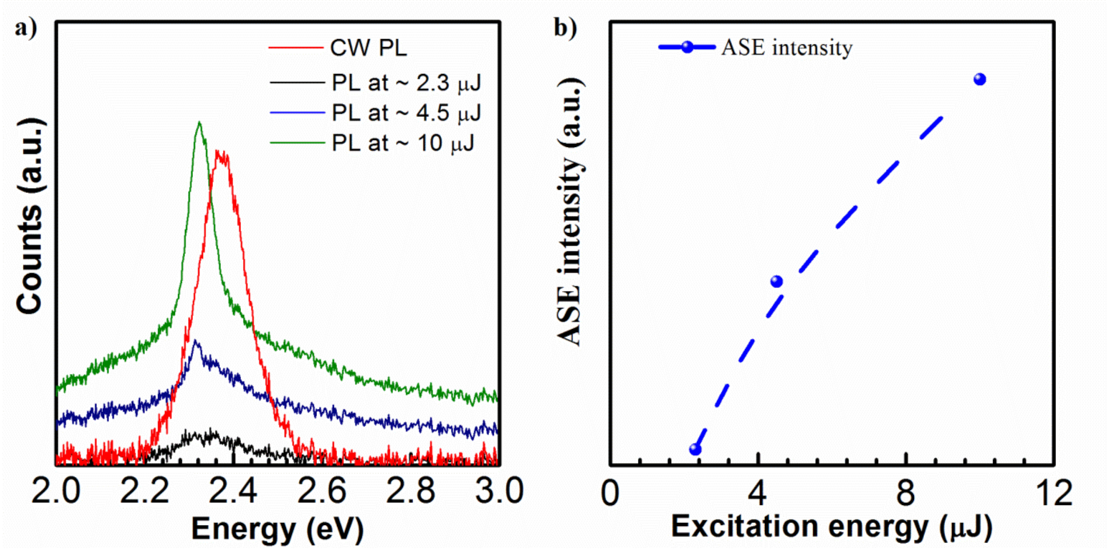

Figure 6.18: *a) ASE observed at (2.32 eV) in PL spectra and b) Excitation energy vs ASE intensity.*

One of the primary conditions for lasing is the observation of ASE which is followed by lasing at higher pulse energy. The steady state PL is shown in red, a similar PL is also visible upon excitation with a femtosecond pulse, at ~ 2.3 μJ energy. At higher excitation energy of ~ 4.5 μJ, a small shoulder is visible at 2.3 eV; selective enhancement of a particular mode in emission spectra is a typical characteristic of ASE. The ASE feature shows a saturating behavior at higher excitation energy (~ 10 μJ) (Figure 6.18b) and the spectral width reduces (~ 0.05 eV) compared to that of macroscopic PL (~ 0.1 eV). However, the emission did not show any further narrowing with further increase in excitation energy, suggesting that the geometry of the fiber does not support lasing. This can arise from the fact that the OIP medium is not continuous across the fiber, which can forbid population inversion. Further tuning of fiber structure and distribution of OIP QDs is required for lasing to occure.

6.3.10: Effects of the different dielectric matrix

The thickness of the fiber plays an important role in controlling the emission properties of the fiber. The emission spectrum of fibers spun from 3 wt % solution of OIP in PMMA and PS using DMF as the solvent is shown in Figure 6.19.

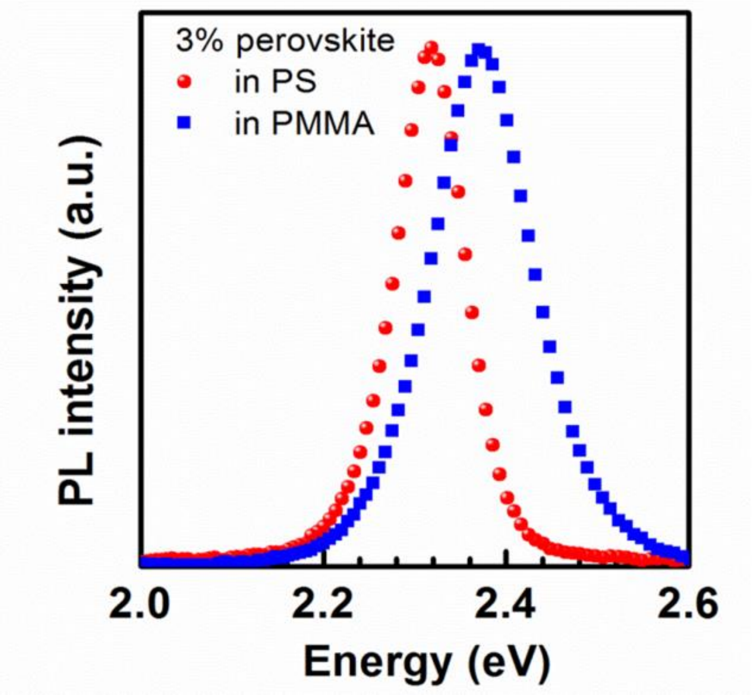

Figure 6.19: *PL profile for fibers spun from PMMA (blue square) and PS (red circles) matrix with 3 wt % OIP precursor.*

The emission E_{peak} is red shifted by ~ 0.1 eV for PS fibers and the emission width decreases by ~ 0.1 eV compared to that of PMMA fibers. Modification in the emission spectrum can be related to the increase in the thickness of PS fiber (~ 30 μm) compared to that of PMMA fiber (~ 2 μm). The thickness of PS fiber is controlled by the solubility of PS in DMF, which is lower than that of PMMA. In thicker fiber, the grain size is large compared to that for PMMA fibers and the emission intensity reduces. The emission properties of larger OIP grains resemble that of bulk OIP emission.

6.3.11: Confinement effects in methylammonium lead iodide perovskite

The blue shift observed in emission spectra of QDs compared to that of bulk, in $MAPbBr_3$, is also seen for $MAPbI_3$. The fluorescence image of PMMA fibers infused with QDs based on iodide and bromide OIP is shown in Figure 6.20a.

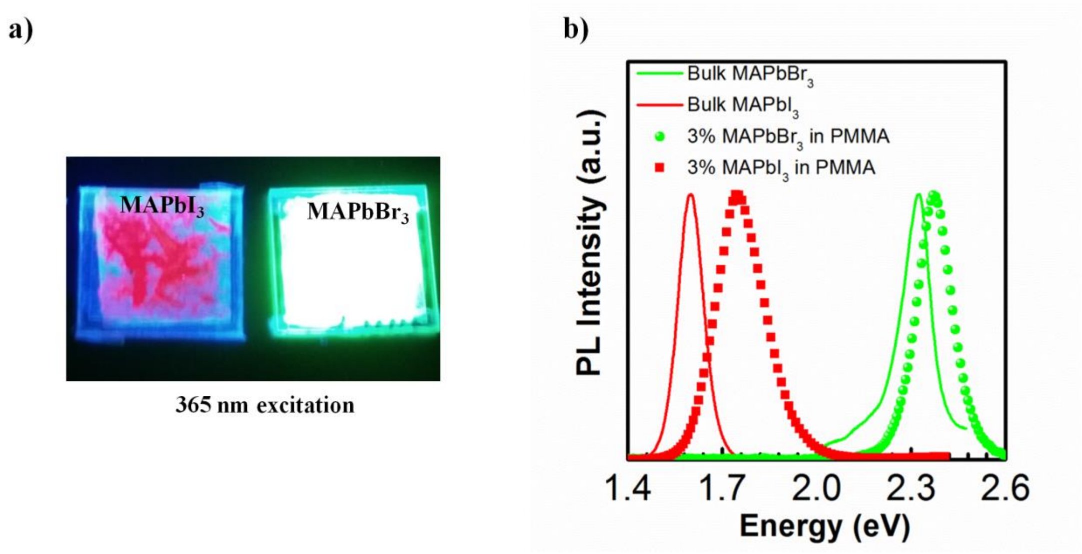

Figure 6.20: *a) Fluorescence image of I and Br-based OIP QD infused in PMMA fibers, (Note that* $MAPbBr_3$ *emission is much stronger than* $MAPbI_3$*), b) The emission spectral profile for iodide and bromide based OIP QD showing a larger shift in former.*

By changing the halide ion the emission range can be easily tuned. However, the magnitude of blue shift (~ 0.35 eV) and FWHM is much larger for $MAPbI_3$ compared to that of $MAPbBr_3$, where the QDs emission E_{peak} is shifted by ~ 0.1 eV from that of bulk (Figure 6.20b). Simultaneously, the emission quantum yield for $MAPbI_3$ is much less compared to that of $MAPbBr_3$. These observations suggest that the effect of quantum confinement has a strong dependence on the composition of OIP system. A better understanding of the formation of OIP QDs in PMMA fibers is required to explain the band gap dependence of blue shift.

6.4: Conclusion

In conclusion, the in-situ fabrication of OIP QDs embedded in a dielectric polymer fiber matrix provides an interesting, new route for the fabrication of OIP QDs based emitters. The emission quantum yield and environmental stability are much better than that of QDs made using conventional techniques. The $\alpha(E)$ and PL(E) properties show strong quantum confinement effects present in terms of the shift in the band gap, increased PLQY and a size dependent exciton-phonon interaction. The excitation power dependence of emission properties also shows a size dependent change in recombination mechanism. The fiber geometry allows wave guiding and formation of cavity modes which is a prerequisite for lasing. The fiber emission is tunable by controlling the fiber thickness and OIP concentration. The blue shift in QDs emission also shows a significant dependence on parent OIP system. Above highlighted properties suggest that the OIP QDs embedded polymer fibers form an interesting system for investigating a variety of properties like photon recycling, whispering gallery modes and lasing. They are also well suited for applications as efficient down converters in various lighting and display applications.

References

[1] H. W. Hu, T. Salim, B. B. Chen and Y. M. Lam. Molecularly Engineered Organic-Inorganic Hybrid Perovskite with Multiple Quantum Well Structure for Multicolored Light-Emitting Diodes. *Scientific Reports* **2016,** *6*, 33546.

[2] Y. H. Kim, H. Cho and T. W. Lee. Metal Halide Perovskite Light Emitters. *Proceedings of the National Academy of Sciences of the United States of America* **2016,** *113*, 11694-11702.

[3] H. Cho, S-H Jeong, M-H Park, Y-H Kim, C. Wolf, C-L Lee, J. H. Heo, A. Sadhanala, N. Myoung, S. Yoo, S. H. Im, R. H. Friend and T-W Lee. Overcoming the Electroluminescence Efficiency Limitations of Perovskite Light-Emitting Diodes. *Science* **2015,** *350*, 1222-1225.

[4] N. K. Kumawat, A. Dey, A. Kumar, S. P. Gopinathan, K. L. Narasimhan and D. Kabra. Band Gap Tuning of $CH_3NH_3Pb(Br_{1-X}Cl_x)_3$ Hybrid Perovskite for Blue Electroluminescence. *ACS Applied Materials & Interfaces* **2015,** *7*, 13119-13124.

[5] Z. Shi, Y. Li, Y. Zhang, Y. Chen, X. Li, D. Wu, T. Xu, C. Shan and G. Du. High-Efficiency and Air-Stable Perovskite Quantum Dots Light-Emitting Diodes with an All-Inorganic Heterostructure. *Nano Letters* **2017,** *17*, 313-321.

[6] P. Kumar, B. Zhao, R. H. Friend, A. Sadhanala and K. S. Narayan. Kinetic Control of Perovskite Thin-Film Morphology and Application in Printable Light-Emitting Diodes. *ACS Energy Letters* **2017,** *2*, 81-87.

[7] H. Huang, A. S. Susha, S. V. Kershaw, T. F. Hung and A. L. Rogach. Control of Emission Color of High Quantum Yield $CH_3NH_3PbBr_3$ Perovskite Quantum Dots by Precipitation Temperature. *Advanced Science* **2015,** *2*, 1500194.

[8] Y. Kim, E. Yassitepe, O. Voznyy, R. Comin, G. Walters, X. W. Gong, P. Kanjanaboos, A. F. Nogueira and E. H. Sargent. Efficient Luminescence from Perovskite Quantum Dot Solids. *ACS Applied Materials & Interfaces* **2015,** *7,* 25007-25013.

[9] Z. Y. Zhang, H. Y. Wang, Y. X. Zhang, Y. W. Hao, C. Sun, Y. Zhang, B. R. Gao, Q. D. Chen and H. B. Sun. The Role of Trap-Assisted Recombination in Luminescent Properties of Organometal Halide $CH_3NH_3PbBr_3$ Perovskite Films and Quantum Dots. *Scientific Reports* **2016,** *6*, 27286.

[10] D. Bryant, N. Aristidou, S. Pont, I. Sanchez-Molina, T. Chotchunangatchaval, S. Wheeler, J. R. Durrant and S. A. Haque. Light and Oxygen Induced Degradation Limits the Operational Stability of Methylammonium Lead Triiodide Perovskite Solar Cells. *Energy & Environmental Science* **2016,** *9*, 1655-1660.

[11] M. B. Gawande, A. Goswami, T. Asefa, H. Z. Guo, A. V. Biradar, D. L. Peng, R. Zboril and R. S. Varma. Core-Shell Nanoparticles: Synthesis and Applications in Catalysis and Electrocatalysis. *Chemical Society Reviews* **2015,** *44*, 7540-7590.

[12] R. G. Chaudhuri and S. Paria. Core/Shell Nanoparticles: Classes, Properties, Synthesis Mechanisms, Characterization, and Applications. *Chemical Reviews* **2012,** *112*, 2373-2433.

[13] S. N. Habisreutinger, T. Leijtens, G. E. Eperon, S. D. Stranks, R. J. Nicholas and H. J. Snaith. Carbon Nanotube/Polymer Composites as a Highly Stable Hole Collection Layer in Perovskite Solar Cells. *Nano Letters* **2014,** *14*, 5561-5568.

[14] S. D. Stranks and H. J. Snaith. Metal-Halide Perovskites for Photovoltaic and Light-Emitting Devices. *Nature Nanotechnology* **2015,** *10*, 391-402.

[15] Y. W. Wang, Y. H. Zhu, J. F. Huang, J. Cai, J. R. Zhu, X. L. Yang, J. H. Shen, H. Jiang and C. Z. Li. Cspbbr3 Perovskite Quantum Dots-Based Monolithic Electrospun Fiber Membrane as an Ultrastable and Ultrasensitive Fluorescent Sensor in Aqueous Medium. *Journal of Physical Chemistry Letters* **2016,** *7*, 4253-4258.

[16] C. Y. Fang, Y. L. Liu, Y. C. Lee, H. L. Chen, D. H. Wan and C. C. Yu. Nanoparticle Stacks with Graded Refractive Indices Enhance the Omnidirectional Light Harvesting of Solar Cells and the Light Extraction of Light-Emitting Diodes. *Advanced Functional Materials* **2013,** *23*, 1412-1421.

[17] K. Saxena, V. K. Jain and D. S. Mehta. A Review on the Light Extraction Techniques in Organic Electroluminescent Devices. *Optical Materials* **2009,** *32*, 221-233.

[18] D. Ficai, A. Ficai, E. Dinu, O. Oprea, M. Sonmez, M. K. Keler, Y. M. Sahin, N. Ekren, A. T. Inan, S. Daglilar and O. Gunduz. Magnetic Core Shell Structures: From 0D to 1D Assembling. *Current Pharmaceutical Design* **2015,** *21*, 5301-5311.

[19] J. Xu, H. D. Yu, L. L. Yang, G. L. Wu, Z. Q. Wang, D. Wang and X. Zhang. Self-Assembling 1d Core/Shell Microrods by the Introduction of Additives: A One-Pot and Shell-Tunable Method. *Chemical Science* **2015,** *6*, 4907-4911.

[20] M. W. Lee, S. An, S. S. Latthe, C. Lee, S. Hong and S. S. Yoon. Electrospun Polystyrene Nanofiber Membrane with Superhydrophobicity and Superoleophilicity for Selective Separation of Water and Low Viscous Oil. *ACS Applied Materials & Interfaces* **2013,** *5*, 10597-10604.

[21] H. S. Bae, A. Haider, K. M. K. Selim, D. Y. Kang, E. J. Kim and I. K. Kang. Fabrication of Highly Porous Pmma Electrospun Fibers and Their Application in the Removal of Phenol and Iodine. *Journal of Polymer Research* **2013,** *20*, s10965.

[22] A. J. Das, C. Lafargue, M. Lebental, J. Zyss and K. S. Narayan. Three-Dimensional Microlasers Based on Polymer Fibers Fabricated by Electrospinning. *Applied Physics Letters* **2011,** *99*, 263303.

[23] L. Persano, A. Camposeo, P. Del Carro, V. Fasano, M. Moffa, R. Manco, S. D'Agostino and D. Pisignano. Distributed Feedback Imprinted Electrospun Fiber Lasers. *Advanced Materials* **2014,** *26*, 6542-6547.

[24] N. J. Pinto, A. T. Johnson, A. G. MacDiarmid, C. H. Mueller, N. Theofylaktos, D. C. Robinson and F. A. Miranda. Electrospun Polyaniline/Polyethylene Oxide Nanofiber Field-Effect Transistor. *Applied Physics Letters* **2003,** *83*, 4244-4246.

[25] J. Y. Chen, H. C. Wu, Y. C. Chiu, C. J. Lin, S. H. Tung and W. C. Chen. Electrospun Poly(3-Hexylthiophene) Nanofibers with Highly Extended and Oriented Chains through Secondary Electric Field for High-Performance Field-Effect Transistors. *Advanced Electronic Materials* **2015,** *1*, 1400028.

[26] Z. Zheng, L. Gan, H. Q. Li, Y. Ma, Y. Bando, D. Golberg and T. Y. Zhai. A Fully Transparent and Flexible Ultraviolet-Visible Photodetector Based on Controlled Electrospun ZnO-CdO Heterojunction Nanofiber Arrays. *Advanced Functional Materials* **2015,** *25*, 5885-5894.

[27] B. Ding, M. R. Wang, X. F. Wang, J. Y. Yu and G. Sun. Electrospun Nanomaterials for Ultrasensitive Sensors. *Materials Today* **2010,** *13*, 16-27.

[28] S. Y. Huang, H. Wu, M. Zhou, C. S. Zhao, Z. F. Yu, Z. C. Ruan and W. Pan. A Flexible and Transparent Ceramic Nanobelt Network for Soft Electronics. *Npg Asia Materials* **2014,** *6*.

[29] M. Pollinger, D. O'Shea, F. Warken and A. Rauschenbeutel. Ultrahigh-Q Tunable Whispering-Gallery-Mode Microresonator. *Physical Review Letters* **2009,** *103*, 053901.

[30] C. Strelow, H. Rehberg, C. M. Schultz, H. Welsch, C. Heyn, D. Heitmann and T. Kipp. Optical Microcavities Formed by Semiconductor Microtubes Using a Bottlelike Geometry. *Physical Review Letters* **2008,** *101*, 127403.

[31] W. Huang, M. J. Wang, C. L. Liu, J. You, S. C. Chen, Y. Z. Wang and Y. Liu. Phase Separation in Electrospun Nanofibers Controlled by Crystallization Induced Self-Assembly. *Journal of Materials Chemistry A* **2014,** *2*, 8416-8424.

[32] K. Mondal and A. Sharma. Recent Advances in Electrospun Metal-Oxide Nanofiber Based Interfaces for Electrochemical Biosensing. *RSC Advances* **2016,** *6*, 94595-94616.

[33] W. K. Son, J. H. Youk, T. S. Lee and W. H. Park. The Effects of Solution Properties and Polyelectrolyte on Electrospinning of Ultrafine Poly(Ethylene Oxide) Fibers. *Polymer* **2004,** *45*, 2959-2966.

[34] H. Fong, I. Chun and D. H. Reneker. Beaded Nanofibers Formed During Electrospinning. *Polymer* **1999,** *40*, 4585-4592.

[35] T. S. Kang, S. W. Lee, J. Joo and J. Y. Lee. Electrically Conducting Polypyrrole Fibers Spun by Electrospinning. *Synthetic Metals* **2005,** *153*, 61-64.

[36] Geoffrey Taylor. Disintegration of Water Drops in an Electric Field. *Proceedings of the Royal Society of London. Series A. Mathematical and Physical Sciences* **1964,** *280*, 383.

[37] N. Savest, T. Plamus, E. Tarasova, M. Viirsalu, I. Krasnou, V. Gudkova, K. A. Kuppar and A. Krumme. The Effect of Ionic Liquids on the Conductivity of Electrospun Polyacrylonitrile Membranes. *Journal of Electrostatics* **2016,** *83*, 63-68.

[38] W. Cheng, Q. Yu, Z. M. Qiu and Y. R. Yan. Effects of Different Ionic Liquids on the Electrospinning of a Polyacrylonitrile Polymer Solution. *Journal of Applied Polymer Science* **2013,** *130*, 2359-2368.

[39] X. H. Zong, K. Kim, D. F. Fang, S. F. Ran, B. S. Hsiao and B. Chu. Structure and Process Relationship of Electrospun Bioabsorbable Nanofiber Membranes. *Polymer* **2002,** *43*, 4403-4412.

[40] J. J. Feng. The Stretching of an Electrified Non-Newtonian Jet: A Model for Electrospinning. *Physics of Fluids* **2002,** *14*, 3912-3926.

[41] P. Kumar, C. Muthu, V. C. Nair and K. S. Narayan. Quantum Confinement Effects in Organic Lead Tribromide Perovskite Nanoparticles. *Journal of Physical Chemistry C* **2016,** *120*, 18333-18339.

[42] L. M. Pazos-Outón, M. Szumilo, R. Lamboll, J. M. Richter, M. Crespo-Quesada, M. Abdi-Jalebi, H. J. Beeson, M. Vrućinić, M. Alsari, H. J. Snaith, B. Ehrler, R. H. Friend and F. Deschler. Photon Recycling in Lead Iodide Perovskite Solar Cells. *Science* **2016,** *351*, 1430-1433.

[43] J. A. Sichert, Y. Tong, N. Mutz, M. Vollmer, S. Fischer, K. Z. Milowska, R. G. Cortadella, B. Nickel, C. Cardenas-Daw, J. K. Stolarczyk, A. S. Urban and J. Feldmann. Quantum Size Effect in Organometal Halide Perovskite Nanoplatelets. *Nano Letters* **2015,** *15*, 6521-6527.

[44] H. P. He, Q. Q. Yu, H. Li, J. Li, J. J. Si, Y. Z. Jin, N. N. Wang, J. P. Wang, J. W. He, X. K. Wang, Y. Zhang and Z. Z. Ye. Exciton Localization in Solution-Processed Organolead Trihalide Perovskites. *Nature Communications* **2016,** *7*.

[45] H. Shibata, M. Sakai, A. Yamada, K. Matsubara, K. Sakurai, H. Tampo, S. Ishizuka, K. K. Kim and S. Niki. Excitation-Power Dependence of Free Exciton Photoluminescence of Semiconductors. *Japanese Journal of Applied Physics Part 1-Regular Papers Brief Communications & Review Papers* **2005,** *44*, 6113-6114.

[46] Y. Yamada, T. Nakamura, M. Endo, A. Wakamiya and Y. Kanemitsu. Photocarrier Recombination Dynamics in Perovskite $CH_3NH_3PbI_3$ for Solar Cell Applications. *Journal of the American Chemical Society* **2014,** *136*, 11610-11613.

[47] B. B. McFarland B. H. Soffer. Continuously Tunable, Narrow-Band Organic Dye Lasers. *Applied Physics Letters* **1967,** *10*, 266-267.

[48] H. M. Zhu, Y. P. Fu, F. Meng, X. X. Wu, Z. Z. Gong, Q. Ding, M. V. Gustafsson, M. T. Trinh, S. Jin and X. Y. Zhu. Lead Halide Perovskite Nanowire Lasers with Low Lasing Thresholds and High Quality Factors. *Nature Materials* **2015,** *14*, 636-U115.

[49] S. A. Veldhuis, P. P. Boix, N. Yantara, M. J. Li, T. C. Sum, N. Mathews and S. G. Mhaisalkar. Perovskite Materials for Light-Emitting Diodes and Lasers. *Advanced Materials* **2016,** *28*, 6804-6834.

Chapter 7: Summary and Future Directions

The thesis investigates different families of solution-processed semiconductors and metal electrodes for printable electronics applications. Adhesion properties of low temperature meltable eutectic solder alloys were studied, the improvement observed in adhesion was attributed to charge transfer state formed between constituent indium metal and donor and/or acceptor polymer. Increase in optical activity and superior electrical properties of alloy result from improved adhesion with the polymer layer. It was concluded that small quantities of indium can be useful in significantly improving the applicability of the solder alloys.

In the next part, the model tunable system of inorganic and organic bilayer hybrid interface was discussed. Large band gap n-doped Gallium nitride was paired with solution processed organic donor/acceptor semiconductors to study the charge transport characteristics of the hybrid interface. Photoresponse of donor polymer/gallium nitride interface showed the strong influence of strain induced polarization in gallium nitride layer. External bias was used to tune the response from antibatic (at no bias) to symbatic (at a reverse bias). Gallium-nitride/polymer hybrid system was shown to function as a detection range tunable photodiode.

Morphology aspects of bulk hybrid perovskite active layer were discussed in next section, organic small molecule mediated anti-solvent route was used to significantly tune the macroscopic morphology. Surface features of perovskite thin films showed resemblance to stacking nature of the organic additive molecules. Modified films demonstrated a significant decrease in below gap energetic disorder and a corresponding increase in photoluminescence yield. Eutectic alloys were used in conjugation with solution processed, pin-hole free perovskite films to fabricated, all solution processed, vacuum free, printable light emitting diode structures, which demonstrated moderate efficiencies.

Perovskite nanocrystals, as a stable alternative to bulk perovskite, were studied in next section. Nanocrystals of average size ~ 6 nm showed signatures of onset of quantum confinement effects as the blue shift observed in absorbance and emission characteristics. The increase in exciton binding energy for nanocrystals becomes evident as a larger excitonic peak in absorbance, observed at lower temperatures (~ 100K). The emission peak shape and broadening changes a function of temperature, the larger variation observed in nanocrystals suggests confinement induced increase in exciton-lattice interaction. Single pixel emitter-detector combination was demonstrated with nanocrystals coupled with organic acceptor molecule in bilayer architecture.

One-dimensional core-shell structure of perovskite quantum dots embedded in Poly(methyl methacrylate) fibers, fabricated using electrospinning, were looked upon in the final section. Quantum dots form in-situ, during the stretching of the polymer solution, resulting from the phase separation of materials with different dielectric constant. A control on particle size, absorption edge and emission characteristics were obtained by changing the perovskite to polymer ratio in the solution. Fibers demonstrate excellent emission yield with a noticeable waveguiding property, which was utilized to display low threshold amplified spontaneous emission. Emission properties show a significant dependence on perovskite composition, with smaller band gap systems showing a larger blue shift in emission.

Future directions

The large area printing of eutectic alloys will be feasible by further improving the adhesion strength with the polymer layer. Indium is critical to realize efficient performance; however, indium is rare and expensive, thus requiring exploration of other abundant metals as a replacement. The processability of eutectic alloy needs further improvement by modeling it into a printer friendly suspension/ink.

Perovskites/polymer hybrid interface is a promising platform which requires further examination for realizing new device structures for novel applications in energy harvesting, sensors, and displays.

Perovskite nanomaterials are versatile systems with notable features suitable for studying fundamental physical aspect while being useful for a multitude of applications in devices. Quantum dot-polymer hybrids require further investigations to understand the emission characteristics and its dependence on material parameters.

Appendix 1: Dark I-V Response

The dark I-V characteristics (equation 1) was simulated in MATLAB,

MATLAB code for simulated absorption is given below,

```
% pv model
clc;
clear all;
k = 1.38065e-23; % Boltzmann constant
q = 1.602e-19; % unit charge
tD = 25+273; % working temperature in K
n = 2.1; % diode ideality factor
izero = 8.0e-11; % reverse saturation current density
rs = 4; % series resistance
rsh = 800; % shunt resistance

Vtn = (n*k*tD/q);

I = zeros(90,1);
i=1;
I(1,1)=0;
for V=0.01:0.01:0.91
    I_part = izero*(exp((V-(I(i,1)*rs))/Vtn)-1)+((V-(rs*I(i,1)))/rsh);
    I(i+1) = I_part;
    V1(i) = V;
    i=i+1;
end
```

```
V1(i)=V1(i-1);
V1=transpose(V1);
plot (V1,I);
```

The I-V response shows small variation with R_s, as is shown in Figure A1.1. Comparing simulation results with the experimental I-V response for 35% indium alloy cathode, suggests a value close to 4 Ω for R_s for alloy cathodes.

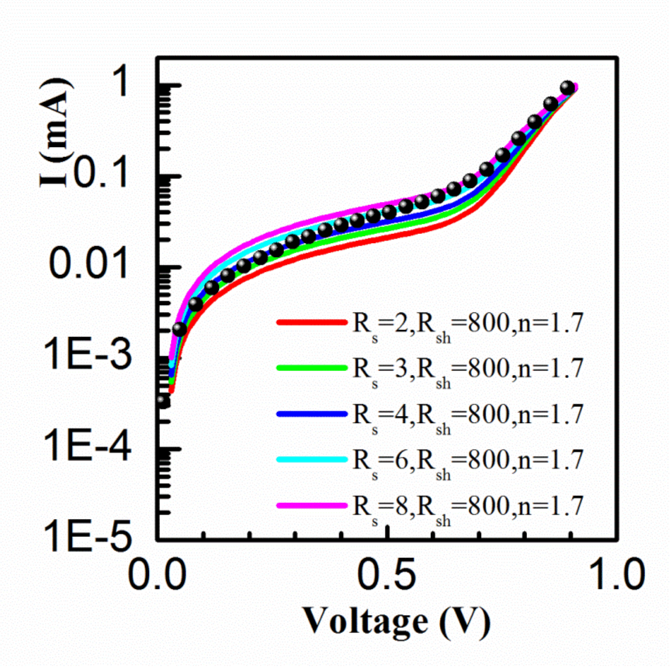

Figure A 1.1: Simulated Dark I-V response as a function of R_s, experimental data is shown as circles.

However, the current magnitude varies significantly with R_{sh} as is shown in Figure A1.2. It should be noted that the magnitude of R_{sh} should be much higher than R_s and large variations in the value are generally permitted. The simulated I-V curve resembles experimental data for R_{sh} value ~ 1000 Ω.

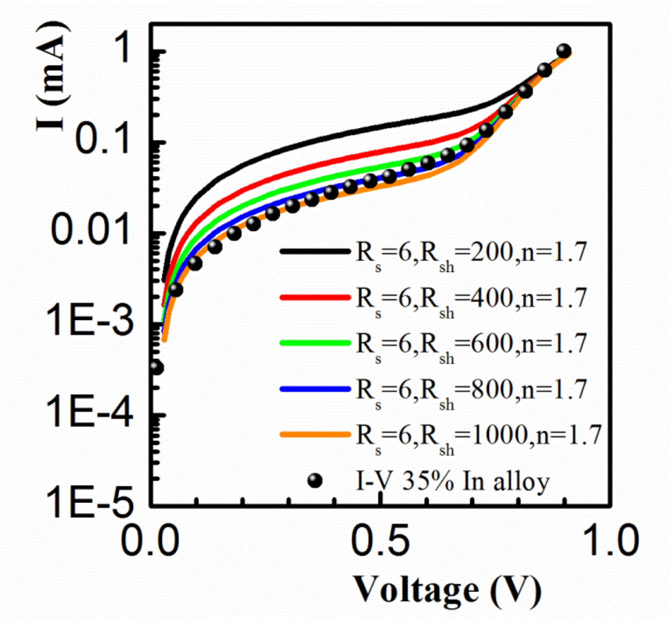

Figure A 1.2: Simulated Dark I-V response as a function of R_{sh}, experimental data is shown as circles.

The manitude of *n* for the experimental curve is close to 1.75, as is evident from Figure A1.3.

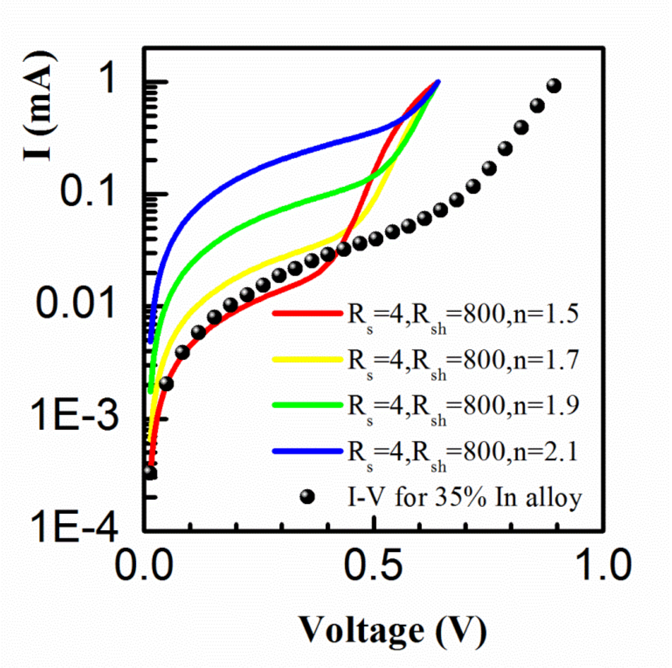

Figure A 1.3: Simulated Dark I-V response as a function of *n*, experimental data is shown as circles.

Appendix 2: Elliot’s Theory for Absorption

Modified Elliot’s theory for Wannier excitons,

$$\begin{aligned}&\alpha(\hbar\omega)\\ &\propto \mu_{cv}^2\sqrt{E_b}\left[\sum_n \frac{2E_b}{n^3}\, sech\left(\frac{\hbar\omega - E_g - \left({}^{E_b}\!/_{n^2}\right)}{\Gamma}\right)\right.\\ &\left.+\int_{E_g}^{\infty} sech\left(\frac{\hbar\omega - E}{\Gamma}\right)\left(\frac{1}{1-exp\left(-2\pi\sqrt{{}^{E_b}\!/_{E-E_g}}\right)}\right)\left(\frac{1}{1-\frac{8\mu_b}{\hbar^3}\left(E-E_g\right)}\right)\right]\end{aligned} \tag{A}$$

Where μ_{CV} is the transition dipole moment, E_b is the exciton binding energy, E_g is the band gap.

MATLAB code for simulated absorption is given below,

```
close all;
 clear all;
  mu_cv=1;
  eg=2.36;
 eb=0.08;
  mubh=1;
  gamma=0.07;
  alpha=0;
  beta=0;
   for k=1:500;
    domega =0.001;
    omega=2+domega.*k;
    omega1(k)=omega;
```

```
 for i=1:100;
     a1=omega-(eg-(eb/i^2));
     beta=beta+(2*eb/i^3)*sech(a1/gamma);
 end
 for j=1:1000;
     deltaeg=eg/10;
     %e=eg+(j-1)*deltaeg;
     e=eg+(j-1)*deltaeg;
     a2=1/(1-exp(-2*pi*sqrt(eb/(e-eg))));
     a3=1/(1-mubh*(e-eg));
     a4=sech((omega-e)/gamma);
     delta(j)=a2*a3*a4;
  end
  alpha=((mu_cv^2)/omega)*(beta+trapz(delta));
 alpha1(k)=alpha;
      end
  y=[omega1' alpha1'];
  %x=100:300;
  dlmwrite('0.05 0.15 1.txt',y);
plot(y(:,1),y(:,2))
hold on;
```

Appendix 3: FDTD Simulation Details

Simulations were performed using Optiwave 32 bit software.

Materials parameter,

Material	Refractive index
PMMA	1.5
Perovskite	2.8-3.0

For simulation, the fiber length was 100 µm and width of 2 µm. Ellipsoidal perovskite particles (length = 100 nm, width = 20 nm) were used replicated the perovskite quantum dots in fiber. Ellipsoidal particles were simulated with 7 point source as shown in Figure A3.1.

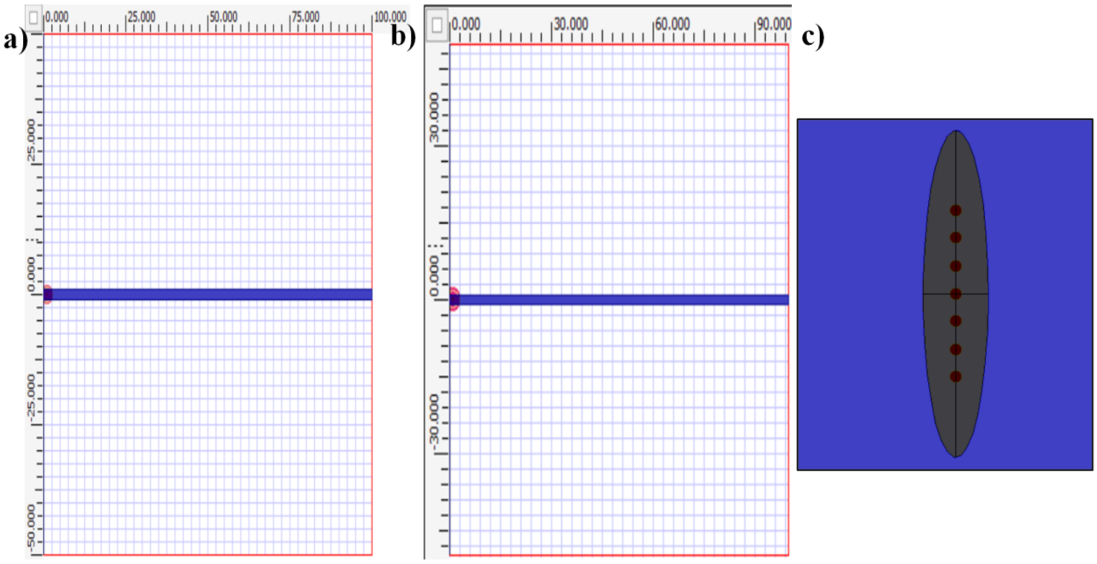

Figure A3.1: Geometry of fiber and perovskite particles used for simulation, a) spherical particle in fiber. B) Ellipsoidal particle. C) Construction of ellipsoidal particles.